Dissertation
submitted to the
Combined Faculties for the Natural Sciences and for Mathematics
of the Ruperto-Carola University of Heidelberg, Germany
for the degree of
Doctor of Natural Sciences

presented by

Diplom-Physicist:	Andreas Lotter
born in:	Füssen

Oral examination: 5.7.2006

Field Measurements of Water Continuum and Water Dimer Absorption by Active Long Path Differential Optical Absorption Spectroscopy (DOAS)

Referees: Prof. Dr. Klaus Pfeilsticker
Prof. Dr. Frank Arnold

Feldmessungen von Wasserkontinuum- und Wasserdimerabsorption mit Hilfe der aktiven Langpfad-DOAS-Methode

Wasserdampf spielt eine entscheidende Rolle für die Strahlungsbilanz der Erde, denn Wassermoleküle absorbieren die einfallende Sonnenstrahlung und behindern die thermische terrestrische Abstrahlung. Eine den Absorptionsbanden des Wassermonomers überlagerte Wasserkontinuumabsorption ist seit langem bekannt, aber deren eigentliche Ursache ist noch immer umstritten. Einerseits wird diese Absorption dadurch erklärt, dass sich aufgrund molekularer Stöße die Form der Wassermonomerlinien ändert. Andererseits tragen Wasserdimere möglicherweise zum Wasserkontinuum bei. Mit Hilfe der Langpfad-DOAS-Methode wurden Feldmessungen durchgeführt, um die Wasserkontinuum- und Wasserdimerabsorption im sichtbaren und nahen infraroten Spektralbereich zu untersuchen. Für die Messungen wurden die Spektralbereiche der 4ν, $4\nu+\delta$ und 5ν Wasserbanden gewählt. Rechnungen zeigen, dass hier drei Wasserdimerbanden existieren, die kaum von den starken Banden des Wassermonomers überlagert sind. In dieser Arbeit wird gezeigt, dass die Qualität verfügbarer spektraler Datenbanken nicht ausreicht, um genaue Referenzspektren des Wassermonomers zu liefern damit die überlagerte Absorption des Wasserdimers eindeutig nachgewiesen werden kann. Deshalb können nur obere Grenzwerte der Wasserdimerabsorption ermittelt werden. Für die Gleichgewichtskonstante des Wasserdimers lässt sich eine Obergrenze von $K_P(301\,K) = 0.055\,atm^{-1}$ ableiten. Die spektrale Breite der Wasserdimerbanden beträgt mindestens $40\,cm^{-1}$ (FWHM). Eine Wasserkontinuumabsorption wurde in allen drei Spektralbereichen nachgewiesen. Die gemessene Kontinuumabsorption liegt in der gleichen Größenordnung wie sie von den semi-empirischen Modellen CKD_2.4.1 und MT_CKD_1.0 vorhergesagt wird. Dagegen liegt die Vorhersage nach der Theorie von Ma und Tipping unter der gemessenen Kontinuumabsorption, eine Größenordnung für die 4ν und 5ν, zwei Größenordnung für die $4\nu+\delta$ Wasserbande. Nach dem heutigen Kenntnisstand der spektroskopischen und thermochemischen Eigenschaften des Wasserdimers, ist ihr Beitrag zum gemessenen Wasserkontinuum im sichtbaren und nahen infraroten Spektralbereich unbedeutend.

Field Measurements of Water Continuum and Water Dimer Absorption by Active Long Path Differential Optical Absorption Spectroscopy (DOAS)

Water vapor plays an important role in Earth's radiative budget since water molecules strongly absorb the incoming solar shortwave and the outgoing thermal infrared radiation. Superimposed on the water monomer absorption, a water continuum absorption has long been recognized, but its true nature still remains controversial. On the one hand, this absorption is explained by a deformation of the line shape of the water monomer absorption lines as a consequence of a molecular collision. One the other hand, water dimers possibly contribute to water continuum absorption. Field measurements addressing water continuum and water dimer absorption in the visible and near-infrared spectral region were carried out by means of active Long Path DOAS. The spectral regions of the 4ν, $4\nu+\delta$, and 5ν water polyads were selected for the measurements. In these regions three water dimer absorption bands are predicted to exist almost free of interference by strong water monomer absorption. Within the scope of this thesis it is shown that the quality of existing spectral line databases is insufficient to provide accurate water monomer references in order to confidently detect superimposed water dimer absorption. Therefore, only upper limits of water dimer absorption are obtained. An upper limit of $K_P(301\,K) = 0.055\,atm^{-1}$ is inferred for the water dimer equilibrium constant. The water dimer band broadening is at least $40\,cm^{-1}$ (FWHM). Water continuum absorption is detected in all three water bands. The measured water continuum absorption and the predictions by the semi-empirical CKD_2.4.1 and MT_CKD_1.0 water continuum models are of same order of magnitude. In contrast, the Ma and Tipping far wing line shape theory underestimates water continuum absorption by one order of magnitude in the 4ν and 5ν water bands, and by two orders of magnitude in the $4\nu+\delta$ water band. Based on the present state of knowledge about the spectroscopic and thermochemical properties of the water dimer, their contribution to the observed water continuum absorption in the visible and near-infrared spectral region is minor.

Contents

1 Introduction

Water plays a decisive role in Earth's ecosystem in its gaseous, liquid, and solid states. Atmospheric water vapor in particular is of central importance in Earth's climate system as it is responsible for approximately 60% of the natural greenhouse effect [*Kiehl and Trenberth* 1997]. The equilibrium state of climate is very sensitive to the abundance of water vapor, which itself is controlled by the atmospheric temperature and hence climate. This feedback is governed by non-linear interaction processes of atmospheric water vapor and temperature. Due to the presence of clouds, the climate system is further complicated.

Solar shortwave radiation is absorbed by water vapor to a great extent. A conspicuous discrepancy between the prediction of climate models and observations has been a major concern for several decades, a problem commonly referred to as anomalous, or excess, absorption [e. g. *Ramanathan and Vogelmann* 1997]. Various attempts have been made to resolve the problem. One suggestion is that the missing absorption in the models is related to water vapor, including concerns about the quality of spectral line databases [*Arking* 1996; *Chagas et al.* 2001], water vapor continuum absorption, and the absorption by water vapor dimers [*Chýlek and Geldart* 1997].

The absorption by water vapor is characterized by a strong and complex ro-vibrational spectrum due to the asymmetry and permanent dipole moment of the water molecule. Various spectral line databases, such as the High Resolution Transmission database HITRAN [*Rothman et al.* 2005], list tens of thousand individual rotational and rotational-vibrational spectral lines of water vapor across a vast spectral region that covers the entire infrared and extends into the visible. Superimposed on this spectral line absorption, a broadband continuum absorption has long been recognized throughout the entire infrared and microwave region. One early suggestion of the nature of water continuum absorption was given by *Elsasser* [1938b] being the cumulative contribution of the far wings of water vapor absorption lines. *Penner and Varanasi* [1967] claimed that water continuum absorption is mainly due to weakly bound water dimers. The climate community, however, evaded this controversy about the true nature of continuum absorption by adopting the semi-empirical Clough-Kneizys-Davies (CKD) water continuum formulation [*Clough et al.* 1989] in the majority of atmospheric line-by-line radiative transfer codes used in climate modeling. The CKD water continuum

model originally was tuned to fit measurements performed in the microwave region and now is consistently applied to all wavelength up to the shortwave region. The latest formulations of the CKD continuum model work well in radiative transfer codes, but lack physical justification. Recently, *Ptashnik et al.* [2004] provided evidence that the CKD continuum implicitly includes water dimer absorption. Although it is now widely accepted by the atmospheric science community that different mechanisms are responsible for water continuum absorption, the far wing contribution, the metastable water dimers, and the truly bound water dimers [*Camy-Peyret and Vigasin* 2003], a lack of fundamental theoretical understanding still remains.

Besides the topic of atmospheric radiative transfer, water dimers may also be important in atmospheric photochemistry, since some gas-phase reactions require two water molecules or possibly the water dimer. Of great interest is the formation of sulfuric acid and sulphate aerosols by the catalytic effect of two water molecules [*Kolb et al.* 1994; *Jayne et al.* 1997; *Loerting and Liedl* 2000]. Also the night time chemistry of nitrogen oxides [*Mentel et al.* 1996; *Wahner et al.* 1998] and HO_2 radical reactions [*Aloisio et al.* 2000] possibly involve the water dimer.

Further, water dimers are of great interest in basic molecular physics and chemistry. The water dimer represents the archetype for aqueous hydrogen bonding, upon which the unusual properties of the liquid and solid phases of water are based. The formation of a water dimer is the first step of homogeneous nucleation of water vapor into bulk water. Studies of water clusters in general can elucidate the basic physics of the hydrogen bond network in liquid water [*Keutsch and Saykally* 2001; *Huneycutt and Saykally* 2003].

Various experimental studies addressing water continuum and water dimer absorption have been published [see, e. g., review by *Ptashnik* 2005]. Most of these experiments are performed under equilibrium laboratory conditions, whereas the number of atmospheric field studies is small, since they require high standards of instrumentation and measurement technique. Hence, it is not surprising that to date atmospheric water dimer absorption has eluded detection. A powerful measurement technique of particular suitability for atmospheric applications is *Differential Optical Absorption Spectroscopy (DOAS)* [*Platt et al.* 1979; *Platt* 1994], which was utilized for the field measurements conducted within the framework of the present thesis.

The present thesis describes measurements carried out during a total of three field campaigns, two of which conducted in the mid latitudes and one in the tropics. As previous attempts to detect atmospheric water dimer absorption by the spectroscopy of scattered sky light yielded negative results [*Daniel et al.* 1999; *Hill and Jones* 2000], the problem is approached by maximizing the sampling in the near-surface atmospheric layer rich in water, by the use of an active Long Path DOAS instrument. It is possible

to realize well defined horizontal absorption paths of 18 – 29 km total length, allowing for a absorption sensitivity of typically $(3 - 5) \times 10^{-10}$cm^{-1} with the used instrumental setup. The spectral regions are chosen to cover the 4ν, $4\nu+\delta$ and 5ν water polyads (550 nm – 760 nm), since three water dimer absorption bands are predicted to exist almost free of interference by strong water monomer absorption there [*Low and Kjaergaard* 1999; *Schofield and Kjaergaard* 2003].

Based on the present long path DOAS measurements, a first evidence of atmospheric water dimer absorption at 749.5 nm by the $|0\rangle_{\mathrm{f}}|4\rangle_{\mathrm{b}}$ OH stretching mode transition was reported recently [*Pfeilsticker et al.* 2003]. The results are in reasonable agreement with the known thermochemistry [*Curtiss et al.* 1979] and predicted spectroscopic signature [*Low and Kjaergaard* 1999] of the water dimer. Unfortunately, this first evidence for atmospheric water dimer detection has to be revoked, as the findings can not be confirmed by subsequent measurements in the tropics.

2 Earth's Radiative Energy Budget

Weather and climate on Earth have a profound influence on any form of life. Changes of climate occurred repeatedly in Earth's history with fatal consequences for some species. Throughout the last 10 000 years the climate has been extremely stable, but now there is strong scientific evidence that human activity is already influencing the climate [*IPCC* 2001], especially global warming. This will lead to large changes in most ecosystems, thus it is essential to understand the system that determines the climate and the processes leading to climate change.

"Climate" is defined as average weather in terms of the mean and its variability of relevant quantities over a certain period of time and a certain area. "Climate change" refers to statistically significant variations of the mean state of climate or of its variability, typically persisting for decades or longer. In general, the climate depends on factors that influence the global radiative balance. These factors are mainly the solar radiation and the atmospheric composition. Nearly every process in Earth's climate system is a consequence of conversion of incoming solar radiation energy into thermal energy, heating the atmosphere, the surface, and the ocean. The climate system is very complex, a multitude of physical and chemical processes and various components have to be considered: the dynamics and composition of the atmosphere and of the ocean, the land surface including ice and snow cover, and many interaction processes between all those constituents. For this work the attention is directed to the atmosphere and the absorption of incoming solar shortwave and outgoing terrestrial infrared radiation.

The following sections introduce the basics of radiative transfer and the interaction processes of electromagnetic radiation with atmospheric constituents (e. g. air molecules, aerosol particles, cloud droplets, ice particles). Earth's global annual mean energy budged is presented and the influence of various greenhouse gases and climate feedbacks is discussed. In particular, the role of water vapor is emphasized, for it is central to climate and its variability and change. A comprehensive discussion of atmospheric radiative transfer is given in the textbook by *Goody and Yung* [1989], scattering and absorption processes are described in detail by *Bohren and Huffman* [1998].

2.1 Basics of Radiative Transfer

2.1.1 Definitions

The *radiant flux density* is defined as *radiant flux* dI per unit area dA, measured in $\mathrm{W/m^2}$. That quantity incident per unit area upon a surface is also called *irradiance*

$$E = \frac{dI}{dA} \tag{2.1}$$

Considering the radiation incident at an angle θ to the normal of the surface and contained within a solid angle $d\Omega$, we obtain the *radiance*

$$L_\theta = \frac{dI}{dA \cos\theta \, d\Omega} \tag{2.2}$$

As can be seen easily, the radiance is defined as the power per unit projected area per unit solid angle and is given in $\mathrm{W/(m^2 sr)}$. The irradiance is obtained from the radiance by integrating over a half sphere

$$E = \int_{\varphi=0}^{2\pi} \int_{\theta=0}^{\pi/2} L_\theta \cos\theta \, d\Omega \qquad (= \pi L \quad \text{for isotropic radiation}) \tag{2.3}$$

Both quantities defined per unit wavelength interval at a given wavelength are called *spectral irradiance* E_λ and *spectral radiance* L_λ respectively.

From a thermodynamic rather than a radiometric point of view, the basic quantity for radiation is the *energy density* ρ, measured in $\mathrm{W/m^3}$. The radiant flux crossing the area dA is $dI = dA\rho c$ for a collimated beam. Following Equation 2.1, the flux density (irradiance) is

$$E = \int_\Omega L \, d\Omega = \rho c \qquad \text{(collimated radiation)} \tag{2.4}$$

with c being the speed of light. If the radiation is isotropic, Equation 2.4 becomes

$$E = L \int_{4\pi} d\Omega = \rho c$$

and therefore

$$L = \rho c / 4\pi \qquad \text{(isotropic radiation)} \tag{2.5}$$

In thermodynamic equilibrium the spectral energy density of radiation is given by the Planck distribution

$$\rho\,(\lambda, T) = \frac{8\pi hc}{\lambda^5} \frac{1}{e^{hc/\lambda kT} - 1} \qquad (\mathrm{J\ m^{-3}\ nm^{-1}}) \tag{2.6}$$

If the radiation is isotropic Equation 2.5 may be applied to give the radiance of a black body source

$$L_B\,(\lambda, T) = \frac{2hc^2}{\lambda^5} \frac{1}{e^{hc/\lambda kT} - 1} \qquad (\mathrm{W\ m^{-2}\ sr^{-1}\ nm^{-1}}) \tag{2.7}$$

2.1.2 Interaction of Radiation and Matter

Two types of processes can be classified, extinction and emission of radiation. Extinction can be divided into scattering and absorption. The subdivision depends on the physical process involved, in particular changes of internal or kinetic energy of the particle. For an elastic scattering process the energy of the incident and scattered photon is the same, no energy is transformed to the scattering particle in form of kinetic or internal energy. Else, the scattering process is inelastic and called absorption. As the matter of interest is basically molecules, exhibiting electronic, vibrational, and rotational internal levels of energy, any change to a higher energetic state is commonly also called absorption. If the absorbed photon, however, is re-emitted, there is no conversion to translational, i. e. kinetic and hence thermal energy. Considering the total energy, then the process is one of pure scattering. The difference in the usage of the term absorption has to be kept in mind and the meaning should be clear from the context. When the question is about Earth's energy budget and heating of the atmosphere, the conversion into thermal energy is of interest. For the method of absorption spectroscopy on the other hand, only the loss of a photon from its initial path is of importance.

The physics of elastic scattering relies on the fact that matter is composed of discrete electric charges. The oscillating electromagnetic field of the incident wave induces oscillating dipoles in the particle, which for themselves radiate electromagnetic waves as scattered light. Scattering depends on wavelength (λ), particle size (d) and particle shape. A first theory of scattering by spherical particles was developed by *Mie* [1908].

If the dimension of a scattering particle is small compared to the wavelength of the incident radiation ($d \ll \lambda$), which is the case for air molecules, the intensity of the scattered radiation shows a $1/\lambda^4$ dependence on wavelength as is predicted by the theory of a single oscillating dipole. This limiting case of the Mie theory is commonly refereed to as *Rayleigh scattering*. The phase function of Rayleigh scattering for initially unpolarized radiation is $p(\theta) = 0.75 \cdot (1 + \cos^2 \theta)$, i. e. only a weak angular dependence is existing. Taking into account a molecular anisotropy and the wavelength dependent refractive index, slight modifications have to be applied [*Penndorf* 1957].

Scattering theory is more complicated if the dimension of a scattering particle is roughly of the same order of magnitude as the wavelength of the incident radiation ($d \geq \lambda$). The scattered radiation results from the interference of a number of oscillating dipoles in the particle. This case is often referred to as *Mie scattering*. A number of numerical models exist to calculate extinction coefficients and phase functions for a given particle size distribution [e. g. *Wiscombe* 1980]. Compared to Rayleigh scattering an important difference is the strong emphasis of the forward direction of the scattered light. The dependence of the extinction coefficients on wavelength for Mie scattering is weak, given by $\lambda^{-0.5 \pm 1}$ for the size distribution of atmospheric aerosol [*Junge* 1961].

Finally, if the dimension of a particle is much larger than the wavelength (d$\gg \lambda$), the laws of geometric optics apply.

Inelastic *Raman scattering* involves a change of the photon's energy and a change of the internal energy of the scatterer. For a polarizable molecule, the incident photon energy can excite rotational or vibrational states. Deexcitation into any state of lower energy results in the emission of a photon which retains its incident energy (Rayleigh scattering), looses some energy (Stokes Raman scattering), or gains some energy (Anti-Stokes Raman scattering).

Electronic, vibrational, and translational energy levels can be excited by the absorption of a photon, if its energy equals the difference of two molecular energy levels. The transition probability shows a linear dependance on the energy density of the radiation field and is obtained from quantum mechanical calculations. Before an absorbed photon is re-emitted, it is possible that non-radiating transitions take place due to molecular collisions. The energy of the photon is then transferred to kinetic energy, a process called absorption. The reverse process is called thermal emission and occurs simultaneously with absorption.

The extinction of light is described by the law of *Lambert-Beer*. Extinction is linear both in intensity of radiation and in quantity of matter. The change of intensity dI_ν along a path dl due to extinction is given by

$$dI_\nu(extinction) = -e_\nu \, I_\nu \, dl \tag{2.8}$$

where e_ν is the extinction coefficient, which is proportional to the density or concentration of the matter. The extinction coefficient can be expressed as the sum of the absorption coefficient k_ν and scattering coefficient s_ν

$$e_\nu = k_\nu + s_\nu$$

Likewise, the change of intensity due to emission can be written as

$$dI_\nu(emission) = e_\nu \, J_\nu \, dl \tag{2.9}$$

with the source function J_ν, consisting of a thermal and a scattering part

$$e_\nu J_\nu = k_\nu J_\nu(thermal) + s_\nu J_\nu(scattering)$$

Since interaction processes are either extinction or emission, the change of intensity is given by the sum of Equations 2.8 and 2.9

$$-\frac{1}{e_\nu}\frac{dI_\nu(P,\mathbf{l})}{dl} = I_\nu(P,\mathbf{l}) - J_\nu(P,\mathbf{l}) \tag{2.10}$$

Equation 2.10 is known as *equation of radiative transfer* and was first given by Schwarzschild. Total intensities can be obtained by integration over all frequencies. From thermodynamical equilibrium with no net change of radiation intensity it follows, that emission equals absorption, which is knows as *Kirchhoff's law*.

2.2 Global Annual Mean Energy Budget

Various attempts have been made to construct a global annual mean surface-atmosphere energy budget. Following the first, provided by *Dines* [1917], a number of studies have been carried out [see, e. g., review by *Hunt et al.* 1986]. But it was not until satellite observations became possible, that great improvements have been made in estimating the global annual mean energy budget [e. g. *Ramanathan et al.* 1989; *Ardanuy et al.* 1991; *Bess and Smith* 1993; *Rossow and Zhang* 1995]. A detailed study of Earth's global annual mean energy budget was carried out by *Kiehl and Trenberth* [1997]. Their radiative fluxes are used throughout this section and are summarized in Figure 2.1.

The radiation received from the sun is the main source of energy that drives the climate system on Earth. At the top of the atmosphere the mean value of total solar irradiance is approximately $1370\,\mathrm{W/m^2}$ (different satellite measurements yield values from $1365\,\mathrm{W/m^2}$ to $1373\,\mathrm{W/m^2}$ [*National Academy of Sciences* 1994]). Dividing by a factor of 4, which is the ratio of surface area to cross section for a sphere, the annual global mean of solar irradiance is $342\,\mathrm{W/m^2}$. Clouds, the atmosphere, and the surface directly reflect $107\,\mathrm{W/m^2}$ back into space, corresponding to a globally averaged planetary albedo of 31 %. The remaining $235\,\mathrm{W/m^2}$ is absorbed by the atmosphere and the surface, the energy which is available for heating the Earth and its atmosphere, either directly or indirectly. For a stable climate, radiative equilibrium at the top of the atmosphere is required, i. e., all of the absorbed solar shortwave radiation is radiated back into space. This radiation is in the thermal infrared part of the spectrum and according to Stefan-Boltzmann's law the effective emission temperature of Earth is 255 K which equals the average temperature of the atmosphere, indicating that much of the radiation escaping into space comes from the atmosphere rather than from the surface. The average emission temperature of the Earth's surface is 288 K, corresponding to a surface radiation of $390\,\mathrm{W/m^2}$. Most of this radiation is absorbed in the atmosphere by greenhouse gases, except for a small spectral range, termed *atmospheric window*, where the Earth's atmosphere is virtually transparent. The absorbed infrared radiation is then reemitted both in upward and downward direction, contributing to the strong back radiation of $324\,\mathrm{W/m^2}$ to the surface. This mechanism that traps heat within the atmosphere is called the natural greenhouse effect. Finally, energy is also transported from the surface to the atmosphere by the fluxes of sensible and latent heat.

The following sections will further address the atmospheric constituents influencing the radiative energy budget. A discussion of the different greenhouse gases, either natural or anthropogenic will be given, as well as an overview on the major interaction and feedback processes.

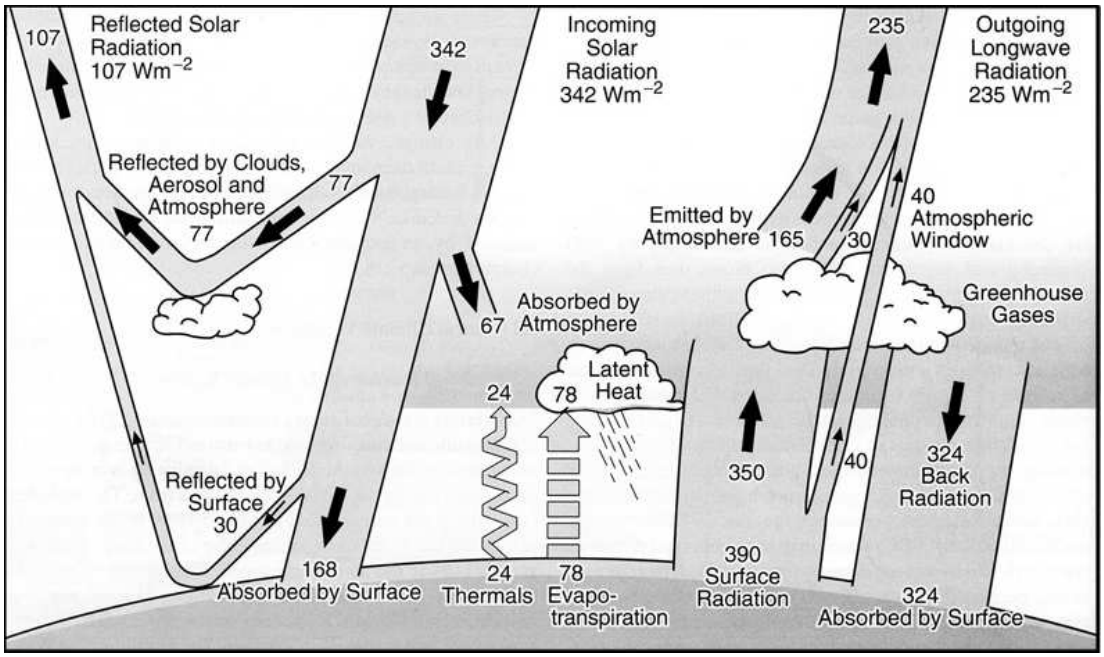

Figure 2.1: *The Earth's global annual mean energy budget for cloudy sky conditions. The fluxes are given in W/m^2. (adopted from Kiehl and Trenberth [1997])*

2.2.1 Radiative Forcing

"Radiative forcing" is defined as the difference between the top of the atmosphere radiative flux density with and without the presence of a forcing, for example a greenhouse gas. The efficiency of any greenhouse gas is a consequence of the combination of its concentration, its absorption cross section and the spectral distribution of the radiation. Figure 2.2(a) shows the normalized black body curves for the incoming shortwave solar radiation and outgoing longwave terrestrial radiation, both as seen from the top of the atmosphere. Since there is almost no overlap of both curves it is convenient to treat the solar and terrestrial radiation independently.

The existence of natural greenhouse gases is essential for making life possible on Earth. Without the natural greenhouse effect the average temperature on Earth would be a chilly -18 °C instead of the current 15 °C. The magnitude of radiative forcing and hence heating of the Earth is controlled by the concentration of greenhouse gases and other atmospheric constituents, and any change in composition eventually leads to a new state of equilibrium of the climate system. At the current temperature of Earth, a change in radiative forcing of 1 W/m^2 leads to a equilibrium change of 0.2 K. By the emission of greenhouse gases due to human activities, climate may already be warming. Although the anthropogenic radiative forcing of 2.4 W/m^2 [*IPCC* 2001] is small compared to the natural one, it is of major importance to the future trend of Earth's climate.

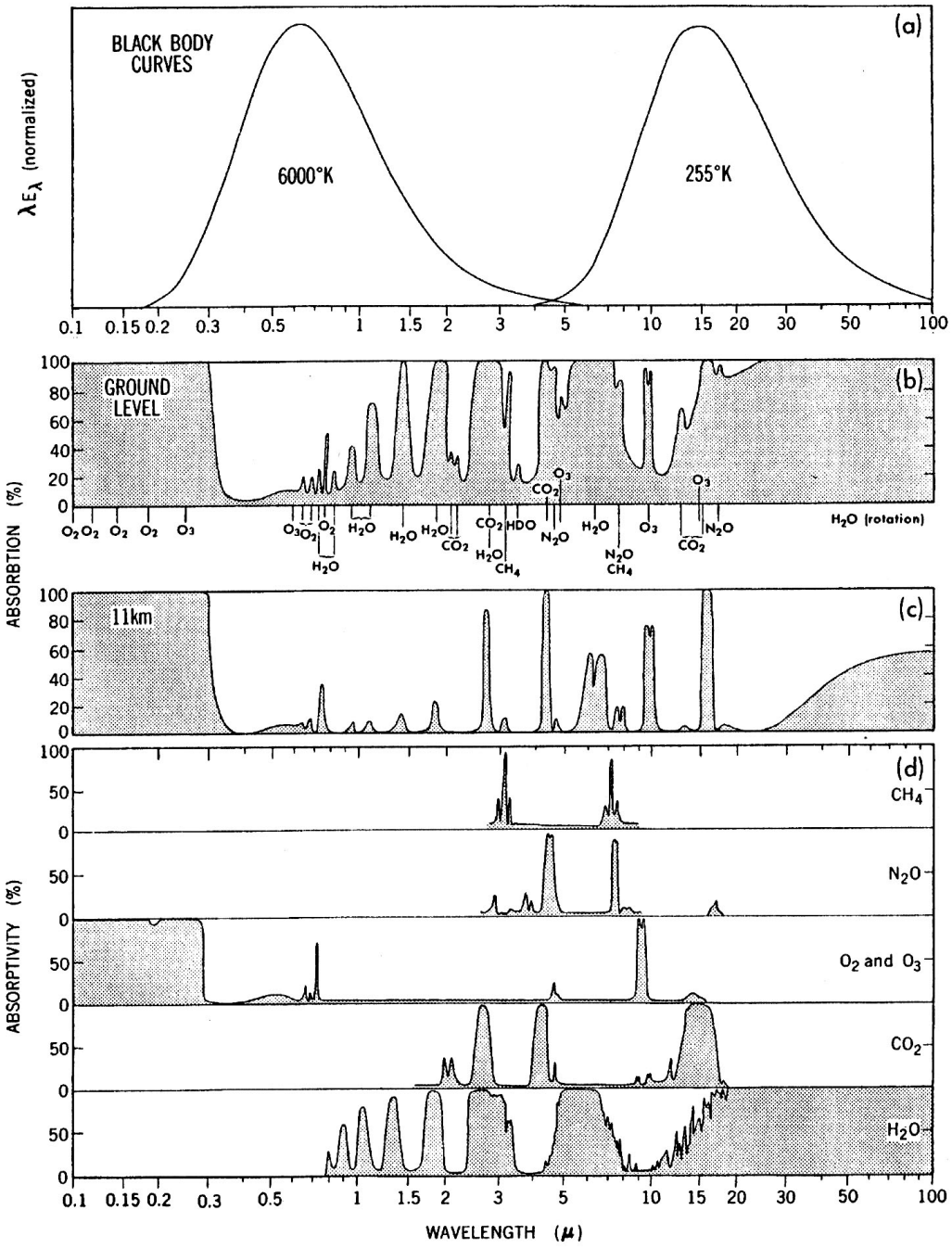

Figure 2.2: *Spectral overview of the atmospheric absorption:* **(a)** *normalized blackbody curves for shortwave solar radiation and longwave terrestrial radiation,* **(b)** *atmospheric absorption spectrum of solar radiation at ground level,* **(c)** *atmospheric absorption spectrum of solar radiation at the temperate tropopause,* **(d)** *contribution of the individual greenhouse gases to the total ground level absorption. (adopted from Peixoto and Oort [1992])*

Table 2.1: *Percent contribution of the major greenhouse gases to the clear sky radiative forcing [Kiehl and Trenberth 1997]. The total radiative forcing is 60 W/m² and 125 W/m² for the shortwave and longwave case, respectively.*

Gas	Shortwave forcing (%)	Longwave forcing (%)
H_2O	72	60
CO_2	2	26
O_3	23	8
Others	3	6

Greenhouse Gases

Figure 2.2 gives an overview of the absorption characteristics of the primary natural greenhouse gases. Absorption of ultraviolet solar radiation occurs in the stratosphere. It is mainly caused by the Hartley and Huggins bands of ozone whereas radiation below 0.2 µm is strongly absorbed by molecular oxygen (Schumann-Runge band and continuum). The most dominant absorber of solar shortwave radiation (i. e. radiation below 4 µm) is water vapor, due to a group of near infrared absorption bands. Because of the large decrease in water vapor concentration with height, absorption is strongest in the lower troposphere.

For the terrestrial infrared radiation (i. e. radiation above 4 µm), water vapor is the most dominant absorber too. The strong rotation band entirely blocks radiation from escaping to space above 20 µm, but also below 8 µm water vapor strongly absorbs. The greenhouse effect of water vapor is most important in the free troposphere, a height at which most of the longwave radiation is radiated into space. Carbon dioxide is the second most important absorber for terrestrial radiation, showing an intense absorption band around 15 µm, near the maximum of terrestrial radiation. The spectral region where absorption by water vapor and carbon dioxide is relative weak (8 – 12 µm) is called "atmospheric window". Inside this window only ozone is a prominent absorber, nitrous oxide and methane flank the window on the shorter wavelength side.

The relative contribution of the major greenhouse gases to the radiative forcing for clear sky conditions is listed in Table 2.1. The most important one is water vapor, accounting for 60 % of the total longwave radiative forcing. The reason is the high abundance of up to 4 % per volume of water vapor in the troposphere. In the stratosphere H_2O, CO_2 and O_3 are of comparable importance.

The gases mentioned so far (H_2O, CO_2, O_3, CH_4, N_2O) are all natural greenhouse gases. Except for water vapor, human activities since the industrial revolution increasingly rise the concentration of these greenhouse gases, resulting in global warming by

an additional anthropogenic greenhouse effect. The most well known example is the rise in carbon dioxide by about 35 % since pre-industrial times [*Keeling et al.* 1976; *Neftel et al.* 1985; *Etheridge et al.* 1996; *Keeling and Whorf* 2005], due to fossil fuel combustion and deforestation. The emission of nitrogen oxides (NO, NO_2) and volatile organic compounds (VOC) by industry and traffic in connection with atmospheric photochemistry has caused an increase of tropospheric ozone. Uncertainties in the quantification of the ozone budget, both at past and present times, remain due to its spatial and temporal variability, its short lifetime and its fast reactivity. However, long term measurements show an increase in tropospheric ozone by a factor of approximately 2.2 since pre-industrial times [*Staehelin et al.* 1994]. Methane and nitrous oxide, the sources of which are from agriculture and industrial sources, has increased as well by 150 % [*Etheridge et al.* 1998] and 15 % [*Machida et al.* 1995] respectively.

Besides the five major greenhouse gases, there are a variety of other minor constituents contributing to the radiative forcing. Although low concentrations in the atmosphere reduce their importance for the total greenhouse effect, they become essential when the question is about human-induced climate change. *Ramanathan* [1975] first pointed out the radiative forcing by chlorofluorocarbons (CFCs). Indeed, a class of synthetic fluorine, chlorine, and bromine containing hydrocarbons are strong anthropogenic greenhouse gases: Hydrofluorocarbons (HFCs), chlorofluorocarbons (CFCs), hydrochlorofluorocarbons (HCFCs), perfluorocarbons (PFCs), halons, and sulphurhexafluoride (SF_6). All these trace gases have not been present in the atmosphere before the 20^{th} century as evident from firm measurements [*Butler et al.* 1999]. These gases originate from a variety of industrial processes and are used as refrigerants, aerosol spray propellants or cleaning solvents. They are the strongest greenhouse gases per molecule due to their large absorption cross section and are photochemically very reactive, quite a few of which are responsible for stratospheric ozone depletion [*IPCC* 2001; *WMO* 2002].

Clouds

Clouds interact with incoming shortwave and outgoing longwave radiation in a very complex and spatially variable manner, which adds a lot of complexity to the climate system. For the radiative balance clouds play an important role, since they act like a greenhouse gas by absorbing and emitting infrared radiation. On the other side clouds also reflect the incoming solar radiation, therefore increasing the Earth's albedo. Assuming random overlap of cloud layers of different height, the global mean cloud cover is 62 % [*Kiehl and Trenberth* 1997; *Rossow et al.* 1993]. The transfer of radiation does not only depend on the cloud fraction but also on the total liquid water contend, the droplet size, the cloud emissivity and the cloud top and base temperatures.

At the top of the atmosphere the upward flux density of longwave radiation is 265 W/m^2 for clear sky condition, but only 235 W/m^2 for the cloudy sky case, yielding a longwave cloud forcing of +30 W/m^2. The strongest emission of the outgoing longwave

radiation of clouds is in the atmospheric window, since for the other spectral regions there is a strong overlap of absorption bands of water vapor and liquid water. In the presence of clouds, the back radiation of the atmosphere to the surface is increased by 46 W/m^2 to 324 W/m^2. This is mainly due to blackbody emission from the cloud base. As a result of the liquid water overlap, the radiative forcing of water vapor is reduced by 22 W/m^2 compared to clear sky conditions. The longwave forcing of the other absorbers is less affected by the overlap, but not negligible. Thus, besides the direct effect of clouds on the absorption and emission of longwave radiation, there is an indirect effect by shielding the absorption and emission of the greenhouse gases.

Shortwave radiation is strongly being scattered inside clouds, with a mean free path of the order of 10 m. Thus increasing the mean photon path due to multiple scattering, the chances of absorption by gases increases too. This adds an additional 7 W/m^2 contribution of shortwave radiative forcing by clouds. Again, the cloud effect is small in spectral region where there is overlap with gaseous absorbers, mainly water vapor. Outside the cloud the mean free path of a photon is several orders of magnitude larger. Thus radiative transfer for clear sky conditions is dominated by direct propagation of sunlight, only in the UV region Rayleigh scattering can be of considerable importance. Diffuse reflection at the cloud top leads to an increase in the planetary albedo and consequently to a decrease of energy available for heating the atmosphere and the surface. The result of all effects is a total shortwave cloud forcing of -50 W/m^2. Combined with the longwave cloud forcing, the global net effect of clouds in our current climate system is a cooling of 20 W/m^2. However, the net cloud forcing strongly depends on latitude and season [*Harrison et al.* 1990].

Aerosol

Of major importance is the radiative forcing of aerosols. Aerosols are solid or liquid particles which are variously classified, e. g. mineral dust, sea salt, sulfates, black carbon, and organic carbon. There have always been natural sources but now there are also large emissions of anthropogenic aerosol from, e. g., industry, traffic, fossil fuel and biomass burning. The quantification of aerosol radiative forcing is very complex and yet not well understood. Due to the short lifetimes the concentrations are highly variable in space and time, and radiative properties strongly depend on parameters like particle size, refractive index and solubility. Moreover, some aerosols cause cooling while others are believed to cause warming, i. e. there is a strong dependence on the single scattering albedo ω_0. Most likely, the contribution of aerosols to the overall radiative forcing is significantly negative [*IPCC* 2001]. Uncertainties in this cooling effect, mainly caused by sulfate aerosols, is a major reason why it is difficult to prove and predict climate warming due to anthropogenic greenhouse gas emissions [*Andreae et al.* 2005].

The direct aerosol effect leads to both positive and negative radiative forcing. Aerosols can directly absorb incoming solar radiation or outgoing infrared radiation, resulting in

positive radiative forcing. Black carbon (soot) is one important agent of this type, with its origin in incomplete fuel combustion. Modeling studies suggest that the abundance of black carbon relative to non-absorbing constituents has a strong influence on the magnitude of heating within the atmosphere, leading to changes in atmospheric stability [e. g. *Haywood and Shine* 1995; *Myhre et al.* 1998; *Penner et al.* 1998]. Negative radiative forcing of aerosols is caused by enhanced scattering of incoming solar radiation back into space. Most eminent is sulfate aerosol, which is produced by chemical reactions from gaseous precursors like anthropogenic and volcanic SO_2 or direct emission of biogenic dimethyl sulfide (DMS) [*Charlson et al.* 1987; *Arnold et al.* 1990]. Aerosols also influence the formation and precipitation efficiency of clouds, thereby affecting radiative forcing indirectly. The first aerosol indirect effect, described by *Twomey* [1977] for the first time, is associated with changes in cloud properties due to aerosols. Increased concentrations of atmospheric aerosol will lead to a higher concentration of cloud condensation nuclei, therefore increased number of cloud droplets which are consequentially smaller. Finally, this results in more reflective clouds. *Albrecht* [1989] suggested that an increased number of cloud condensation nuclei also suppresses precipitation and results in larger liquid-water paths and longer lifetimes of individual clouds (second indirect effect).

2.2.2 Feedbacks

A process is denoted as *feedback* when the results of this process affect its origin in a way of intensifying (positive feedback) or reducing (negative feedback) the original effect. Feedbacks largely control climate sensitivity and therefore are of major importance when one is interested in the response of the climate system to changes in radiative forcing.

The most important feedback in Earth's climate system is that of water vapor. It is the reason for large responses of the climate system due to increased anthropogenic greenhouse gases. As climate changes, the abundance and distribution of water vapor will change too. According to the Clausius-Clapeyron relation, the saturation water vapor pressure of the atmosphere increases non-linearly with temperature. So, if water vapor increases as climate warms, the reduction in outgoing longwave radiation by the additional water-absorption lead to a warmer equilibrium state of climate than it would have been if water vapor content had remained fixed. This is called the *positive water vapor feedback* [*Goody and Yung* 1989].

Investigations of the water vapor feedback and its influence on an increase of anthropogenic greenhouse gases have been carried out by use of various climate models. Due to the water vapor feedback alone, a doubling of the CO_2 content, results in an additionally factor two in the temperature rise compared to fixed water vapor content [*Cess et al.* 1990; *Hall and Manabe* 1999; *Schneider et al.* 1999; *Held and Soden* 2000].

This factor can increase up to 3.5 , when taking into account that the water vapor feedback amplifies other feedbacks, such as the cloud feedback [*Hall and Manabe* 1999]. By far the strongest effect is observed in the free troposphere, as most of it is highly undersaturated with respect to water vapor. 55 % of the total water vapor feedback occurs in the tropic free troposphere and 35 % in the extra-tropic free troposphere. The boundary layer however, which contains about half of the atmospheric water vapor, accounts for only 10 % globally due to the high relative humidity there.

Clouds are intimately connected to the atmospheric water vapor pattern and cloud processes in turn affect the water vapor distribution. Cloud feedbacks not only involve chances in cloud height, cloud cover and cloud optical thickness, but also in latent heat released form the condensation. The interaction with radiation is governed by the three-dimensional cloud geometry, the water content and the cloud droplet size for instance. The subtle balance between cloud impact on the solar shortwave and terrestrial longwave radiation may be altered by a change in cloud parameters. In response to any climate perturbation the response of cloudiness thereby introduces feedbacks whose sign and amplitude is still a matter of uncertainty [*IPCC* 2001]. Studies carried out by *Yao and Genio* [1999] using the GISS GCM model and a doubled CO_2 scenario results in a slight positive cloud feedback.

2.2.3 Excess Absorption

Disagreement in Earth's radiation budget between observations and global climate models has been a major concern in the climate community for several decades. Many attempts have been made to explain the observed excess of solar shortwave absorption, which is commonly referred to as anomalous, or excess, absorption. The solar shortwave absorption is by far the largest uncertainty in modeling the global radiative budget. Summaries of the history of the excess absorption problem are given by *Stephens and Tsay* [1990], *Liou* [1992] and *Ramanathan and Vogelmann* [1997]. Widespread scientific interest in this topic was revived in the 1990s by a comprehensive analysis of satellite, aircraft and ground-based measurements, supporting the existence of excess absorption and quantifying its magnitude to be about $25 - 30\,\mathrm{W/m^2}$ [*Ramanathan and Vogelmann* 1997]. The work by *Cess et al.* [1995], *Ramanathan et al.* [1995] and *Pilewskie and Valero* [1995] suggest a significant level of shortwave cloudy-sky absorption beyond the ability of any model to predict. However, it is indicated by the work of *Li et al.* [1995] and *Arking* [1996] that the disagreement is mostly a clear-sky effect, largely independent of clouds. Others again contend that there is no excess absorption [*Imre et al.* 1996; *Stephens* 1996].

Numerous attempts have been made to resolve the problem, but all potential mechanisms on its own fall far short of explaining the estimated $25 - 30\,\mathrm{W/m^2}$ excess absorption. It is the significant cumulative impact of all the small individual contributions

which has to be considered. The Lambert-Beer law only allows that either unknown absorbers or absorption mechanism exist, or the discrepancy is caused by an enhancement of the photon path length due to clouds. The solution may partly be found by directly considering the cloud properties. This includes the absorption by large cloud droplets [*Wiscombe et al.* 1984; *Lubin et al.* 1996] and effects of the cloud morphology, i. e. inhomogeneities due to the fractal nature of clouds [*Marshak et al.* 1995; *Marshak et al.* 1997; *Barker et al.* 1998], resulting in an enhancement of the photon free mean path [*Davies* 1978; *Byrne et al.* 1996; *Marshak et al.* 1998; *Pfeilsticker et al.* 1998].

Contrary to the reports attributing the problem to clouds, *Arking* [1996] suggests that the source of the missing absorption is related to water vapor by missing physics in both water vapor and aqueous aerosol absorption. The missing physics of water vapor absorption includes firstly the concerns about the quality of spectral line databases [*Chagas et al.* 2001; *Bennartz and Lohmann* 2001; *Casanova et al.* 2005], secondly the water vapor continuum absorption, an unstructured absorption underlying the water vapor bands, which was first noticed more than half a century ago by [*Hettner* 1918; *Elsasser* 1938a], and thirdly the absorption by water clusters, especially that by water vapor dimers, which has been suggested to be of significant importance for the absorption of solar radiation *Chýlek and Geldart* [1997]. Although laboratory measurements of water vapor continuum and water vapor dimer absorption are available in the infrared region [e. g. *Ptashnik et al.* 2004; *Cormier et al.* 2005] and a semi-empirical water continuum model by *Clough et al.* [1989] has partly success in explaining atmospheric infrared absorption, the importance of the water vapor continuum and the water complexes concerning the atmospheric shortwave absorption is still controversial due to the lack of laboratory and atmospheric observations [*Daniel et al.* 2004]. Since it is the principal topic of this thesis, both the water vapor continuum and the water vapor dimer absorption is discussed in detail in Chapter 3. More generally the missing absorption may be attributed to a variety of weakly bound transient species involving water and other atmospheric gases, such as H_2O–H_2O, H_2O–O_2 , H_2O–N_2 or O_4 [*Pfeilsticker et al.* 1997; *Solomon et al.* 1998; *Kjaergaard et al.* 2003]. Although these species are believed to be short-lived, the large atmospheric concentration of the parent molecules make them very abundant and therefore efficient greenhouse species.

Anomalous absorption may also be due to aerosol embedded within the clouds [*Arking* 1996; *Li and Moreau* 1996; *Li* 1998]. Since cloud properties and precipitation characteristics are related to the aerosol content of the atmosphere (aerosol indirect effect), the aerosol contribution to the excess absorption is correlated with the water vapor and cloud effects previously discussed. For resolving the clear-sky excess absorption problem, *Halthore et al.* [1998] suggests to reduce the vertical aerosol optical thickness together with a compensating increase in a continuum-like atmospheric absorption of solar radiation.

3 Water Vapor and Interacting Species

Water is an ubiquitous molecule both here on Earth and elsewhere in the universe. As discussed previously, water vapor is the primary atmospheric constituent contributing to the natural greenhouse effect and, in its liquid phase, is absolutely necessary for life to exist. In our solar system water is found in the atmospheres of other planets (Venus, Mars, Gas Planets), on numerous icy moons of the outer solar system (e. g. Europa, Ganymede) and on comets, where water easily vaporizes and enriches the interplanetary medium. Water is also a well known constituent of stellar atmospheres [*Bernath* 2002]: it can be observed in sunspots [*Wallace et al.* 1995; *Tennyson and Polyansky* 1998], in the atmospheres of oxygen-rich cool stars [*Allard et al.* 1997] and brown dwarfs [*Tsuji* 1995], where it is the most abundant molecule after hydrogen. In interstellar space, water is observable in nearly all giant molecular clouds [*Snell et al.* 1999].

In physics, water is an exceptional molecule showing many unusual behaviors, such as the density anomaly, the high melting point and a large heat capacity, only to mention a few of them. This unusual behavior also manifests itself in the spectrum as the infrared vibration-rotation bands reach up far into the visual spectral region. The spectrum of water is arguably the most important of all molecules due to its various applications: in astrophysics, in modeling atmospheric circulation and climate, in modeling processes in flames and exhausts, and in monitoring forest fires from aircraft [*Worden et al.* 1997].

Water has a strong tendency to form hydrogen bonds leading to the formation of various weakly bound molecular complexes both homomolecular and heteromolecular. Of particular interest in atmospheric science is the interaction of two water molecules, resulting in a short-lived collision complex or the formation of a metastable or truly bound water dimer $(H_2O)_2$. This mechanism is of importance for the propagation of radiation through Earth's atmosphere and possibly accounts partly for the observed excess of solar shortwave absorption (see Section 2.2.3). In cometary atmospheres, water dimers are important for the gas-phase chemistry and recondensation processes [*Crifo* 1990; *Crifo and Slanina* 1991; *Scherer et al.* 1998].

The following chapter is addressed to the basic principles of bimolecular water interactions resulting in the formation of short-lived collision pairs up to truly bound water dimers. An overview of the spectroscopic signature of the water molecule, the water continuum, and the water dimer is given. The role of the water dimer in atmospheric physics and photochemistry is discussed.

3.1 Physics of Interacting Molecular Species

3.1.1 Intermolecular Forces

Neutral molecules interact by weak electrostatically attracting forces, commonly termed *van der Waals forces*, which are some orders of magnitude smaller than the bonding forces holding together an individual molecule. Two forms of intermolecular attractions are known, *dispersion forces*[1] and *dipole-dipole attractions*. When cooling a gas, these are the forces causing the formation of a liquid or a solid. In the gas phase it is possible that weakly bound complexes, also termed van der Waals molecules, consisting of two or more molecules can form. It is interesting that all molecules and even atoms experience dispersion forces and therefore are capable to form weakly bound complexes. The origin of dispersion forces are temporary fluctuating dipoles which give rise to relatively weak intermolecular attractions. The strength of attraction increases with the size and the number of electrons of the molecule. If a molecule shows a permanent dipole moment in addition, dipole-dipole interactions occur. Surprisingly, dipole-dipole attractions may be fairly minor compared to dispersion forces. It is possible that larger dispersion forces due to a bigger molecule with more electrons can more than compensate for the absence of a permanent dipole moment (e. g. see $CHCl_3$ and CCl_4). In summary, the strength of an intermolecular attraction considerably depends on the charge distribution of the individual molecules. For a molecular complex this results in a wide range of binding energies from 0.1 – 10 kcal/mol (compared to about 100 kcal/mol for a covalent bond).

One type of a relatively strong intermolecular interaction with a strength of about a tenth of an average covalent bond is the *hydrogen bond*, which involves hydrogen atoms and a strongly electronegative atom such as nitrogen, oxygen or fluorine. In a molecule consisting of these atoms (NH_3, H_2O, HF), the electronegative element attracts the electron cloud and leaves the hydrogen atoms with a rather strong positive charge. A hydrogen bond results when the positive charge of the hydrogen atom of one molecule (hydrogen-bond donor) attracts a lone pair of electrons of the electronegative atom of another molecule (hydrogen-bond acceptor). The existence of an active lone pair of electrons is necessary for the formation of the hydrogen bond, which is significantly stronger than an ordinary dipole-dipole interaction. Water is a perfect example of hydrogen bonding, since there is just the right number of two hydrogen atoms and two lone pairs of electrons of the oxygen atom in each individual molecule. This explains the unusual high melting and boiling point of water, for example.

[1] Dispersion forces are also known as *London forces*

3.1.2 Thermodynamics

Molecular complexes in their general outline can be described by the known principles of chemical thermodynamics. But there are some peculiarities to be considered, distinguishing the weakly bound species from truly chemically bound compounds. The dissociation energy of a complex may be some tens to hundreds times lower than it is for ordinary molecules, resulting in the population of high-lying ro-vibrational states close to, or above the dissociation limit, even near room temperature. The concept of a complex being a molecule as an unit is not longer valid. Truly bound states of a molecular complex is bridged with the free states of the progenitor molecules via a manifold of intermediate quasibound states.

The formation of a molecular complex can be written just like an ordinary chemical reaction of particles A_i with stoichiometric factors ν_i

$$\nu_1 A_1 + ... + \nu_{k-1} A_{k-1} = \nu_k A_k \quad \rightarrow \quad \sum_i \nu_i A_i = 0 \tag{3.1}$$

In thermodynamical equilibrium at fixed temperature T and pressure P, the Gibbs free energy $G(T, P, N)$ is known to be minimal. Applying standard thermodynamics leads to the law of mass-action and the definition of the equilibrium constant

$$K \quad = \quad \exp\left(-\frac{\Delta G^\circ}{RT}\right) \quad = \quad \prod_i \left(\frac{P_i}{P_0}\right)^{\nu_i} \tag{3.2}$$

with the P_i being the partial pressures of the progenitor particles. The pressure at standard conditions P_0 is often merged with the equilibrium constant K to give

$$K_P \quad = \quad K P_0{}^{\sum_i \nu_i} = \quad \prod_i P_i{}^{\nu_i} \tag{3.3}$$

The change of enthalpy ΔH° and entropy ΔS° for the reaction can be calculated from the equilibrium constant and vice versa by

$$\Delta G^\circ = \Delta H^\circ - T\Delta S^\circ \tag{3.4}$$

The basis for calculating thermodynamic functions is given by the concept of the partition function

$$Z = \sum_{j=1} g_j \exp\left(-\frac{E_j}{k_B T}\right) \tag{3.5}$$

The summation is carried out over all quantum states j of the species, with degeneracy g_j and energy E_j. The total partition function can be factorized in terms of individual partition functions for translational, rotational, vibrational, electronic and nuclear spin motion. For tightly bound states, the sum of the overall rotational and vibrational energies has to be limited by the dissociation threshold D_0 , so for truly bound

complexes the partition function has to be truncated. Molecular complexes having an energy in excess of the dissociation limit are called metastable, since they are capable of spontaneously decay.

In the classical limit, the summation over the cells in phase-space, each of which corresponds to a different state, is approximated by an integration over all phase-space. For N interacting indistinguishable particles the partition function is given by

$$Z = \frac{1}{N!}\frac{1}{h^{3N}} \int \exp\left(-\frac{H(\vec{p},\vec{q})}{k_B T}\right) d(\vec{p},\vec{q}) \tag{3.6}$$

$H(\vec{p},\vec{q})$ is the Hamilton function and the factor of $1/N!$ has to be modified if particles are distinguishable. The often used assumption of the rigid rotator–harmonic oscillator approximation for calculating the partition function is very poor for weakly bound species. To remedy this shortcoming, the complete intermolecular potential energy surface has to be considered, which also provides an efficient tool to describe molecular association processes in a gas. This process can be seen thermodynamically as the result of the deviation from non-ideal behavior of the gas, which is accounted for in terms of a virial expansion with virial coefficients B_i

$$\frac{P}{k_B T} = \frac{N}{V} + B_2(T)\left(\frac{N}{V}\right)^2 + B_3(T)\left(\frac{N}{V}\right)^3 + \ \ldots \tag{3.7}$$

The first virial gives the equation of state for a perfect gas without any intermolecular interaction. Applying thermodynamics it can be shown that the second virial coefficient B_2 is determined entirely by the intermolecular pair potential and the third virial coefficient B_3 is mainly due to interactions involving three molecules [*Hill* 1956].

3.1.3 Bimolecular Complexes

The most simple type of a molecular complex is that of a bimolecular one, also called a dimer. In the following, only the formation of a dimer D from two equal monomers M in a three-body collision with particle X will be considered.

$$\mathrm{M} + \mathrm{M} + \mathrm{X} \quad \longleftrightarrow \quad \mathrm{D} + \mathrm{X} \tag{3.8}$$

Applying the law of mass-action[2], the calculation of the equilibrium constant for dimerisation, given by Equation 3.3, reduces to

$$K_P(T) = \frac{P_D}{P_M^2} \tag{3.9}$$

It is easily seen that the partial pressure and therefore the number density of the dimer is proportional to that of the monomer squared if the temperature is held fixed. To determine the dependence upon temperature, the calculation of the Gibbs free energy should be carried out by use of standard thermodynamics and the concept of the partition function.

[2]Convention: the signs of the stoichiometric factors of the reaction's products are assigned positive

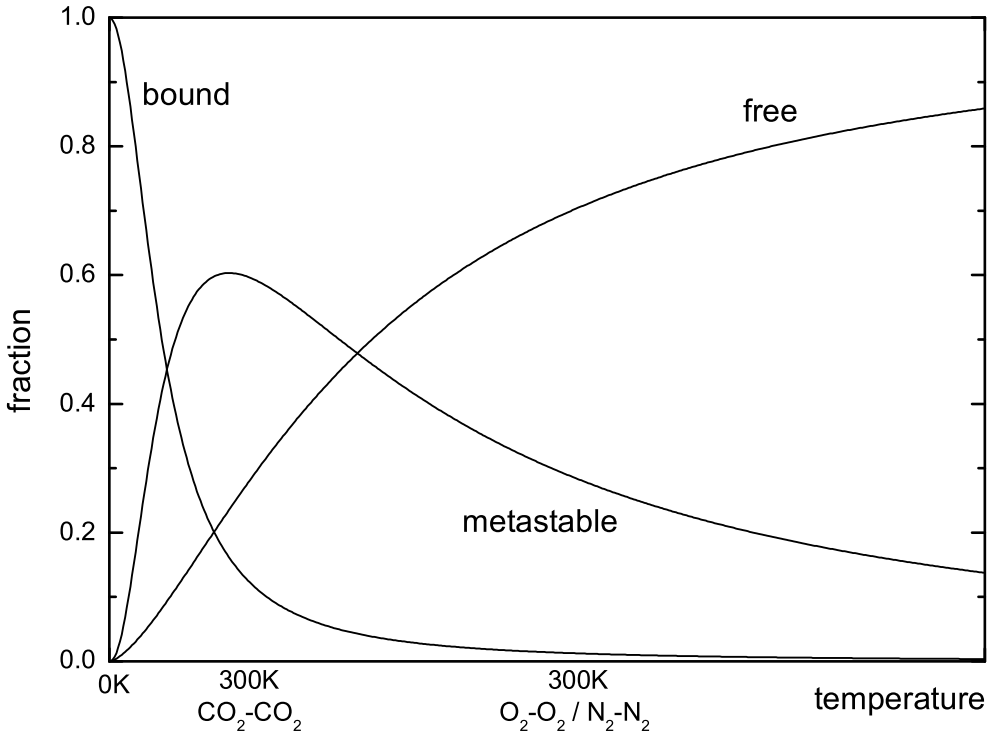

Figure 3.1: *Qualitatively illustration of the temperature-dependent subdivision into domains of dimeric states. The temperature scale is arbitrary, as it depends on the individual dimer (three examples are shown for T=300 K). The water dimer bond is expected to be considerably stronger than CO_2 [Epifanov and Vigasin 1997; Vigasin 1998; Vigasin 2003].*

Due to the weak intermolecular interaction forces, a large number of ro-vibrational states near or above the dissociation threshold are populated even at room temperature. This leads to the classification of various types of pair states (Figure 3.1): truly bound states, also called dimeric states; metastable states, also termed quasibound states; free pair states. The free pair states must not to confused with continuum states of the monomers. Differentiation between these types of pair states requires the consideration of the phase space and its partitioning into the three domains of states for determining the corresponding partition functions. For a bimolecular complex the phase space is 12-dimensional, three each for the coordinates (x, y, z) and momenta (p_x, p_y, p_z) of the center of mass and three each for the coordinates (θ, ϕ, r) and momenta (p_θ, p_ϕ, p_r) determining the relative position of the two molecules. The partition function can be split up in three parts for the bound, metastable and free pair sates

$$Z = Z_b + Z_m + Z_f \tag{3.10}$$

whereas the difficulty is to find appropriate integration limit, i. e. phase space subdivision, for the different domains. In case of two structureless interacting particles the problem was solved first by *Hill* [1956] and *Stogryn and Hirschfelder* [1959]. A

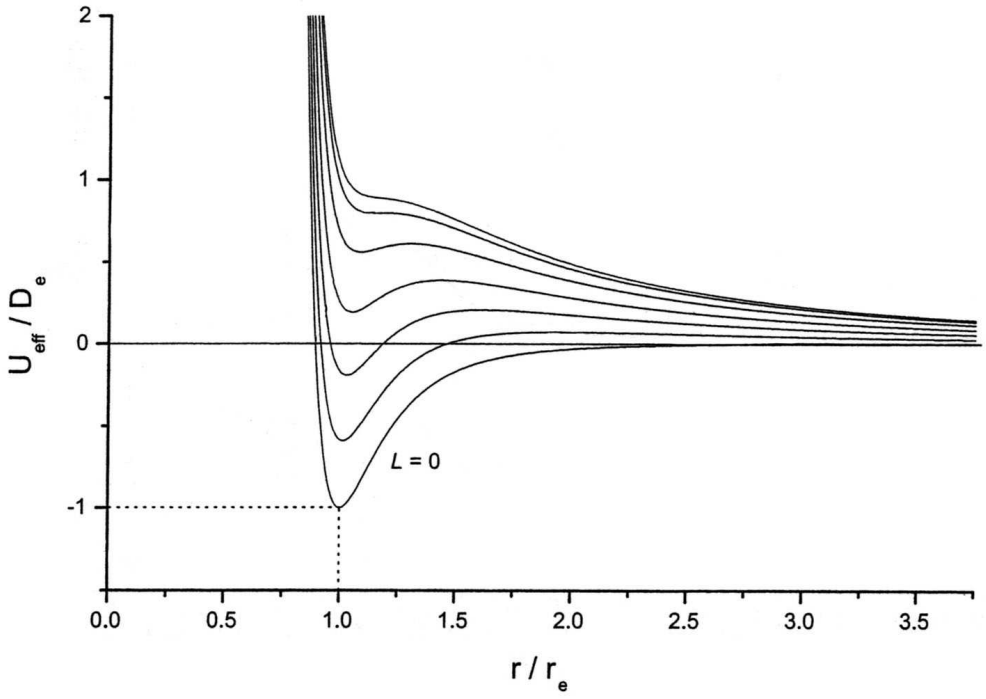

Figure 3.2: *Effective intermolecular potential energy U_{eff} (in units of well depth D_e) as a function of molecular separation r (in units of equilibrium separation r_e), shown for different values for the end-over-end rotational quantum number L. (adopted from Vigasin [2003])*

detailed study for bimolecular complexes of arbitrary complexity has been carried out by *Vigasin* [1998]. The distinction between truly bound, metastable and free states is described by an effective intermolecular potential energy U_{eff}, the sum of potential energy and centrifugal energy

$$U_{eff} = U(R) + \frac{\hbar^2}{2\mu} \frac{L(L+1)}{R^2} \tag{3.11}$$

where R is the intermolecular distance, L the rotational quantum number and μ the reduced mass. The radial dependence of the effective intermolecular potential for several rotational quantum numbers is illustrated in Figure 3.2. It is seen that there exists a certain L_{max} for which the potential curves show a local minimum for $L \leq L_{max}$ but don't for $L \geq L_{max}$. Obviously, the states with negative U_{eff} belong to the truly bound dimers and states for values of L exceeding L_{max} belong to the free pair states. Intermediate states for which U_{eff} is positive but below the local maximum of the potential curve with the selected L are called metastable states. These states are capable of dissociating through the potential barrier by quantum mechanical tunneling. From a classical viewpoint they are indistinguishable from the truly bound dimeric states, since dissociation is only possible by a three body collision with a further particle. Metastable states can be thought of as molecular pairs similar to highly exited dimers, therefore

also termed metastable dimers. It is quite evident that truly bound dimers dominate in the low temperature regime, whereas free pair states prevail at high temperatures. At an intermediate temperature the fraction of metastable dimers will show a maximum. Starting from low temperature the population of truly bound dimers decreases at the expense of the metastable dimers which themselves give way to the free pair states as the temperature rises. Of course as indicated in Figure 3.1, the temperature at which a certain domain prevails depends strongly on the strength of the intermolecular bond.

3.2 Interacting Water Molecules

3.2.1 The Water Molecule

The water molecule, H_2O , cannot have a linear structure, but is rather a bent symmetric molecule, as can be concluded from the observation of its rotational and rotation-vibrational spectra. In its equilibrium state the length of each O–H bond is 0.9575 Å and the bending angle is 104.51° [*Lide* 1995] (see Figure 3.3a). The molecule symmetry is of point group C_{2v} , showing two mirror planes of symmetry and a 2-fold axis of rotation, which is necessarily the line of intersection of both mirror planes (see Figure 3.3a). All three principal moments of inertia are different, therefore the water molecule is categorized as an asymmetric top molecule. The principal axis with the smallest moment of inertia is parallel to the H–H direction, the principal axis with the intermediate moment of inertia coincides with the symmetry axis and the principal axis with the largest moment of inertia is perpendicular to the H–O–H plane (see Figure 3.3b). The bent shape leads to an electron density distribution giving the molecule a permanent dipole moment which coincides with the axis of symmetry. The hydrogen atoms may posses parallel (*ortho*-H_2O) or antiparallel (*para*-H_2O) nuclear spin, with an equilibrium ratio of 3:1 *ortho*:*para* for temperatures higher than about 50 K. Water exists in different isotopic compositions as follows, with the natural abundance given in parenthesis: $H_2{}^{16}O$ (99.732%), $H_2{}^{18}O$ (0.200%), $H_2{}^{17}O$ (0.037%), $HD^{16}O$ (0.031%), all others (less than 0.00006%) [*de Bievre et al.* 1984]. Note that, e. g. HDO is not a symmetric molecule.

As a triatomic bent molecule, water has three rotational and three vibrational degrees of freedom, which are depicted in Figure 3.3b and Figure 3.3c respectively. The degeneracy of the rotational and vibrational states is cancelled since water is an asymmetric top molecule, resulting in many allowed transitions with almost no discernible spectral structure. Because the water molecule has a permanent dipole moment, a strong infrared rotation spectrum occurs at a wavelength of about 15 µm upwards to the microwave region. The three normal modes of vibration are shown in Figure 3.3c with the corresponding fundamental frequencies: one symmetric stretching mode ($\nu_1 = 3\,657\,\mathrm{cm}^{-1}$), one bending mode ($\nu_2 = 1\,595\,\mathrm{cm}^{-1}$) and one asymmetric stretching mode ($\nu_3 = 3\,756\,\mathrm{cm}^{-1}$) [*Lide* 1995]. All three vibration modes occur in the

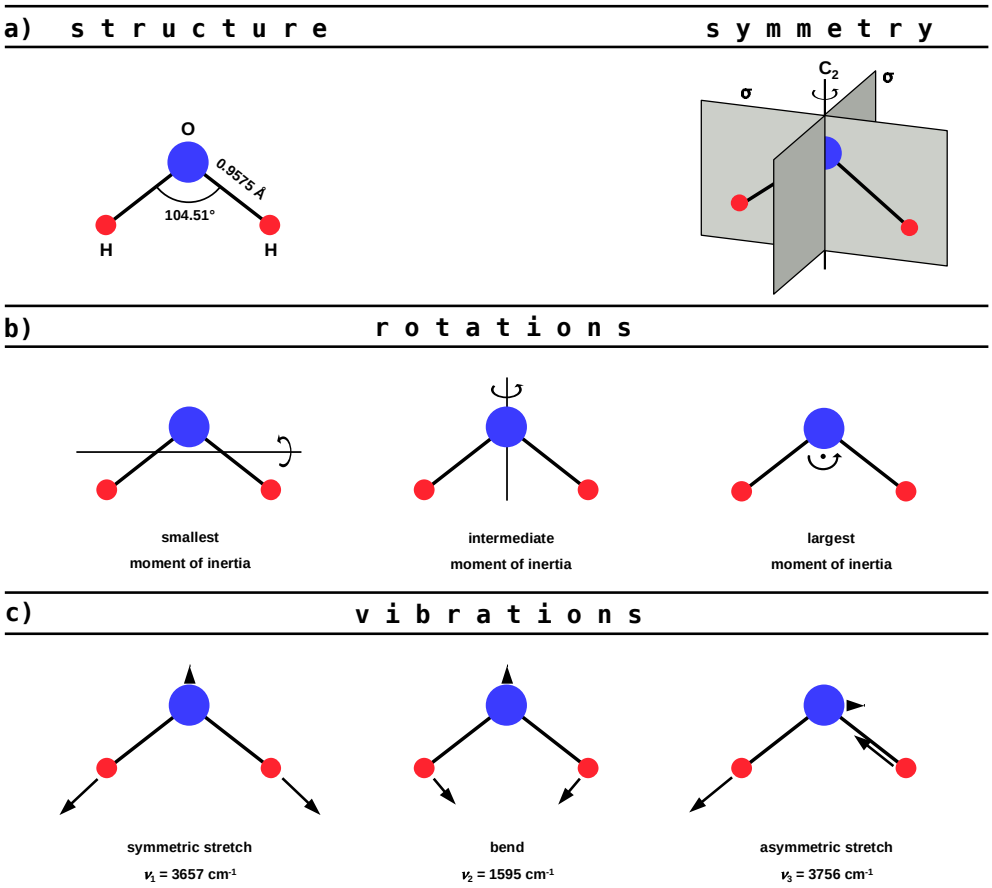

Figure 3.3: *The water molecule:* **(a)** *molecular structure and symmetry,* **(b)** *principal axes of rotation,* **(c)** *fundamental modes of vibration.*

spectrum since they all are correlated with a change of the dipole moment of the water molecule. The notation for labelling vibrational states is (ν_1, ν_2, ν_3) with ν_i being the number of quanta in vibrational mode ν_i , with the fundamental vibrations set to zero. It can be seen that the frequency of the bending fundamental is nearly half the frequency of the stretching fundamentals, so that states with $2n$ quanta of bend lie close in energy to states with n quanta in stretch. In practice the normal mode model only approximately represents the true vibrational motions. The local mode model is better suited, where vibrational excitation is localized in a single O–H bond rather than being shared. The transition from the normal mode to the local mode model is a manifestation of mixing between vibrational states and leads to the concept of *polyads*, which are groups of states close in energy. In water each polyad is made up of states interacting with the $(\nu, 0, 0)$ stretching mode, for example the $\nu = 2$ polyad is made up of states $(2, 0, 0)$, $(1, 0, 1)$, $(0, 0, 2)$, $(1, 2, 0)$, $(0, 2, 1)$ and $(0, 4, 0)$. If the number of quanta in the bending mode is odd, this is denoted by adding a δ, for example $\nu = 2 + \delta$ if one quantum of bend is added to the former example. The concept of polyads becomes

decreasingly useful for higher excitation levels, since for $\nu = 5$ upwards the polyads begin to overlap. An entire rotation-vibration spectrum of water vapor is shown in Figure 3.4, with an evident polyad structure.

For an asymmetric top molecule like water there is no analytic solution to the harmonic oscillator–rigid rotator model, from which it would be possible to build an entire rotation-vibration spectrum. Moreover, the water molecule is far from being rigid and it is important to consider the interaction between rotational and vibrational motions due to Coriolis forces. It has been shown that standard expansions upon perturbation theory based on the rigid rotator model are insufficient to describe the water molecule spectrum [*Polyansky* 1985]. For treating the nuclear motion problem the direct solution of the underlying quantum mechanical equations is applied from first principles based upon the variational principle. An excellent example of this procedure is the calculation of the frequencies of over 300 million water transitions by *Partridge and Schwenke* [1997]. Besides calculated water line lists there exist further experimental databases. The most popular for atmospheric applications is the HITRAN database [*Rothman et al.* 2005], currently containing about 63 000 water transitions and being continuously upgraded. An overview of several spectral water databases is given in Section 4.5.1.

3.2.2 The Water Continuum

Besides the local line absorption of water vapor, interacting molecular species involving water molecules give rise to an underlying low-frequency absorption component, that is referred to as the water vapor continuum. To avoid confusion one has to keep in mind that the water vapor continuum exclusively results from molecular interactions and should not be identified with continuum states of the isolated water monomer. The water continuum can be classified in one component proportional to the square of water vapor partial pressure, which is due to interactions of water molecular pairs (self-broadened continuum), and a second component proportional to the product of water vapor and foreign-gas partial pressures, resulting from interactions involving a water and a foreign-gas molecule (foreign-broadened continuum). Also characteristic for water continuum absorption is its negative temperature dependence, i. e. the absorption cross section decreases with increasing temperature.

The first evidence of water continuum absorption was seen by *Hettner* [1918] in laboratory measurements in the wavelength region of the atmospheric window around 10 µm. These measurements were inconsistent with the theoretical analysis of the rotational water vapor spectrum by *Elsasser* [1938a]. Ever since, the mechanisms causing the continuum absorption have long been debated.

Since *Elsasser* [1938b] first suggested the accumulated contribution of the far wings of strong water vapor absorption lines as the reason of continuum absorption, substantial

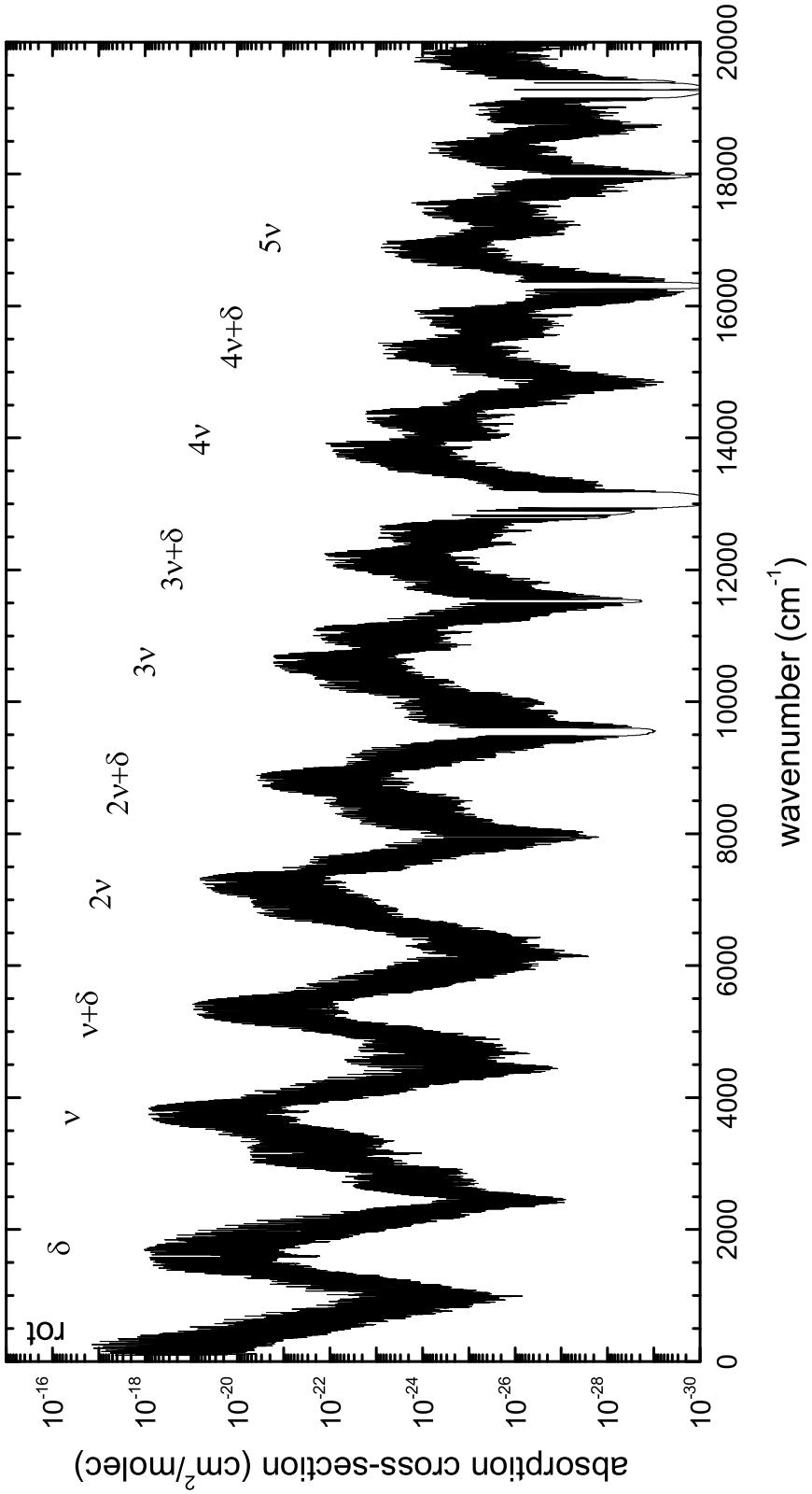

Figure 3.4: *Absorption cross-sections of water vapor, containing about 60 000 rotation-vibration transitions from the HITRAN04 database [Rothman et al. 2005].*

progress has been made to develope a theory, often referred to as *far wing line shape theory* [*Bignell et al.* 1963; *Davies et al.* 1982; *Rosenkranz* 1985; *Ma and Tipping* 1990; *Tipping and Ma* 1995]. The water continuum can be explained in terms of sub-Lorentzian absorption in the far wings of water monomer lines [*Tipping and Ma* 1995], a theory based on binary molecular collisions which alter an originally sharp water absorption line to a strongly broadened one during the short time of molecular interaction. In terms of the partitioning discussed in Section 3.1, the far wing line shape theory represents the absorption due to the free pair states of molecular collisions.

However, it was shown by [*Epifanov and Vigasin* 1997] that at room temperature the role of free pair states is almost negligible compared to the stable and metastable water dimers (see Figure 3.1). Therefore water continuum absorption could be attributed to bound or metastable water dimers or higher collision complexes rather than to the far wing absorption, which also may easily explain the negative temperature dependence of continuum absorption. In fact, a potential contribution to water continuum absorption by the bound water dimer was already suggested by *Penner and Varanasi* [1967]. Currently it is believed that metastable water dimers dominate at atmospheric conditions [*Epifanov and Vigasin* 1997]. Details of the properties and spectroscopy of water dimers are addressed in Section 3.2.3.

Despite many laboratory and atmospheric studies, the fundamental theoretical basis for continuum absorption is not firmly established and the possible contributions by water dimers represent one of the most challenging open questions in spectroscopy. The representation of water continuum absorption generally applied in line-by-line radiative transfer codes is based on empirical extrapolation of laboratory measurements.

Ma and Tipping Theory

A far wing line shape theory from first principles was introduced by *Ma and Tipping* [1990] and improved subsequently by the same authors [1991, 1992a, 1992b, 1995, 1999a, 1999b, 2002]. This first-principles theory has been applied to calculate the far wing line shapes and their temperature dependent contribution to continuum absorption both for the self-broadened and foreign-broadened part. The theory is based on the binary collision and quasistatic approximations and assumes for the interaction potential an isotropic Lennard-Jones part and the leading long-range anisotropic multipolar (dipole-quadrupole) term. Calculations for asymmetric-top molecular systems require the use of the Monte Carlo method to evaluate multidimensional integrals over the angular coordinates necessary to specify the positions before and after the collision (11-dimensional for the self and 9-dimensional for the foreign continuum, respectively). In short, the far wing line shape theory describes water continuum absorption by two mechanisms occurring during a binary collision: (1) The line shape of an absorption line, especially in the far wings, is changed due to the perturbation of the ro-vibrational wavefunctions.

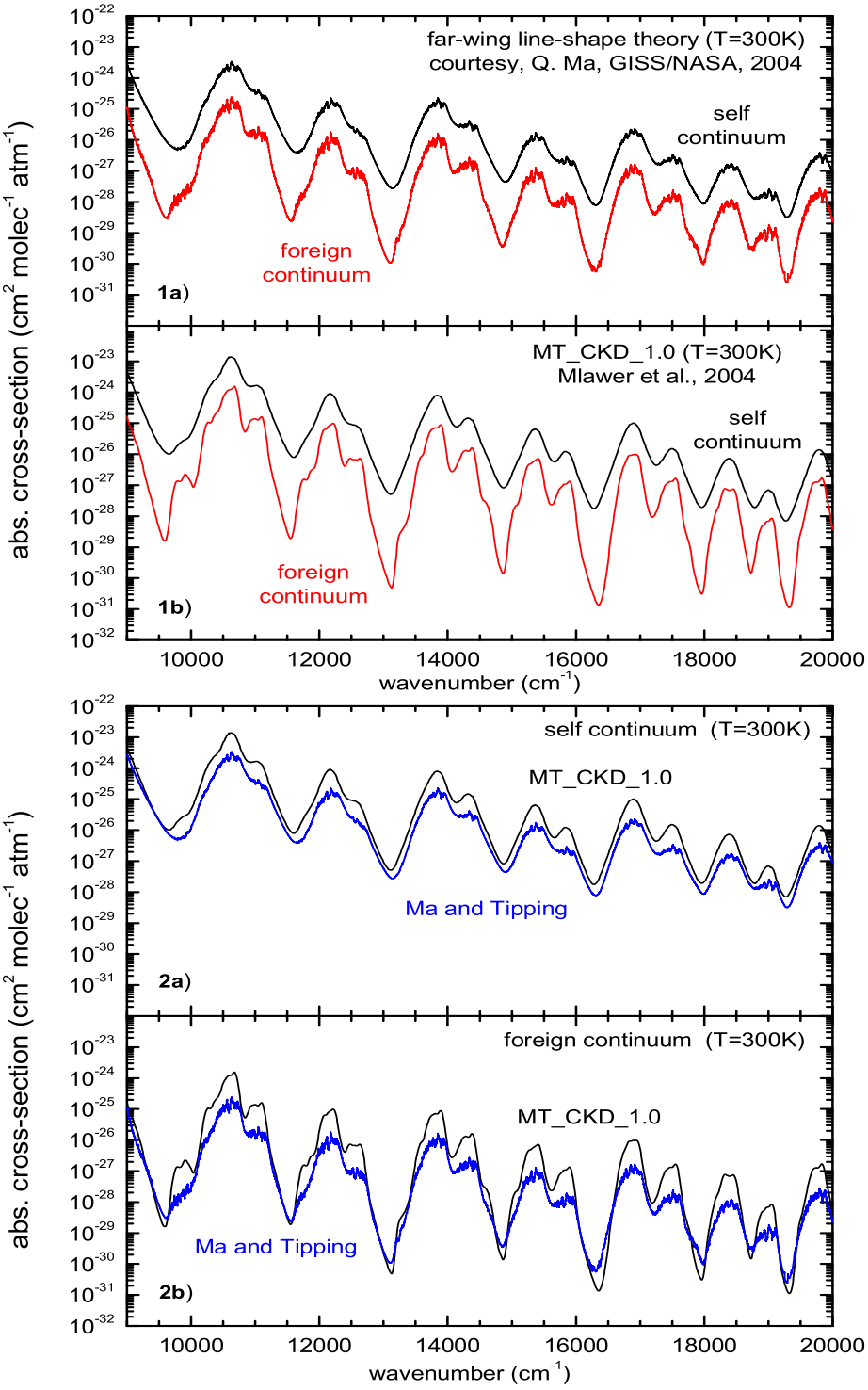

Figure 3.5: *Illustration of the water vapor continuum absorption cross-sections (T=300 K): The self- and foreign-broadened components according to* **(1a)** *the Ma and Tipping far wing line shape theory and* **(1b)** *the MT_CKD model; Comparison of both water continuum characterizations for* **(2a)** *the self-broadened and* **(2b)** *the foreign-broadened component.*

(2) Induced transient dipole moments give rise to new molecular bands, an effect called collision-induced absorption (for a comprehensive overview see *Frommhold* [1993]).

Figure 3.5 illustrates the calculated absorption cross-section for the self- and foreign-broadened continuum components in the 9 000 – 20 000 cm^{-1} spectral region. Generally, without the introduction of any adjustable parameters in the far wing line shape theory, the obtained results compare well with existing laboratory data both in magnitude and in temperature dependence [*Cormier et al.* 2002; *Ptashnik et al.* 2004].

CKD Continuum Model

To describe the contribution of the far wings of collision-broadened water monomer lines to the water continuum absorption, the semi-empirical Clough-Kneizys-Davies (CKD) continuum model [*Clough et al.* 1989] was derived from measurements in the microwave region and consistently applied to all water vapor lines up to the shortwave region. The first version of the model (CKD_0) is based on (1) the sub-Lorentzian behavior of the far wing line shape which follows from the assumption of a finite duration of a collision involving the radiating water vapor molecule, and (2) a super-Lorentzian intermediate wing behavior to obtain agreement with the existing laboratory data of *Burch et al.* [1967, 1981], but without any physical justification. This formulation of the CKD continuum is consistent with the interpretation that the water continuum is due to the intermediate and far wings of allowed transitions of the water monomer. As more accurate spectral observations became available, both from field campaigns and laboratory measurements, a series of revisions to the data-determined CKD continuum model have been developed up to the CKD_2.4 version [*Mlawer et al.* 1999]. It is important to note that every revision to the CKD continuum model contains adjusted values of the continuum coefficients in limited spectral regions, but did not result from a revision of the originally derived line shape formalism.

Based on the most highly regarded measurements of continuum coefficients, a new continuum model formulation (MT_CKD_1.0) of a different functional form than the previous CKD approach has been developed [*Mlawer et al.* 2004]. In addition to the sub-Lorentzian behavior of the far wings, a substantial portion of the continuum in the modified MT_CKD_1.0 version is attributed to collision-induced transitions of the water monomer instead of the super-Lorentzian behavior of the intermediate wings of allowed transitions. This formulation is consistent with the interpretation that the water continuum is due to two distinct effects, (1) the far wings of allowed transitions which are dominant in between water vapor bands, and (2) collision-induced absorption which is dominant within the bands, resulting from the generation of a short-lived complex of a water vapor and a colliding molecule. An illustration of the latest version of the CKD water continuum model as well as a comparison to the Ma and Tipping far wing line shape theory is given in Figure 3.5.

Since the CKD continuum models are derived by fitting to experiment, it is effectually employed in the majority of atmospheric line-by-line radiative transfer codes which account for water continuum absorption [*Soden et al.* 2000]. *Sierk et al.* [2004] recently reported the first observation of atmospheric water continuum absorption in the visible and near infrared region. Their results favor the CKD parameterization of the water vapor continuum, but inconsistencies still exist in either one of the used versions of CKD models (CKD_2.4.1 and MT_CKD_1.0) for different water bands. Taking into account the semi-empirical character of CKD continuum models, in some spectral regions in-band continuum absorption may be also attributed to bound or metastable water clusters. In fact, *Sierk et al.* [2004] admit that they are not able to distinguish between dimer and line shape component of the continuum and recently *Ptashnik et al.* [2004] provided evidence that water dimer absorption may be implicitly included in the CKD self-continuum. However, the authors of the CKD continuum prefer to explain in-band continuum by self- and foreign-broadened water monomer lines and not water dimers.

3.2.3 The Water Dimer

The water dimer represents the archetype for aqueous hydrogen bonding. Understanding the nature of the water dimer is of highest interest in molecular physics, because the pairwise interaction appears to be of paramount importance for expounding a complete molecular description of the liquid and solid phases of water [*Goldman and Saykally* 2004]. In the gas phase a water dimer molecule can form in a three-body collision involving two water molecules and particle X

$$\mathrm{H_2O} + \mathrm{H_2O} + \mathrm{X} \quad \longleftrightarrow \quad (\mathrm{H_2O})_2 + \mathrm{X} \tag{3.12}$$

According to Equation 3.9, the balance of the reaction is described by a temperature dependent constant, the water dimer equilibrium constant

$$K_P(T) = \frac{P_{(H_2O)_2}}{P_{H_2O}^2} \tag{3.13}$$

At fixed temperature, the partial pressure and therefore the number density of the water dimer is proportional to that of the water monomer squared. Despite many theoretical and experimental studies, the magnitude and extent of the negative temperature dependence of the water dimer equilibrium constant as well as further thermodynamic properties is still a controversial issue in molecular physics.

The basic physical properties and spectroscopic signature of water dimers and further water clusters are usually studied in supersonic molecular beam experiments or in solid matrices at very low temperatures, by infrared predissociation spectroscopy [*Vernon et al.* 1982; *Page et al.* 1984; *Coker et al.* 1985; *Huisken et al.* 1996] and

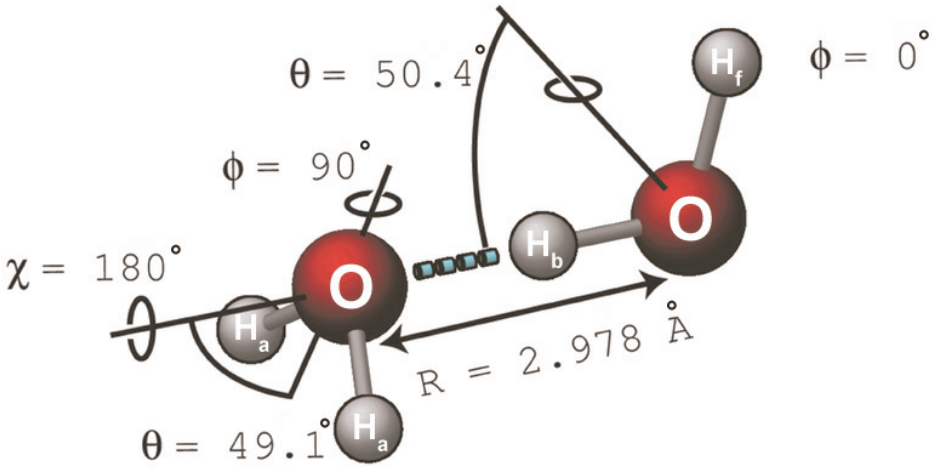

Figure 3.6: *The equilibrium structure of the water dimer. (adopted from Keutsch and Saykally [2001])*

direct absorption spectroscopy of the fundamental O–H stretching and H–O–H bending modes in the infrared [*Van Thiel et al.* 1957; *Huang and Miller* 1989; *Paul et al.* 1997; *Paul et al.* 1999] or by vibration-rotation-tunnelling (VRT) spectroscopy in the microwave region [*Dyke et al.* 1957; *Busarow et al.* 1989; *Zwart et al.* 1991; *Braly et al.* 2000]. Especially the far-infrared tunnelling splittings of ro-vibrational energy levels, which result from hydrogen bond rearrangements, provide a direct insight into the complex water intermolecular potential-energy surface. Assuming rigid monomers, the potential-energy surface of the water dimer is six-dimensional and shows eight identical global minima [*Smith et al.* 1990]. The hydrogen bonding pattern can be rearranged by three distinct low barrier tunnelling pathways connecting the eight degenerate minima of the potential-energy surface, resulting in a splitting of each ro-vibrational band into six subbands [*Fellers et al.* 1999].

Figure 3.6 illustrates the equilibrium structure of the water dimer as determined by calculations on one of the most accurate water dimer potential obtained to date, the recently determined vibration-rotation tunnelling VRT(ASP-W)II and III water dimer intermolecular potential-energy surfaces [*Goldman et al.* 2002]. The water dimer is a trans-linear molecule, consisting of two H_2O units, the hydrogen acceptor unit, H_aOH_a, and the hydrogen donor unit, H_bOH_f. The O–O distance, reflecting the length of the H-bond is 2.952 Å and deviates 2.3° from linearity. The molecule shows only one plane of symmetry and therefore belongs to symmetry group C_s. The water dimer can been regarded as a prolate symmetric top molecule, since two moments of inertia are nearly identical and the third, corresponding to the rotation around the O–O axis, is much smaller.

One of the most interesting properties of the water dimer is the intermolecular pair potential's well depth D_e and the hydrogen bond strength or dissociation energy D_0 (zero-point corrected well depth plus centrifugal barriers of the separated monomers). The VRT(ASP-W)III potential-energy surface gives values of $D_0 = 3.09\,\text{kcal/mol}$ and $D_e = 4.79\,\text{kcal/mol}$ respectively. But an evident variance of these values as derived from theory and experiment exists (Table 3.1), with the most recent and confident values converging to $D_0 = 3.0\,\text{kcal/mol}$ and $D_e = 4.8\,\text{kcal/mol}$.

For determining water dimer concentrations one has to know the magnitude of the water dimer equilibrium constant $K_p(T)$. *Goldman et al.* [2004] has calculated the water dimer equilibrium constant and a number of other thermodynamical data (ΔG°, ΔH°, ΔS°) from the VRT(ASP-W)III potential-energy surface, which they compared with existing experimental and theoretical data summarized in Table 3.1. As pointed out by *Schenter et al.* [2002], one controversial issue is the treatment of quasi-bound states by adequately truncating the partition function for the calculation of thermodynamic properties, since it is known that a substantial number of quasi-bound states exist above the dissociation limit [*Vigasin* 1998; *Vigasin* 2003]. The original calculations by [*Goldman et al.* 2004] were carried out by discarding any ro-vibrational state above the dissociation limit, but a detailed reinvestigation of the treatment of dissociative states yielded a 20% higher value for the water dimer equilibrium constant.

Experimental values of the water dimer equilibrium constant have often been obtained from water steam measurements, where it can be derived form the second viral coefficient (see Equation 3.7) [*Kell et al.* 1968; *Kell et al.* 1989], from the Joule-Thomson coefficient [*McGlashan and Wormald* 2000] or from the thermal conductivity of water vapor [*Curtiss et al.* 1979]. The latter is often cited as the classical experimental work of determining the water dimer equilibrium constant. The matter of fact, that these measurements commonly were carried out at high temperatures beyond atmospheric temperatures is unfavorable for atmospheric applications. One has to rely on extrapolations and the assumption of nearly temperature independent values for the dimerization entropy and enthalpy change, which implicitly assumes the same occupation of bound, metastable, and free pair states for any temperature.

The highly nonrigid water dimer molecule has 15 nontrivial degrees of freedom, three of which correspond to the overall rotation of the dimer and twelve vibrational modes, which can be classified as six intramolecular vibration modes and six intermolecular vibration-rotation modes. The intermolecular vibration-rotation modes, representing the relative motion of the two water molecules, occur at low frequencies ($\nu \leq 800\,\text{cm}^{-1}$) and are expected to be strongly mixed. These intermolecular fundamentals are strongly broadened due to the anharmonicity of the intermolecular interaction and the rotation of the dimer. On the other hand, the six intramolecular vibrational modes show fre-

Table 3.1: *Thermodynamical data of the water dimer: full well depth D_e ; hydrogen bond strength D_0 ; equilibrium constant K_p ; dimerization enthalpy change ΔH°; dimerization entropy change ΔS°.*

	D_e (kcal/mol)	D_0 (kcal/mol)	K_p [a] (atm^{-1})	ΔH° (kcal/mol)	ΔS° (cal/(mol K))
Curtiss et al. [1979]	-5.45		0.0371	-3.59	-18.59
Slanina and Crifo [1992] [b]	-4.86	-3.10	0.0388		
Vaida and Headrick [2000]			0.0147	-3.38	-20.44
Keutsch and Saykally [2001]	-4.85	-3.09			
Goldman et al. [2001]	-4.91		0.1229		
Goldman et al. [2004]	-4.79	-3.09	0.1151	-3.40	-15.93

[a] corresponding temperatures for K_p to be read in the same order as appearing in the table: T=298K (extrapolated), T=298K, T=280K, T=296K, T=292K

[b] based on the BJH/G potential

quencies similar to that of the isolated monomer due to the weakness of the hydrogen bond and the small mass of hydrogen atoms. Consequently, the position of the infrared water dimer bands approximately coincide with that of the monomer, with the fundamental HOH-bending and OH-stretching vibrational bands at about 1 600 cm^{-1} and 3 600 cm^{-1} respectively. Since the hydrogen bond strength is comparatively weak, the absorption of one quantum of energy into an OH-stretching vibration is sufficient to dissociate the dimer [*Huisken et al.* 1996]. Excitation of high rotational modes can also result in dissociation of the dimer (see Figure 3.2). The intramolecular fundamentals and overtones are broadened by mixing with intermolecular excitations and rotational excitations of the dimer. This broadening effect is more pronounced for higher overtones because there are more excitations to be mixed at high frequencies. Additionally, strong spectral broadening occurs due to the short but still very uncertain lifetime of the water dimer molecule. This broadening effect is also expected to increase with overtone number because of the shorter lifetimes of the predissociative overtone states.

Theoretical studies of the spectroscopic signature of the water dimer have been performed extensively, but have mainly focused on the fundamental bands below frequencies of 4 000 cm^{-1}. [*Reimers et al.* 1982; *Coker et al.* 1985; *Reimers and Watts* 1984; *Muñoz-Caro and Niño* 1997]. Our knowledge about the water dimer cross section spectrum has considerably changed during recent years. The fundamental and overtone vibrational spectrum up to 20 000 cm^{-1} were calculated for the first time by *Tso et al.* [1998]. The studies by *Low and Kjaergaard* [1999] (including OH-stretching modes only) and *Schofield and Kjaergaard* [2003] (including OH-stretching and HOH-bending

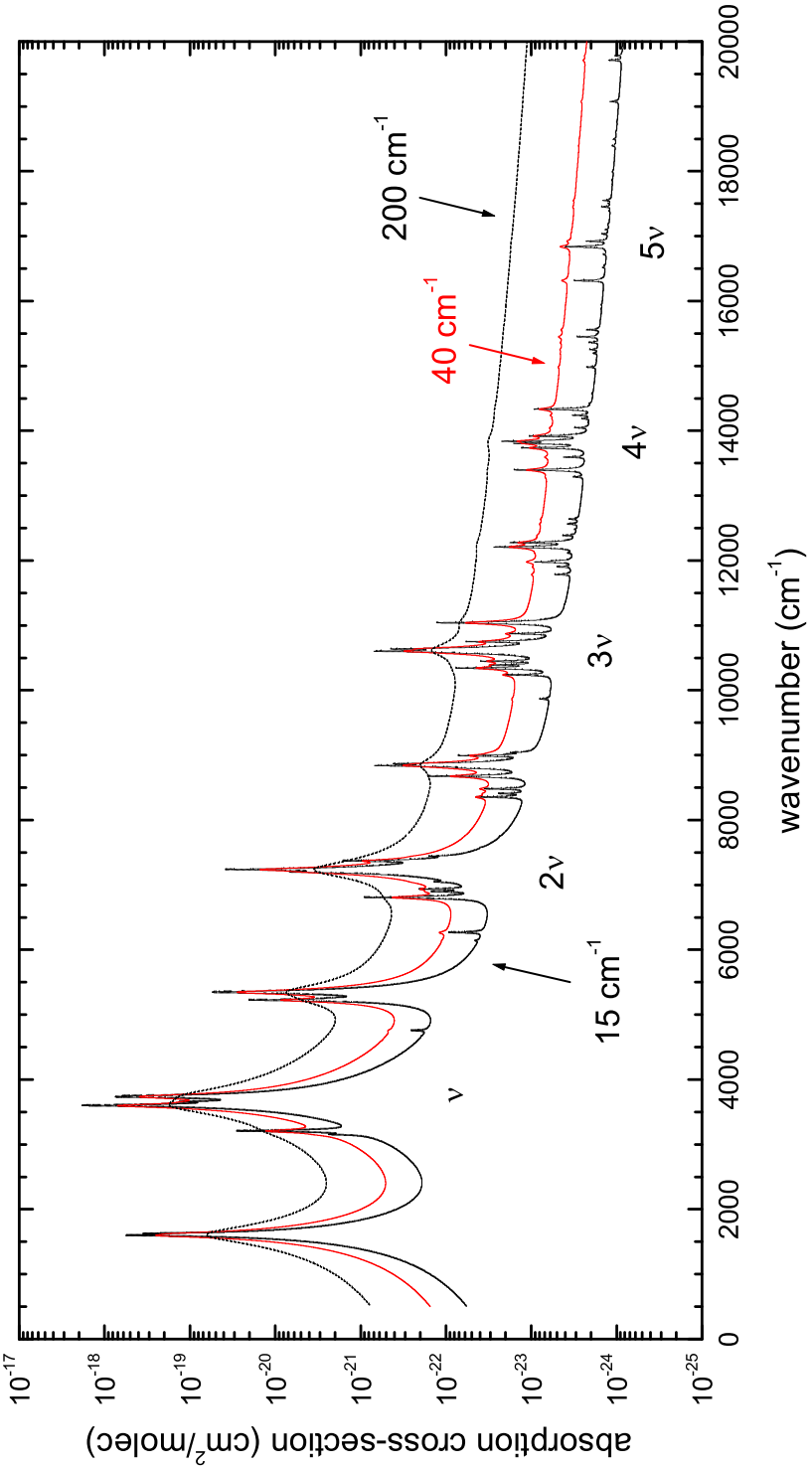

Figure 3.7: *Calculated absorption cross-sections of the water dimer molecule, including OH-stretching and HOH-bending modes according to [Schofield and Kjaergaard 2003]. Pure rotational and intermolecular transitions are not included. Three spectra are shown for different dimer band widths: 15 cm^{-1} , 40 cm^{-1}, 200 cm^{-1}; with 40 cm^{-1} being the likeliest case [Vaida et al. 2001].*

modes) presumably yielded the most accurate water dimer fundamental and overtone absorption cross sections to date (see Figure 3.7). Vibrational modes in the dimer's donor unit are labelled $|x\rangle_{\mathrm{f}}|y\rangle_{\mathrm{b}}|z\rangle$, where x is the vibrational quantum number of the OH_f stretching mode, y the vibrational quantum number of the OH_b stretching mode and z the vibrational quantum number of the H_fOH_b bending mode (see Figure 3.6). In the dimer's acceptor unit the hydrogens are equivalent and the notation used is $|xy\rangle_{\pm}|z\rangle$, where x and y are the vibrational quantum numbers of the OH_a stretching modes and z the the vibrational quantum number of the bending mode. The $\pm$ refers to the symmetry of the vibration around the C_s plane of symmetry. Their calculations are accurate to 40 – 250 cm^{-1} (increasing with the overtone number) for the band frequencies and 10 – 20% for the band intensities. In general, the dimer absorption cross sections decrease exponentially with frequency, about one or two orders of magnitude per overtone. The total intensity of a particular overtone in the dimer is about two times the intensity of the corresponding overtone for the monomer. The most predominant feature in the spectrum is a significantly red shifted hydrogen bonded OH_b-stretching transition, whereas the other OH-stretching transitions occur in regions very close to the corresponding transitions of the water monomer. Therefore, attempts of atmospheric water dimer observation should be carried out in the red shifted bands, where water monomer overlap is small.

Low concentrations of water dimers in comparison to the monomers and the spectroscopic overlap with strong water monomer absorption makes it a challenging task to observe the dimer. Currently, measurements exclusively have identified the fundamental vibrational modes, the HOH-bending mode around 1600 cm^{-1}, the OH-stretching mode around 3600 cm^{-1} and the combination band of both around 5300 cm^{-1} [*Van Thiel et al.* 1957; *Vernon et al.* 1982; *Page et al.* 1984; *Coker et al.* 1985; *Huang and Miller* 1989; *Huisken et al.* 1996; *Paul et al.* 1997; *Paul et al.* 1999; *Ptashnik et al.* 2004; *Ptashnik* 2005]. The band widths of the fundamental modes have been measured to be about 15 cm^{-1} FWHM [*Huang and Miller* 1989; *Huisken et al.* 1996]. As overtone spectra of the water dimer have not been observed to date, one has to rely on measurements of hydrogen-bonded systems of similar size to the water dimer (e. g. CH_3OH). These show a tendency of increasing band width with increasing overtone number to typically several tens per cm at ambient temperatures [*Kjaergaard et al.* 1991; *Kjaergaard et al.* 1993]. Based on this information, *Vaida et al.* [2001] estimates 15 cm^{-1} FWHM as the lower limit and 200 cm^{-1} FWHM as the upper limit for the water dimer band width, assuming a Lorentzian line shape. These values, as well as an average of 40 cm^{-1} FWHM as best estimate, are consistent with calculations by *Tso et al.* [1998].

3.3 Water Dimers in the Earth's Atmosphere

3.3.1 Abundance and the Absorption of Solar Radiation

As already discussed in detail in Chapter 2, inconsistencies between the modeled and measured magnitude of absorbed solar radiation lead to the concept of excess absorption [e. g. *Ramanathan and Vogelmann* 1997], with water dimers being suggested among other species and mechanisms to account for the discrepancies [*Chýlek and Geldart* 1997]. Water vapor is by far the largest contributor to the greenhouse effect due to its high concentration. Therefore water dimers are expected also to be present in considerable abundance and possibly represent an important greenhouse gas as well. The question arising is the following: are the water dimer absorption bands sufficiently intense, broad and shifted with respect to the water monomer band, to not be completely overlapped by the monomer absorption and therefore become significant for the absorption of solar radiation?

The controversy also includes water continuum absorption which is most effective in atmospheric window regions where the water line absorption is small. Nevertheless, the idea of water dimers as potential greenhouse absorbers has not to be abandoned, since the semi-empirical CKD continuum model probably includes water dimer absorption [*Ptashnik* 2005]. Whatever one may call it – dimers or continuum – the most challenging task today is to unveil the physics in which water bimolecular interactions manifest themselves in atmospheric radiative transfer.

Despite various experimental and theoretical studies, there remains considerable uncertainty in the atmospheric concentration of water dimers and their contribution to the absorption of solar radiation. In general, applying the formalism of equilibrium thermodynamics to calculate water dimer concentrations in the atmosphere, the fraction of water molecules that are in the form of dimers ranges between 10^{-5} and 10^{-3} near the surface [*Suck et al.* 1982; *Slanina* 1988; *Mhin et al.* 1993; *Pilewskie and Valero* 1995; *Chýlek and Geldart* 1997; *Vaida and Headrick* 2000; *Vaida et al.* 2001]. These numbers correspond to a concentration of 2.5×10^{12} to 2.5×10^{14} dimers/cm^3, assuming a water vapor mixing ratio of 0.01 as global average. Due to the quadratic dependence of the water dimer partial pressure upon that of the water monomer, the dimer to monomer fraction is highest in the boundary layer where most of the water vapor is present and with increasing altitude the dimer concentration decreases with a scale height about half the monomer's. With additional information on the water dimer spectroscopy it is possible to infer the magnitude of absorbed solar radiation. *Vaida et al.* [2001] performed extensive studies of this quantity by using experimental and theoretical information about the water dimer to evaluate the necessary input parameters for a line-by-line atmospheric radiative transfer model in the wavelength range of 0.4 – 5 µm. They estimated the atmospheric absorption due to water dimers

to be 1.6 – 3.3 W/m^2 in the tropics and 0.3 – 0.7 W/m^2 on global average. This absorption particularly occurs in the 1.5 – 1.8 µm and 1.9 – 2.5 µm window regions of the monomer, since the strong dimer absorption bands around 1.4 µm and 1.9 µm occur at wavelengths coincident to saturated monomer bands. Most of the light in these regions is absorbed by the monomer and therefore reduces the dimer absorption's significance. However, one crucial point is the spectral band-width of the water dimer, which isn't well known up to date. As the width is made larger, more absorption is transferred to the wing of a spectral band and possibly into a window region where significant dimer absorption could occur. For a given dimer abundance broader dimer bands would lead to increased absorption. This is especially important for an enhanced water dimer absorption of terrestrial radiation in the atmospheric window region around 10 µm. Additionally, this enhancement is important for a global warming scenario when an increased temperature is expected to lead to an increase in atmospheric water vapor and therefore a nonlinear increase in the water dimer concentration, providing a positive feedback to anthropogenic climate change.

Laboratory studies in supersonic molecular beams or in solid matrices at very low temperatures can only give indirect information about the occurrence of atmospheric water dimers. Attempts to detect water dimers in the atmosphere failed so far and therefore can only provide upper limits [*Daniel et al.* 1999; *Hill and Jones* 2000]. All atmospheric measurements are based on optical absorption spectroscopy of direct or scattered sunlight in the visible and near-infrared spectral range. *Daniel et al.* [1999] and *Hill and Jones* [2000] conclude from their negative results that predictions of dimer concentrations are seriously in error or the predicted water dimer band intensities of *Tso et al.* [1998] are by far to large (up to a factor of 10), otherwise dimer absorption should not have gone unnoticed in their measurement. In the 0.3 – 2 µm range however, *Daniel et al.* [1999] could give an upper limit of water dimer absorption of 1.5 W/m^2 in the tropics and 0.8 W/m^2 for a clear-sky mid-latitude summer day.

3.3.2 Water Dimer Chemistry

Water molecules are involved in various chemical reactions in the atmosphere, both in the gas- and condensed-phase. Some of the gas-phase reactions require two water molecules or possibly the water dimer. The formation of acid rain and sulfate aerosols will be discussed in detail, as it is of outstanding interest for atmospheric photochemistry, the Earth's radiative budget, and environmental pollution. In addition, the abundance of water dimers in the atmosphere may be important for the formation of radical complexes like $HO_2 \cdot H_2O$ which have been predicted to exist in relatively high concentrations in the atmosphere [*Aloisio and Francisco* 1998; *Aloisio et al.* 2000].

Sulfuric Acid and Sulfates

The formation of sulfuric acid (H_2SO_4) and sulfates (SO_4^{2-}) is of great interest in atmospheric chemistry and the Earth's climate. As effective cloud condensation nuclei, sulfate aerosols play a major role in the process of cloud formation leading to a negative climate forcing both directly and indirectly (for details see Section 2.2.1), which is estimated to be $1 - 2\,W/m^2$ on a global average [*IPCC* 2001]. Accompanied by clouds containing acidic aqueous sulfates is the occurrence of acid rain, especially occurring in densely populated areas. Large amounts of direct input of sulfate precursor gases into the stratosphere result from volcanic eruptions [*Arnold et al.* 1990], but also air traffic is believed to be a contributor [*Reiner and Arnold* 1993]. Sulfate aerosols in the stratosphere lead to the formation of polar stratospheric clouds (PSC), which provide an active surface to catalytically convert chlorine and bromine reservoir species to halogen radicals which lead to ozone hole formation.

Atmospheric precursor gases of sulfuric acid are anthropogenic and volcanic SO_2 [e. g. *Arnold et al.* 1990] and biogenic dimethyl sulfide (DMS) [e. g. *Charlson et al.* 1987] which is subsequently oxidized to SO_2. Following the Stockwell-Calvert mechanism [*Stockwell and Calvert* 1983], the SO_2 is oxidized to sulfur trioxide (SO_3) by the reaction with the hydroxyl radical (OH) and O_2

$$SO_2 + OH + X \longrightarrow HSO_3 + X$$

$$HSO_3 + O_2 \longrightarrow SO_3 + HO_2$$

In the final stage SO_3 is hydrated to form sulfuric acid and sulfates, either in the homogeneous reaction of SO_3 with water vapor or in the heterogeneous reaction with condensed water in aerosols or cloud droplets. The mechanism and kinetics of this reaction have been the subject of various theoretical and experimental studies [*Castleman et al.* 1975; *Wang et al.* 1988; *Reiner and Arnold* 1993; *Kolb et al.* 1994; *Morokuma and Muguruma* 1994; *Lovejoy et al.* 1996; *Jayne et al.* 1997; *Loerting and Liedl* 2000]. Earlier studies assume a linear dependence of the SO_3 loss rate on water vapor pressure but *Kolb et al.* [1994] first of all indicated a second-order dependence of this rate with respect to water vapor pressure, and further indicated a strong negative temperature dependence. The importance of a second water molecule was thereafter considered in molecular orbital calculations for the first time by *Morokuma and Muguruma* [1994], who demonstrated that the activation barrier of sulfuric acid formation is considerably lowered by the catalytical effect of a second water molecule. The results of these studies imply that the homogeneous gas-phase reaction mechanism involves two water molecules and is qualitatively consistent with a mechanism possibly involving the water dimer and the $SO_3 \cdot H_2O$ adduct

$$SO_3 + H_2O \cdot H_2O \longrightarrow H_2SO_4 + H_2O$$

$$H_2O + SO_3 \cdot H_2O \longrightarrow H_2SO_4 + H_2O$$

Both reactions are not simple elementary reactions but proceed via the formation of bound intermediate states [*Morokuma and Muguruma* 1994; *Jayne et al.* 1997].

The 1:1 reaction of H_2O + SO_3 is not likely to contribute significantly below room temperature due to the high activation barrier of 28 kcal/mol, which reduces to about 10 – 11 kcal/mol by the catalytical effect of a second water molecule [*Loerting and Liedl* 2000]. Allowing a third water molecule to participate the same authors calculate an activation barrier of only 4 kcal/mol and by adding further water molecules to the reaction, *Akhmatskaya et al.* [1997] have shown that for clusters of more than approximately twelve water molecules the reaction proceeds with nearly no energy barrier. However, the water content and temperature of Earth's atmosphere precludes the formation of large water clusters. Even the water trimer with about 10^{-3} the abundance of the dimer is of minor importance.

In addition to the gas-phase reactivity, SO_3 is effectively converted to H_2SO_4 on condensed water in aerosols or cloud droplets. *Jayne et al.* [1997] have investigated the competition between homogeneous gas-phase loss of SO_3 versus heterogeneous loss for several cases of atmospheric aerosols and clouds. They conclude that in the troposphere the heterogeneous process cannot compete with the gas-phase reaction because of the relatively large water vapor content. However, with increasing altitude the heterogeneous pathway becomes more efficient as the water vapor concentration drops. But the relevance of the heterogeneous process is only equal to that of the gas-phase process even in a volcanically perturbed stratosphere.

Photochemistry of Nitrogen Oxides

The nitrogen oxides NO and NO_2 (often referred to as NO_x) are of major interest in atmospheric photochemistry as they play a key role in tropospheric ozone formation, stratospheric ozone depletion, acid deposition and formation of other reactive atmospheric oxidants (e. g. NO_3). NO_x species are produced when N_2 reacts with O_2 in high-temperature combustion processes, with the main sources being any kind of fossil fuel combustion, especially traffic, biomass burning and continental biogenic emissions. The overall chemistry which is of great complexity and not subject of this study can be found in *Finlayson-Pitts and Pitts, Jr.* [2000] and references therein.

The NO_2 – O_3 system was recognized to be important for tropospheric nighttime chemistry due to the formation of the nitrate radical NO_3 [*Noxon et al.* 1978; *Noxon*

et al. 1980; *Platt et al.* 1980; *Platt et al.* 1984], which reacts with NO_2 to form N_2O_5

$$NO_2 + NO_3 \quad \longleftrightarrow \quad N_2O_5$$

The formation of N_2O_5 and its reaction with water to form nitric acid (HNO_3) is a major sink of tropospheric NO_x during night time. This reaction can occur either homogeneously in the gas-phase or heterogeneously on aqueous aerosols. The experiments by *Mentel et al.* [1996] and *Wahner et al.* [1998] provided evidence that the gas-phase reaction is a superposition of two processes

$$N_2O_5 + H_2O \quad \longrightarrow \quad 2HNO_3$$

$$N_2O_5 + 2H_2O \quad \longrightarrow \quad 2HNO_3 + H_2O$$

which are first order and second order in water vapor respectively. The authors suggest that the second process possibly involves the water dimer. Although it is well known that the formation of HNO_3 proceeds much faster on aqueous aerosols [*Mozurkewich and Calvert* 1988], *Wahner et al.* [1998] conclude from their measurements that the combined process including both gas-phase pathways and the heterogeneous reaction on aerosols should be considered in atmospheric chemistry.

3.3.3 Water Complexes

It is well-known that water is able to form complexes with both itself and with other molecules. The study of these complexes is of interest to many fields of physics, chemistry, biology and multidisciplinary research.

The complexes containing only water molecules, also called water clusters, starting with the dimer as the smallest and growing through the trimer, tetramer, pentamer to larger oligomers, provide a key for the understanding of the molecular description of the liquid and solid phases of water, the process of homogeneous nucleation of water vapor into droplets and the solvation phenomenon [*Huisken et al.* 1996; *Keutsch and Saykally* 2001]. Different aspects of the role of water dimers in the atmosphere have already been discussed in this section, in addition they may also be important for modeling water condensation [*Slanina and Crifo* 1992] as the dimer is the first step from the vapor to the liquid. Water clusters higher than the dimer are expected to be of minor significance for the absorption of solar radiation and atmospheric photochemistry due to their low abundance and cyclic structure [*Vaida and Headrick* 2000; *Vaida et al.* 2001].

Considerations concerning the water vapor continuum, the heterogeneous complexes H_2O–N_2 H_2O–O_2 and H_2O–Ar may be important in the context of the foreign-broadened continuum part, in a similar manner as water dimers are for the self-broadened part [*Kjaergaard et al.* 2003; *Daniel et al.* 2004]. The physicochemical properties of the hydrated complexes H_2O–HNO_3 and H_2O–O_3 in Earth's atmosphere have been studied extensively by *Vaida and Headrick* [2000], which also give references to studies about a myriad of other species.

4 Methodology

Absorption spectroscopy is an efficient measurement technique in atmospheric physics and chemistry. Although only an averaged information along the absorption path is obtained, the technique is particularly suitable for remote sensing Earth's atmosphere in large spatial and temporal coverage without any interference with the environment.

The following chapter describes the basics of absorption spectroscopy. In particular, the widely used technique of Differential Optical Absorption Spectroscopy (DOAS) is introduced. Within this work, an active Long Path DOAS system is employed. The instrumental details are described in the following.

4.1 Absorption Spectroscopy

4.1.1 Basics of Line Absorption

This section addresses the basic definitions and concepts of describing an individual absorption line[1], as far as needed to calculate absorption cross sections from molecular databases such as HITRAN, or dealing with line saturation effects. A comprehensive overview of the basics in molecular physics and spectroscopy is found in the textbooks of *Bransden and Joachain* [1983] and *Thorne* [1988].

A molecule may absorb a photon from an electromagnetic radiation field by an upward transition into a state of higher electronic, vibrational or rotational energy, if the difference of the energies of two states equals the energy of the photon. The transition probability depends linearly on the energy density of the radiation field. The constant of proportionality is the Einstein coefficient for absorption, which is obtained from calculating the corresponding electric dipole transition matrix element. The quantity describing the strength of absorption is the line strength S_{ij}, which is given by the integral of the absorption cross section $(\sigma_\nu)_{ij}$ over the entire line. The line strength can also be calculated from the Einstein coefficient of absorption B_{ij} or the dimensionless oscillator strength f_{ij}

[1] In view of atmospheric absorption only molecules will be considered, but the concepts certainly apply to any absorption line, both atomic and molecular.

$$S_{ij} \;=\; \int_{line} (\sigma_\nu)_{ij}\, d\nu \;=\; \frac{h\nu_{ij}}{c}\, B_{ij} \;=\; \frac{e^2}{4\varepsilon_0 m_e c}\, f_{ij} \tag{4.1}$$

where h is Planck's constant, c the speed of light, ν_{ij} the line central frequency, e the electron charge, m_e the electron mass and ε_0 the permittivity of vacuum. S_{ij} is in dimensions of m^2/s per molecule. It is convenient to use the numerical version of Equation 4.1, which is obtained by the insertion of the numbers and expressing frequencies in terms of wave numbers $\bar{\nu} = \nu/c$. Then, the conversion from oscillator strengths to line strengths per molecule is written as

$$S_{ij} \;=\; \int_{line} (\sigma_{\bar{\nu}})_{ij}\, d\bar{\nu} \;=\; 8.853 \times 10^{-13} cm \cdot f_{ij} \tag{4.2}$$

In this notation S_{ij} is in dimensions of cm per molecule. Assuming a Lorentzian line profile with a band's half width at half maximum Γ, the band strength is related to the peak absorption cross section by the relation

$$\sigma_{ij} = S_{ij}/(\pi\Gamma) \tag{4.3}$$

The line strength is directly related to the power absorbed by the respective transition and can be interpreted as the area enclosed by the absorption line.

Line strengths[2] are listed in spectral line databases such as HITRAN for each individual transition as defined by the change of at least one of its electronic, vibrational or rotational quantum numbers. The quantity "band strength", describing the absorption strength of an entire vibrational band, is used in molecular physics as well. For details the reader is be referred to further reading [e. g. *Thorne* 1988].

The light's intensity as a function of frequency is usually available from measurement. Hence, of more interest than the absorption strength is the profile of the absorption line. Three different processes lead to a broadening of a spectral line: natural broadening, Doppler broadening and collision broadening. Natural broadening is a consequence of the uncertainty principle in the form $\Delta E \Delta t \sim \hbar$. A finite lifetime Δt of a state implies an energy uncertainty ΔE and results in a Lorentzian line profile. However, for atmospheric conditions natural line widths are small compared to both other effects and can be neglected. Thermal motion of the absorbing molecule results in a frequency shift of the indivual line due to the Doppler effect. The spread of shifts corresponds to the spread of velocities of the molecules which follows the Maxwell distribution and depends on temperature and molecular mass. Therefore, the Doppler profile is a Gaussian. Collision or pressure broadening is based upon interactions between a absorbing molecule and further particles. This broadening is more effective with increasing gas pressure. The treatment of pressure broadening requires to go into much more detail which is not within the scope of this work. Assuming instantaneous collisions, i. e. the collision time

[2] More precisely "rotational line strengths"

is small compared to the time between collisions, a Lorentzian distribution is obtained. This assumption is sufficient for atmospheric conditions, where pressure broadening is the prevailing process. However, Doppler broadening should not be neglected entirely and one should use a Voigt profile, which is the profile obtained by convolving a Gaussian and a Lorentzian line shape function.

4.1.2 The Law of Lambert-Beer

Absorption spectroscopy is an ideal technique to identify and quantify atmospheric trace gases. The method is based on the attenuation of light while travelling through the atmosphere. The attenuation is caused by processes of scattering and absorption, of which the most important for the atmosphere are Rayleigh scattering, Mie scattering, and discrete line absorption as already outlined in Section 2.1.2. It is the discrete line absorption from which atmospheric trace gas concentrations are derived due to the unique spectral characteristic of each absorbing species. Therefore, line absorption has to be separated from superimposed scattering attenuation, which is achieved successfully by the DOAS technique. However, the spectral analysis is complicated when absorption is in saturation and cannot be described by a linear curve of growth.

In general, the extinction of light is described by the law of *Lambert-Beer*, which is obtained by integrating Equation 2.8

$$I_\nu(l) = I_\nu(0)\, \exp\left\{ - \int_0^L e_\nu dl \right\} \tag{4.4}$$

Introducing the *absorbance* or *optical depth* $\tau_\nu = \int_0^L e_\nu dl$ leads to

$$I_\nu(l) = I_\nu(0)\, \mathrm{e}^{-\tau_\nu} \tag{4.5}$$

The extinction coefficient e_ν is the sum of the scattering coefficient s_ν and absorption coefficient k_ν. It is convenient to express absorption in terms of absorption coefficient per number density of the absorbing species, referred to as *absorption cross section* $\sigma_\nu = k_\nu / n$. Taking into account all absorbers gives

$$k_\nu = \sum_i (\sigma_\nu)_i\, n_i$$

Considering only one absorber which is homogenously distributed along the absorption path L, the law of Lambert-Beer can be written as

$$I_\nu(L) = I_\nu(0)\, \mathrm{e}^{-\tau_\nu} = I_\nu(0)\, \mathrm{e}^{-\sigma_\nu n L} \tag{4.6}$$

The Lambert-Beer law is often seen in the form of its logarithm

$$\ln \frac{I_\nu(0)}{I_\nu(L)} = \tau_\nu = \sigma_\nu n L \tag{4.7}$$

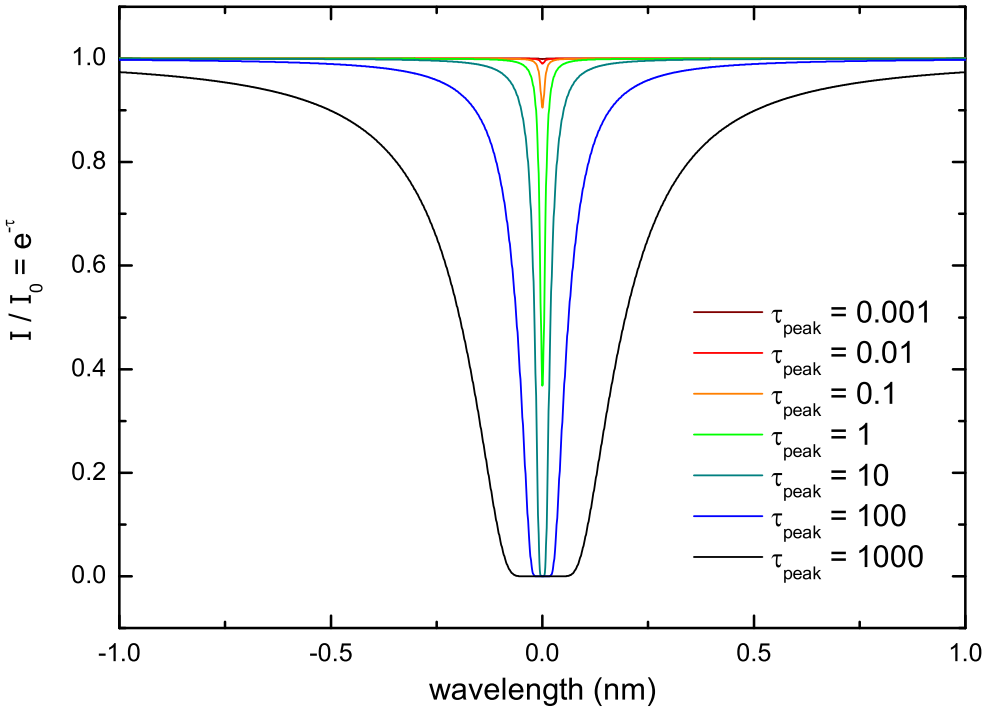

Figure 4.1: *Schematic illustration of an absorption line going into saturation. A Voigt profile is used for the absorption cross section.*

Curve of growth

The absorption strength is proportional to the enclosed area by the absorption line. Increasing the line's optical depth, for example due to an increase in the number of absorbing species or the absorption path length, results in an increase in the line's dip. Obviously, the dip does not fall below the baseline. The absorption saturates first at the line center and then out towards the wings as illustrated in Figure 4.1. The area framed by the absorption line defines the equivalent width[3]

$$W_\nu = \int_{line} (1 - \mathrm{e}^{-\tau_\nu})\, d\nu \qquad \text{or} \qquad W_\lambda = \int_{line} (1 - \mathrm{e}^{-\tau_\lambda})\, d\lambda \tag{4.8}$$

For a given absorption line the curve of growth (Figure 4.2) describes the behavior of the line's equivalent width as the optical depth is changed. In the optically thin case ($\tau \ll 1$) the absorption is linear, but exhibits to a square root dependence in the optically thick case ($\tau \gg 1$).

[3]Equal to the width of a rectangle with unity height and same area.

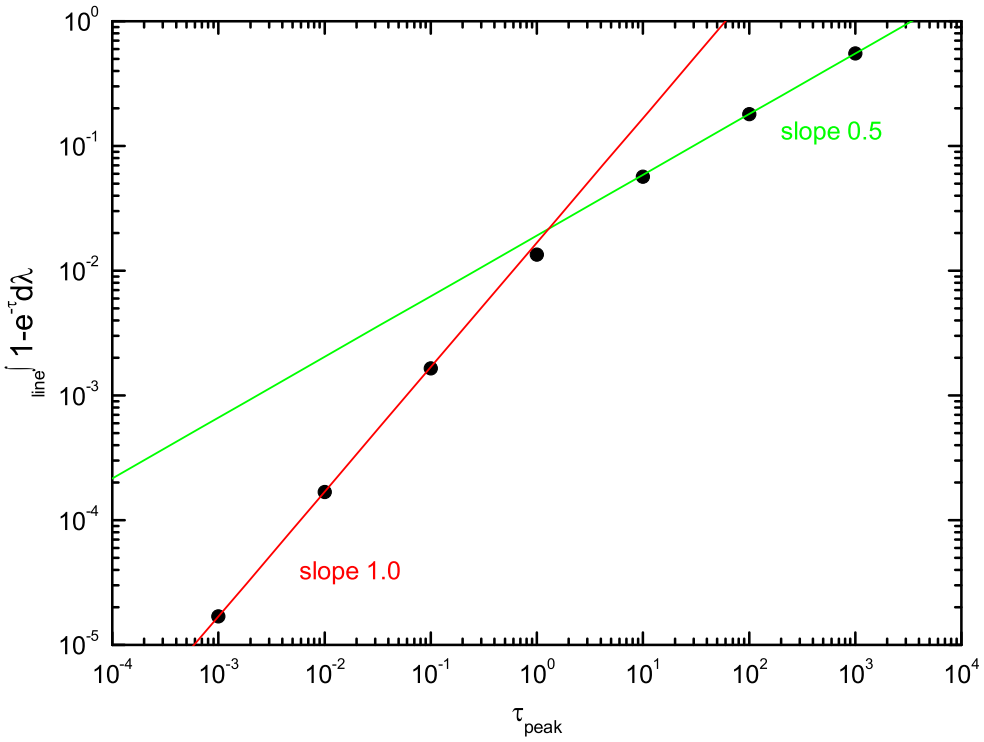

Figure 4.2: *Curve of growth: The strength of absorption in dependence on the line's peak optical depth. The data points correspond to the absorption lines shown in Figure 4.1.*

4.1.3 Principles of Differential Optical Absorption Spectroscopy

Applying the law of Lambert-Beer directly to a measured spectrum with intensity[4] $I(\lambda)$ requires the exact knowledge of the source intensity $I_0(\lambda)$. In contrast to absorption spectroscopy in the laboratory, the absolute absorption signal cannot be accessed due to the lack of information about $I_0(\lambda)$ in the absence of the atmosphere. To match the needs of atmospheric absorption spectroscopy, i. e. to distinguish between the extinctions due to trace gas absorption, Rayleigh scattering, and Mie scattering, the technique of Differential Optical Absorption Spectroscopy (DOAS) was developed [*Platt et al.* 1979; *Platt* 1994].

The DOAS technique is based on the fact that molecular absorption cross sections usually consist of narrow absorption bands superimposed on a broad continuum. The continuum part, as well as Rayleigh scattering and Mie scattering, show only a smooth wavelength dependence. These continuum parts can be well separated from the highly structured part, from which direct information about a trace gas concentration is obtained. As illustrated in Figure 4.3, the absorption cross section σ may be split into a

[4]Instead of the spectral flux I_ν used previously, it is convenient to interpret $I(\lambda)$ as the intensity of a measured spectrum, commonly in arbitrary units.

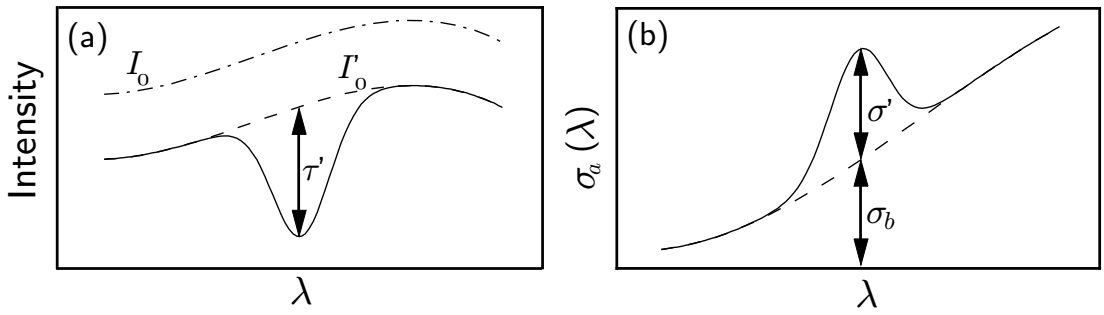

Figure 4.3: *Illustration of the DOAS principle:* **(a)** *the differential optical depth τ' defined by the baseline intensity $I'_0(\lambda)$ omitting broadband spectral parts,* **(b)** *the absorption cross section split up into a broadband component σ_b and a narrowband component σ'.*

low frequency component σ_b and a high frequency component σ'

$$\sigma = \sigma_b + \sigma'$$

Accordingly, this can be applied to each absorbing species and the Lambert-Beer law can be written as

$$I(\lambda) = I_0(\lambda)\, \exp\left\{ - \int_0^l \Big(s_R(\lambda, l) + s_M(\lambda, l) + \sum_i \big(\sigma_{b,i}(\lambda) + \sigma'_i(\lambda)\big)\, n_i(l) \Big) dl \right\} \quad (4.9)$$

with the extinction coefficients s_R and s_M for Rayleigh and Mie scattering, respectively. The broadband terms do not need to be specified and can be merged to yield $I'_0(\lambda)$, which is interpreted as a new source intensity (Figure 4.3)

$$I(\lambda) = I'_0(\lambda)\, \exp\left\{ - \int_0^l \sum_i \sigma'_i(\lambda)\, n_i\, dl \right\} \quad (4.10)$$

According to Equations 4.4 and 4.5 the *differential optical depth* is defined

$$\tau'(\lambda) = -\ln \frac{I(\lambda)}{I'_0(\lambda)} = \sum_i \int_0^l \sigma'_i(\lambda)\, n_i\, dl = \sum_i \tau'_i(\lambda) \quad (4.11)$$

In general, the absorption cross section depends on temperature and pressure. Assuming these values and the absorber's number density to be constant along the absorption path L, which is justified for the Long Path DOAS technique performed within this work, the differential optical depth for each absorbing species can be expressed as

$$\tau'_i(\lambda) = \sigma'_i(\lambda)\, C_i = \sigma'_i(\lambda)\, n_i\, L \quad (4.12)$$

with the *number column density* $C_i = n_i\, L$, the quantity which is directly obtained from the evaluation procedure.

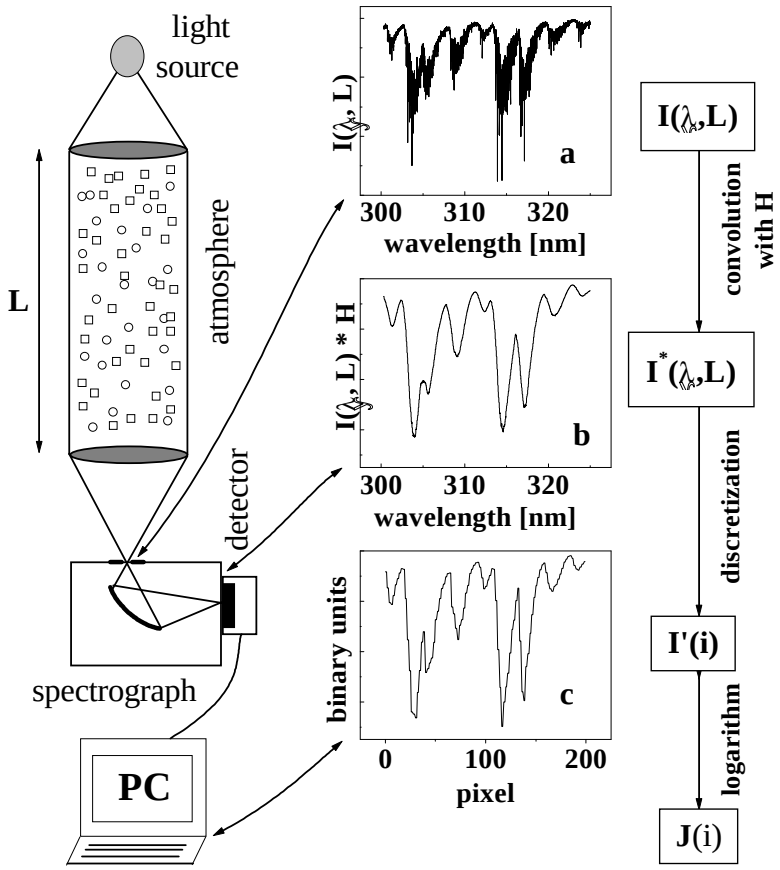

Figure 4.4: *Spectra recording process using a typical DOAS-setup:* **(a)** *original atmospheric spectrum containing all spectral information,* **(b)** *degradation due to the finite resolution of the spectrograph,* **(c)** *discretization due to the given properties of the detector and the analog-digital conversion.*

Figure 4.4 illustrates a simplified DOAS setup and the modifications to an original atmospheric spectrum until it is finally stored to the hard-disk of a PC and available for analysis. After its way through the atmosphere, the light of initial intensity $I_0(\lambda)$ is reduced to the intensity $I(\lambda)$ obeying Lambert-Beer's law. When reaching the entrance slit of the spectrograph, the light contains all the spectral information imprinted from the atmosphere. However, the spectrum is degraded to the resolution of the spectrograph which depends on the width of the entrance slit and the properties of the optics and grating. This degradation is mathematically described by a convolution of $I(\lambda)$ with the instrumental line shape function $H(\lambda)$

$$I^*(\lambda) = I(\lambda) \circ H(\lambda) = \int I(\lambda - \lambda')H(\lambda')d\lambda' \tag{4.13}$$

Usually, the instrumental line shape function is obtained from an atomic emission line spectrum of a low pressure lamp (e. g. Neon, Mercury). The true spectral line widths of

those emission lines may be considered to be infinitely small compared to the resolution of the spectrograph. During spectra recording the wavelength range is mapped to N discrete detector pixels i, each integrating the light in a wavelength interval $\lambda(i)$ to $\lambda(i+1)$

$$I'(i) = \int_{\lambda(i)}^{\lambda(i+1)} I^*(\lambda')d\lambda' \tag{4.14}$$

The wavelength to pixel mapping is derived from a low pressure lamp spectrum as the wavelengths of emission lines are well known. The mapping is generally approximated by a low order polynomial.

The specific realization of the spectral retrieval by the use of the Long Path DOAS technique is given in Sections 4.3 and 4.4. For a comprehensive overview see also the work of *Stutz* [1996].

4.2 Instrumentation

In order to perform absorption spectroscopy it is mandatory to have an adequate light source. For atmospheric applications the light source is either an artificial *active* one or a *passive* one, e. g., sun- or moonlight.

By means of an active Long Path DOAS instrument (LP-DOAS) as used for this work, a beam of light is sent through the atmosphere on a well defined light path, is collected thereafter by suitable optics and is then directed to a spectrograph-detector system where the spectrum is recorded. Due to the fact that each gas has a characteristic absorption structure, the type and concentration of atmospheric trace gases occurring along the absorption path can be determined simultaneously.

For passive DOAS instruments the sun is commonly used as a light source, either direct sunlight or scattered sunlight. An overview of this technique and its applications are given in *Hönninger et al.* [2004].

4.2.1 Long Path Telescope

In general, an active LP-DOAS system consists of a light transmitting and a light receiving optics. To avoid the operation of instruments at two sites in a distance of several kilometers, the light path is folded by the use of a reflector which can be set up anywhere in the field. It is convenient to use quartz corner cube retro-reflectors, as they reflect the light exactly by 180° independent on the angle of incidence. Therefore, only coarse adjustment of the reflector is needed. Depending on the reflector distance arrays of up to 200 retro-reflector units are constructed.

As an advantage of the 180° reflection, the light transmitting and light receiving optics can be combined in one instrument realized by a coaxial Newton telescope as depicted in Figure 4.5. The main mirror with parabolic shape has a diameter of 300 mm

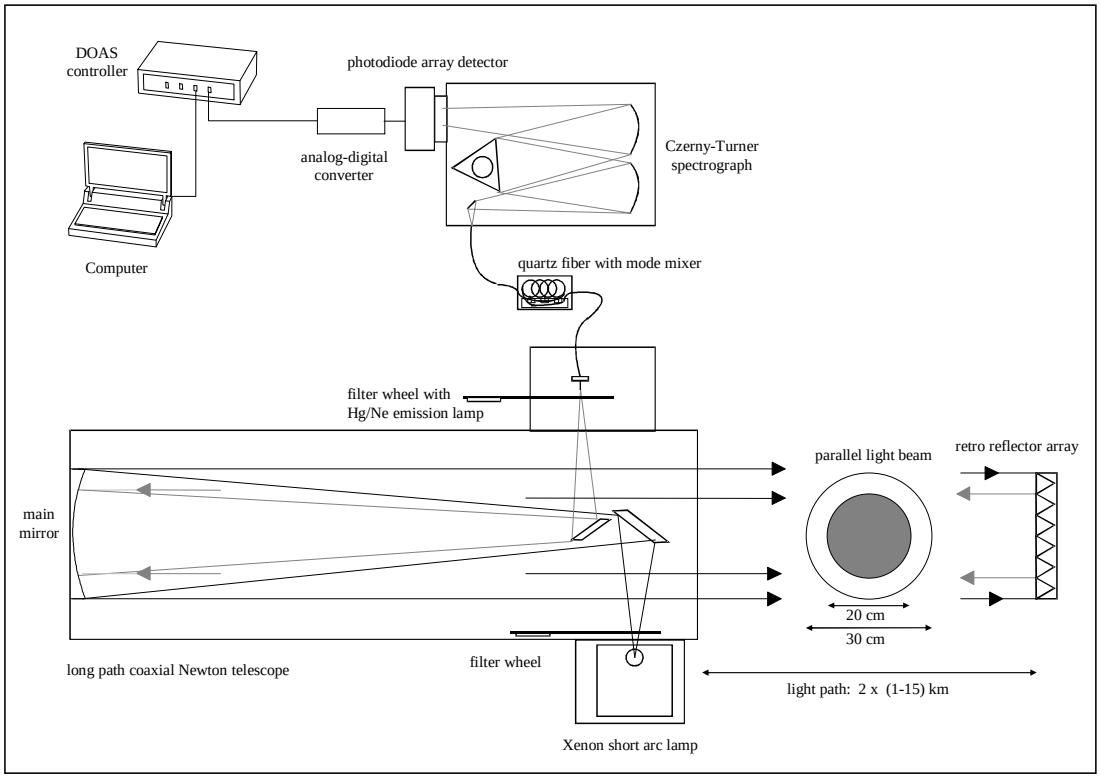

Figure 4.5: *Active long path DOAS system. The main optical components are shown.*

and a focal length of 1500 mm. Two differently sized secondary elliptical plane mirrors are mounted in such a way that two Newton telescopes are obtained, sharing the same main mirror. The light receiving telescope operates with the inner part of the main mirror (diameter of 200 mm), the light transmitting telescope with the remaining outer ring (width of 50 mm). A Xenon short arc lamp, acting as a nearly point light source, is placed in the focal plane associated with the large secondary mirror. Thus, a ring-shaped parallel beam of light is sent through the atmosphere. Due to the fact that the light source is not really point sized and the distance to the retro-reflectors is large, the outgoing ring is getting blurred and the reflectors are lit uniformly. The light coming back into the telescope is focused on a quartz fiber positioned in the focal plane associated with the small secondary mirror.

The LP-DOAS telescope is equipped with several stepper motors in order to perform automated measurements. Two motors horizontally rotate and vertically tilt the whole telescope in order to center the light beam on the retro-reflectors. Two further motors move filter wheels, of which one is placed in front of the Xenon lamp. This filter wheel is equipped with long pass filters to reduce stray light entering the spectrograph and to suppress the second order of diffraction which otherwise would overlap with the red part of the first order spectrum. Schott GG475 and RG630 filters are used for the

measurements. Additionally, a black baffle is mounted to prevent the lamp's light from entering the telescope in order to record background spectra. The second filter wheel, equipped with Neon and Mercury emission lamps, is mounted in front of the quartz fiber. These emission line spectra are recorded regularly for wavelength calibration and to determine the instrument's line shape function. The entrance of the fiber is mounted on a device containing two motors for movement within the telescope's focal plane. Thus, fine alignment of the fiber is carried out if the telescope motors act too coarse. This additional method of alignment was introduced for path length longer than $\approx 8\,\mathrm{km}$ [*Peters* 2005]. Regular alignment is necessary due to changes in ambient temperature and pressure affecting the refractive index of air and causing thermal expansion of the telescope tube assembly. Finally, one motor moves an optics to directly record Xenon lamp spectra, the light which has not passed the long distance through the atmosphere. This system is also known as *shortcut system* and is described in detail in Section 4.2.6.

4.2.2 Light Sources

A LP-DOAS instrument is commonly operated with a high pressure Xenon short arc lamp as a light source. However, new developments in semiconductor technology will make light emitting diodes (LED) a good alternative [*Kern et al.* 2006]. Within this work quartz tungsten halogen lamps are tested for their suitability for LP-DOAS measurements.

Xenon Short Arc Lamps

Xenon short arc lamps are used for all field measurements within this thesis. The design of this type of lamp is shown in Figure 4.6. Within the Xenon gas bulb, a continuous high pressure arc discharge is maintained. For lamp ignition, a high voltage is applied to provide the required initial ionization. Due to the high operating pressure of up to 100 bar, the spectrum is a superposition of thermal emission according to the Planck function and Xenon emission lines which are strongly pressure broadened. The color temperature of Xenon lamps is about 6 000 K which is comparable to that of the sun. A high intensity output throughout the visible and near-infrared spectral region is provided.

The bulb of a Xenon arc lamp is made of quartz glass, which is very resistant to high pressure and temperature. The material of the electrodes is tungsten, with an edged peaked cathode to enhance electron emission and a massive anode to withstand the electron bombardment and efficiently dissipate the heat produced. As the distance between the electrodes is small ($\approx 1\,\mathrm{mm}$) the size of the arc point is small as well. The lamp almost acts as a point light source, therefore the divergence of the light beam transferred through the atmosphere is small.

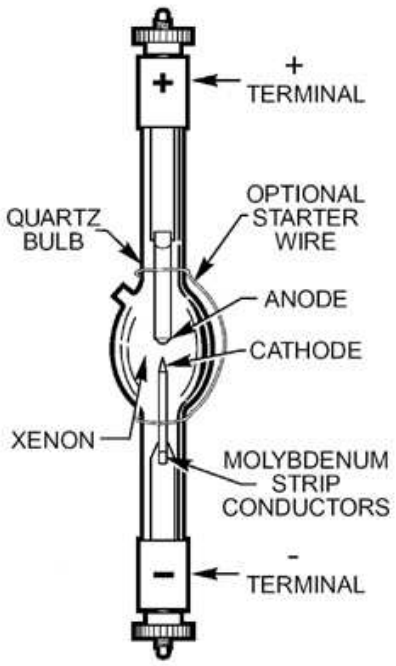

Figure 4.6: *Design of a high pressure Xenon short arc lamp.*

The same type of Xenon arc lamps (PLI HSA-X5002, manufactured by Professional Lamp Inc., USA) is used for all field measurements. The lamps of 500 W total power are operated at ≈ 28 A and have a mean lifetime of 200 hours. The arc size is $0.3 \times 0.3\,\mathrm{mm}^2$. Studies on the characteristics of Xenon short arc lamps have been carried out by *Hermes* [1999]. A common problem is the shifting of the arc point and unstable light emission at the wavelengths of Xenon emission lines. The strength and pressure broadening of these emission lines vary in time, which makes spectra analysis difficult. Strong Xenon emission lines are found in the near-infrared near 820 nm and some weaker lines are present in the blue spectral region.

Quartz Tungsten Halogen Lamps

Quartz Tungsten Halogen (QTH) lamps (Figure 4.7) may possibly be used as a light source for LP-DOAS. The usability is limited to the red and near-infrared spectral region due to a color temperature of only about 3 000 K. The advantage of this type of lamp is a smooth and steady spectrum. However, the lamp's filament is too large to act as a point source, therefore only light emitted from a small part of the filament is transferred is usable. A small and dense filament design is more important than lamp power. Usually a higher power is associated with a larger filament.

The usability of quartz tungsten halogen lamps is investigated during test measurements on a short light path of 1 km. Adjustment is performed by replacing an adjusted

Figure 4.7: *Quartz Tungsten Halogen Lamp (OSRAM Xenophot HLX series).*

Xenon lamp by a QTH lamp mounted in such a way that its filament is located at the same position as the arc point of the Xenon lamp. Lamps of the OSRAM Xenophot HLX series, showing a comparatively high color temperature of 3 300 K, are tested and compared with an OSRAM XBO 450 W Xenon lamp. Examples of spectra are shown in Figure 4.8 for both types of lamps. An overview of the characteristics of the tested lamps is given in Table 4.1, in particular the intensity transmitted through the entire LP-DOAS system including the atmosphere is listed. It is clearly seen that the total power of a QTH lamp is not correlated with the intensity. The 250 W QTH lamp is problematic due to large spacings in the spiral-wound filament. All in all, the PLI Xenon lamp provides at least ten times the intensity of the best QTH lamp. In conclusion, Xenon lamps should be preferred. Only for short light paths with short integration times the QTH lamp type is an option.

Table 4.1: *Characteristics of different light sources. The intensity, i. e. the total light throughput of the LP-DOAS instrument, is measured at a wavelength of 750 nm. The dimension of the filament or the arc point is given.*

Lamp	Power (W)	Voltage (V)	Current (A)	Dimension (mm×mm)	Intensity relative
Xenon Lamps					
XBO	450	22.5	20	2.7×0.9	1
PLI	500	18	28	0.3×0.3	≈ 5
Quartz Tungsten Halogen Lamps					
Xenophot	20	6	3.3	2.3×0.8	0.15
Xenophot	50	12	4.2	3.3×1.6	0.43
Xenophot	100	12	8.3	4.2×2.3	0.32
Xenophot	150	24	6.3		0.32
Xenophot	250	24	10.4	7.0×3.5	0.13

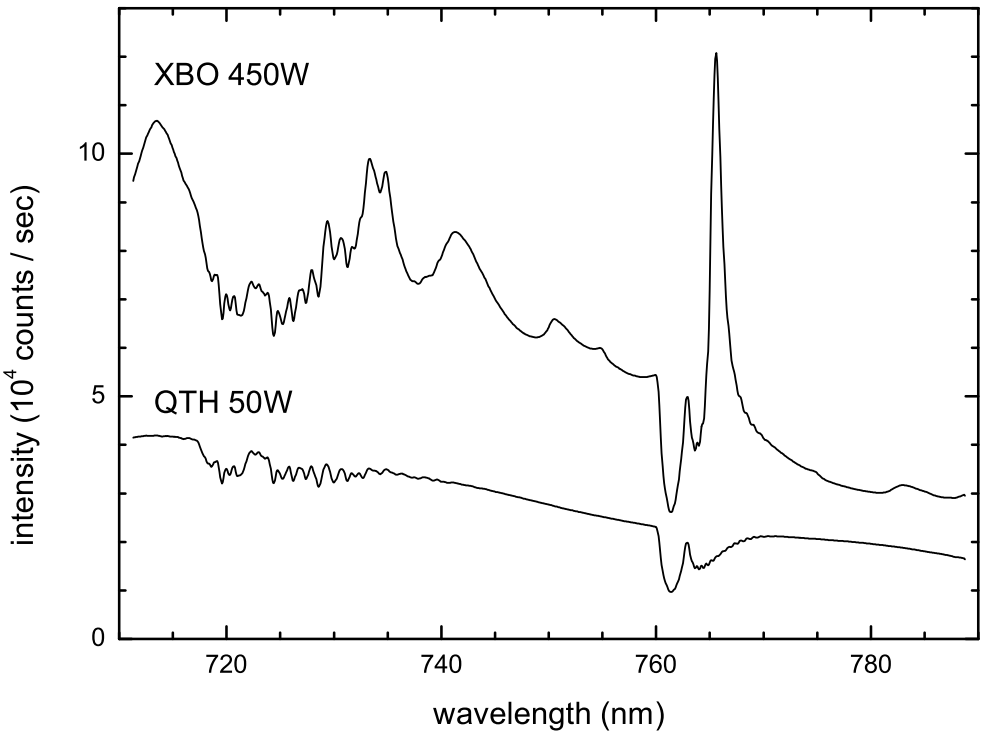

Figure 4.8: *Atmospheric absorption spectrum when using an OSRAM XBO 450 W Xenon short arc lamp or an OSRAM HLX 50 W Quartz Tungsten Halogen lamp as a light source.*

4.2.3 Quartz Fiber

The quartz fiber transmits the light from the telescope to the entrance slit of the spectrograph. A multi mode step-index fiber with 200 µm diameter and a numerical aperture of 0.12 is used. The numerical aperture corresponds approximately to the aperture ratio of both the telescope and the spectrograph.

One common problem when using quartz fibers is a non-uniform illumination of the emitted light cone which enters the spectrograph. This leads to a non-uniform illumination of the spectrograph's diffraction grating and detector, resulting in high residual structures in the spectral analysis. A mixing of the transmitted fiber modes is required to achieve a homogenous illumination. For this purpose a *quartz fiber mode mixer* is used [*Stutz and Platt* 1997]. The bare quartz fiber is bent and slightly squeezed as seen in Figure 4.9. For temporal averaging, a fan causes the loops of the fiber to jiggle. The use of a quartz fiber mode mixer leads to a reduction in residual noise of the spectral evaluation and leads to an considerable improvement of the instrument's performance. Nevertheless, the residual noise is generally higher compared to laboratory measurements without using fibers.

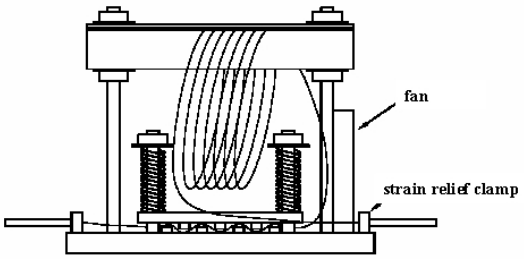

Figure 4.9: *Design of a quartz fiber mode mixer.*

4.2.4 Spectrograph

Two diffraction grating spectrographs of the Czerny-Turner type [*Czerny and Turner* 1930] are used for the field measurements. The quartz fiber is mounted on the entrance slit which is adjusted to the fiber's diameter of 200 µm. The entering light is parallelized by the spectrograph's collimating mirror, directed onto the diffraction grating, and the dispersed light is then focused on the detector.

To avoid a loss of adjustment due to changes in ambient temperature, each spectrograph is thermally isolated and the temperature is controlled by a thermostat. Since the thermal stabilization is technically easier to realize by heating, the spectrograph's temperature is set somewhat above the highest ambient temperature expected for a measurement campaign.

Acton 500

An Acton Spectra Pro 500 spectrograph was operated during all field campaigns. The focal length is 500 mm and the aperture ratio is f/6.9 . The installed turret allows to mount three gratings, two of which were used at the field measurements. These both are gratings with 600 grooves per millimeter, one is blazed for 300 nm and the other for 750 nm. At a wavelength of 750 nm the dispersion is 3.04 nm/mm or 0.076 nm/pixel. An overview of the relevant data is given in Table 4.2.

SPEX 750

During the field campaign in Brazil a Yobin Yvon SPEX 750 spectrograph was operated in addition to the Acton 500. The focal length is 750 mm and the aperture ratio is f/6.0 . It is only possible to mount one grating. Within this work a grating with 1 200 grooves per millimeter and blazed for 630 nm is used. The dispersion at a wavelength of 750 nm is 1.04 nm/mm or 0.026 nm/pixel. An overview of the relevant data is given in Table 4.2.

Table 4.2: *Characteristics of the spectrographs. The dispersion is valid for a wavelength of 750 nm. The resolution corresponds to the FWHM of a sharp atomic emission line, typically 6 detector pixels.*

	F-length (mm)	F-ratio f/	Grooves (mm^{-1})	Blaze (nm)	Dispersion (nm/pixel)	Resolution (nm)
Acton 500	500	6.9	600	300 , 750	0.076	0.45
SPEX 750	750	6.0	1 200	630	0.026	0.15

4.2.5 Detector Unit

The major component of the detector unit is the photo diode array (PDA) consisting of 1024 NMOS photo diodes, each 25 µm wide and 2.5 mm high. Different types of PDAs, but identical electronics and detector housings are used for both spectrographs. The Acton spectrograph operates with a Hamamatsu type S3904-1024 PDA, whereas the SPEX uses a Hamamatsu type S8381-1024 PDA, which is an infrared enhanced version of the former one (Figure 4.10). The PDA is mounted inside a camera housing which can be evacuated and refilled with ≈ 1.2 bar Argon gas, in order to prevent water from entering and condensing on the photo diodes. A peltier element is used for cooling the PDA. A detailed discussion of the usability of photo diode arrays for DOAS applications is found in *Stutz* [1991] and *Stutz and Platt* [1992].

Each single photo diode is a np-semiconductor junction with a capacity of 10 pF. The full well depth corresponds to 1.48×10^8 photo electrons. During operation an inverse voltage of 2.37 V is applied, inducing a depletion layer almost over the entire diode area. At the beginning of the measurement the power supply is disconnected from the photo diodes. Incoming photons subsequently excite electrons to the conducting layer of the semiconductor, which reduces the initially applied inverse voltage. The number of excited photons is proportional to the intensity of the incoming light. However, thermal excitation of the electrons is also possible, an effect called dark current. For its reduction, the PDA is cooled by a peltier element to temperatures of typically -20 °C. According to Boltzmann's equation, the dark current decreases exponentially with temperature. The dark current also depends on integration time and on the signal operation of the diode array.

After integration time is over, the PDA is read out by reconnecting the diodes to the power supply and measuring the current necessary to recharge the diodes. The signal is amplified electronically and digitized by a 16 bit analog-digital converter. To avoid negative values when light intensity is low, an additional offset signal is added before digitization. Thus, the dynamic range of 0 to 65 535 instead of -32 767 to 32 768 is used.

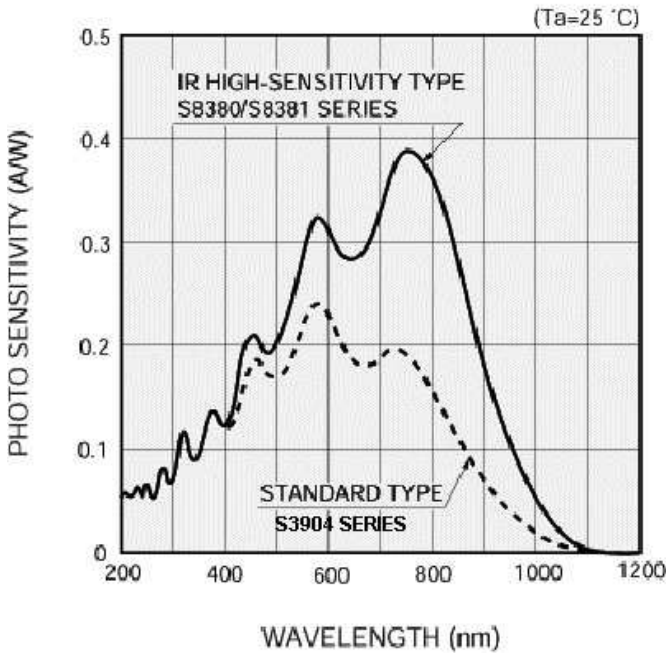

Figure 4.10: *Spectral sensitivities of both operated photo diode arrays [`http://sales.hamamatsu.com`].*

After digitalization the signal is transmitted to the DOAS controller. It is possible to sum up several detector readouts[5] before the spectrum is sent to the PC. Note that in this case each individual readout carries an offset signal, therefore the total offset signal is proportional to the number of readouts per spectrum.

The photo diodes are coated with a thin silicon dioxide protection layer. This leads to a broadband Fabry-Perot etalon structure, caused by the interference of multiply reflected light inside the protection layer. Water may also freeze on the cooled PDA, resulting in strong etalon structure and a drastically degradation in spectrum quality. The water vapor inside the camera housing is removed by evacuating.

A major problem arising with the use of an array detector is the variability of the sensitivity from pixel to pixel. This variation is caused by inhomogeneities of the SiO_2 protection layer, shadowing by microscopical dust particles covering the diodes, and different incident angles of the incoming light. The variability is up to 1 % [*Stutz* 1996]. Since it is intended to measure optical depths smaller than 10^{-3}, it is necessary to compensate for the different pixel sensitivities. One simple idea is to divide each atmospheric spectrum by a corresponding lamp reference spectrum recorded directly before or thereafter. Another method is to apply the *multi channel technique* (MCT), which is described in detail in Section 4.3. A further effect causing residual structures is the *memory-effect*: Strong structures from the previous spectrum are seen in the

[5]Informally called "scans", not to confuse with wavelength scanning done by a monochromator

present one. This effect is discussed in detail by *Stutz* [1996], however its origin is still unclear. The memory effect may be ignored when dummy readouts[6] are performing before a new readout is started.

4.2.6 Lamp Reference System

The purpose of the lamp reference system[7] is to record an I_0 reference spectrum, i. e. the spectrum of Xenon arc lamp. Therefore, the light of the Xenon lamp is guided to the quartz fiber by an appropriate optical system and only some meters path length. Then, absorption is negligible compared to the atmospheric path length. Two different systems are used.

The version of lamp reference system applied during the Dagebüll campaign is shown in Figure 4.11. A small part of the outgoing light is reflected sideways by a plane mirror. By the use of a parabolic and a further plane mirror the light is focused on the quartz fiber. A stepper motor allows to move the two plane mirrors into the light beam, whereas the parabolic mirror is fixed. Therefore lamp reference spectra can be recorded automated during the measurements – the advantage of this system. However, the great disadvantage of this system arises due to the inhomogeneity of the plasma which forms the arc between the Xenon lamp's electrodes. The temperature drops drastically from center outwards, causing a spatial variability of the thermal emission and the Xenon emission line characteristics. As the lamp reference system produces an image of the lamp's arc in the focal plane where the fiber is placed, the whole system has to be adjusted very accurately. Due to the fact that the angle between the light beam and the optical axis of the parabolic mirror is large, image quality suffers considerably. Finally, the question arises, if that part of the light used for recording reference spectra is representative for all the light used for recording atmospheric absorption spectra.

The former problems are avoided by the lamp reference system shown in Figure 4.12. It consists of three retro-reflectors mounted on a rotating disc. The system is set up directly in front of the LP-DOAS telescope. Almost all of the light is reflected back to the telescope and is focused on the quartz fiber. Note that the use of retro-reflectors instead of plain mirrors is important, because of the displacement of the reflected light from the outer ring into the inner part. Otherwise the light would be reflected back to the lamp and not the fiber. The advantage of this system is, that the image properties are identical to that of the atmospheric spectra, only on a shorter light path. However, as the system is not automated but has to be set up manually, reference spectra are commonly recorded only once per day. Variability of the Xenon lamp may be insufficiently accounted for.

[6] Multiple readouts with the absence of light.
[7] Also called "shortcut system"

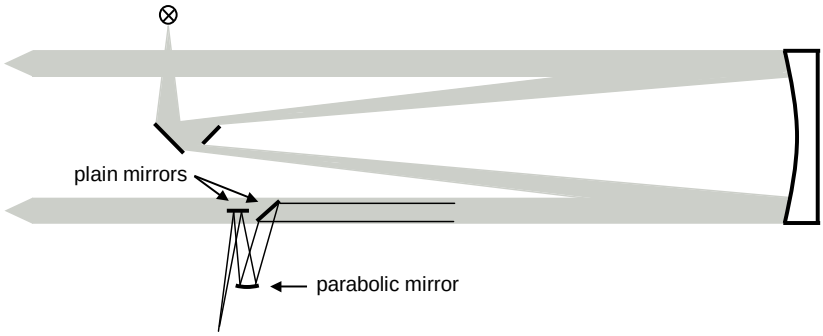

Figure 4.11: *Lamp reference system used for the Dagebüll campaign. A small part of the outgoing light is reflected sideways and focused on the quartz fiber.*

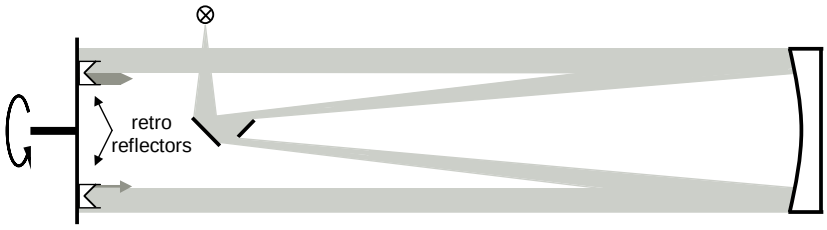

Figure 4.12: *Lamp reference system used for the campaigns in Lilia and Alcântara. A rotating disc containing three retro-reflectors (only two are shown for clarity) is set up directly in front of the LP-DOAS telescope.*

4.2.7 Meteorological Station

During all field campaigns a meteorological station (Hoffmann Messtechnik GmbH, Rauenberg, Germany) was operated. It is adjusted to monitor meteorological conditions on a five-minute-mean interval. The station is equipped with sensors for ventilated temperature, relative humidity, wind speed, wind direction, air pressure and global shortwave irradiance. Of special interest for this work are the sensors for temperature and relative humidity. Using this data it is possible to calculate the total concentration of water vapor for comparison with the water vapor concentration obtained from the DOAS measurement. It has to be considered that the meteorological station yields in-situ results, whereas the DOAS technique averages along the absorption path.

The temperature and relative humidity are measured by a psychrometer according to "Frankenberger". The instrument consists of two Platinum resistance thermometers, one of which is permanently bathed in pure water. Due to evaporative cooling the thermometers show a difference in temperature which can be correlated to the relative humidity by using Sprung's formula. The psychrometer is mounted 2 m above the ground, ventilated by ambient air and shielded from direct solar radiation. The accuracy is $\pm 0.2\,^{\circ}\mathrm{C}$ in temperature and $\pm 2\,\%$ in relative humidity.

4.3 Spectra Recording and Processing

The DOASIS software package, which has been developed at the Institute for Environmental Physics, Uni Heidelberg [*Kraus* 2003] is used to automatically control field measurements, and to process and prepare the spectra for the final analysis (Section 4.4). For individual demands on measurement and processing routines, the software is able to execute user-written programs in j-script code. The software is updated regularly and always one of the latest available versions is used for every field measurement campaign.

The field measurements are controlled semi-automatically, primarily by individually programmed measurement routines which meet the requirements for each field campaign. Measurements are also controlled manually for the tasks which turned out to be too time consuming, too difficult, or even fatal for an automated routine. Especially for the very long light paths established for all field campaigns, the alignment of the telescope onto the retro-reflectors (Section 4.2.1) in order to yield a maximal light throughput is problematic when performed automatically. Also the more subtitle automated glass fiber alignment, which works well for retro-reflector distances of about 10 km, has to be operated manually for the 15 km distance. Regular alignment is necessary on time scales of hours.

4.3.1 Multi Channel Technique

To counter a slight variable sensitivity of the individual photo diode pixels, the *multi channel technique* (MCT) is applied. The technique was introduced by *Knoll et al.* [1990], further improved by *Brauers et al.* [1995] and explicitly scrutinized with regard to Long Path DOAS applications by *Stutz* [1996]. The more detailed technique described by *Brauers et al.* [1995] is not applied within this work since test runs of spectral retrievals have shown that this technique is not suitable for highly structured and irregular spectra like water vapor absorption.

The basic idea of the used multi channel technique is to statistical average by constructing one spectrum from several individual spectra of slightly different wavelength to pixel mapping. As illustrated in the flowchart 4.13, this is obtained by subsequently recording 9 spectra with each being shifted in wavelength relative to the previous one by 0.4 nm for the Acton 500 and 0.15 nm for the SPEX 750 spectrograph. The spectral shift is performed automatically during the measurement routine. For the later analysis, the 9 spectra are shifted back to match in wavelength and are summed up. The required shifts are obtained from the spectrum of a wavelength calibration lamp (Neon or Mercury low pressure lamp). In a nutshell, one spectrum for the final analysis is obtained from each MCT-block consisting of nine cycles (Figure 4.13).

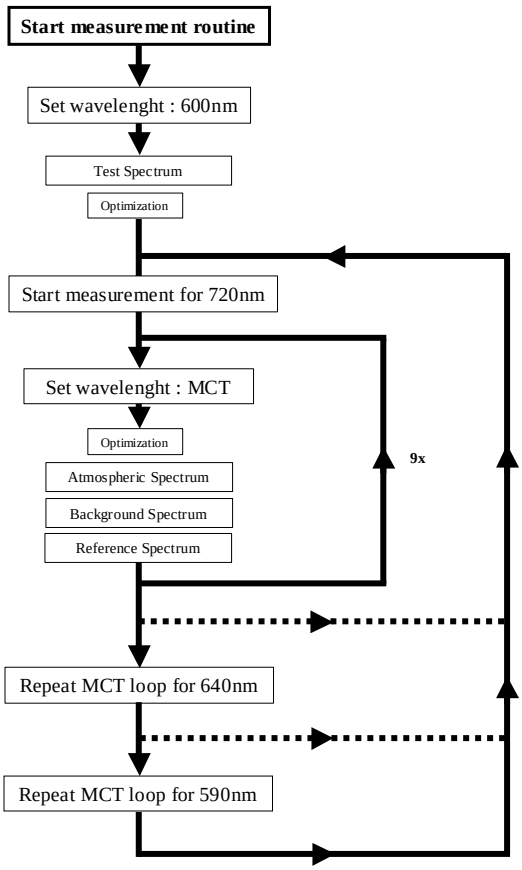

Figure 4.13: *The flowchart shows the basic steps of a automated measurement routine. The program loop of the multi channel technique (MCT) applies in the same manner to the other wavelength intervals. According to the required measurements, the wavelength intervals are set before the routine is started. Mercury or Neon lamp reference spectra are recorded to determine the wavelength to pixel mapping.*

4.3.2 Measurement Routine

Figure 4.13 shows a program flowchart[8] containing the basic steps of a field measurement routine. The program initializes by recording a test spectrum at appropriate wavelength, checking the required exposure time and optimizing the quartz fiber alignment if desired. Thereafter, an optional number of MCT-blocks are run alternately for different wavelengths (only one MCT-block is shown in detail). The user is able to set and arrange the wavelength blocks before starting the program. However, the measurements can also be controlled by the program itself, depending on parameters like the solar zenith angle in order to check for daylight or nighttime conditions, for example.

[8]This flowchart is an example taken from the campaign in Brazil, but the basic idea is the same for all field campaigns. Particular differences are pointed out elsewhere if being of interest

One individual MCT-block consists of the following sequence: optimization, atmospheric-, background-, and reference-spectrum. The optimization procedure determines the required exposure time for an optimal detector readout signal of about 60 – 80% of the PDA's saturation level. On this basis, the number of readouts required not to exceed a given limit of total accumulation time is determined. The first recorded spectrum in the sequence is the *atmospheric spectrum*, i. e. the spectrum containing the atmospheric absorption signal (telescope → retro-reflectors → telescope). Depending on the atmospheric visibility the number of detector readouts per spectrum vary drastically between 1 and about 50. For the *background spectrum* the Xenon lamp's light is completely blocked by a baffle, but everything else is left unchanged. These background spectra recorded at the absence of the light source contain any kind of stray light reaching the spectrograph. To save measurement time the number of readouts and the exposure time are reduced to appropriate values depending on the respective measurement site and daylight conditions. Finally, a *reference spectrum*, i. e. a emission line spectrum of a Neon or Mercury lamp, is recorded to derive the wavelength calibration. This calibration is required after each positioning of the spectrograph's grating, but also wavelength shifts due to a temperature change can be corrected. One complete MCT-cycle takes up to one hour. Setting the upper limit to 10 readouts per single atmospheric spectrum results in a better temporal resolution if the atmospheric visibility is good.

Note that for each field campaign the measurement routine is individually modified. The wavelength intervals and optimization procedures are adjusted to the scientific requirements and to the meteorological and atmospheric conditions.

4.3.3 Xenon Lamp Reference Spectra

It is not possible to obtain complete knowledge of $I_0(\lambda)$, since this would require to remove the atmosphere. Using one of the lamp reference systems introduced in Section 4.2.6, it is at least possible to get relative information of the light source spectrum (Xenon lamp reference spectrum). This is sufficient because the DOAS technique does not require absolute intensities. When using the fully automated version of the lamp reference system (Figure 4.11), one Xenon lamp reference spectrum is recorded in each measurement sequence, between the background spectrum and the calibration lamp spectrum (Neon or Mercury lamp). The more sophisticated lamp reference system (Figure 4.12) has to be set up manually in front of the telescope. Therefore, Xenon lamp reference spectra are only recorded occasionally, usually once per day. The applied measurement routine is similar to the atmospheric measurement procedure, with only the difference being a shorter light path length. Thus, the program sequence for the Xenon lamp reference spectra, which is run for exactly one complete cycle, includes all necessary wavelengths and multi channel runs.

4.3.4 Spectra Processing

First, each recorded individual spectrum is corrected for the offset signal. From all the atmospheric spectra the corresponding background spectra are subtracted. It is important to scale the atmospheric and background spectra to an equal total exposure time, that means, considering also a possible difference in the number of readouts. A subtraction of the dark current is implicitly included in the background correction. Inaccuracies of positioning the spectrograph's grating and thermal distortion result in small shifts in wavelength. The Neon or Mercury lamp emission spectra are used to bring all the processed spectra to the same wavelength to pixel mapping. A single separately measured and well exposed spectrum is chosen as global reference. In case of using the multi channel technique, corresponding spectra are summed up. The same processing is applied to the Xenon lamp reference spectra except for the background correction. No additional correction for the dark current is needed due to the high intensity of the Xenon lamp and therefore short integration times.

4.4 Spectral Analysis

The analysis of the spectra is performed using the WinDoas software [*van Roozendael and Fayt* 2001], which was developed at IASB/BIRA (Belgian Institute for Space Aeronomy) and has been particularly designed for the analysis of UV-VIS spectra based on the DOAS method. The software is used for convolution and for the fitting procedure to determine trace gas concentrations as discussed in the following sections.

4.4.1 Convolution

The spectrum projected onto the detector is a convolution of the high resolution atmospheric absorption spectrum with the instrumental line shape function. In order to use absorption cross sections or modeled optical depths as references for the spectral fit to the measurements, these references need to be convolved with the instrumental line shape function. This function is defined by the properties of the spectrograph-detector-system and is obtained from an individual emission line of a well exposed Neon or Mercury lamp spectrum. For each recorded wavelength interval a separate emission line is used, located as close as possible to the wavelength region of the later analysis. To use each line as a convolution kernel, the line is separated from the lamp spectrum, the line peak is shifted to 0 nm and the area enclosed by the line is normalized.

The mathematical formulation of the convolution (Equation 4.13), may also be written in relative intensities $(I/I_0)(\lambda)$. Taking the negative logarithm yields the optical depth (Equation 4.7) and the convolution becomes

$$\tau^*(\lambda) = -\ln\left((I/I_0)(\lambda) \circ H(\lambda)\right) = -\ln \int (I/I_0)(\lambda - \lambda')H(\lambda')d\lambda' \tag{4.15}$$

It would be convenient to permute the logarithm and the convolution here, but this operation is not allowed since the logarithm is a non-liner function. However, for small optical depths $\tau \ll 1$, that is $I \approx I_0$, the logarithm[9] may be approximated by a linear function which allows the permutation of the logarithm and the convolution. Then, Equation 4.15 can be written as

$$\tau^*(\lambda) = \int \tau(\lambda - \lambda')H(\lambda')d\lambda' = C \cdot \int \sigma(\lambda - \lambda')H(\lambda')d\lambda' \tag{4.16}$$

In this approximation, the convolution can be applied directly to the absorption cross section. The permutation is also allowed for a sum of absorption cross sections if different absorbers are to be considered, therefore each singe absorption cross section may be convolved separately. Note that in the optically thin case ($\tau \ll 1$) the absorption is linear as illustrated by the curve of growth from Figure 4.2.

Things are not as simple if the optical depth becomes large, that is $\tau \approx 1$ or above, which unfortunately is true for water vapor absorption. The optical depths[10] of the strongest absorption lines of the water 4ν band is as large as some 100. Instead of convolving the water absorption cross section, a high resolution spectrum for the transmittance I/I_0 is calculated from Lambert-Beer's law (Equation 4.6) using the absorption cross section, the light path length and a plausible value for water vapor concentration. According to Equation 4.15, this transmittance spectrum is first convolved with the instrumental line shape function and thereafter taken to the negative logarithm. Thus, a modeled spectrum in terms of optical depth is obtained, matching the resolution of the spectrograph system. A whole series of such spectra is generated for a number of different water vapor concentrations assuming to cover the entire range present in the probed air masses.

Performing the convolution using the WinDoas software, the calibration file which provides the correct wavelength to pixel mapping is required. Therefore the result of a convolution includes the discretization specified by equation 4.14.

4.4.2 Fitting Procedure

The procedure for the evaluation of the atmospheric absorption spectra is based on Equation 4.9. Assuming constant ambient conditions along the light path and the discretized wavelength scale, its logarithm can be written as

$$\ln I(i) = \ln I_0(i) - \sum_{j=1}^{m} \tau_j(i) + R(i) + N(i) + A(i) \tag{4.17}$$

Superimposed absorption of several trace gases are represented by the sum and for each single species the absorption is specified by the respective optical depth $\tau_j(i)$.

[9] The series expansion of the logarithm is: $\ln(1+x) = x - x^2/2 + x^3/3 - \ldots$

[10] Derived from calculated high resolution spectra for typical field conditions and path lengths

The broadband components of Rayleigh and Mie scattering are represented by a low-order polynomial $R(i)$, the noise of the detector and the photon noise are described by $N(i)$ and any variations in the spectral sensitivity of the detector or spectrograph are summarized by $A(i)$.

In practice, the number of absorbers in a given wavelength interval can be limited to those trace gases with sufficiently strong absorption above the detection limit of the instrument. As the strength of absorption varies with wavelength, the number of trace gases to be included varies with the observed wavelength interval and the trace gas composition of the probed air mass. Typically, the absorption of 2 – 10 trace gases can be identified in one single atmospheric spectrum, therefore their concentrations can be measured simultaneously [*Platt* 1994]. For the spectral retrieval the superimposed absorption structures have to be separated numerically.

Optically Thin Case

In the UV-VIS-NIR spectral region trace gas absorption is optically thin for almost all species due to their low abundance in the atmosphere. Particularly these species are usually of interest in atmospheric chemistry and physics, therefore the WinDoas software has been designed for the purpose of evaluating optically thin spectra.

As stated previously and given by Equation 4.16, the convolution with the instrumental line shape function may be performed directly on the cross sections $\sigma_j(i)$ of the absorbers involved and Equation 4.17 becomes

$$\ln I(i) = \ln I_0(i) - \sum_{j=1}^{m} C_j \cdot \sigma_j(i) + R(i) + N(i) + A(i) \tag{4.18}$$

The evaluation procedure is based on an appropriate model function $F(i)$ for the approximation of $J(i)$

$$F(i) = \ln I_0(i, d_{0,0}, d_{1,0}, ...) - \sum_{j=1}^{m} C_j \cdot \sigma_j(i, d_{0,j}, d_{1,j}, ...) \; + \; P_r(i) \tag{4.19}$$

The source intensity $I_0(i)$ and the cross sections $\sigma_j(i)$ are input data to the fitting procedure. Broadband components of absorption as well as Rayleigh and Mie scattering are approximated by a polynomial $P_r(i)$ of low order r

$$P_r(i) = \sum_{h=0}^{r} a_h (i - i_c)^h \tag{4.20}$$

whereas i_c represents the center pixel of the spectral range used for the evaluation. The scaling factors C_j and the additional parameters $d_{x,j}$ are the output data of the fitting procedure. The number C_j corresponds to the number column density of the respective trace gas which directly provides the average number density $\bar{n}_j$ along the

line of sight since the total absorption path length[11] L is well defined for long path DOAS applications.

$$\bar{n}_j = C_i/L \tag{4.21}$$

To account for possible differences in the wavelength to pixel mapping of $I_0(j)$ and $\sigma_j(i)$ with respect to the measured intensity $I(j)$, both $I_0(j)$ and $\sigma_j(i)$ are allowed to be shifted and stretched. The misalignment of the spectra and cross sections is a result of different measurement conditions, e. g. ambient temperature and pressure, an effect that cannot completely be avoided even if the spectrograph is thermally stabilized. The magnitude of shift and stretch is given by the spectral alignment parameters $d_{x,j}$. Here, the parameter $d_{0,j}$ describes a shift and $d_{1,j}$ a linear stretch of the wavelength to pixel mapping, a stretch of higher order is usually not applied. The shift and stretch can be applied separately for each absorbing species, but in order to reduce the number of degrees of freedom it is advantageous to use one set of parameters $d_{x,j}$ for two or more molecular cross sections if their wavelength calibration is identical.

The spectral analysis consists of a *linear least squares fit* [*Bevington* 1969; *Albritton et al.* 1976] to derive the parameters C_j and a_h and a *non-linear Levenberg-Marquardt fit* [*Levenberg* 1944; *Marquardt* 1963] to determine the values $d_{x,j}$ in a sense that

$$\chi^2 = \sum_{i=0}^{n} \big(\ln I(i) - F(i) \big)^2 \tag{4.22}$$

is minimized, where n is the detector pixel number. The number of pixels contained in the spectral fitting range has to be clearly larger than the number of parameters of the fitting procedure (sum of the number of cross sections and the order of the polynomial). Also required for a valid fitting procedure is the linear independence of the cross sections σ_j. The procedure starts with a linear least squares fit and initial values for $d_{x,j}$. The retrieved values for C_j and a_h are then input data for one iterative step of the Levenberg-Marquardt fit, by which new values for $d_{x,j}$ are obtained. In turn these values are used for a new call of the linear fit, the result of which is again used for a new call of the non-linear fit and so on. If one of several termination conditions for the Levenberg-Marquardt fit is fulfilled the analysis procedure is stopped. Normally this occurs if the fit has converged, i. e. the relative changes of χ^2 in subsequent steps falls below a given limit, but the fit also stops if a maximum number of iteration steps determined by the user is exceeded or if the non-linear method becomes unstable [*Stutz and Platt* 1996].

Statistical Error Estimation: The precision of the results is determined by the statistical fluctuations of the measured intensities due to noise (see Section 4.4.3). Provided that the measurement error for individual pixels are independent and that the error

[11] Note that this length is twice the distance from the telescope to the retro-reflectors.

of each pixel has a mean value of zero and a finite variance, the linear least squares procedure yields errors of the parameters C_j and a_h and the Levenberg-Marquardt fitting routine provides errors of the parameters $d_{x,j}$. The errors are given in terms of one standard deviation of the respective parameter, i. e. its true value is within the given error range with 68.3% probability. However, the influence of the errors of the non-linear parameters on the parameters of the linear fit are not accounted for.

Only if the residual spectrum $Res(i) = \ln I(i) - F(i)$ consists of pure noise the errors can be appropriately described by the provided numbers of the retrieval. Unfortunately, this does not completely hold for actual spectra, as normally the residuals reveal groups of interdependent neighboring pixels. *Stutz and Platt* [1996] showed that the influence of interdependent residual structures on the fitting results can be estimated by a numerical procedure. The influences on the fitting parameters are found to be negligible but the fitting errors have to be corrected by a factor which depends on the spectral resolution, the width of the absorption structures and the applied operations for shift and stretch. Usually a factor 3 is applied to the statistical errors of the fit.

Optically Thick Case

As demonstrated in Section 4.4.1, one may not fit convolved absorption cross sections to the measured spectra in case of optically thick absorption. Instead, the modeled optical depth spectra described therein have to be used. However, the WinDoas software can be used for the evaluation in a slightly modified way. Instead of providing the absorption cross section spectra as input data, optical depth spectra are used. By comparing Equations 4.17 and 4.18 it can be easily seen that the scaling factors C_j resulting from the fitting procedure have to equal $C_j = 1$ if the trace gas concentration used to calculate the optical depth is correct. If the scaling factor is higher or lower than 1, the fit is repeated with a new input spectrum of a respective higher or lower concentration until $C_j = 1$. Note that due to the non-linear behavior it is not allowed to scale the water concentration, which is used as input data for calculating the fitted optical depth spectrum, by the number of the retrieved scaling factor. However, it is allowed to linearly interpolate the water concentration from the change of the scaling factor and change of input water concentration of two fits, if both yield values C_j close to 1, i. e. about $C_j = 1 \pm 0.02$.

Admittedly, the procedure is a kind of trial and error method which cannot be done automatically by the WinDoas program itself since it requires a convolution for every repeating step. But taking into account the manageable number of spectra to be handled for this work, a manually conducted evaluation is feasible.

Statistical Error Estimation: Due to the fact that a well structured optically thick absorption spectrum is conspicuous even in the raw measurement, the absorption signal is well above the noise level and the evaluation procedure is capable of fitting the input

optical depth spectrum to the measurement very well in just a few iterations. Therefore, the relative statistical error is expected to small in general. This error resulting from the applied evaluation procedure is due to an error of the fit itself and an error in the assumed gas concentration which is the input data to the fit. The first is obtained from the WinDoas fitting result and is a good criterion for checking the quality of the fit. This value is typically about 10^{-3} for the evaluation of the water absorption spectra within this thesis. Since it is not feasible to generate and use a series of calculated optical depth spectra of such a fine gradation, the total statistical error in the retrieved concentrations is dominated by the gradation. In practice it is possible to generate a series such a way to yield scaling factors in the interval between 0.995 and 1.005. Then the statistical error is estimated to be plus-minus half the step size of the gradation.

4.4.3 Error Sources

Detector Noise

The instrument noise is an important parameter for the fitting procedure because the statistical errors of the retrieved parameters are determined by the noise of the measurement. Different types of effects contribute to the total noise.

The *photo electron noise* σ_{ph} is based on the statistical distribution of the number of electrons generated by the photons illuminating the detector pixels. The number of photo electrons N_{ph} is distributed according to Poisson statistics. Therefore the noise is given by

$$\sigma_{ph} = \sqrt{N_{ph}} \tag{4.23}$$

The *dark current noise* σ_{dc} is due to the statistical variance of the dark current across a photo diode's junction, which depends strongly on the temperature of the detector. The distribution of dark current electrons obeys the Poisson statistics. Thus, for an integration time t and a mean number $\bar{N}_{dc}$ of dark current electrons per unit time the noise is obtained by

$$\sigma_d = \sqrt{\bar{N}_{dc} \cdot t} \tag{4.24}$$

Additionally a constant distributions σ_{el} to the total noise exists, originating from the readout, amplification and digitalization electronics. According to the Gaussian error propagation, the total noise is given by

$$\sigma_{tot} = \sqrt{\sigma_{ph}^2 + \sigma_{dc}^2 + \sigma_{el}^2} \tag{4.25}$$

In general, the detector is operated to give a maximum signal number of about 60 – 80% the saturation level which corresponds to approximately 200 counts per readout due to photo electron noise. For a detector temperature of -20 °C the dark current is below 2 counts per second integration time and the electronic noise is a few counts per

readout. Thus, if integrations times are sufficiently short the total noise is dominated by the photo electron noise. By adding up a number N of detector readouts, the signal to noise ratio can be increased by a factor of $\sqrt{N}$.

Systematic Errors

If only statistical errors occur, the residual spectra $Res(i) = \ln I(i) - F(i)$ are to be of pure noise, i. e. no spectral structures are present indicating the independence of the individual diode pixels. However, a common problem encountered in spectral evaluation is the occurrence of structured residuals which cause systematic errors that cannot be described by statistical methods. Permanent structures may indicate unknown absorbers or inadequate absorption cross sections and randomly occurring structures may be caused by the instrument itself.

For the instrumental structures, groups of adjacent pixel intensities appear to change simultaneously in a random way. Therefore the errors of these pixel intensities are assumed to be dependent of each other. A way of simulating this effect is smoothing a pure noise spectrum, e. g. by a running mean. Smoothed noise spectra look similar to residuals normally found in the analysis of atmospheric spectra. This finding confirms that the single pixel errors are not independent of each other, which is accounted for by a correction factor applied to the derived statistical errors as described in Section 4.4.2 [*Stutz and Platt* 1996].

Permanent structures often appear in the residual spectra of the retrieval. Possibly further absorbers, commonly termed X-absorbers which might not be known, are present in the observed air mass. Therefore their contribution to absorption is still present in the residual spectra. However, as these X-absorbers influence the residual structure they don't necessarily influence the retrieved trace gas concentration of the known absorbers. A further source of permanent residual structures are errors in the fitted absorption cross-sections. These may be errors existing in literature data, e. g. incorrect strength or missing lines, both of which notably arise for weak absorption lines. Errors may also emerge later when correct literature data is processed. For example, if temperature and pressure are not matching the experimental conditions or the field instrument shows a variable line shape function across the covered spectral region. Permanent residual structures can be partially corrected by fitting a mean residual of a series of spectra to the measured atmospheric spectrum as an additional reference. This is justified, if residual structures due to unknown X-absorbers show strong diurnal or seasonal variations and therefore can be separated from other systematic errors [*Hönninger* 2002], otherwise this method has to be handled with care. The method is not applied within this work since the nature of the residual structure is ambiguous, either due to a deficit in water monomer absorption or owing to the water dimer acting as a missing X-absorber.

Detection Limit

For each trace gas considered in the spectral retrieval, a detection limit can be determined from the residual spectrum. In particular, if trace gas absorption is below the detection limit for a certain species, an upper limit of its concentration can be inferred. This limit is calculated from the differential optical depth of the residual spectrum, the differential absorption cross section of the trace gas and the absorption path length. There is no general concept for the determination of the residual's differential optical depth, because it strongly depends on the shape and width of the spectral structures. Actually it is inadequate to draw on the value given by the root mean square ($\sqrt{\chi^2}$ given by Equation 4.22) of a residual spectrum, if the spectral structures evidently depart from statistical noise. A better choice is to rely on peak to peak values within typical structures occurring in the spectral region of interest. In order to eliminate statistical outliers of single pixels, a running mean of the residual should be used instead.

In the case of the residual spectra consisting predominantly of noise, the statistical error of the fit, scaled by the correction factor given by *Stutz and Platt* [1996], can be used as detection limit. Another approach was introduced by *Hausmann et al.* [1999]: a Monte-Carlo algorithm is used to compute the detection limit with respect to the fitting algorithm and the residuals. This more sophisticated algorithm requires a lot of computation time and is not applied in this work.

4.5 Absorption Cross Sections

The spectral retrieval requires the absorption cross sections of the considered trace gases as input data. This data, being adopted from a variety of sources, is generally based on measurements but also on theoretical work to some extent. In the former case this data is usually provided directly in the form of absorption cross sections of particular resolution which only have need to be convolved with the instrumental line shape function to be ready for use[12]. In case of water vapor, the data is provided by spectral line databases, the most common of which is the HITRAN database. Such a database lists single molecular transitions with a set of their fundamental spectroscopic parameters, i. e. line frequency, line strength, line broadening parameters, et cetera. In the following, different water vapor databases is compared and the procedure to calculate absorption cross sections from this data is described. Finally, a brief overview of existing water vapor databases is summarized in Table 4.3.

[12] Of course, the literature data should have been recorded at better resolution than is achieved by the operated instrument. But this is not necessarily required for broad band absorbers, for example O_4.

4.5.1 Spectral Water Line Databases

Partridge-Schwenke (PS)

Based upon first principle quantum mechanics *Partridge and Schwenke* [1997] carried out large scale *ab initio* electronic structure calculations of the potential energy surface and dipole moment surface for H_2O . The result is a list containing the frequencies of about 370 million water transitions of the four most common isotopes. The calculations cover the frequency range from 28 280 cm^{-1} (353.6 nm) far upwards into the radio wave bands. *Schwenke and Partridge* [2000] performed a refinement of the calculations and were able to additionally predict the line intensities. Most of the lines listed in the database are very weak in intensity. If the line strength cut off is set to 10^{-30} cm/molec, which is three orders of magnitudes lower than the weakest lines listed in HITRAN, there are about 500 000 lines left in the entire frequency range of the line list.

The authors also provide a program to process their line database allowing for specification by the user, e. g. temperature, line strength cut off and choice of isotopes. The output file is written in HITRAN-format.

Bxl-Reims

The Bxl-Reims water vapor database is based on laboratory measurements carried out by a Brussels-Reims collaboration using high-resolution (0.06 cm^{-1}) Fourier Transform Spectroscopy and a White-type multiple reflection cell. The database includes values for frequencies, intensities, self-broadened half widths, N_2-broadened half widths and N_2-induced pressure shifts [*Coheur et al.* 2002]. An update to air-broadened half widths and air-induced pressure shifts is also available [*Fally et al.* 2003]. The measurements were performed at a temperature of 290 $\pm$ 2 K, but a correction to the HITRAN standard temperature of 296 K is applied, except for unassigned lines.

The line list contains a total number of 9 353 lines within the frequency range of 13 180 cm^{-1} to 25 230 cm^{-1} and line intensities of at least 5×10^{-28} cm/molec. With regard to the earlier measurements compiled in HITRAN, which only list 4 610 lines within the same interval, the Bxl-Reims data set represents a significant improvement. Therefore, it has been implemented in the HITRAN04 database recently by replacing the previously listed entries therein [*Rothman et al.* 2005].

The Bxl-Reims line list given in HITRAN-format as well as. The list and a documentation is available via the Internet (`http://www.ulb.ac.be/cpm/`).

HITRAN

HITRAN is an acronym for "High-resolution transmission molecular absorption database", which is a compilation of spectroscopic parameters used by a majority of computer codes to predict and simulate the radiative transfer in the atmosphere. It is

a long-running project which started in the 1960's in response to the need for detailed knowledge of the infrared properties of the atmosphere and resulted in a database that involved seven molecules (H_2O, CO_2, O_3, N_2O, CO, CH_4, O_2) [*McClatchey et al.* 1973]. Over the course of time the database has been expanded beyond the infrared region and to further molecules now totaling 39. Updates for single molecules are frequently performed and a new compilation of the whole database is released every few years. In recent years the versions HITRAN96 [*Rothman et al.* 1998], HITRAN2k [*Rothman et al.* 2003] and HITRAN04 [*Rothman et al.* 2005] were released. The data as well as the documentation can be requested via the Internet (`http://cfa-www.harvard.edu/hitran//`).

Within this work the versions HITRAN2k and HITRAN04 are used for the spectra analysis of water vapor. The overall number of listed water lines including six of its isotopologues is 51 930 and 63 196 respectively. An update to HITRAN2k for the water molecule was released in 2001, but no chances were applied in the frequency interval of interest for this work which is between 13 000 cm^{-1} and 18 000 cm^{-1}. A fundamental modification was introduced in the data of HITRAN04 [*Rothman et al.* 2005] by the implementation of the Bxl-Reims database [*Coheur et al.* 2002; *Fally et al.* 2003]. Thereby the number of water transitions in the above frequency range has been increased from 3 823 to 7 691 and the minimum line intensity has been lowered from 2.6×10^{-27} cm/molec to 9.3×10^{-29} cm/molec.

ESA-WV

The data contained in the ESA-WV line list [*Schermaul et al.* 2001] is the main result of an ESA funded study which was carried out by a consortium involving three UK research groups (The Molecular Spectroscopy Facility at the Rutherford Appleton Laboratory, the Spectroscopy Group at Imperial College and the Molecular Theory Group at University College London). The line list is constructed combining laboratory measurements and theoretical calculations. For the experimental data high-resolution (0.03 cm^{-1}) Fourier Transform Spectroscopy was carried out using White-type multiple reflection cells. This contributes some 4 000 stronger lines. The theoretical calculation is based on the potential energy surface of *Partridge and Schwenke* [1997] yielding about 32 000 weaker lines with a lower limit of line strength set to 1×10^{-28} cm/molec at 296 K.

Strictly speaking, two line lists both in HITRAN-format are compiled, the ESA-WVR list for the red and near-infrared (8 592 – 15 000 cm^{-1}) and the ESA-WVB list for the visible (15 000 – 20 000 cm^{-1}) part of the spectrum. The ESA-WVR line list was generated by merging the corresponding experimental and theoretical data whereas the ESA-WVB line list results from theory only. The authors note that the latter lacks experimental validation, hence it should be treated with caution.

The databases ESA-WVR and ESA-WVB, together with a documentation can be downloaded from the Web (`http://badc.nerc.ac.uk/data/esa-wv/`).

Ptashnik

The work by *Ptashnik and Shine* [2003] presents line-by-line calculations in the spectral region 2 000 – 20 000 cm^{-1} to assess the impact of a variety of water vapor spectral databases on the accuracy of solar flux calculation in the atmosphere. In particular, the influence of weak lines, which are listed in the Partridge-Schwenke database [*Schwenke and Partridge* 2000] but not in HITRAN , on the radiative flux was investigated. For this purpose two line lists are generated by merging HITRAN2k and Partridge-Schwenke (PS):

a) HITRAN2k + PSWL

A database is created by cancelling each line in the PS list which has an equivalent in HITRAN2k. This modified list, termed Partridge-Schwenke weak lines (PSWL), is merged with the HITRAN2k database. Some 2 000 lines of HITRAN2k (total of 52 000) remain unidentified and are not removed from the PS database, therefore the 2k+PSWL list definitely includes some lines twice.

b) PS ← HITRAN2k

In this case all identified HITRAN2k equivalents are substituted to the PS list. No line are included twice because in this case one line list is not added into another, but lines are only replaced in PS by their HITRAN2k equivalent. As a matter of course, the lines in PS which have an equivalent in HITRAN2k but are not recognized as those (the 2 000 lines), are still included in PS with their PS-parameters.

CRDS-Grenoble

Initiated by the potential detection of atmospheric water dimer absorption at 749.5 nm [*Pfeilsticker et al.* 2003], a small interval of the water vapor spectrum was measured at the Laboratoire de Spectrométrie Physique, Grenoble by using high resolution Cavity Ring Down Spectroscopy [*Kassi et al.* 2005]. A absorption sensitivity of 3×10^{-10} cm^{-1} was achieved. The covered spectral interval of 13 312.4 – 13 377.8 cm^{-1} is rather small, 286 water lines as weak as 5×10^{-29} cm/molec were recorded. The original CRDS-Grenoble line list provides only the observed frequencies, intensities and rovibrational assignments. To construct a HITRAN-like database the missing values, especially the line broadening parameters, are fixed to the values found for lines in the HITRAN database that also lack data from the measurement for those values. In fact, for our instrument's resolution the values for the line broadening can be set to any value much weaker than the resolution without altering the convolved spectrum.

Table 4.3: *Overview of databases used for the analysis of water absorption spectra. Given are the number of lines and the smallest line strength S listed in the frequency range 13 000 – 18 000 cm^{-1}. A description of each database is found in the text and the references.*

Database	No. of lines	S_{min} (cm/molec)	Reference
HITRAN2k	3 823	2.6×10^{-27}	*Rothman et al.* [2003]
HITRAN04	7 691	9.3×10^{-29}	*Rothman et al.* [2005]
Bxl-Reims	6 913	4.5×10^{-28}	*Coheur et al.* [2002]
ESA-WV	13 193	1.0×10^{-28}	*Schermaul et al.* [2001]
PS	85 906	1.0×10^{-30}	*Schwenke and Partridge* [2000]
2k+PSWL[a]	76 180	1.0×10^{-30}	*Ptashnik and Shine* [2003]
2k-to-PS[a]	75 805	1.0×10^{-30}	*Ptashnik and Shine* [2003]
CRDS-Grenoble	286	4.7×10^{-29}	*Kassi et al.* [2005]

[a] frequency interval 13 000 – 17 162 cm^{-1}

When the spectral analysis is performed in a wider frequency range than covered by the CRDS-Grenoble measurements, line lists are generated by replacing the corresponding spectral interval of a comprehensive database (e. g. HITRAN, PS) by the CRDS-Grenoble line data.

4.5.2 Water Dimer

As already stated in Section 3.2.3, the fundamental and overtone vibrational spectrum of water dimer has been calculated for the first time by *Tso et al.* [1998]. The most accurate fundamental and overtone absorption cross sections of the water dimer to date result from the theoretical studies by *Low and Kjaergaard* [1999] for the OH-stretching modes and by *Schofield and Kjaergaard* [2003] for both the OH-stretching and the HOH-bending modes. Table 4.4 gives the frequency range and number of bands contained in both lists. Neither further calculations nor any measurements of the water dimer overtone cross section are known at present.

The lists of *Low and Kjaergaard* [1999] and *Schofield and Kjaergaard* [2003] give only the frequencies and band intensities, the band width is still an open issue and is believed to range between 15 cm^{-1} and 200 cm^{-1} FWHM [*Vaida et al.* 2001]. To construct a HITRAN-like database the air broadening parameter was set to the desired water dimer HWHM, the other missing parameters were set to zero.

Table 4.4: *Overview of both water dimer line lists used within this thesis. Low and Kjaergaard [1999] consider only OH-stretching bands, whereas Schofield and Kjaergaard [2003] also include HOH-bending modes.*

Line list	No. of bands	Frequency coverage
Low and Kjaergaard [1999]	119	3593 – 23273 cm^{-1}
Schofield and Kjaergaard [2003]	390	1596 – 30370 cm^{-1}

4.5.3 Calculation of Absorption Cross Sections

In order to generate absorption cross sections or optical depth spectra from the data provided by the various line lists, it is necessary to process this data by an adequate algorithm. Considering the ambient temperature and pressure, each transition is converted into a Voigt line shape profile from the parameters listed in the database (line strength, line broadening, lower state energy, etc.). In the end, all profiles are added up to give an absorption cross section spectrum or an optical depth spectrum, if a column density is also specified. In the following, some computer codes for performing this task will be introduced.

HitranVoigt

As indicated by its name, the C++ computer program *HitranVoigt* (developed at the Institute of Environmental Physics, University of Heidelberg by *Frankenberg* [2006]) is capable of extracting the line data from the HITRAN-database, calculating for each line a Voigt line shape profile and merging all lines to an absorption cross section spectrum. For the numerical calculation of the Voigt line shape profile the implementation by *Kuntz* [1997] is used, which is based on the algorithm by *Humlíček* [1982]. HitranVoigt is compared with the powerful RFM line-by-line radiative transfer code [*Dudhia* 2004]. For this purpose two optical depth spectra of the 4ν water vapor band for identical conditions are calculated using both HitranVoigt and RFM. When integrating both spectra over the entire band, the difference is found to be two parts per thousand, which indicates good agreement.

Of course, any other database which is compiled in the HITRAN-format[13] will work as well. Note that if the database includes several molecules, the transitions of all molecules of the chosen frequency range will be processed. *JavaHAWKS*, an efficient tool to extract data from a comprehensive database is available for download on the HITRAN-Webpage (`http://cfa-www.harvard.edu/hitran/`).

[13]These files are commonly labelled *.par

RFM- and LBLRTM-code

The Reference Forward Model (RFM) [*Dudhia* 2004] is a line-by-line radiative transfer code originally developed to provide reference spectral calculations for the MIPAS instrument launched on the ENVISAT satellite. It has subsequently developed into a general purpose code suitable for a variety of different spectroscopic calculations. Within this work it is used to calculate optical depth spectra of water vapor continuum absorption (CKD_2.4.1 and MT_CKD_1.0), either with or without spectral line absorption due to the water monomer. The RFM code is available via the Internet (`http://www.atm.ox.ac.uk/RFM/`).

Ptashnik [pers. comm.] finds the RFM code to be in very good agreement with the Line-By-Line Radiative Transfer Model (LBLRTM) by *Mitsel et al.* [1995], which is also freely available via the Internet (`http://rtweb.aer.com/main.html`).

5 Field Measurements

5.1 Approach

Previous studies addressed to the challenge of observing atmospheric water dimer absorption in the visible or near infrared spectral region by the spectroscopy of scattered sky light yielded negative results [*Daniel et al.* 1999; *Hill and Jones* 2000]. Limitations of both studies are: (1) The water dimer absorption is probed only by sky light that crossed the atmosphere vertically and thus on a relatively short light path. But the dimer concentration[1] is highest in the boundary layer where most of the atmospheric water vapor is present; (2) In the considered wavelength intervals structured water monomer absorption largely dominates the expected less structured and much weaker water dimer absorption. The experiences accumulated in this previous atmospheric water dimer studies lead to the following measurement strategy: (1) To maximize the sampling in the atmospheric water dimer layer, a near surface long path DOAS setup is chosen, whereby total light path lengths between 18 km and 29 km are realized; (2) Because overtone water monomer and water dimer absorption bands are predicted to be largely overlapping in the near-infrared region and their spectral features are likely to present similar spectral shapes when examined with medium resolution instruments, the weakly absorbing long wavelength end of the 4ν absorption band is selected for water dimer detection. In this spectral region, as illustrated in Figure 5.2, a single medium to strong absorption band of the water dimer is predicted to exist almost free of interference from the water monomer absorption [*Schofield and Kjaergaard* 2003]. Although being an order of magnitude less intense, two further interference-free water dimer bands which flank the $4\nu+\delta$ and 5ν water bands were investigated. The choice of spectral intervals is especially important, because many water monomer lines become saturated for long atmospheric paths and their contribution to the total absorption is known to increase with the square root rather than linearly with the absorber's concentration along the optical path. Consequently, water monomer line saturation then might prevent unambiguous detection of the atmospheric water dimer absorption. Since the quadratic increase of the water dimer partial pressure with that of the water monomer (see Equation 3.13) is precisely what is used as a marker to distinguish between water dimer and water monomer absorption.

[1] The scale height of the water dimer is about half the monomer's of typically 2 km.

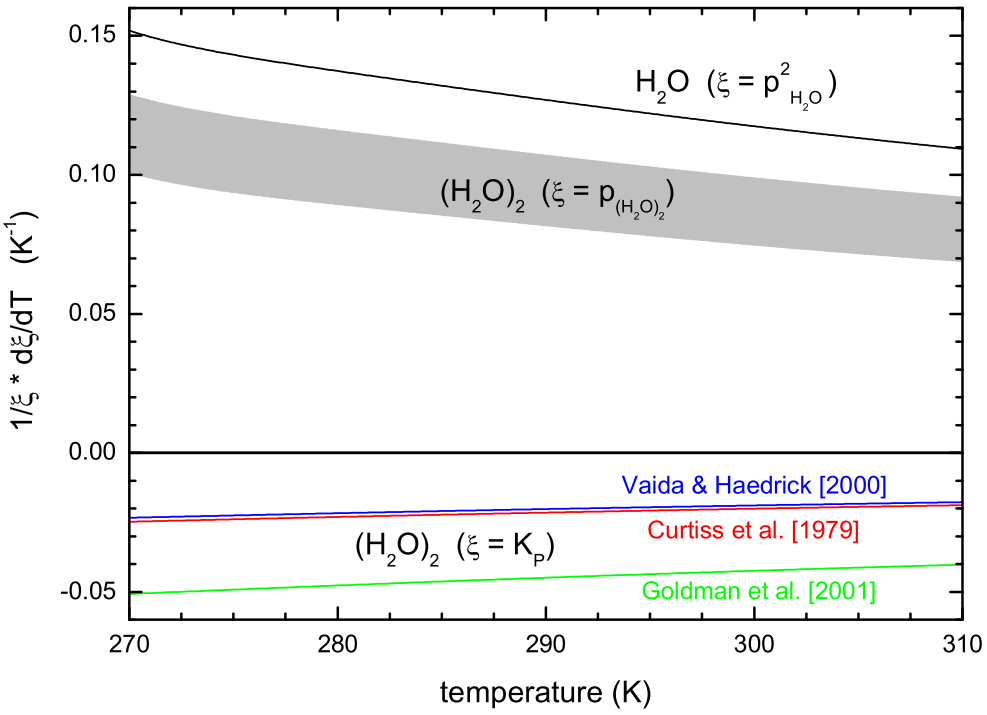

Figure 5.1: *The relative change with temperature of different quantities (ξ acts as a wildcard) is shown for a typical range of temperatures observed in Earth's atmosphere. With rising temperature the square of the water vapor partial pressure ($\xi = p^2_{H_2O}$) increases by about 13% per Kelvin. The dimerization equilibrium constant ($\xi = K_P$) on the other hand decreases by values found in the range between 2% and 5% per Kelvin, depending on the reference of K_P (blue line: Vaida and Headrick [2000], red line Curtiss et al. [1979], green line Goldman et al. [2001]). According to Equation 3.13, this results in an increase of water dimer partial pressure ($\xi = p_{(H_2O)_2}$) with rising temperature of about 10% per Kelvin, as indicated by the shaded area.*

Due to the fact that the quadratic dependence of the water dimer partial pressure is used to identify water dimer absorption, the measurement sites are chosen to cover a wide range of temperatures and therefore of water vapor partial pressures. However, it has to be considered that the water dimer equilibrium constantly decreases with rising temperature and counteracts or possibly compensates the benefit of a higher water vapor concentration. Fortunately, the effect is small for atmospheric temperatures as illustrated in Figure 5.1. Considering Earth's mean surface temperature of 288 K, a rising temperature results in an increase of water monomer and water dimer concentrations by about 6.5% and 9.5% per Kelvin respectively.

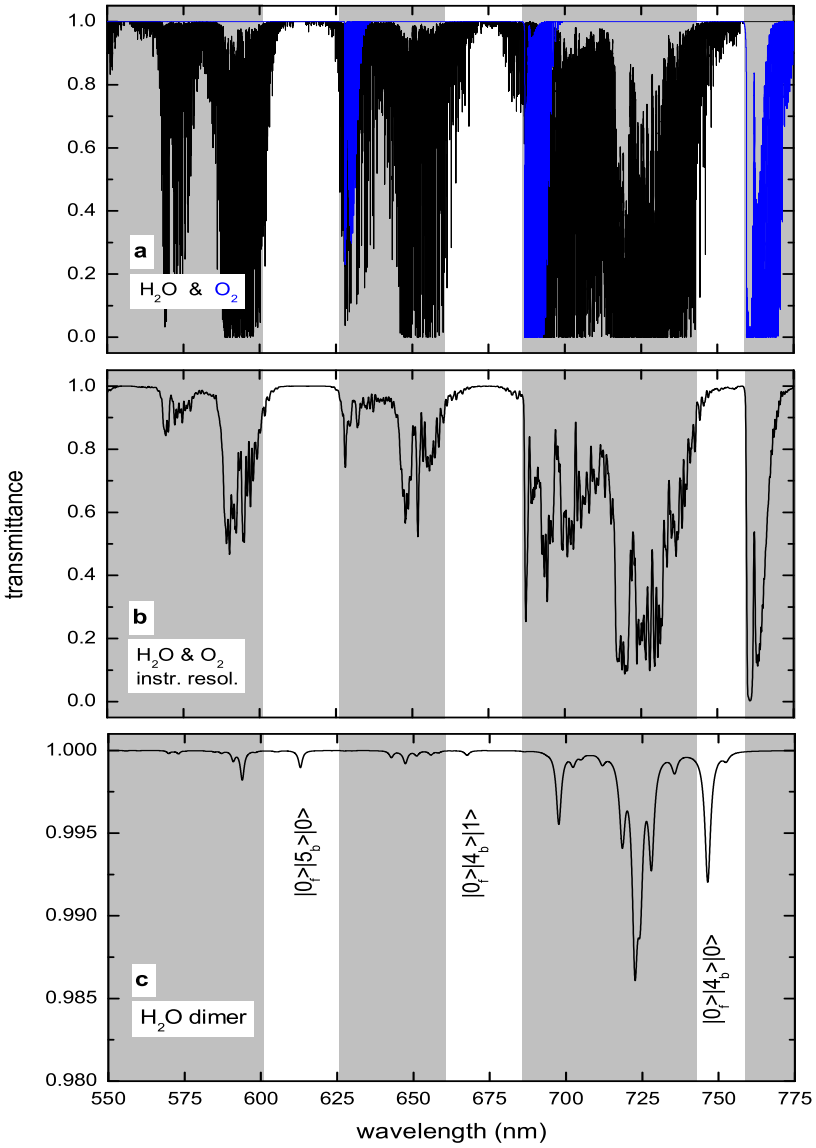

Figure 5.2: *Modeled transmittance spectra of water monomer, water dimer and oxygen. The wavelength region includes the three water dimer bands, which are predicted to be accessible by DOAS due to their offset from strong water monomer absorption. The calculation is performed for typical conditions prevailing in the tropics (T=300 K, p_{H_2O}=25 mbar) and a total light path length of 29 km.* **(a)** *Absorption due to H_2O and O_2 using the data of HITRAN04. The highlighted areas indicate the spectral intervals without saturated absorption which therefore are suitable for the analysis.* **(b)** *The same spectrum as shown above but convolved to the instrument's spectral resolution (FWHM=0.45 nm).* **(c)** *Water dimer absorption calculated from the cross section data of Schofield and Kjaergaard [2003] assuming a line broadening of 40 cm^{-1} FWHM, and a dimerization equilibrium constant of K_P(300 K)=0.036 atm^{-1} (extrapolated from the experimental data of Curtiss et al. [1979]). Note the different scales given for the transmittance.*

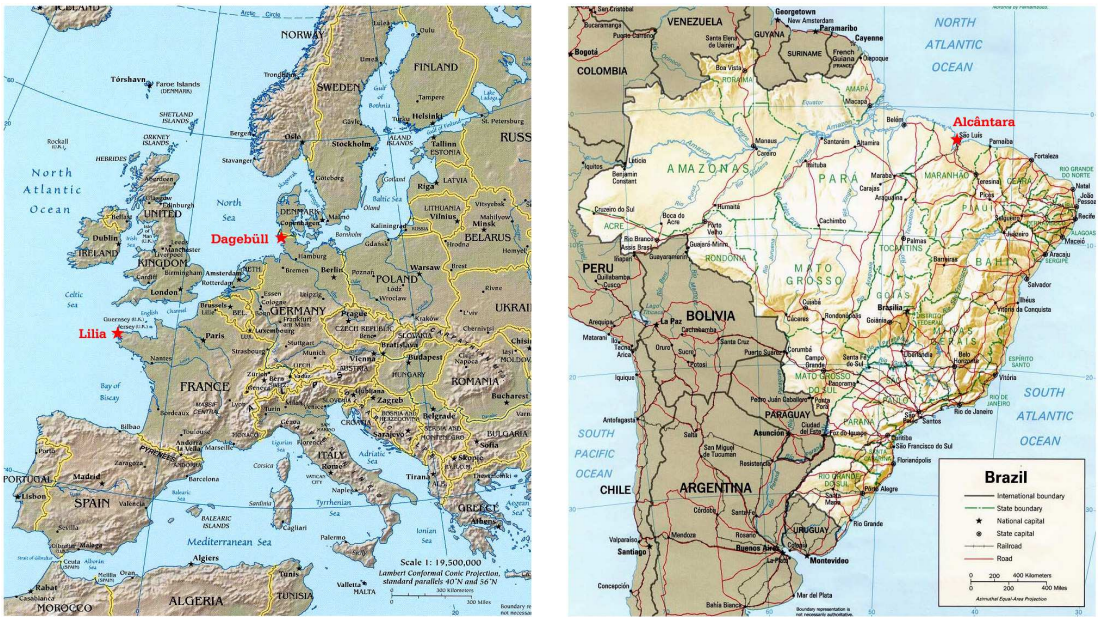

Figure 5.3: *The field measurements were conducted at the three sites marked in the maps:* **(a)** *Dagebüll, German North Sea Coast (54.7°N, 8.7°E),* **(b)** *Lilia, French Atlantic Coast (48.6°N, 4.6°W),* **(a)** *Alcântara, Atlantic Coast of Northeast Brazil (2.4°S, 44.4°W),*

5.2 Field Measurement Campaigns

A total of three field measurement campaigns were carried out at the sites marked in Figure 5.3, all of which are located directly at the coastline. In all cases, a near surface absorption path was established, which crossed for the most part above ocean water. A homogenous distribution of water vapor along the line of sight is ensured by this way.

Two field measurement campaigns were carried out at mid latitudes, the first one at the German North Sea Coast in spring 2002 and the second one at the French Atlantic Coast in late spring 2003. Since both campaigns took place in a maritime climate and at about the same time of year, the prevailing meteorological conditions are very similar. The observed temperature range there is about 5 – 20 °C. Characteristic for both measurement sites is the large area of intertidal zone due to an extremely flat topology or a high tidal range. A third field measurement campaign was performed in equatorial Brazil during the turn from year 2004 to 2005. Due to the proximity to the equator the meteorological conditions are settled, the humidity is high and temperatures are almost constant, oscillating only some degrees around 30 °C.

Both campaigns at the mid latitudes are performed within the framework of a project addressed to the sources, distribution and effects of reactive halogen species in the

troposphere (ReHaTrop), which is part of the German Atmospheric Research Program *AFO2000* [*AFO* 2005]. Unfortunately, the amount of data acquired for the investigation of water dimers is somewhat sparse due to the constraint in available measurement time. The campaign in the tropics is primarily devoted to the the study of water and water dimers, but also some measurement time is used to look for reactive halogen species.

An almost identical instrumental setup is used for all three field measurement campaigns. The DOAS telescope system equipped with an Acton 500 spectrograph and a photo diode array detector makes it possible to record atmospheric absorption spectra at 0.45 nm spectral resolution. For the campaign in Brazil the instrumentation is expanded by a further spectrograph, a SPEX 750, which allows a higher spectral resolution of 0.15 nm. At all times a meteorological station was installed nearby to monitor ambient conditions. From this data the in-situ water vapor partial pressure is also derived. A detailed description of the operated instruments is given in Section 4.2. At the mid latitude campaigns supplementary in-situ instruments are deployed, although their data is not needed within the scope of this thesis: Instruments to measure in-situ ozone and nitrogen monoxide concentrations, an optical particle counter to obtain information about number and size distribution of aerosols, a spectral radiometer to retrieve photolysis frequencies and a sonic anemometer to retrieve three-dimensional wind profiles.

5.2.1 Measurement Sites

Dagebüll

The field measurement site close-by the town of Dagebüll is located at latitude 54.73 ° Noth and longitude 8.70 ° East, directly at the German North Sea Coast. The LP-DOAS instrument is set up in a container positioned on top of the dike about 8 m above mean sea level and in some 50 m distance to the shoreline. An array of about 180 retro-reflectors is installed on the island of Langeneß in 9 170 m distance[2] to the DOAS instrument. The course of the light path from the measurement site to the retro-reflector position is indicated by the arrow in Figure 5.4. It emanates from the map, that the light path entirely crosses the intertidal zone which is indicated by the area colored in light blue. The mean tidal range is approximately 3 m. Due to the extremely flat topology vast tidelands of several kilometers outward from the protective dikes exits. This stretch of land, which is flooded by sea water during high tide and remaining dry during low tide, is the largest natural reserve in central Europe, called “Wadden Sea”. During times of low tide, the light beam completely crosses the uncovered land which mainly consists of wet silt. In times of high tide the light beam directly traverses atop the sea surface in just a few meters height, because the retro-reflectors are only

[2]The distance is measured by a laser range finder and is regarded as exact, since the instrument's error is in the order of centimeters.

Figure 5.4: *The field measurement site at Dagebüll, German North Sea Coast. An array of retro-reflectors is set up on the island of Langeneß in 9 170 m distance to the DOAS-instrument. The light path entirely crosses the intertidal zone, which is color coded in light blue.*

mounted in approximately 2 m height above high tide sea level. For periods of bad atmospheric visibility a second light path to retro-reflectors located on the island of Oland is established. However, for performing measurements of water dimer absorption, this short light path of approximately 5.7 km single length is not used. It turned out that the low height of the light beam causes a significant loss in intensity due to a layer of aerosols, sea spray, and ground fog.

Lilia

The field measurement campaign is conducted at the French Atlantic Coast of Brittany nearby the town of Lilia, which is located some 25 km north of the city of Brest. Located at latitude 48.63 ° North and longitude 4.57 ° West, the LP-DOAS instrument is set up in a container on a parking lot just some meters from the ocean in times of high tide.

Figure 5.5: *The field measurement site at Lilia, French Atlantic Coast of Brittany. An array of retro-reflectors is set up in 9 472 m distance to the DOAS-instrument. The light path partially crosses the intertidal zone, color coded in light blue.*

In 9 472 m distance[3] to the DOAS instrument, an array of about 180 retro-reflectors is installed directly at the shoreline. The arrow in Figure 5.5 shows the course of the light path from the instrument to the retro-reflector site. A second light path of about half the length is available in case of bad weather conditions, but it is never used for measurements within this work.

The Northwest of the French Atlantic Coast is characterized by a craggy coastline and a huge but very variable tidal range. The tidal range reached up to 7.5 m at the measurement site during the time of campaign. The intertidal zone consists of sandy and rocky terrain, and extended fields are covered by algae of a great variety. About 60% of the light path crosses the intertidal zone in times of low tide, whereas at high tide all is flooded along the total length. In contrast to the near surface light path at the North Sea campaign, the height remains more than 10 m above the water surface here, even at high tide.

[3]The distance is measured by a laser range finder and is regarded as exact, since the instrument's error is in the order of centimeters.

Figure 5.6: *The field measurement site at Alcântara, Brazil, close to the city of São Luís. The DOAS instrument is set up on the "CLA" rocket base near Alcântara. The retro-reflectors are installed on the island "Ilha do Medo" in 14 500 m distance.*

Alcântara

The field measurement campaign is conducted at the Atlantic Coast of Northeast Brazil, nearby the city of São Luís, the state capital of Maranhão. At latitude 2.40 ° South and longitude 44.38 ° West, the instruments are set up inside of the residential area of the "Centro de Lançamento de Alcântara (CLA)", a Brazilian rocket base which is located close-by the town of Alcântara, approximately 20 km northwest of São Luís. The map 5.6 does not show the rocket base, but the instrument's site marked by the start of the arrow. It is situated a few 100 m distant to the shoreline and is about 30 m above sea level. The same array of about 180 retro-reflectors as used for the previous campaigns is installed on the island "Ilha do Medo" in 14 500 ± 25 m distance[4]. Since the reflectors are positioned some 10 m above sea level, the course of the light path is in adequate height above the water surface in order to avoid loss in intensity due to sea spray and aerosol. Although pronounced tides with a height of 3 – 5.5 m are present, the intertidal zone stretches outwards only some 100 m in the region of interest. Vast regions covered by mangrove woods exit further inland, the land bordering the bay of "São Marcos". That's why going overland to São Luís is an almost 400 km travel.

[4]Determined by the use of a GPS receiver, as the distance is too long to be measured by the laser range finder.

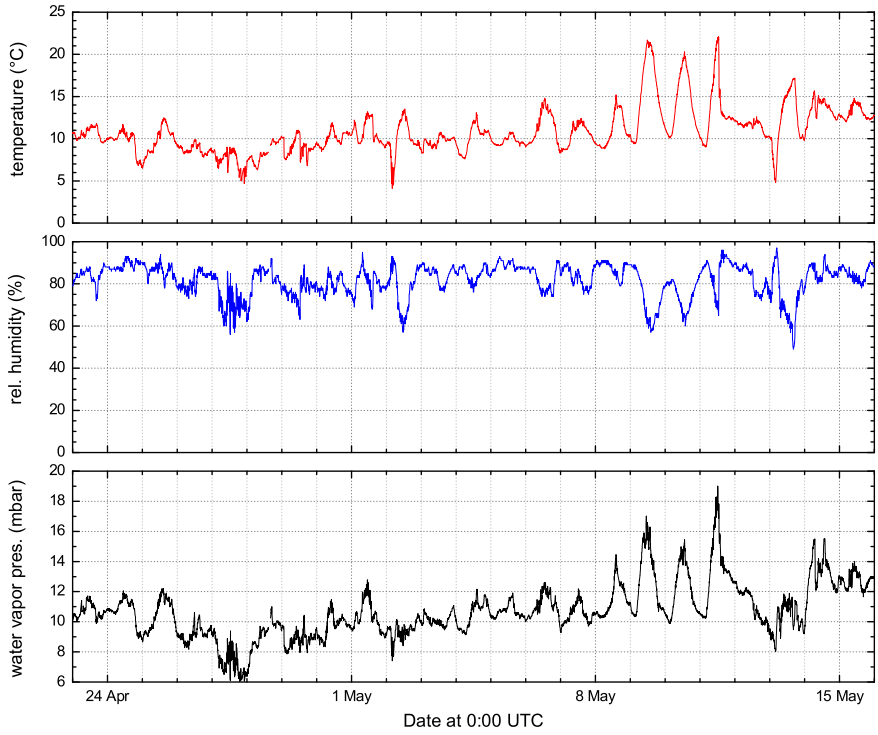

Figure 5.7: *Temperature, relative humidity, and water vapor partial pressure for the field campaign carried out in Dagebüll at the German North Sea Coast. The ticks of the abscissa are set to 0:00 UTC. Local Mean Time (12:00 noon LMT corresponds to the passage of the mean Sun across the meridian) is offset by +35 min with respect to UTC.*

5.2.2 Meteorology

Dagebüll

The campaign took place in spring 2002 between April 18th and May 17th. The generally stormy and rainy weather conditions are not supportively for the measurements, which require good atmospheric visibility. Therefore, considerable measurement time is lost. The meteorological data of pressure, temperature, relative humidity, wind direction, wind speed and solar radiation is recorded by the mobile weather station described in Section 4.2.7, which is set up close to the container housing the DOAS instrument. An overview of the meteorological data of interest, i. e. temperature, relative humidity and derived water vapor partial pressure, is shown in Figure 5.7. The temperature pattern is very irregular due to the unsettled weather conditions. The diurnal temperature range is moderate as is typical for a maritime climate. Almost at all times the relative humidity is very high around 80%, only occasionally dropping down to 60%. Therefore, the water vapor pressure remaines within a small range of 8 – 12 mbar for most of the time. Three warm and sunny days (May 9, 10, 11) are outstanding in the data series.

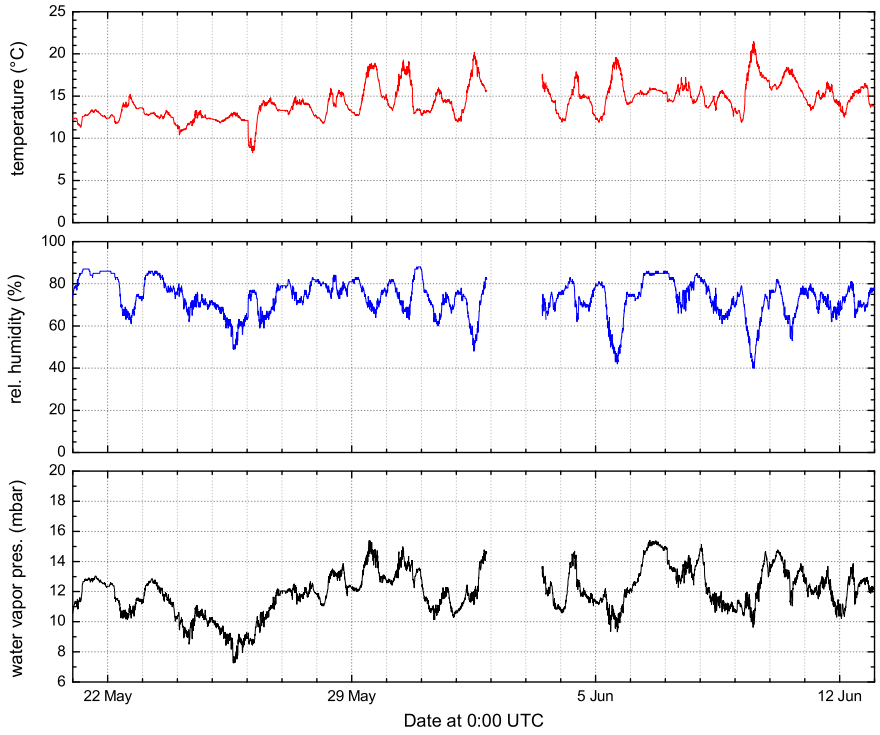

Figure 5.8: *Temperature, relative humidity, and water vapor partial pressure for the field campaign carried out in Lilia at the French Atlantic Coast. The ticks of the abscissa are set to 0:00 UTC. Local Mean Time (12:00 noon LMT corresponds to the passage of the mean Sun across the meridian) is offset by -18 min with respect to UTC. The gap is caused by a failure of the weather station.*

Those days show the highest values of water vapor pressure, peaking between 14 and 18 mbar at local noon. Unfortunately, this period of sunny weather ended abruptly by the arrival of a local storm front accompanied by a change from easterly to westerly winds.

For the purpose of comparison a data set of the meteorologic service of Wittdün was provided. Wittdün is situated on the island of Amrum in 22 km distance to the measurement site. The weather record of this meteorologic station is in reasonable agreement with the data of our measurement.

Lilia

The field campaign was conducted in late spring 2003 from May 6th to June 13th. Many times pristine air was transported to the measurement site by westerly flows, yielding good visibility for the use of the long distance absorption path. Only during the last days of May the air was strongly influenced by easterly flows, when highly polluted air masses were transported over land to the site. This caused poor atmospheric visibility

due to a very hazy sky. To measure the meteorological data of pressure, temperature, relative humidity, wind direction, wind speed and solar radiation, the mobile weather station described in Section 4.2.7 is set up nearby the container housing the DOAS instrument. The meteorological data of temperature, relative humidity and derived water vapor partial pressure, is given in Figure 5.8 for the time period of interest. Similar to the North Sea data the maritime influence is evident, but a somewhat more regular pattern and a diurnal variation is seen. The temperature remains within the range of 10 – 20 °C virtually all the time and the relative humidity mostly is between 60% and 80%, occasionally dropping down to 40 – 50% around local noon. The partial pressure of water vapor peaks at values of 15 mbar. For most of the time it remains above 10 mbar, except for some days at the beginning when it drops to 8 mbar.

Alcântara

The field measurement campaign was performed from November 23, 2004 to January 18, 2005, but the acquisition of data did not start before mid-December due to several organizational tasks we were confronted with. Except for the very end of the campaign, the weather is dominated by the very settled and predictable conditions of the dry season, which usually prevails during roughly the second half of the year. Easterly flows and low level scattered clouds were observed during most of the time and sometimes thundery clouds were seen inland on the horizon. Since the trade winds are arriving from the open ocean, the atmospheric visibility is acceptable in general and sometimes even excellent. The period of steady weather ended abruptly on January 15th by the beginning of the rainy season. Figure 5.9 shows the data of temperature, relative humidity and thereof derived water vapor pressure during the time of the field measurements. This data, as well as further meteorological data, is recorded by the mobile weather station (description in Section 4.2.7), which is set up nearby the the DOAS instrument. The equatorial location of the site is quite obvious in the data. The ambient air pressure (not shown in the graph) is nearly constant throughout, even a 12 hour cycle of approx. 3 mbar is discernible. A regular diurnal pattern is seen in the data of temperature with highs of 32 °C and lows of 27 °C, resulting in a daily temperature range of only some 5 °C. An inverse pattern is observed in the data of relative humidity. There, the values range between 55% at daytime and 75% at nighttime. Two periods deviating from this regular pattern, the night of December 28/29 and January 15th, are seen. Those are the times when there was rain, the latter of which finally marked the start of the rainy season. The opposite direction of the temperature and relative humidity indicates an almost constant pattern of absolute humidity, thus water vapor pressure. However, variations in water vapor pressure are seen on a longer timescale of a couple of days. During the time of measurements values are found in the range of about 24 – 29 mbar.

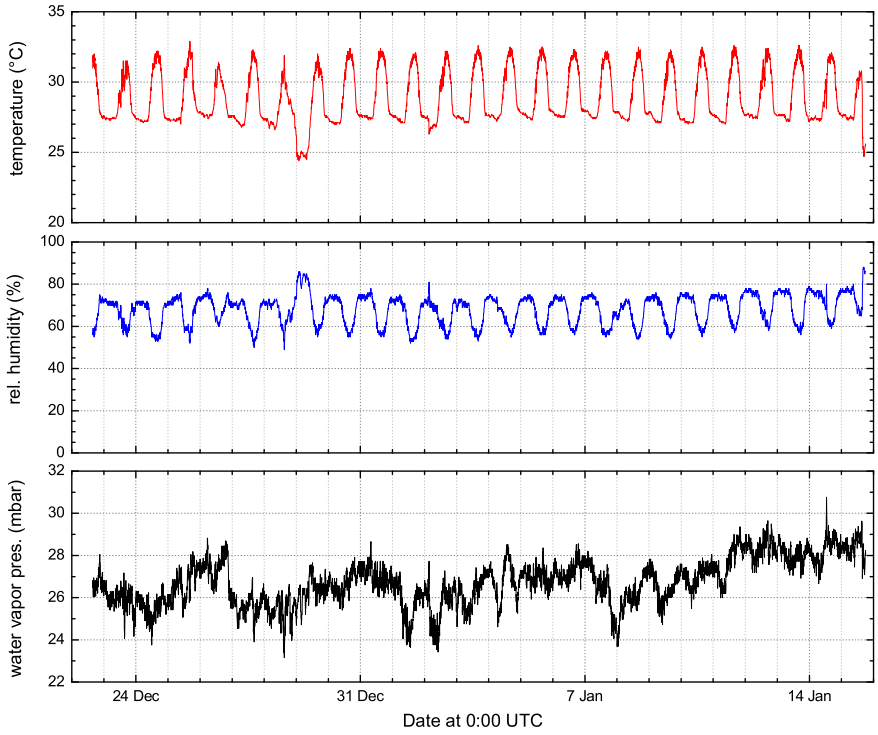

Figure 5.9: *Temperature, relative humidity and water vapor partial pressure for the field campaign carried out in Alcântara at the Atlantic Coast of Northeastern Brazil. The ticks of the abscissa are set to 0:00 UTC. Local Mean Time (12:00 noon LMT corresponds to the passage of the mean Sun across the meridian) is offset by -2 h 58 min with respect to UTC.*

5.3 Data Acquisition

5.3.1 Campaigns in the Mid-Latitudes

The investigation of water dimer absorption is focused on the $|0\rangle_f|4\rangle_b|0\rangle$ band, which is supposed to be sufficiently strong for getting detected. The wavelength range of 740±40 nm is selected for measurements, which also includes the most part of the water vapor 4ν band. Additionally, the data recorded at a wavelength of 640±40 nm, intended for the analysis of nocturnal NO_3 absorption, is also checked for water dimer absorption by the $|0\rangle_f|5\rangle_b|0\rangle$ and $|0\rangle_f|4\rangle_b|1\rangle$ bands. Actually, it is not expected to detect water dimer absorption at these bands, first because of their weak strength and second due to the low water vapor partial pressure especially during nighttime. Nevertheless, these spectra are analyzed for water dimer absorption.

Dagebüll

Since the primary objective of the field campaign is the study of reactive halogen species and the measurements often suffered from bad weather conditions and poor atmospheric visibility, the investigation of water dimers is very constrained in measurement time.

In the wavelength region around 740 nm, a total of 75 single spectra are recorded. Due to the fact that the multi channel technique (MCT) is applied (for details see Section 4.3), only eight final spectra[5] are obtained, each of which is added from a total of 27 (9×3) detector readouts. The individual exposure times for a single readout range between 1 – 3 s for six of the final spectra, and 8 – 16 s for the remaining two, i. e. the spectra are recorded at the very best and normal conditions of atmospheric visibility, respectively. These eight spectra which are finally used for the analysis, are recorded on four different days, whereas attention was payed to cover a wide range of ambient water vapor pressure. For the sake of data reliability both spectra of each day are recorded subsequently. An overview of the acquired data during the campaign is given in Table 5.1. Unfortunately, for the three outstanding days involving the peaks of high water vapor pressure, measurement time for the study of water dimers was only available on May 10th at a water vapor pressure averaging 14.4 mbar during data acquisition. About 50 spectra are acquired at a wavelength around 640 nm, all of which during nighttime. No multi channel technique is applied. Depending on the respective exposure time (in the range of 1 – 30 s), 15 or 30 readouts are added for a single spectrum.

Lilia

The weather conditions and atmospheric visibility which prevailed during the time of the field measurement campaign at the French Atlantic Coast are conspicuously better than at Dagebüll. Although the primary subject is the investigation of reactive halogen species, a satisfactory amount of data is acquired for the study of water dimers.

Spectra, both with and without applying the multi channel technique (MCT), are recorded in the 740 nm spectral region. An overview of the acquired data is given in Table 5.1. Altogether, 16 final spectra by the application of the multi channel technique from the nights of June 9/10 and 11/12, and 75 non MCT spectra taken during the period June 2rd through June 6th are available. In contrast to the Dagebüll data, the number of detector readouts is increased to reduce statistical noise: One final MCT-spectrum is added from a total of 270 (9×30) detector readouts and the non MCT-spectra consist of 100 readouts each. Due to the good atmospheric visibility exposure times are below 10 s most of the time, even values below 2 s could be achieved.

[5] Nine spectra of one MCT-cycle are merged to give one final spectrum

Table 5.1: *Accompanying data of the spectra acquired in the 740 nm wavelength region. Derived from the data of the meteorological station, the water vapor partial pressure is listed either as average or range during the given time of spectra acquisition. The data of the campaign conducted in Brazil, which is described in detail in Section 5.3.2, is also listed for comparison.*

Date in UTC	p_{H_2O} (mbar)	Remarks
Dagebüll 2002		
Apr 27, 19:25 – 19:50	6.7	MCT, low tide at 20:10
May 10, 11:50 – 12:35	14.4	MCT, high tide at 12:18
May 12, 21:25 – 22:00	10.0	MCT, low tide at 20:06
May 14, 16:40 – 17:40	13.5	MCT, high tide at 14:30
Lilia 2003		
Jun 02 – Jun 06	9.6 – 14.3	no MCT, day and night time
Jun 09/10	13.1 – 14.6	MCT, night time
Jun 11/12	10.3 – 11.7	MCT, night time
Alcântara 2004/05		
Dec 21 – Jan 15	24 – 29	miscellaneous data recording

The water vapor partial pressure ranges between approximately 10 – 14 mbar, i. e. is similar to the values encountered at Dagebüll. In the wavelength region around 640 nm nearly 300 spectra (100 detector readouts each) are recorded without using the multi channel technique. The measurements were performed sporadically both at day and night during the entire duration of the field campaign.

5.3.2 Campaign in Equatorial Brazil

The field campaign conducted in equatorial Brazil is primarily dedicated to study atmospheric water and water dimers, therefore plenty of data is collected. In contrast to the previous campaigns two spectrograph-detector systems are available, an Acton 500 providing 0.45 nm spectral resolution and a SPEX 750 yielding 0.15 nm spectral resolution. Note, that both systems do not operate simultaneously, as this is technically not feasible. Although most attention is payed to the $|0\rangle_f|4\rangle_b|0\rangle$ water dimer band predicted near 746 nm, absorptions due to the weaker bands $|0\rangle_f|5\rangle_b|0\rangle$ and $|0\rangle_f|4\rangle_b|1\rangle$ are also studied in detail. Because of the high water vapor partial pressure and the very long absorption path length of 29 km it is assumed that detection of these bands may be possible.

An increase of about 50% in light path length in comparison to both previous campaigns is quite obvious, when the overall light throughput is compared. Integration times for a single well exposed spectrum at the very best conditions of atmospheric visibility are about 5 s and 10 s for the SPEX and Acton spectrograph, respectively, but typical times are a factor four larger. Due to the low light intensity entering the quartz fiber, the optimizing and measurement routines have to be modified slightly. The quartz fiber alignment is optimized manually from time to time since statistical variations of the already low intensity do not lead to satisfactory results of the automated alignment. In general, exposure times for one single detector readout are limited to a maximum of three minutes. The number of readouts is dynamically allocated in dependence on the exposure time in that way, that the total integration time for a spectrum is close to three minutes but does not exceed this value. Thus, at a better atmospheric visibility, more readouts of shorter integration time are added. Hence, the signal to noise ratio is increased. However, the number of readouts is restricted to a maximum of 10, that in case of good atmospheric visibility, a better temporal resolution is obtained.

The low resolution spectra (Acton 500 spectrograph) cover a 78 nm wavelength interval and are centered on 730 nm, 640 nm and 590 nm, corresponding to the 4ν, $4\nu+\delta$ and 5ν water polyads, respectively. Thus, the data can be used for the evaluation of water monomer, water dimer and water continuum absorption. For the spectra recorded at the start of the field measurements during the period December 21st through 25th no multi channel technique was applied. Anyway, due to the poor atmospheric visibility during those days and an therefore unfavorable signal to noise ratio, these spectra had to be analyzed with care. Some of which even are useless. The spectra acquired in the end of the campaign were recorded in multi channel mode. After the processing of these MCT-spectra a total of 50 final spectra in the 730 nm region and about half of that in both other spectral regions each are available.

The high resolution spectra (SPEX 750 spectrograph) providing a coverage of 26 nm are exclusively probed for water dimer absorption. Here, the 745 nm, 670 nm and 615 nm are selected. Measurements are performed during the time period from January 3rd to January 15th only by using the multi channel technique. In the spectral region of the $|0\rangle_f|4\rangle_b|0\rangle$ water dimer band a total of 50 final spectra is available for analysis and for both other water dimer bands the yield is 30 spectra.

5.3.3 Xenon Lamp Reference Spectra

During the field campaign carried out at Dagebüll, Xenon lamp reference spectra were recorded by the use of the shortcut system no.1, which is described in detail in Section 4.2.6 (see Figure 4.11 there). These reference spectra are acquired in each measure-

ment cycle[6], i. e., for each atmospheric absorption spectrum there exists a corresponding Xenon lamp reference spectrum, recorded a few minutes afterwards. If the multi channel technique is applied to measure atmospheric spectra, the reference spectra are also recorded by this technique. Since the light's path length is drastically shortened for the reference spectra, the light intensity is enormous and even by the use of a neutral density filter exposure times are in the range of a few 100 ms.

The shortcut system no.2 (see Section 4.2.6 for details) was used for recording Xenon lamp reference spectra during both field campaigns performed in Brittany and Brazil. As this system needs to be set up in front of the DOAS telescope manually, it is not possible to implement the recording of the reference spectra in the measurement routine as it is possible for the system no. 1. Therefore, spectra of the Xenon lamp are acquired only once per day, preferably in the evening hours when the routine has to be stopped anyway in order to check the adjustment of the telescope. In the case of MCT measurements the references are also recorded by the applying the MCT.

5.4 Characterization of the Detector System

Detector units manufactured by Hoffmann Messtechnik GmbH, Rauenberg, Germany were operated at all field measurement campaigns. The only difference is the type of mounted photo diode array (PDA) as described in Section 4.2.5: A Hamamatsu S3904-1024 PDA and a Hamamatsu S8381-1024 PDA for the Acton and SPEX spectrograph, respectively. Actually three different PDAs were used, since the PDA of the Acton system was replaced by a new one of the same type. The first PDA was used only during the Dagebüll campaign and the second one during the two other campaigns. The operating temperature of the PDAs was set to -20 °C for all field measurements.

5.4.1 Offset and Dark Current

Spectra of the electronic offset signal are recorded by adding 10 000 detector readouts of minimum integration time (60 ms) at dark conditions. The dark current may be neglected since the ratio of dark current to offset signal is in the order of 10^{-4} for 60 ms integration time. From two offset signals of the same number of readouts N the electronic noise is determined by subtracting the spectra and dividing by a factor of $\sqrt{2N}$. The result is around 5 counts per readout for the detectors used at the field campaigns. For comparison, a well exposed atmospheric spectrum shows about 50 000 counts per readout.

Dark current spectra are measured by performing one detector readout of long integration time (typically $\geq$100 s) at dark conditions. All detectors yield dark currents of 1.5 – 2 counts per second integration time at a detector temperature of -20 °C. The

[6] Atmospheric spectrum -> background spectrum -> Xenon lamp reference spectrum -> calibration lamp spectrum

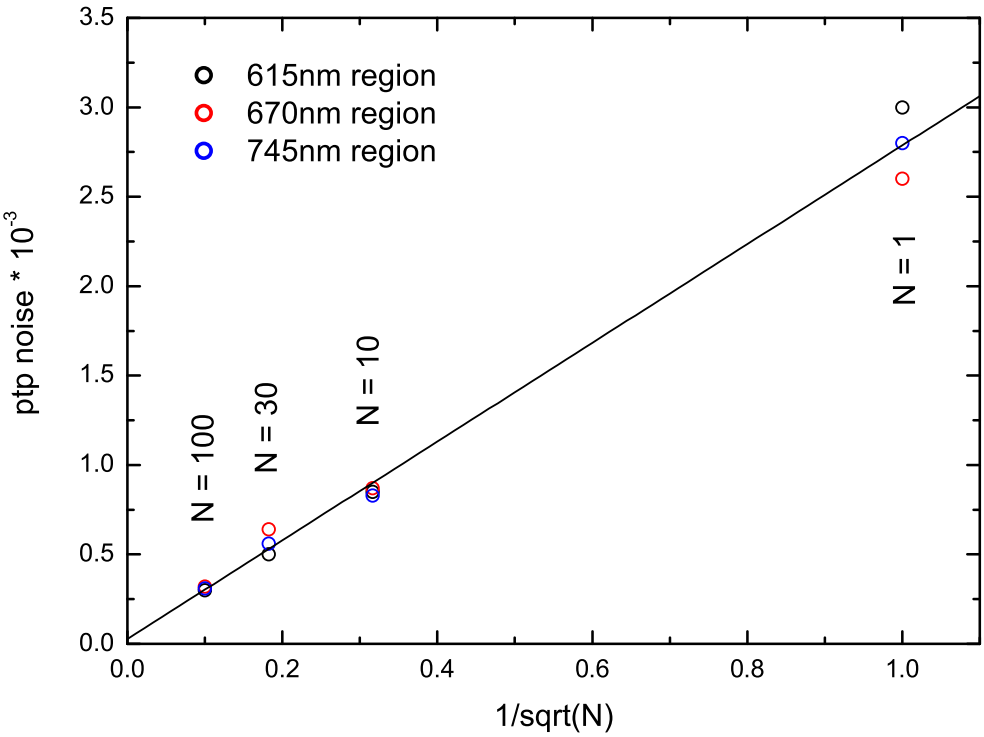

Figure 5.10: *Peak to peak noise in dependence on the number of detector readouts and wavelength. The data is taken from the campaign in Brazil, recorded by the SPEX spectrograph. The line is a linear fit to all 12 data points.*

second PDA of the Acton system shows about 10 hot pixels with dark current peaks up to five times the average intensity, whereas the first PDA has only two hot pixels of slightly enhanced intensity. The PDA of the SPEX system is free of hot pixels.

5.4.2 Detector Noise

The different types of effects contributing to the total noise are described in detail in Section 4.4.3. To summarize, the total noise consisting of photo electron, dark current and electronic noise is dominated by the photo electron noise, which is about 200 counts per readout versus an electronic noise of approximately 5 counts per readout and a dark current noise of about 15 counts per readout at the maximum exposure time of three minutes.

Experimentally, the total noise is determined by the division of two halogen lamp[7] spectra, which are recorded in succession with the same integration time and are corrected for offset and dark current. The values of *peak to peak* (ptp) and *root mean square* (rms) are taken from the spectra resulting from the division and a further high-pass filtering. This procedure is performed for each wavelength interval of interest and with

[7]The halogen lamp was mounted directly in front of the quartz fiber.

Table 5.2: *Overview of the total detector noise. The data is experimentally derived by the division of two halogen lamp spectra. Peak to peak (ptp) and root mean square (rms) of the residual noise spectra are given in 10^{-3} (parts per thousand).*

	North Sea Acton 500 PDA1		Brittany, Brazil Acton 500 PDA2		Brazil SPEX 750	
number of readouts	ptp	rms	ptp	rms	ptp	rms
	$\times 10^{-3}$		$\times 10^{-3}$		$\times 10^{-3}$	
1	2.10	0.32	3.00	0.45	2.20	0.33
10	0.73	0.12	0.95	0.15	0.72	0.11
100	0.44	0.07	0.48	0.08	0.30	0.08

different numbers of readouts. Figure 5.10 illustrates the ptp-values for the detector mounted to the SPEX spectrograph. It is seen that the noise is independent of the wavelength interval here. As predicted by Poisson statistics the total noise, which is mainly photo electron noise, is indirect proportional to the square root of the number N of detector readouts. However, by increasing this number N the noise is limited by systematical effects and fluctuations of the light source. Tests show that an increase of N to values beyond some 100 readouts does not result in an enhancement of the signal to noise ratio. The data characterizing the total noise of each spectrograph-detector setup which was in use at the field measurements is listed in Table 5.2. Differences of the specified values for the different investigated wavelength regions are marginal, so the data is averaged for each detector.

6 Results and Discussion

6.1 Concept

The analysis of atmospheric absorption spectra in the visible and near infrared spectral regions of water vapor absorption is a challenging task in many respects: (1) Spectral features induced by absorbers other than water are masked by highly pronounced water vapor absorption. (2) Saturation of water lines already occurs for short absorption path lengths, resulting in the relationship of water absorption and water concentration to be non-linear (Section 4.1.2). (3) The water absorption cross section is not well characterized and sensitive on temperature. These problems decisively affect the analysis procedure. Within this thesis, the absorption by the water monomer, the water continuum, and the water dimer is considered. All are overlapping in wavelength and differing in absorption strength by some orders of magnitude. Figure 6.1 illustrates the absorption spectra of these three components in the spectral region of the 4ν water band. As a major step towards unraveling the true nature of combined water monomer, water continuum, and water dimer absorption, the bulk contribution by water monomer absorption has to be accurately characterized. Several spectral line databases (Section 4.5.1) are used in order to qualify and quantify water monomer absorption. Although some of these databases have been continuously updated, a well-known inaccuracy and incompleteness is still remaining, especially in the visible and near infrared spectral regions [*Ptashnik and Shine* 2003; *Sierk et al.* 2003].

Two fundamental spectral analysis procedures are applied in order to derive the atmospheric water vapor content and obtain information about possible water continuum absorption. The latter is generally difficult to access by the DOAS technique due to its broadband character. The evaluation of each individual water absorption spectrum is performed in two wavelength intervals. One evaluation covers an entire water polyad. This analysis is complicated by saturated water absorption throughout a wide spectral range almost entirely across a water band. A second evaluation is performed in a narrow spectral interval of unsaturated water absorption, located at the red end of the respective polyad. Discrepancies between derived water vapor concentrations from the spectral retrievals performed in both these intervals indicate water continuum absorption. Complementary to the spectroscopic measurements, in-situ water vapor concentrations are available from the data recorded by the meteorological station.

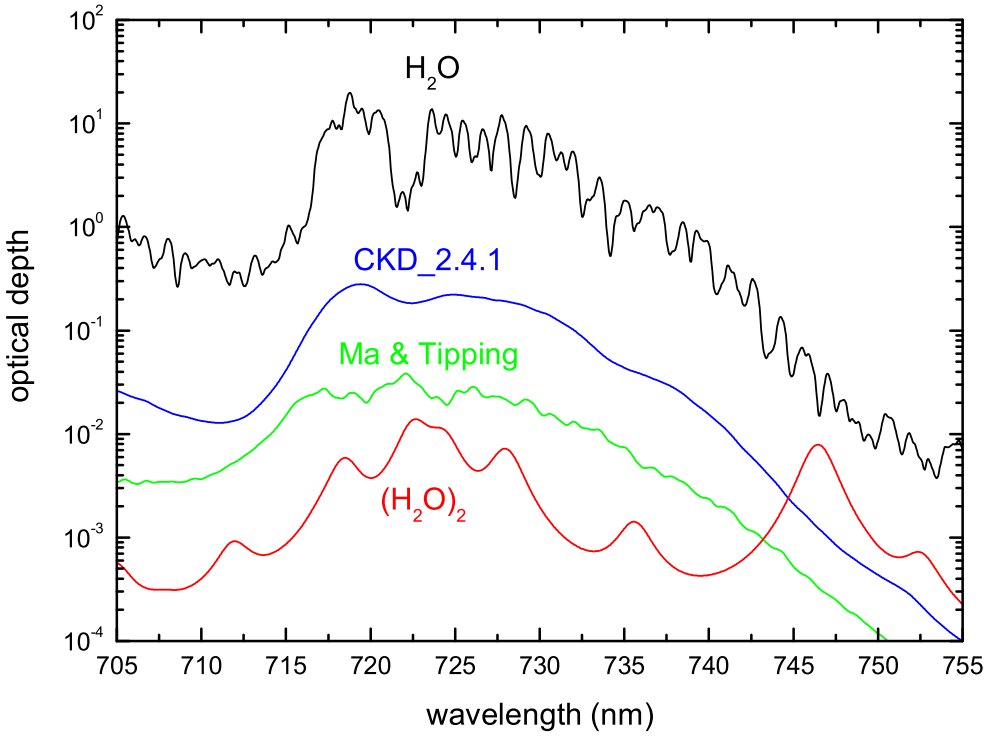

Figure 6.1: *Optical depths in the spectral region of the 4ν water band. The spectra are calculated for tropical conditions (T = 300 K, p_{H_2O} = 25 mbar), a total light path length of 29 km and are convolved to the field instrument's resolution (Acton 500 spectrograph). Top down, spectra are shown for the water monomer, the water continuum according to the CKD_2.4.1 model, the water continuum due to the Ma and Tipping far wing line shape theory, and the water dimer using the cross section of Schofield and Kjaergaard [2003], an equilibrium constant of K_P(300 K) = 0.036 atm^{-1} [Curtiss et al. 1979] and a reasonable band broadening of 40 cm^{-1} FWHM [Vaida et al. 2001].*

Water dimer absorption is accessible more directly than continuum absorption by the DOAS technique. As an indicator for water dimer absorption, the quadratic dependence of its partial pressure upon that of the water monomer is used (Equation 3.13). The spectral retrieval is based on the calculated absorption cross sections provided by the research group of Henrik Kjaergaard [*Low and Kjaergaard* 1999; *Schofield and Kjaergaard* 2003]. Some inaccuracies of water dimer band strengths and positions are still existing, but the spectral retrieval is mainly complicated by the unknown water dimer band broadening. From Figure 6.1 it is obvious that the spectral feature located at 746 nm is ideal for attempting to detect water dimer absorption in the atmosphere.

In the following, the spectral retrievals and results with regard to water monomer, water continuum, and water dimer absorption are described in detail.

6.2 In-situ Water Vapor Concentration

In-situ water vapor concentrations are derived from the ambient temperature and relative humidity, which were measured by a mobile meteorological station (Section 4.2.7) during all field campaigns. The station was always setup close to the DOAS instrument. Time series of the relevant meteorological data are shown in the previous chapter. For direct comparison with the water concentration obtained from the spectroscopy, the in-situ data is averaged over time corresponding to the recording time of each absorption spectrum.

The conversion of temperature to water vapor saturation pressure is performed by applying a third order polynomial. The polynomial's coefficients are derived by fitting to standard physical reference data of the water vapor pressure curve as tabled in *D'Ans-Lax* [1967]. Then, the water vapor concentration follows from the relative humidity and the ideal gas law. The manufacturer of the meteorological station quotes a maximum inaccuracy of $\pm\,0.2\,^{\circ}\mathrm{C}$ in temperature and $\pm\,0.02$ in relative humidity.[1] By checking up the water vapor pressure curve, it is found that an inaccuracy of $0.2\,^{\circ}\mathrm{C}$ in temperature translates into an 1.1 – 1.4% error of water vapor partial pressure for the temperature range prevalent at all field campaigns. Considering relative humidities between 0.6 and 0.9, the inaccuracy of $\pm\,0.02$ corresponds to an 2.2 – 3.3% error. The total error is dominated by the inaccuracy of the relative humidity. To simplify matters, the error is assumed to be 3% for all measurements.

6.3 Preliminary Investigation of Water Vapor Absorption

6.3.1 Pressure and Temperature Dependence

The water vapor absorption spectrum throughout the visible and near-infrared spectral region is of pure vibration-rotational nature (Section 3.2.1). The strength and broadening of each individual spectral line is controlled by ambient temperature and pressure. For typical conditions encountered in Earth's boundary layer, individual rotational lines are well separated to be distinguishable by a high resolution instrument. Even by the use of a medium resolution instrument as applied for all field measurements within this work, clusters of individual rotational lines are observable. With regard to the spectral analysis the question arises how strongly the water vapor absorption cross section is affected by the change in temperature and pressure as observed during the course of a field measurement campaign. Therefore, a study is performed by simulating the spectral retrieval with modeled absorption spectra calculated for different ambient conditions. All calculations are based on the HITRAN04 spectral line database and are performed by the use of the *HitranVoigt* line-by-line radiative transfer code (Section 4.5.3).

[1] The relative humidity is given without using the common percent-notation here, in order to rule out confusion of absolute and relative errors.

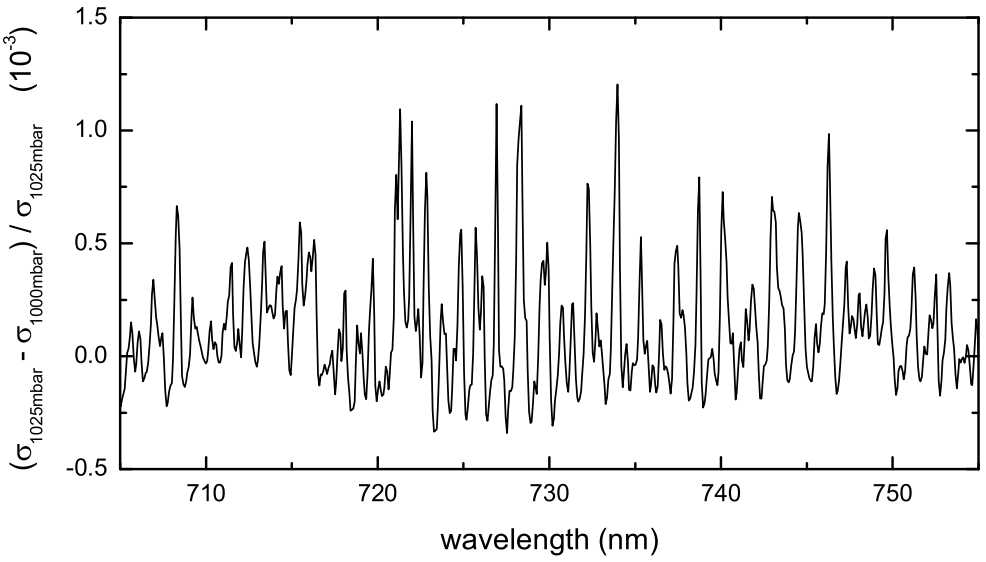

Figure 6.2: *The relative change of the water vapor absorption cross section σ due to a pressure shift from 1 000 mbar to 1 025 mbar. Both cross sections are calculated by using the HITRAN04 spectral line parameters, a Voigt line profile, and a temperature of 290 K. The spectral region of the 4ν water band is shown.*

Pressure Dependence

All three field measurement campaigns were conducted at the coastline and therefore at sea level. During the times of spectroscopic data acquisition the total atmospheric pressure remained within a range of 1 000 – 1 025 mbar. Two water vapor absorption cross sections are calculated for those two extremal values of pressure but for the same temperature of 290 K. A convolution with the field instrument's line shape function is performed (Acton 500 spectrograph, 0.45 nm resolution). The relative change of the water vapor cross section resulting from the applied pressure difference is shown in Figure 6.2 for the 4ν spectral region as an example. The peak to peak variation is within a range of 1.5×10^{-3}. Similar values are found for the $4\nu+\delta$ and 5ν water bands. Comparing a calculation performed for a pressure of 1 013 mbar with the calculations for the extremal values of 1 000 mbar and 1 025 mbar leads to about half the peak to peak variation as shown in Figure 6.2. This is definitely less than the instrument's detection limit of about 10^{-3}. With respect to typical peak to peak residuals found in the spectral retrievals (see, e. g., Figure 6.23), systematic errors attributed to the water absorption cross section are determined by other effects than pressure. To conclude, calculating all water vapor absorption cross sections for a pressure of 1 013 mbar is sufficient for the spectral analysis.

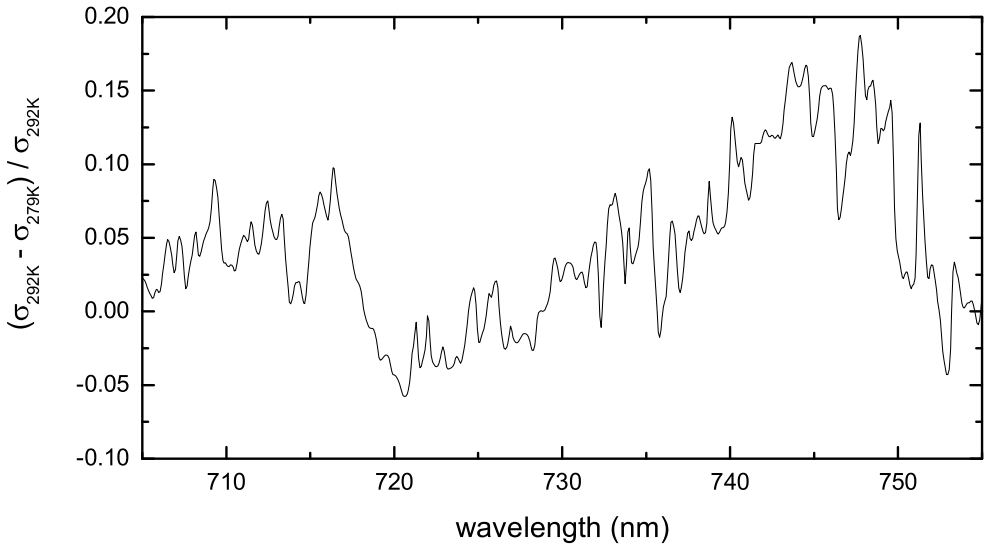

Figure 6.3: *The relative change of the water vapor absorption cross section σ due to a temperature difference of 13 K. The temperatures of 279 K and 292 K correspond to the extremes during the Dagebüll campaign. Both cross sections are calculated by using the HITRAN04 spectral line parameters, a Voigt line profile, and a total pressure of 1013 mbar. The spectral region of the 4ν water band is shown.*

Temperature Dependence

The ambient temperature range encountered at all field measurement campaigns together is $\Delta T = 29\,^{\circ}C$, with a minimum value of $4\,^{\circ}C$ and a maximum value of $33\,^{\circ}C$. However, the observed range of temperatures encountered during the times of spectra acquisition is quite moderate for each field campaign: 6 – 19 °C for Dagebüll, 10 – 21 °C for Lilia, and 25 – 33 °C for Alcântara. Does a temperature difference of some more than 10 °C significantly affect the water vapor absorption cross section?

A first estimate of the temperature's influence on the water vapor absorption cross section is performed by comparing two cross sections (HITRAN04) calculated for a temperature of 279 K and 292 K. These values correspond to the extremes of the Dagebüll campaign, showing the largest temperature range of all. Both cross sections are convolved with the field instrument's line shape function (Acton 500 spectrograph, 0.45 nm resolution). The relative change of the water vapor absorption cross sections due to the temperature difference is shown in Figure 6.3. The difference is striking – a total variation of 25% is apparent in the spectral region of the 4ν water band. This fact leads to several implications for the spectral analysis if an absorption cross section of inadequate temperature is used. In case of optically thin absorption, i. e. the analysis is performed in regions of non-saturated absorption at wavelength larger than 742 nm,

large deviations occur both in absolute value and differential structure. This not only may result in systematical errors of derived water vapor concentrations, but also may affect the detection of water dimer absorption, as the $|0\rangle_f|4\rangle_b|0\rangle$ dimer band is predicted to be located at 746 nm [*Schofield and Kjaergaard* 2003]. A large temperature dependence is evident at 749.5 nm, where a measured absorption feature is erroneously assigned to water dimers (*Pfeilsticker et al.* [2003], Section 6.6). In case of optically thick absorption, i. e. the analysis interval includes the region of strongest water vapor absorption between 715 nm and 735 nm, the differential deviations are large but oscillate around zero. This may result in large residual structures but acceptable retrievals of water vapor concentrations. In the following, the optically thick and thin cases are studied in detail for the 4ν,$4\nu+\delta$ and 5ν water polyads.

Using Lambert-Beer's law (Section 4.1.2) six absorption spectra, i. e.

$$\frac{I}{I_0}(\lambda) = \exp\big(-\tau(\lambda)\big) = \exp\big(-\sigma(\lambda)\cdot C\big)$$

are generated from the absorption cross sections corresponding to the temperatures of 280 K, 285 K, 290 K, 295 K, 300 K, and 305 K. The same water vapor column density $C = 1\times10^{24}\,\mathrm{cm}^{-2}$ is used in each case. This column density is a typical value representing the field measurements. Additionally, one water reference spectrum, i. e.

$$OD(\lambda) = -\tau(\lambda) = -\sigma(\lambda)\cdot C$$

is calculated for the temperature of 280 K. All spectra are convolved with the field instrument's line shape function (Acton 500 spectrograph, 0.45 nm resolution). The water reference spectrum is then sequentially fitted to the six absorption spectra by using the WinDoas software (see Section 4.4 for details of the fitting procedure). The program's output is the scaling factor required for the fitted reference to match the absorption spectrum at the best. The results are shown in Figure 6.4 for optically thick and optically thin absorption. As expected, fitting the reference to the absorption spectrum generated for the same temperature (280 K) yields exact agreement, i. e. a scaling factor of 1 and an error only determined by the computational accuracy. However, if the two temperatures differ, the deviation of the resulting scaling factor from 1 is an indicator for the temperature dependence. Note that the choice of the temperature used for the fitted reference spectrum is arbitrary. Any other temperature does only change the absolute values of the scaling factors but not their relative change with temperature. The following discussion is about the consequences for the spectral retrieval due to the temperature dependence of the water vapor absorption cross section.

Optically Thin Case: The above fitting procedure is performed in three wavelength intervals of unsaturated water vapor absorption at the red end of the 4ν, $4\nu+\delta$, and 5ν water band. The results are plotted in the upper panel of Figure 6.4. In each case, the

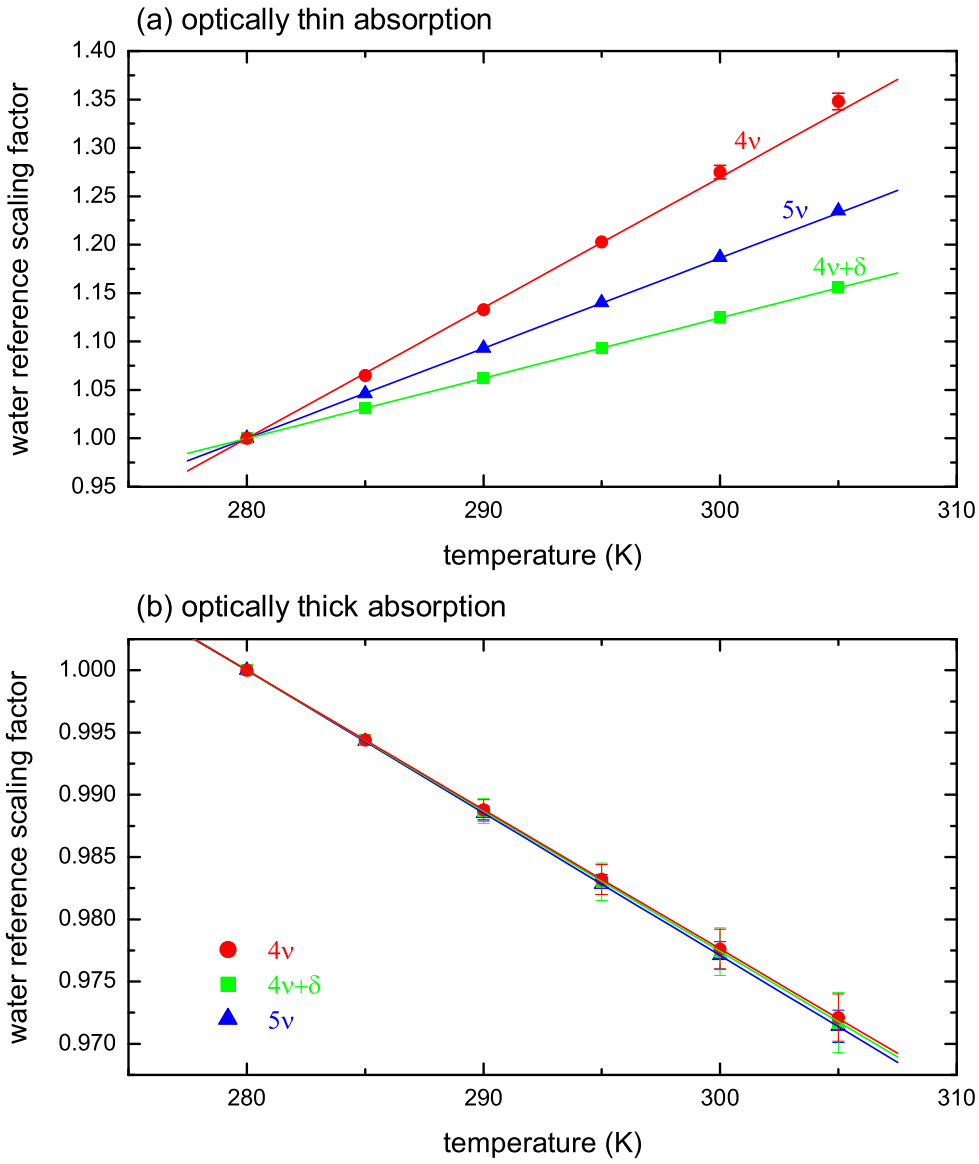

Figure 6.4: *Temperature dependence of the water absorption cross section (HITRAN04). A water reference spectrum is calculated for a temperature of 280 K and a water column density of 1×10^{24} cm^{-2}. The reference is fitted to absorption spectra generated for six different temperatures but the same water column density as used for the reference. The required water reference scaling factors are plotted (see accompanying text for details). Error bars smaller than symbol size are omitted. The lines represent linear fits to the corresponding data points.* **(a)** *The analysis is performed in spectral regions of unsaturated water vapor absorption: 744.5 – 756 nm (4ν polyad), 660.5 – 675 nm ($4\nu+\delta$ polyad), and 602 – 620 nm (5ν polyad).* **(b)** *The analysis is performed in spectral regions covering the strongest and hence highly saturated parts of absorption: 705 – 755 nm (4ν polyad), 640 – 675 nm ($4\nu+\delta$ polyad), and 560 – 620 nm (5ν polyad).*

scaling factor is almost linear in temperature and the overall deviation from unity is large. If a temperature difference of 1 K between the fitted and measured spectrum is existent, the error of retrieved water vapor concentration will be 1.4%, 0.6% and 0.9% for the 4ν, $4\nu+\delta$ and 5ν band, respectively.

There are three possibilities to account for the temperature dependence: (1) Using a cross section of correct temperature, (2) applying a temperature correction based upon the study above, or (3) using two mathematical orthogonal[2] cross sections corresponding to different temperatures. The last method is commonly used for passive DOAS of scattered skylight, for which the temperature considerably varies along the absorption path. This method is not applied in the present work, as for long path DOAS measurements the temperature of the probed air mass is assumed to be constant. The analysis is much more straightforward by using the correct absorption cross section. In practice, this is not feasible due to a large number of spectra, all of which recorded at a different temperature. Therefore, an absorption cross section of a specific temperature is used for all retrievals of those spectra recorded within ± 1.5 K. As the temperature is obtained in-situ, its variation or uncertainty along the absorption path may be assumed to be of same magnitude anyway. Nevertheless, the option of applying a temperature correction factor is used for the evaluation in the water 4ν spectral region, where the temperature dependence is most pronounced.

Optically Thick Case: The fitting procedure is performed in the strongly saturated spectral regions of the 4ν, $4\nu+\delta$ and 5ν water bands. The results are plotted in the lower panel of Figure 6.4. All three bands show an identical linear temperature dependence. The deviation from unity is small, less than 3% for a 25 K temperature range.

In order to decide how to account for the temperature dependence, the following has to be considered: The analysis in spectral regions of saturated absorption is performed by the a-priori method described in Section 4.4.2, i. e. optical depth spectra of a-priori water vapor number densities have to be used for the fitting procedure. Accounting for temperature requires to calculate a whole set of reference spectra for each temperature. Further, reference spectra have to be calculated separately for each field campaign due to different absorption path lengths. Fortunately, the temperature range observed at each field campaign is moderate. Pinning down the temperature to the mean value in each case gives a deviation of ± 6 K at maximum, corresponding to an 0.7% error in obtained water vapor concentrations. Therefore it is sufficient to fix the temperature for the analysis to one or two values.

[2]The orthogonalisation is performed by the WinDoas software.

6.3.2 Comparison of Spectral Line Databases

All water vapor absorption cross sections used within this thesis are based on the spectral line databases described in Section 4.5.1. A case study is performed to receive a first impression of their characteristics and applicability for DOAS. Thereby an insight into the key points of analyzing the field measurements and interpreting the results is provided.

The spectrum chosen for the case study was recorded in the spectral region of the 4ν water band on June 9, 2003 between 23:00 and 23:15 UTC (Lilia field campaign). The multi channel technique was applied. A total of 270 readouts was summed up, each with an integration time of less than one second due to an excellent atmospheric visibility. The ambient temperature was 16.9 °C. All following calculations are performed for exactly this temperature.

In order to calculate water vapor references, the required line parameters are extracted from each database. First, absorption cross sections as well as optical depth spectra are calculated without including any continuum absorption. Further, optical depth spectra including both water monomer and CKD_2.4.1 continuum absorption are calculated from each water database by using the RFM line-by-line radiative transfer code [*Dudhia* 2004]. Since the Bxl-Reims database is given in a format not compatible to the RFM-code, the continuum part is calculated from the HITRAN04 database. This approach is possible since the Bxl-Reims data has been implemented in HITRAN04. The CRDS-Grenoble line list is omitted in this case study due to the small wavelength coverage of only 3.7 nm.

The first part of the case study is addressed to qualitatively characterize the spectral line databases. For this purpose the analysis is performed in two spectral regions: (1) Optical depth spectra and a polynomial of first order are fitted to the measured spectrum in the spectral region of optically thick absorption (705 – 755 nm), (2) absorption cross sections and a polynomial of third order are fitted in the spectral region of optically thin absorption (744.5 – 756 nm). The results are shown in Figures 6.5 and 6.6, respectively.

Figure 6.5 shows the analysis performed in the wavelength interval covering the entire 4ν water band, therefore indicating the characterization of the strong water absorption lines. The water references based on the HITRAN2k, HITRAN04, and Bxl-Reims databases are quite similar and are in good agreement with the measurement. This is precisely what is expected due to their nature of data compilation (Section 4.5.1). Compared to those three databases, only some larger residual structures occur when the ESA-WV database is used as reference. In contrast, the Partridge-Schwenke (PS) line parameters are inadequate to describe the measured absorption, especially in the

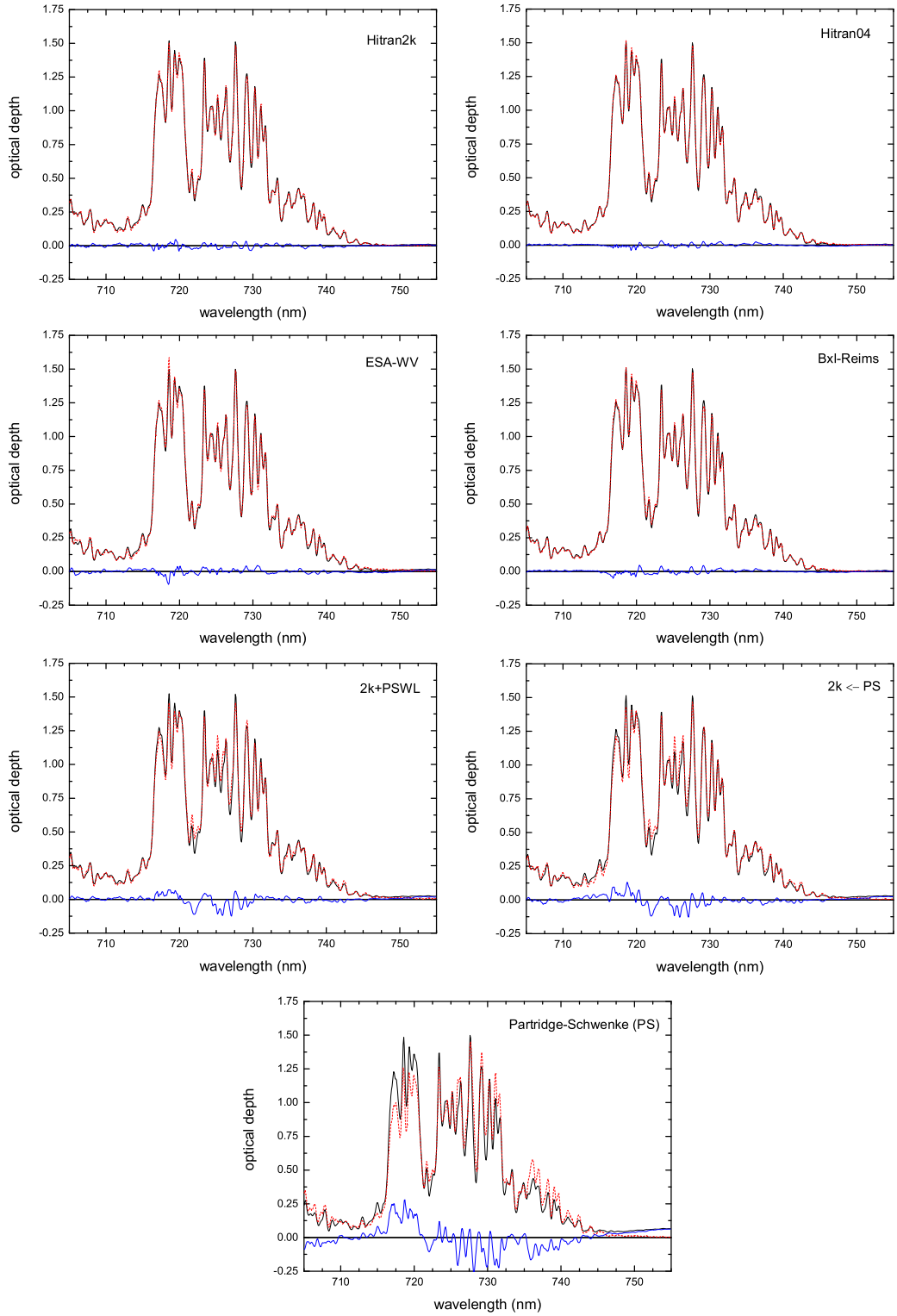

Figure 6.5: *Different spectral line databases are used as reference for the analysis of the same atmospheric absorption spectrum. The spectral interval covers the entire optically thick 4ν water band. Dashed red curve: Water vapor reference; Black curve: Measurement minus a polynomial of first order; Blue curve: Residual, i. e. measurement minus water vapor reference minus polynomial.*

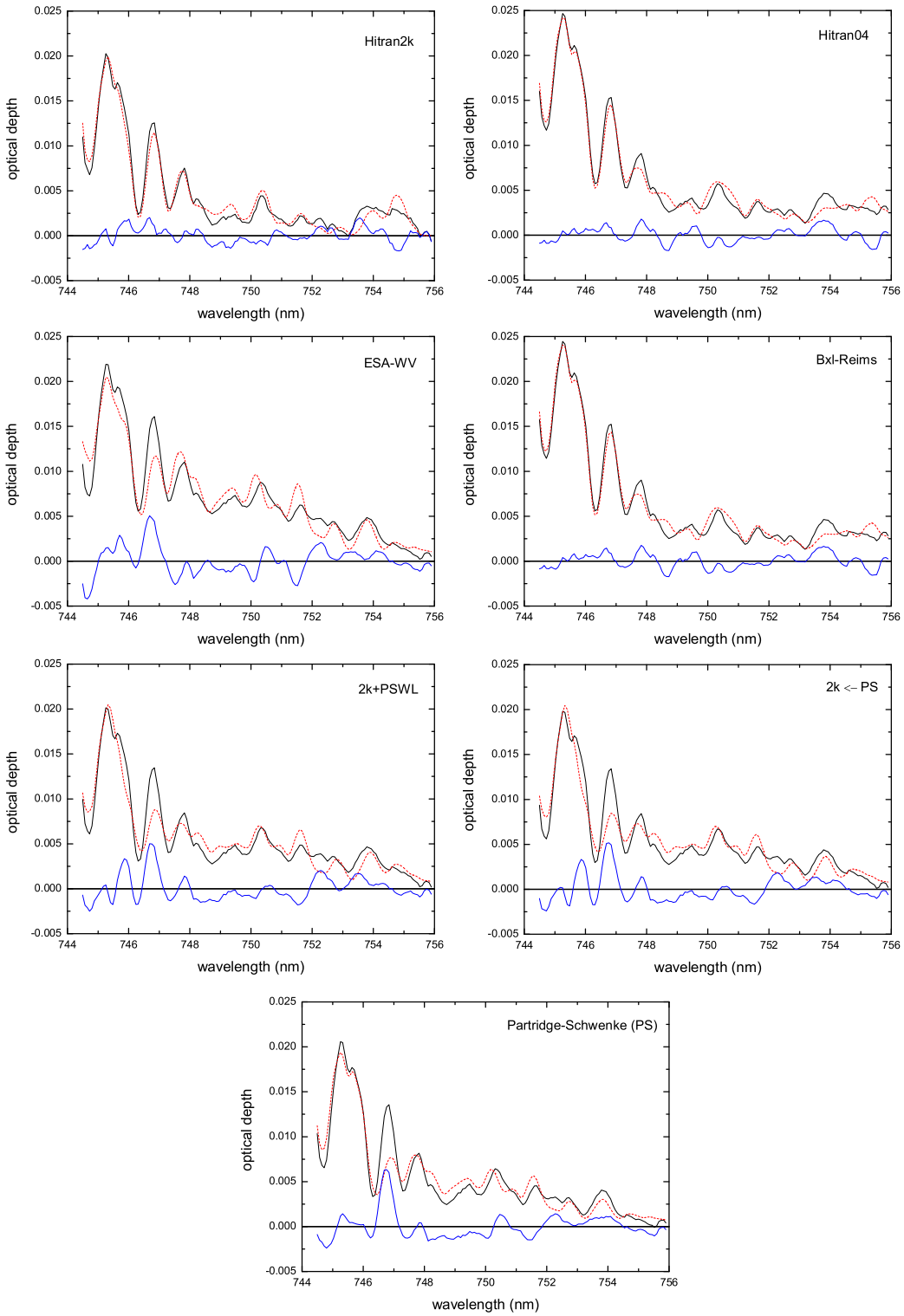

Figure 6.6: *Same as Figure 6.5 but for a spectral interval that covers the optically thin absorption at the red end of the 4ν water band. A polynomial of third order is used here.*

spectral region where water absorption is strongest: At 716 – 721 nm absorption is strongly underestimated and at 723 – 732 nm large residual structures up to 30% of the measured optical depth are evident. This indicates that the strong water lines in the Partridge-Schwenke database are large in error. *Ptashnik and Shine* [2003] carried out a study by merging the HITRAN2k and Partridge-Schwenke compilations in two slightly different ways (details are given in Section 4.5.1 or see the authors). Roughly speaking, the strong lines are represented by the HITRAN2k and the weak lines by the PS parameters. These line lists, 2k + PSWL and PS ← 2k, yield quite similar fitting results and show a considerable improvement on the PS list. The agreement with the measured spectrum however is still poor compared to the databases other than containing PS data.

Figure 6.6 shows the results when the spectral evaluation is constrained to a wavelength interval of non-saturated water absorption. Water dimer absorption is predicted to occur in this spectral region and may be observable in the atmosphere [*Schofield and Kjaergaard* 2003]. As is the case for the entire 4ν band, the HITRAN2k, HITRAN04, and Bxl-Reims databases give residuals of same magnitude and the best agreement with the measurement. Obviously, HITRAN04 and Bxl-Reims are identical. A difference between these both and HITRAN2k is evident, especially at wavelengths larger than 748 nm where water absorption becomes very weak. The ESA-WV database is the most inadequate of all, showing large residual structures across the whole spectral region. The line lists containing Partridge-Schwenke data show ambiguous behavior. For wavelengths smaller than 748 nm agreement is poor, but upwards it is quite good and the residuals are of same magnitude as those of the HITRAN-based analysis. In order to check if the PS-based analysis benefits from the inclusion of many weak lines, the evaluation should be further constrained to wavelengths larger than 748 nm and performed on spectra of higher spectral resolution.

The second part of the case study deals with the quantification of water vapor absorption. Water vapor reference spectra are calculated from the various databases. Then, the following analysis is performed: (1) In two spectral regions of optically thin absorption (742 – 756 nm and 744.5 – 756 nm), the water vapor cross section and a polynomial of third order are fitted to the measurement. (2) In the optically thick spectral region of 705 – 755 nm, water reference spectra and a polynomial of first order are fitted to the measurement, once with and once without accounting for water continuum absorption. The CKD_2.4.1 continuum model is used in this case study. The obtained water vapor number densities are shown in Figure 6.7.

The results of the evaluation performed in the 705 – 755 nm interval are discussed first. This spectral region includes the strongest part of the 4ν water band absorption. Water continuum absorption may be regarded as a smooth addition to water monomer absorption nearly two orders of magnitude less intense (Figure 6.1). Thus, the fitted

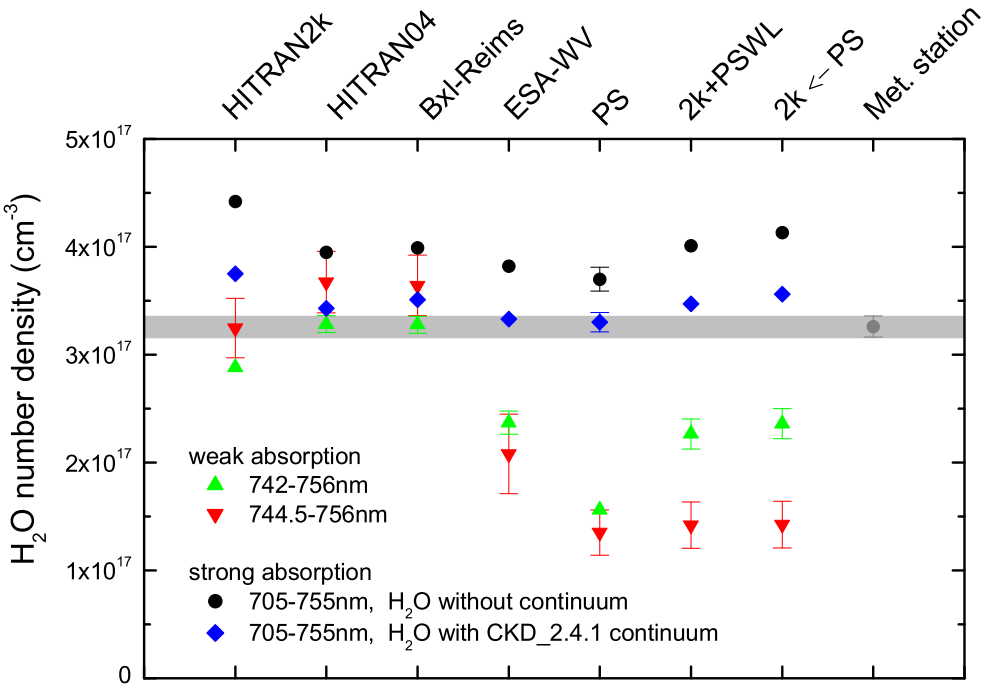

Figure 6.7: *Different spectral line databases are used as water reference for the analysis of the same atmospheric absorption spectrum. For each database four options are used for the analysis. (1) Circles: 705 – 755 nm spectral interval, water reference without continuum absorption, polynomial of first order; (2) Diamonds: 705 – 755 nm spectral interval, water reference with CKD_2.4.1 continuum absorption, polynomial of first order; (3) Upward triangles: 742 – 756 nm spectral interval, polynomial of third order; (4) Downward triangles: 744.5 – 756 nm spectral interval, polynomial of third order. The in-situ water vapor number density is also plotted. Error bars smaller than symbol size are omitted.*

polynomial is restricted to first order to avoid water continuum absorption being represented by a polynomial of higher order. Without structured absorption, both could be of similar shape.

For all databases it is obvious that there is a systematic shift to lower water vapor number densities when continuum absorption is included in the analysis. This shift is significant, since the resulting statistical errors are negligible. If neglecting continuum absorption, the obtained number densities are by a factor of 0.12 – 0.18 higher than including continuum absorption. The other way round, this leads to the conclusion that 12 – 18% of the total absorption is due to the water vapor continuum. Whether or not continuum absorption is included, the water vapor number densities derived in the spectral region of 705 – 755 nm depend evidently on the used water reference. For an assessment which of the databases gives the best actual water vapor concentration, further information is required. Such information is provided by the meteorological data. However, as this is an in-situ measurement and the spectroscopy averages along the

absorption path, the meteorological data can only give an indication of the water vapor concentration along this path. The water vapor in-situ measurement is also plotted in Figure 6.7. Clearly, the results obtained by including water continuum absorption are supported by the in-situ measurement. Further information is provided by the spectroscopy of water vapor absorption itself. The key point for the analysis is to choose a narrow spectral region where first, water absorption is not saturated and second, continuum absorption is a smooth monotone function. Then, the absorption cross section may be fitted directly and the polynomial accounts for water continuum absorption. The results corresponding to the spectral intervals of 742 – 756 nm and 744.5 – 756 nm are shown by the green and red data in Figure 6.7, respectively. As expected, the statistical error is larger when some of the spectral interval is truncated at the blue side, towards which the water absorption is increasing. By comparing those water number densities with the in-situ data and the previous spectral analysis in the 705 – 755 nm interval, three groups of data can be discerned: (1) HITRAN2k, HITRAN04, Bxl-Reims: The results of both narrow intervals are consistent and in good agreement with the other data; (2) ESA-WV, PS: The results of both narrow intervals are consistent but far off the other data; (3) 2k + PSWL, PS ← 2k: All data is inconsistent.

To draw a first conclusion, using water references based on the HITRAN04 compilation (this includes Bxl-Reims), the results are in very good agreement with the in-situ measurement, the spectroscopy, and the CKD_2.4.1 continuum model. The precursor database HITRAN2k gives some less good agreement. Especially the evaluation performed across the entire 4ν water band yields an evident offset to both in-situ measurement and narrow-band spectroscopy. The second conclusion is, that the water line parameters listed in the ESA-WV and Partridge-Schwenke databases are inadequate to describe the observed water vapor absorption in the 742 – 756 nm and 744.5 – 756 nm intervals. Although over those intervals there are consistent results, the retrieved water vapor concentrations are unrealistic when compared to the more reliable data obtained by the entire 4ν spectroscopy and the in-situ measurement. However, these databases seem to be adequate for the quantification of water vapor concentrations considering the whole 4ν band.

Recapitulating the conclusions drawn from this case study, it can be ascertained that the HITRAN04 database together with the CKD parameterization of water continuum absorption yields the best characterization of water vapor absorption in the 4ν band. Since only one atmospheric spectrum was chosen as an example for the measurements, the findings have to be verified. However, this case study provides a first insight into the spectral analysis, which is the scope of the next sections.

6.4 Water Monomer Absorption

In order to detect and quantify atmospheric water continuum and water dimer absorption, the knowledge of the exact water vapor concentration averaged along the absorption path is required. Unfortunately, it is not possible to monitor the water vapor concentration on various positions along the entire path as it is possible for laboratory experiments. Only one in-situ measurement carried out at one end is available. This measurement gives only an indication of the true water vapor content along the absorption path. However, further information of the actual atmospheric water vapor content is provided by the spectroscopy itself. If the spectral region in the analysis procedure is chosen well, water vapor number densities can be obtained regardless of a superimposed water continuum absorption. As already carried out within the previous case study (Section 6.3.2), the analysis has to cover a wavelength interval where water monomer absorption is not saturated and water continuum absorption shows a smooth monotone behavior. These requirements are satisfied at the very red end of the studied 4ν, $4\nu+\delta$ and 5ν water band.

Within the previous case study water databases are tested for their suitability to provide water reference spectra for the analysis in the 4ν water band. It emerged that the water reference based on the HITRAN04 compilation gives the most consistent results, both regarding the quality of the fit and the quantification of water absorption. The analysis procedure performed in the case study is revised for further spectra. It turns out that the results obtained in the case study are representative. For example, derived water number densities in the 744.5 – 756 nm spectral interval are smaller by a factor of 1.5 when the ESA-WV and by a factor of 3 when the Partridge-Schwenke databases are used instead of HITRAN04.

This section is addressed to characterize water monomer absorption in non-saturated regions of the 4ν, $4\nu+\delta$ and 5ν water bands, whereas exclusively the HITRAN04 water absorption cross section is used.

6.4.1 Spectral Intervals for Analysis

Concerning the wavelengths where water vapor line saturation occurs, the campaigns conducted in the tropics and mid-latitudes have to be considered separately, since the typical water optical depths differ by a factor of 3 (water concentration → factor 2, absorption path length → factor 1.5). By choosing the analysis intervals at the red end of each water band, line saturation determines the lower limits of these intervals. In order to check these limits, high resolution optical depth spectra for the tropics ($n_{H_2O} = 7 \times 10^{17}\, cm^{-3}$, $L = 29\, km$) and the mid-latitudes ($n_{H_2O} = 3.5 \times 10^{17}\, cm^{-3}$, $L = 19\, km$) are calculated. Based on the curve of growth given in Figure 4.2, linearity in absorption is assumed for optical depths smaller than approximately 1 – 2. This

Table 6.1: *Wavelength intervals for the spectral analysis in regions of non-saturated water vapor absorption at the red end of the respective water polyad. In the mid-latitudes no measurements were carried out in the region of the 5ν water band.*

	4ν	$4\nu+\delta$	5ν
Tropics	744.5 – 756 nm	663 – 675 nm	602 – 620 nm
Mid-latitudes	742 – 756 nm	660.5 – 675 nm	

leads to the determination of the analysis intervals as listed in Table 6.1. These intervals are also roughly illustrated in Figure 5.2. To achieve the best signal to noise ratio the intervals should be expanded as far as possible towards the water band. Therefore, different intervals are given for the tropics and mid-latitudes. The upper limits are determined by further water vapor and oxygen bands.

Considering the 4ν water band as an example, the effect of line saturation is illustrated in Figure 6.8, showing the correlation of the water number densities obtained from the analysis in both the 742 – 756 nm and 744.5 – 756 nm interval. Obviously, absorption gets into saturation below 744.5 nm for the conditions prevalent in the tropics. In the additional wavelength interval of 742 – 744.5 nm six individual water lines of optical depths within the range of $2 \leq \tau \leq 4$ are present for the tropics, but only one line of $\tau \approx 1$ for the mid-latitudes. Even for the mid-latitude measurements saturation possibly can be assumed for the spectra corresponding to higher water number densities. Note that the deviation from a linear absorption is characterized by a slope smaller than 1 and not by an offset to one-to-one correlation but the same slope. The latter would indicate systematic effects like an inaccurateness in the water line database.

6.4.2 Water Vapor Number Densities

Water vapor number densities are derived from the spectral evaluation in the wavelength intervals given in Table 6.1. From the intercomparison of these results obtained from different analysis intervals, their suitability for the water vapor retrieval can be checked. It is further possible to detect inaccuracies existing in the HITRAN04 database. A comparison with the in-situ measurement also provides an indication of its data reliability. Although the DOAS measurements cannot be performed simultaneously in two or more different wavelength regions, it is sufficient for the intercomparison if the spectra are recorded within adequate time, i. e. the ambient conditions do not change significantly.

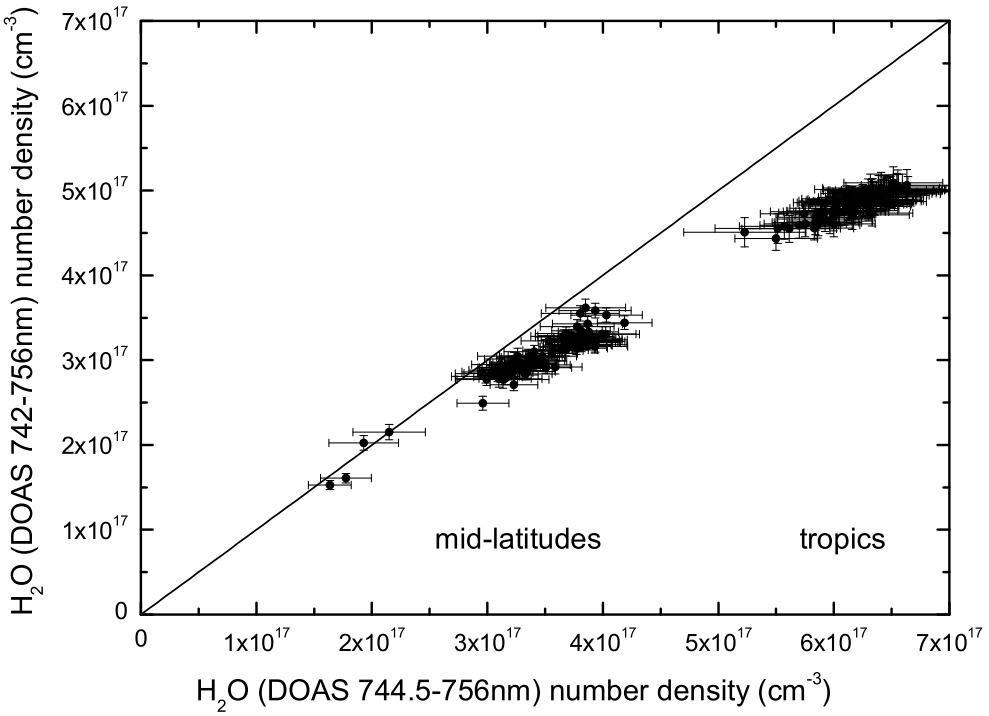

Figure 6.8: *Correlation of the water vapor number densities obtained from the spectral analysis in the wavelength intervals of 742 – 756 nm and 744.5 – 756 nm. The data includes all measurements given in Figure 6.11. The diagonal line corresponds to one-to-one correlation.*

During the tropical field campaign spectra were recorded in all three water bands: 4ν, $4\nu{+}\delta$ and 5ν. These spectra are evaluated in the wavelength intervals of non-saturated absorption as given in Table 6.1. Besides the water vapor reference and a polynomial of third order, NO_2 (cross section by *Vandaele et al.* [2002]) and NO_3 (cross section by *Sander* [1986]) are fitted in the $4\nu{+}\delta$ and 5ν regions; O_3 (cross section by *Anderson and Mauersberger* [1992]) is fitted in the 5ν region. The results are shown in Figure 6.9 for those times when measurements were carried out alternately in all three water bands. Some further data is also available but not shown here – the results are very similar. One time series is given for the measurements performed with and one without applying the multi channel technique (MCT). In case of using the MCT, spectra are available at about one hour temporal resolution, since the MCT combines 9 individual measurements in only one final spectrum (see Section 4.3). However, an intercomparison of the MCT-results corresponding to the different analysis intervals is possible, as the change in ambient conditions in a tropical climate is slow. It is evident from Figure 6.9 that there is very good agreement within all spectroscopic results obtained in the three different wavelength regions. Additionally, the in-situ measurement yields similar values too. Only an offset to slightly higher values can be

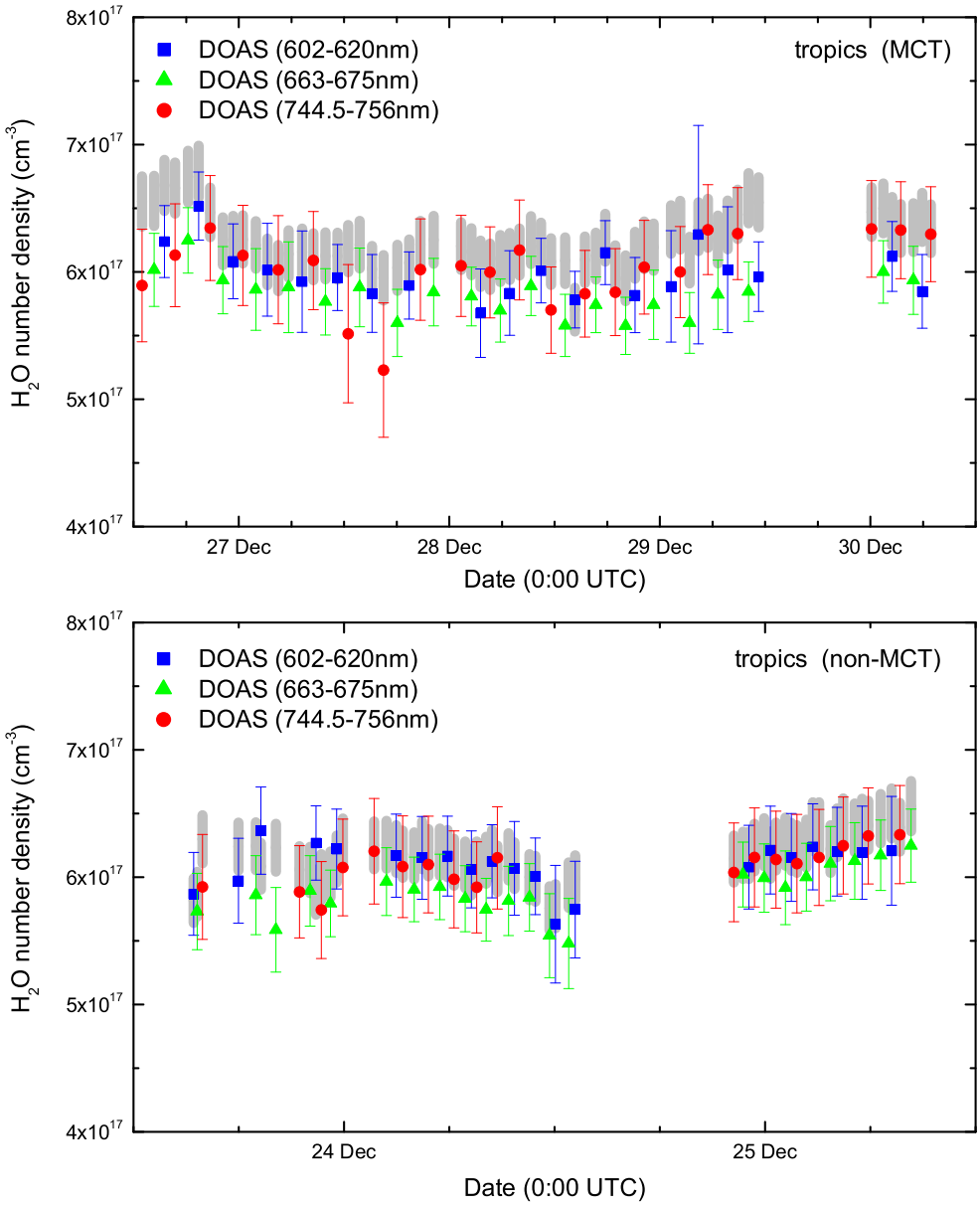

Figure 6.9: *Time series of water vapor number densities for the field campaign carried out in Alcântara, Brazil. The results are obtained in three spectral regions from the analysis of individual measurements covering either the 5ν (blue symbols), the 4ν+δ (green symbols) or the 4ν (red symbols) water band. The in-situ measurement is indicated by the shaded area.*

discerned. The consistency of the results justifies the choice of the spectral intervals used for the evaluation. It also indicates that the HITRAN04 database is adequate for obtaining water number densities in those three spectral regions, unless there occurs the same unidentified systematic error in all of them.

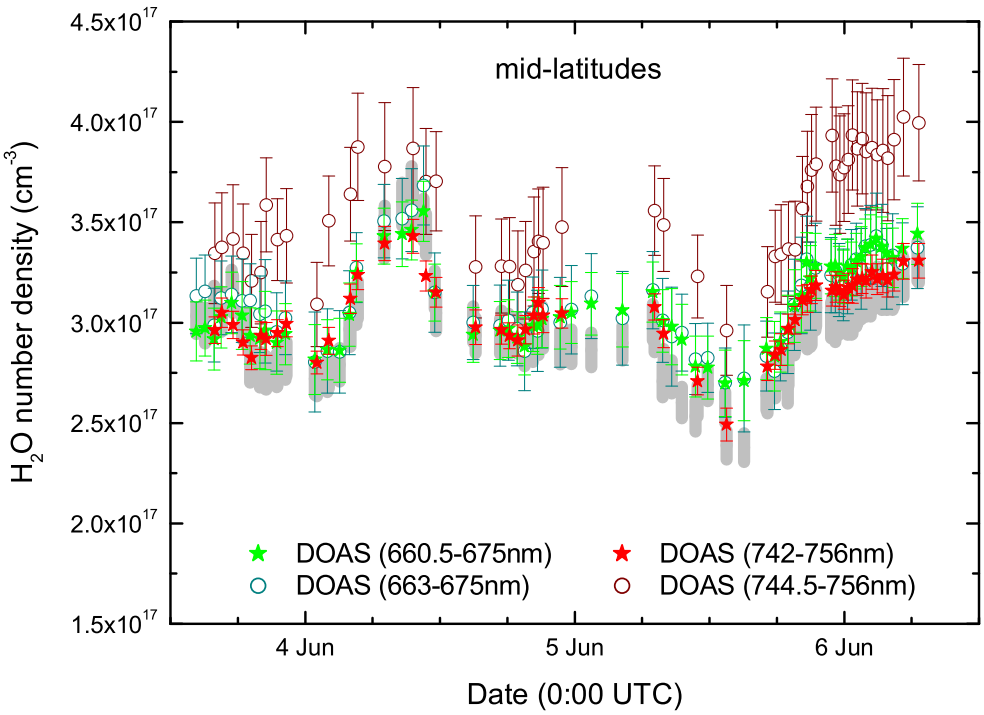

Figure 6.10: *A time series of water vapor number densities for the field campaign conducted in Lilia, Brittany. The results are obtained in four spectral regions from the analysis of individual measurements covering either the $4\nu+\delta$ (green symbols) or the 4ν (red symbols) water band. The in-situ measurement is indicated by the shaded area.*

During both field campaigns carried out in the mid-latitudes, spectra were recorded in the 4ν and $4\nu+\delta$ water bands. Most of the data was acquired during the second campaign held in Lilia. The spectra are evaluated in four wavelength intervals of non-saturated water vapor absorption. Besides the water reference and a polynomial of third order, NO_2 (cross section by *Vandaele et al.* [2002]) and NO_3 (cross section by *Sander* [1986]) are fitted in the $4\nu+\delta$ region. The results are shown in Figure 6.10 for all times when measurements were carried out alternately in the 4ν and $4\nu+\delta$ spectral regions. A good temporal resolution is achieved, since the multi channel technique is not applied.[3] Comparing the results obtained from the analysis in the wavelength intervals of 660.5 – 675 nm and 742 – 756 nm (designated by the star symbols in Figure 6.10) shows very good agreement. These results are also consistent with the in-situ measurement, which is only slightly shifted to smaller values. Further, water monomer absorption in the wavelength intervals as used for the tropical campaign (663 – 675 nm and 744.5 – 756 nm) is checked. Comparing both time series corresponding to the $4\nu+\delta$ retrievals (green symbols in Figure 6.10), the results are in excellent agreement – the smaller analysis interval only gives some larger errors. In the case of the 744.5 – 756 nm

[3]For the mid-latitude campaigns, only a few MCT-spectra in the 4ν water band region are available

analysis interval, the errors of the spectral fit are large, probably due to the weak water absorption together with poorly characterized line parameters. In addition, derived water number densities are larger with respect to the other data. This fact is also seen in the correlation plot given by Figure 6.8. Due to the consistency of the further spectroscopic and in-situ results, the observed offset may indicate a systematic effect caused by inaccuracies in the water database used. Water vapor continuum absorption, which is not explicitly considered in the retrieval, cannot cause the offset. First, water continuum absorption is a smooth monotone function which is accounted for by the fitted polynomial. Second, water continuum absorption should appear more pronounced in the 742 – 756 nm spectral interval. This interval reaches farther towards the 4ν water band where water continuum absorption is stronger. The observed offset is possibly caused by water dimer absorption. In fact, the omission of water dimer absorption in the analysis should emphasize discrepancies for the 744.5 – 756 nm spectral interval, as water monomer absorption is less intense there. However, the consistency in the results of the tropical campaign (Figure 6.9) does not support the water dimer option.

To draw a conclusion, the wavelength intervals given in Table 6.1 are suitable for the spectral retrieval of water number densities. By the application of spectroscopy to those spectral intervals, all results are self-consistent. Additionally, the acceptable agreement with the in-situ data indicates that the water vapor concentration along the absorption path is well represented by the in-situ measurement. This is precisely what is expected due to absorption paths almost completely above water. Further, many measurements were carried out during nighttime when no solar radiation and therefore selective heating or evaporation above ground and water is present.

6.5 Water Continuum Absorption

Within Section 6.3.2, the fundamental analysis technique of water vapor continuum absorption is introduced on the basis of a case study. There, water databases are checked for their suitability to provide water references for the spectral analysis in the region of the 4ν water band. It turned out that the water line parameters compiled in HITRAN04 give the best results for the spectral evaluation, both regarding the quality of the fit and the quantification of water absorption. As already stated in the previous section, the results obtained in the case study are representative. Hence, the HITRAN04 database is used exclusively for calculating water vapor references for the analysis of all field measurements. Additionally, the study of water continuum absorption is expanded to the $4\nu+\delta$ and 5ν water bands.

To summarize the analysis technique, the water number density is derived for each individual absorption spectrum by two basically different methods: First, in a wave-

length interval covering the entire polyad, water reference spectra including continuum absorption based on the different models are fitted successively to the measured atmospheric spectrum. Second, in a wavelength interval of non-saturated absorption (Table 6.1), the water absorption cross section is fitted to the measurement. The used interval here is always located at the very red end of the respective polyad. The key point of the analysis procedure is the fact, that in the first case the retrieval depends on water continuum absorption but in the second case it should not, as the analysis interval is narrowed to a spectral region where the water continuum spectrum is similar in shape to a monotone low order polynomial. All continuum-like parts of extinction, e. g. scattering and the water continuum, are removed by the fitted polynomial. The intercomparison of water number densities obtained for the same spectrum from both analysis methods as described above, provides information about possible water continuum absorption. The in-situ water concentration is further available for comparison.

Performing the spectral analysis across an entire water band requires water optical depth spectra as references. The details of the analysis procedure are described in Section 4.4. Four different types of reference spectra are calculated: (1) Considering only water monomer absorption, i. e. omitting any kind of water continuum absorption. As before, these spectra are calculated directly from the HITRAN04 water absorption cross section. (2) Including water continuum absorption as predicted by the Ma and Tipping far wing line shape theory. Water line and continuum contributions are calculated separately from the HITRAN04 absorption cross section and the continuum coefficients for self- and foreign-broadening [*Ma*, pers. comm.]. The calculation is performed in terms of an empirical relation [*Varanasi and Chudamani* 1987; *Cormier et al.* 2002]. (3) Including water continuum absorption based on the semi-empirical CKD_2.4.1 and (4) the semi-empirical MT_CKD_1.0 model. In both cases reference spectra are calculated by using the RFM line-by-line radiative transfer code [*Dudhia* 2004].

Since the absorption path length is required for calculating optical depths, a set of reference spectra[4] has to be generated separately for each field campaign. Further, the calculations are repeated for several temperatures differing by about 3 – 5 °C as far as required for the respective campaign. This subdivision into small temperature intervals is adequate to account for a temperature dependence, so no further correction has to be applied (Section 6.3.1).

For all retrievals covering the spectral region of an entire water polyad, the fitted polynomial is restricted to first order to avoid water continuum absorption being represented by the polynomial.

In the wavelength intervals where absorption is not saturated, the analysis procedure is straightforward for LP-DOAS measurements: The result of the spectral fit directly

[4]Each set consists of several reference spectra with a different a-priori water vapor concentration

gives the column density, which can be easily converted into the number density due to the exact knowledge of the absorption path length (Section 4.1.3). The required water absorption cross section as input data is calculated from the HITRAN04 database by using the *HitranVoigt* software tool (Section 4.5.3). Since the water absorption cross section strongly varies with temperature, the cross section calculated for the correct temperature should be used for each individual measurement (Section 6.3.1). In practice, cross sections are calculated for some temperatures differing by 3 – 5 °C, therefore the difference to the condition prevalent at the time of measurement is only a few degrees. Nevertheless, a temperature correction based on the study described in Section 6.3.1 is applied. For all retrievals in the weakly absorbing spectral regions, a polynomial of third order is fitted to account for scattering and continuum absorption.

6.5.1 Water Vapor 4ν Band

Absorption spectra in the region of the 4ν water band were recorded during all three field measurement campaigns, both with and without applying the multi channel technique (MCT, for details see Section 4.3). Comparing three water continuum models and pure water monomer absorption, the spectral evaluation is first performed in the 705 – 755 nm interval, which covers most of the 4ν water band (see Figure 6.5). Additionally to the water reference spectrum, a polynomial of first order is fitted. No further absorbers have to be taken into account. A second evaluation is carried out in a spectral interval of non-saturated water absorption at the red end of the 4ν water band. The choice of that interval is based on the study given in Section 6.4: 742 – 756 nm for the mid-latitudes and 744.5 – 756 nm for the tropics. An example of the spectral retrieval for the latter is shown in Figure 6.6. No further absorbers have to be considered. A polynomial of third order is used to account for scattering and continuum absorption. For all fitted water references a shift and first order stretch in wavelength is allowed.

The analysis results of the 4ν water vapor spectra acquired during all three field campaigns are illustrated in Figure 6.11. Although no time series to scale but only a chronological enumeration is shown, arrangements in groups can be discerned. Evidently, the data resulting from the campaigns carried out in the mid-latitudes and the tropics can be distinguished by the magnitude of the derived number densities. In the upper panel of Figure 6.11, showing the results of the spectra recorded in multi channel mode, all three field campaigns are represented. Dagebüll: The first eight data points, recorded on April 27, Mai 10, Mai 12 and Mai 14, 2002; Lilia: The two further groups of the mid-latitude data set, recorded on June 10 and June 12, 2003; Alcântara: Several groups recorded during the time between December 26, 2004 and January 12, 2005. In case of not applying the MCT as shown by the lower panel of Figure 6.11, the data can roughly be considered as a time series (compare with Figure 6.10): The data of the

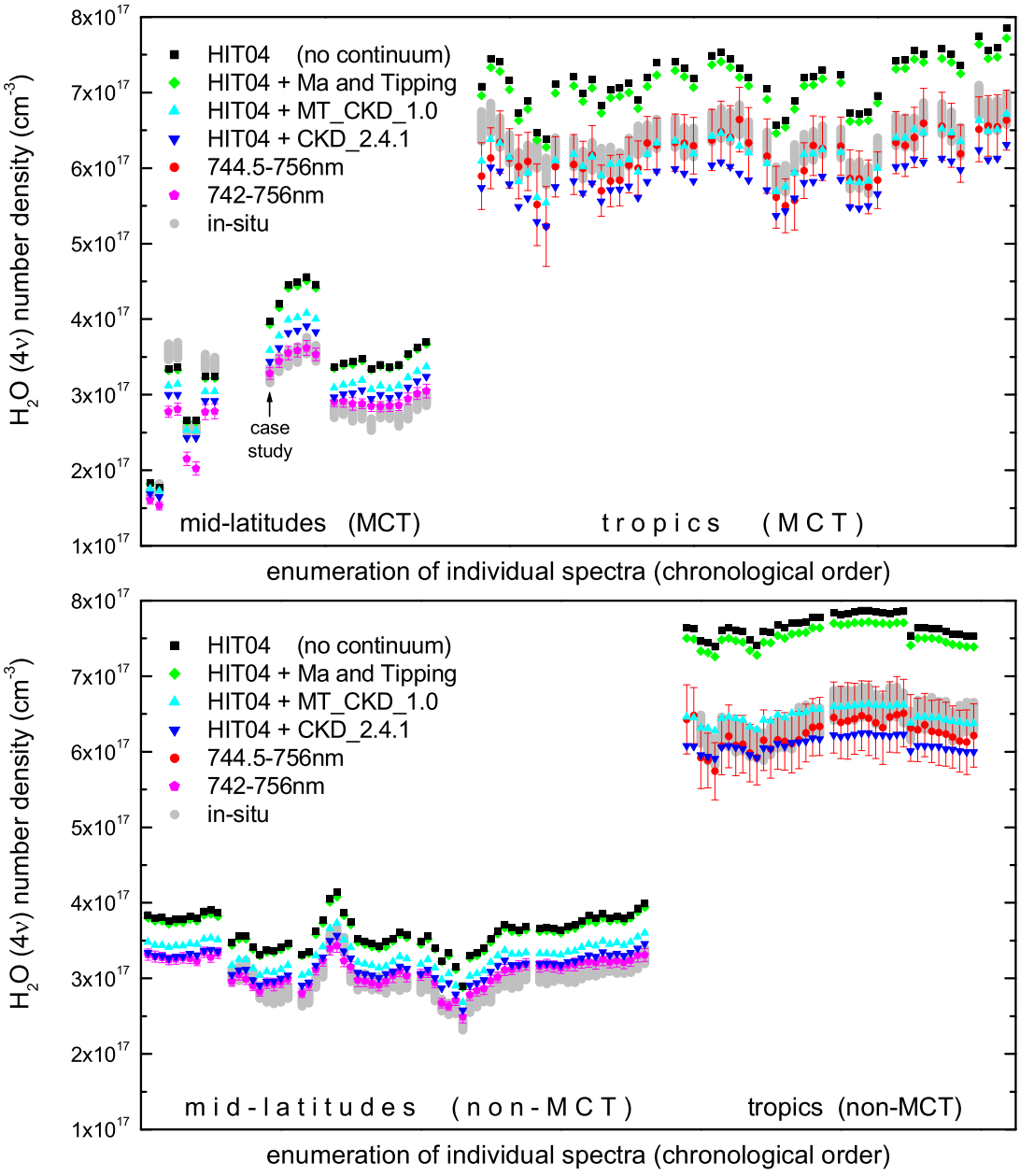

Figure 6.11: *Water vapor number densities obtained from the spectral analysis in the 4ν water band. The upper panel shows the results from spectra recorded with the multi channel technique (MCT) and the lower panel without. Comprising the measurements of all field campaigns, individual spectra are simply enumerated in chronological order but not to scale. Each individual spectrum is analyzed repeatedly in the indicated wavelength regions and by considering different water continuum models. The evaluation applied to the entire 4ν water band yields statistical errors smaller than symbol size. All water reference data is based on HITRAN04. The in-situ water vapor concentration is indicated by the shaded area. The spectrum chosen for the case study performed in Section 6.3.2 is marked.*

mid-latitudes acquired during the Lilia campaign[5] between June 2 and June 6, 2003; The data of the tropics recorded on December 24 through 25, 2004 for the first group[6] and on December 26, 2004 for the second group.

Apparently, the data series corresponding to the different analysis methods and continuum models are offset to each other but follow the same trend, a trend which is also seen in the in-situ data. This indicates systematic effects. Regarding the four series of analysis considering the entire 4ν spectral region, the uniformness of the offset is remarkable. Those results are highly reliable since the statistical error of the fit is typically smaller than 1% due to the strong and extremely structured water vapor absorption. Omitting the water continuum always gives the highest water vapor number densities. By additionally accounting for water continuum absorption the obtained water vapor concentrations are lower. For the Ma and Tipping theory, the difference is small but significant, for both CKD-based continuum models the difference is substantial. In summary, by additionally accounting for water continuum absorption the obtained water vapor number densities are decreasing as the magnitude of the continuum part of absorption is increasing. The reasons are: First, the overall water optical depth is given by the sum of the local line and the continuum contribution. The former is equal for all four fitted water references, regardless of the continuum model used. Second, both the water monomer and continuum absorption show a similar large scale structure, only differing in absorption strength (Figure 6.1). This smooth large scale structure cannot be mimicked by the fitting polynomial of first order. If continuum absorption occurs in the atmosphere, a missing water continuum in the fitted reference has to be compensated for by a larger water line contribution. Therefore, the resulting water number densities are too high. The other way round, if no continuum absorption occurs in the atmosphere, a water continuum contribution included in the reference compensates for some part of the water line absorption, hence resulting in water number densities too low. In order to figure out which way is the correct one, further information of the actual water vapor content is required. This information is provided by the in-situ measurement or the spectroscopy corresponding to the intervals of non-saturated water absorption.

For the analysis in the spectral regions of non-saturated water vapor absorption, the wavelength interval is set to 742 – 756 nm for the mid-latitude measurements and 744.5 – 756 nm for the measurements in the tropics (Section 6.4). These results are compared with the corresponding data obtained from the entire 4ν water band spectroscopy. Although the measurement series shown in Figure 6.11 give an indication of this intercomparison, more appropriate to this task is the illustration given by Fig-

[5]The meteorological data is missing for the first day due to a failure of the weather station
[6]The first two spectra are recorded earlier; at that time no in-situ data is available.

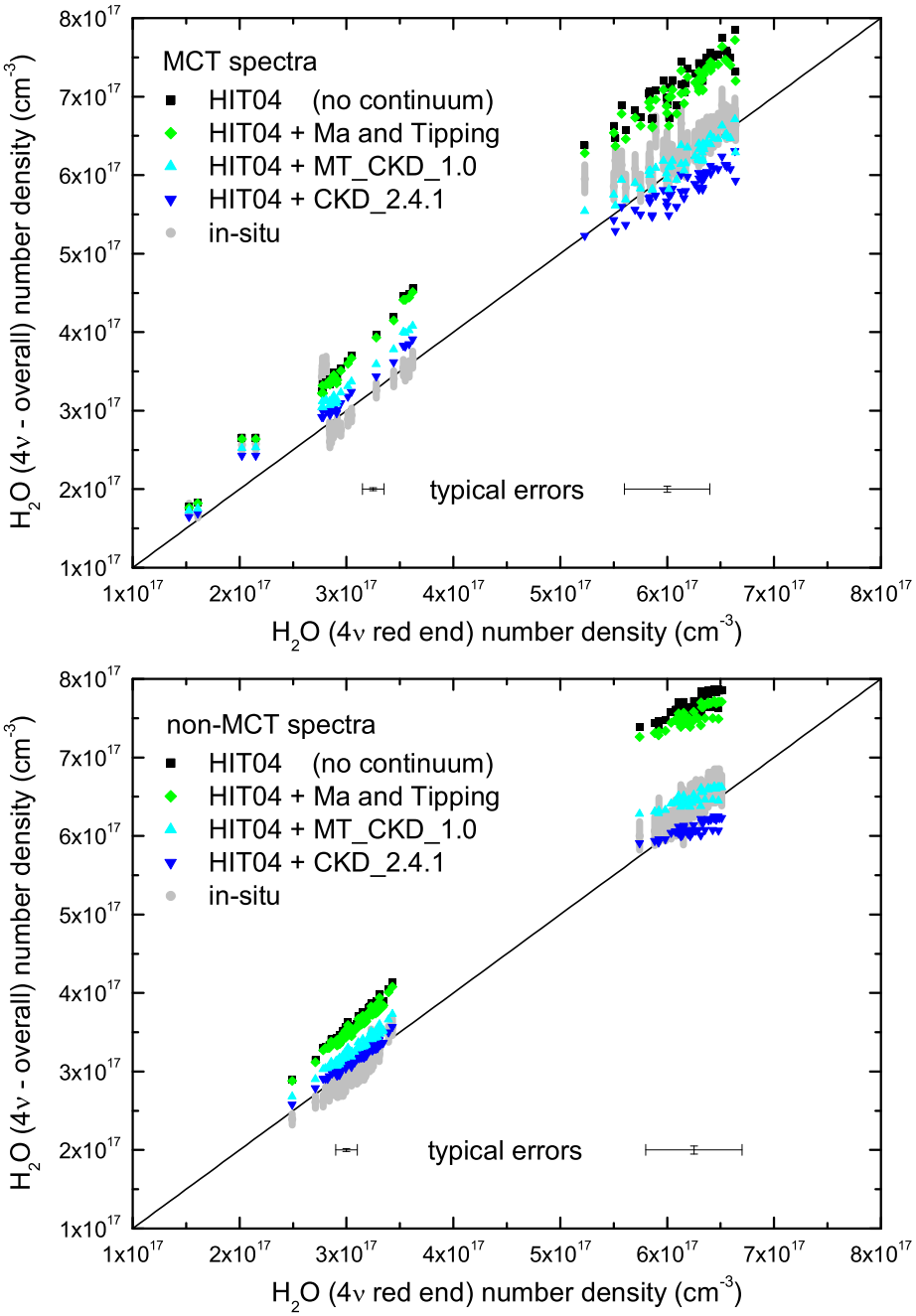

Figure 6.12: *The correlation of water vapor number densities obtained by two fundamentally different analysis procedures: (x-axis) Spectral analysis applied to a wavelength interval at the red end of the 4ν water band where water continuum absorption is negligible; (y-axis) Spectral analysis applied to the entire water 4ν band where water continuum absorption is of importance. The upper plot shows the measurements with applying the multi channel technique (MCT), the lower plot without. Instead of assigning error bars to each data point, a typical statistical error is given at the bottom, separately for the data groups representing the measurements performed in the mid-latitudes and in the tropics. The diagonal lines correspond to one-to-one correlation.*

ure 6.12. The correlation of derived water vapor number densities is shown when first, the analysis is applied to the entire 4ν water band, and second, the analysis is applied to the narrowed spectral region at the red end of the 4ν polyad. In the first case continuum absorption affects the analysis results, but in the second case it does not. Assuming ideal measurements and an ideal analysis procedure, the results would yield one-to-one correlation if water continuum absorption is correctly accounted for.

The results are given separately for the measurements performed with and without applying the multi channel technique. Although the MCT-results are considered more reliable due to the more sophisticated measurement technique [*Knoll et al.* 1990; *Brauers et al.* 1995], no significant difference is recognized. All measurements clearly support the semi-empirical CKD water continuum models. However, the results obtained from CKD_2.4.1 and MT_CKD_1.0 are ambiguous. The measurements carried out in the tropics somewhat favor the revised MT_CKD_1.0 model. This is also supported by the in-situ data. On the other hand, the measurements conducted in the mid-latitudes favor the CKD_2.4.1 model. However, taking into account the measurement errors it cannot be concluded which one of both semi-empirical models is superior. Concerning the Ma and Tipping far wing theory, the results are close to those with no continuum absorption included. For these two analysis series the difference in water number density is small but significant and it is more pronounced for the tropical data due to the higher water concentration. As the water monomer plus Ma and Tipping continuum yields water number densities too high to be in agreement with both the spectroscopy in the weakly absorbing intervals and the in-situ data, the predicted water continuum absorption based on the Ma and Tipping far wing theory is considerably too small.

6.5.2 Water Vapor $4\nu+\delta$ Band

Absorption spectra in the region of the $4\nu+\delta$ water band were recorded during all three field campaigns. However, the few spectra of the Dagebüll campaign are not further considered in the analysis. The spectral evaluation in various weakly absorbing regions yield inconsistent results, probably caused by noisy Xenon lamp reference spectra owing to the inadequate recording technique used at Dagebüll (see Secton 4.2.6). Concerning the other field campaigns, the multi channel technique was only applied to a part of the measurements performed in Alcântara.

The analysis procedure is conform with the previous one used for the 4ν water band. Water continuum and water monomer absorption are considered in the spectral evaluation covering the entire $4\nu+\delta$ water band. The analysis interval is set to 640 – 675 nm. Besides water vapor additional absorbers are considered: NO_2 (cross section by *Vandaele et al.* [2002]), NO_3 (cross section by *Sander* [1986]) and O_4 (cross section by *Greenblatt et al.* [1990]). Further, a polynomial of first order is fitted to the measurements. In the spectral region of non-saturated water absorption at the red end of

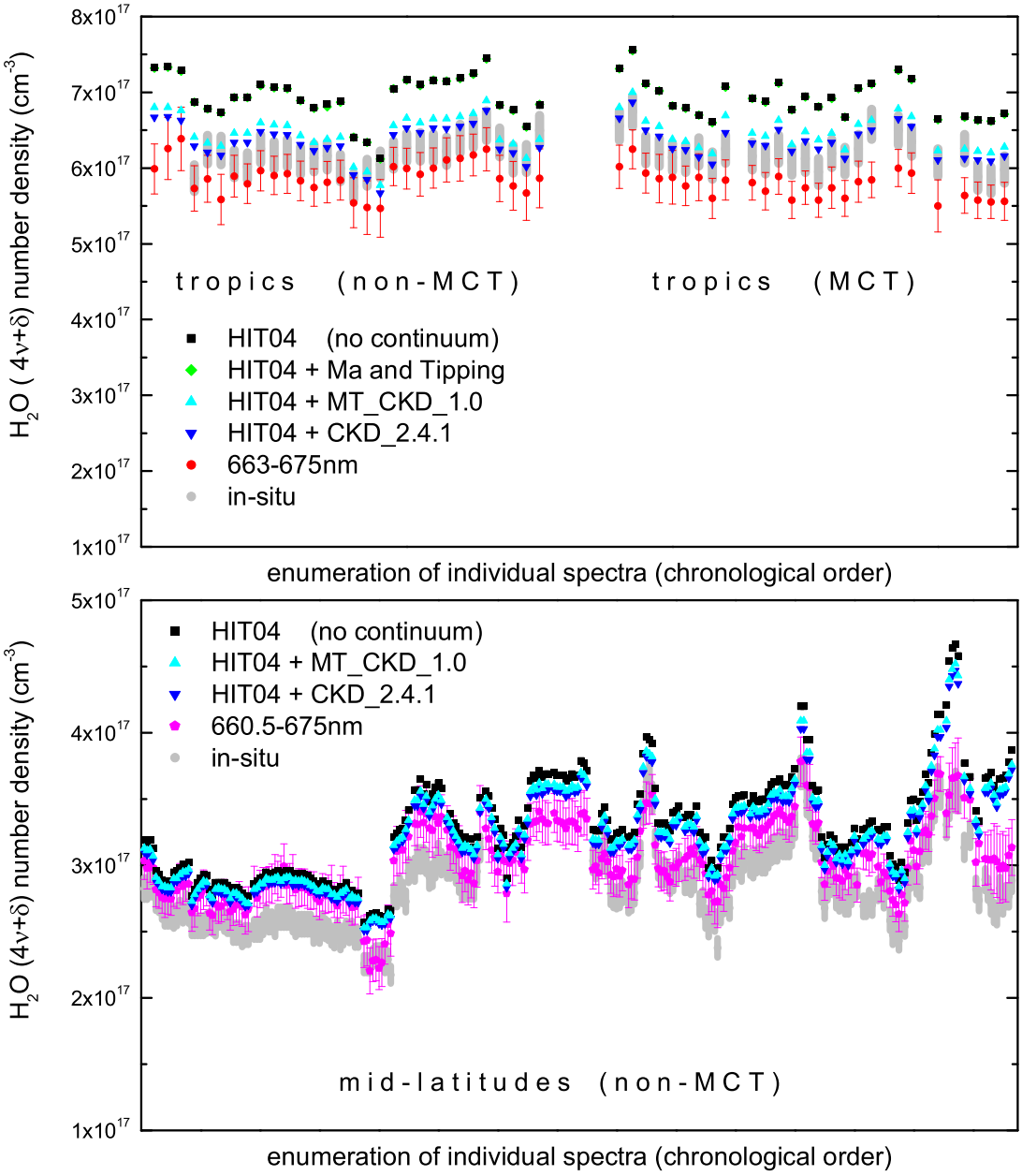

Figure 6.13: *Water vapor number densities obtained from the spectral analysis in the $4\nu+\delta$ water band. The upper panel shows the measurements performed in Alcântara, Brazil and the lower panel the measurements carried out in Lilia, Brittany. The individual spectra are simply enumerated in chronological order but not to scale. Each individual spectrum is analyzed repeatedly in the indicated wavelength regions and by considering different water continuum models. For the mid-latitude measurements the Ma and Tipping results are not shown as they are almost identical to those without continuum absorption. The evaluation applied to the entire $4\nu+\delta$ water band yields statistical errors smaller than symbol size. All water reference data is based on HITRAN04. The in-situ water vapor concentration is indicated by the shaded area.*

the $4\nu+\delta$ band, the evaluation is carried out in the wavelength intervals given in Section 6.4: 660.5 – 675 nm for the mid-latitudes and 663 – 675 nm for the tropics. NO_2 and NO_3 are considered as further absorbers and a polynomial of third order is applied to account for scattering and continuum absorption. All fitted references are allowed for a linked shift and a first order stretch in wavelength.

The results of all $4\nu+\delta$ measurements are illustrated in Figure 6.13 by simply enumerating the individual spectra in chronological order. The upper panel shows the results obtained from the field measurements carried out in Alcântara. The bulk of spectra[7] were recorded between December 24, 2004 and January 2, 2005. Comparing both measurement techniques, no considerable difference in the quality of the spectral retrieval is apparent. The results from the mid-latitude campaign in Lilia are given in the lower panel. This data was acquired between May 24 and June 12, 2003. The groups of spectra showing a continuous gradient are roughly to scale in time. For some data points the in-situ measurement is missing due to a failure of the meteorological station. Since it was also intended for this campaign to derive NO_3 concentrations at a high temporal resolution, numerous spectra were recorded.

The overall picture is similar to the results found for the 4ν measurements. The data series corresponding to the different analysis procedures are offset to each other but follow the same trend, a trend also seen in the in-situ measurements. The obtained water vapor number densities are decreasing as the magnitude of the water continuum absorption is increasing. However, this manner is less evident for the $4\nu+\delta$ water band than it is for the 4ν band. For further discussion it is convenient to switch to Figure 6.14, which is of same type as Figure 6.12. The correlation of derived water number densities is shown when first, the analysis is applied to the entire $4\nu+\delta$ water band, and second, the analysis is applied to the narrowed spectral intervals of 660.5 – 675 nm or 663 – 675 nm. Water number densities are overestimated if continuum absorption is completely excluded in the fitted water references. Including continuum absorption based on the Ma and Tipping far wing line shape theory does not considerably change the results – the predicted continuum absorption is negligible. For the high water concentrations in the tropics, a marginal but not significant difference is detectable when including the Ma and Tipping continuum. For the mid-latitudes however, with only a third in optical depth, the results are almost identical. The water continuum based upon the CKD models clearly contributes to the overall absorption but is not enough to bring all the results into agreement. The water concentrations prevalent in the mid-latitudes are too small to draw a reliable conclusion on the CKD continuum absorption.

[7] The three leftmost spectra were recorded earlier; at that time no in-situ data is available.

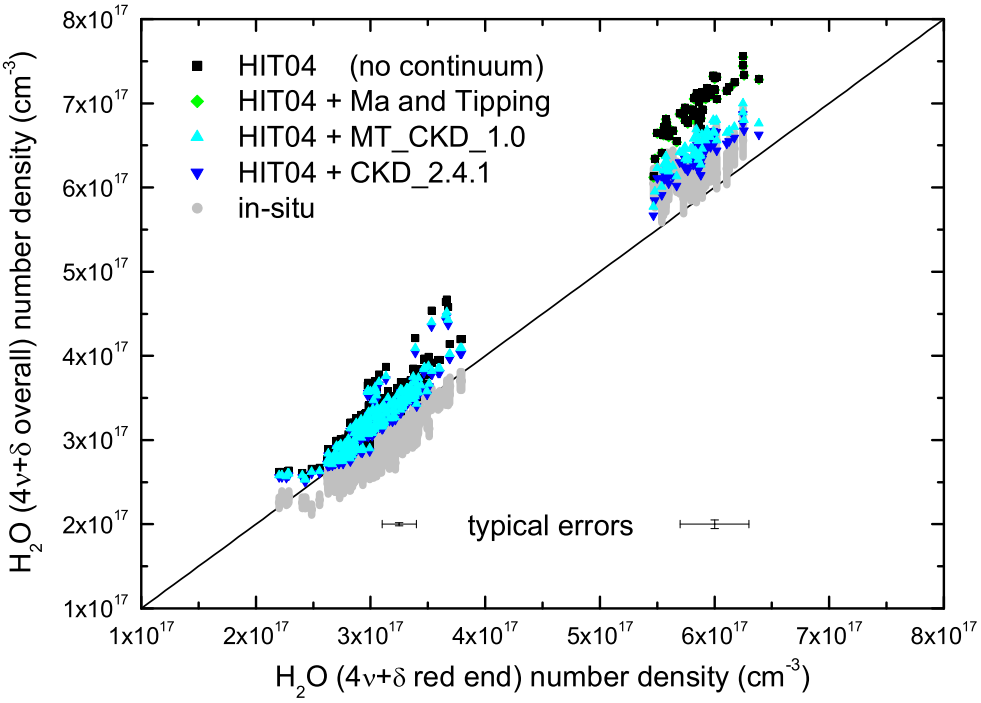

Figure 6.14: *The correlation of water vapor number densities obtained by two fundamentally different analysis procedures: (x-axis) Spectral analysis applied to a wavelength interval at the red of the $4\nu+\delta$ water band where water continuum absorption is negligible; (y-axis) Spectral analysis applied to the entire water $4\nu+\delta$ band where water continuum absorption has to be considered. Instead of assigning error bars to each data point, a typical statistical error is given at the bottom, separately for the groups of data representing the measurements performed in the mid-latitudes and in the tropics. The diagonal line corresponds to one-to-one correlation.*

6.5.3 Water Vapor 5ν Band

Absorption spectra in the region of the 5ν water band were only recorded during the field measurement campaign carried out in the tropics. The analysis procedure is conform to the previous ones used for the 4ν and $4\nu+\delta$ water bands. Water continuum and water monomer absorption are considered in the spectral evaluation covering the entire 5ν water band. The analysis interval is set to 560 – 620 nm. Besides water vapor, O_3 (cross section by *Anderson and Mauersberger* [1992]) and O_4 (cross section by *Greenblatt et al.* [1990]) are considered as further absorbers. NO_2 and NO_3 are omitted since their absorption is too weak to be detectable in the region of strong water absorption. A polynomial of first order is fitted to the measurements. For the spectral evaluation in the region of non-saturated water absorption, the 602 – 620 nm interval located at the red end of the 5ν water band is used. Here, O_3 (cross section by *Anderson and Mauersberger* [1992]), NO_2 (cross section by *Vandaele et al.* [2002]) and

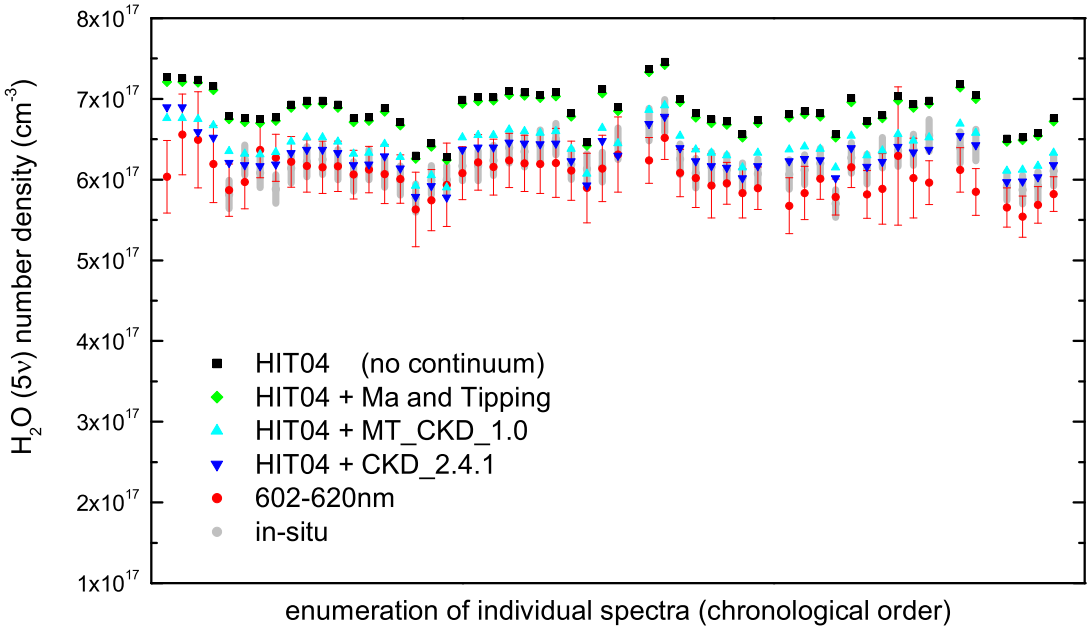

Figure 6.15: *Same as Figure 6.13 but for the 5ν water absorption band. Measurements in this spectral region were only performed during the tropical field campaign. The multi channel technique (MCT) was applied temporarily.*

NO_3 (cross section by *Sander* [1986]) are considered as further absorbers and a polynomial of third order is applied to account for scattering and continuum absorption. All fitted references are allowed for a linked shift and a first order stretch in wavelength.

The results of the 5ν measurements are illustrated in Figure 6.15 by simply enumerating the individual spectra in chronological order. The bulk of spectra[8] were recorded between December 24, 2004 and January 2, 2005. Both measurement techniques (with and without MCT) do not show a considerable difference in the quality of the spectral analysis. The overall characteristics of the 5ν measurements is similar to the other water bands. The different analysis procedures show an offset to each other. A same trend is reflected in all data including the in-situ measurements. For further discussion it is convenient to switch over to Figure 6.16, showing the correlation of derived water number densities when first, the analysis is applied to the entire 5ν water band, and second, to the 602 – 620 nm interval. If continuum absorption is accounted correctly, an one-to-one correlation is expected.

In general, the obtained water vapor number densities are decreasing as the magnitude of the continuum part of absorption is increasing. No continuum model predicts a sufficiently high absorption in order to bring the spectroscopic results into agreement.

[8]The first four spectra were recorded earlier; at that time no in-situ data is available.

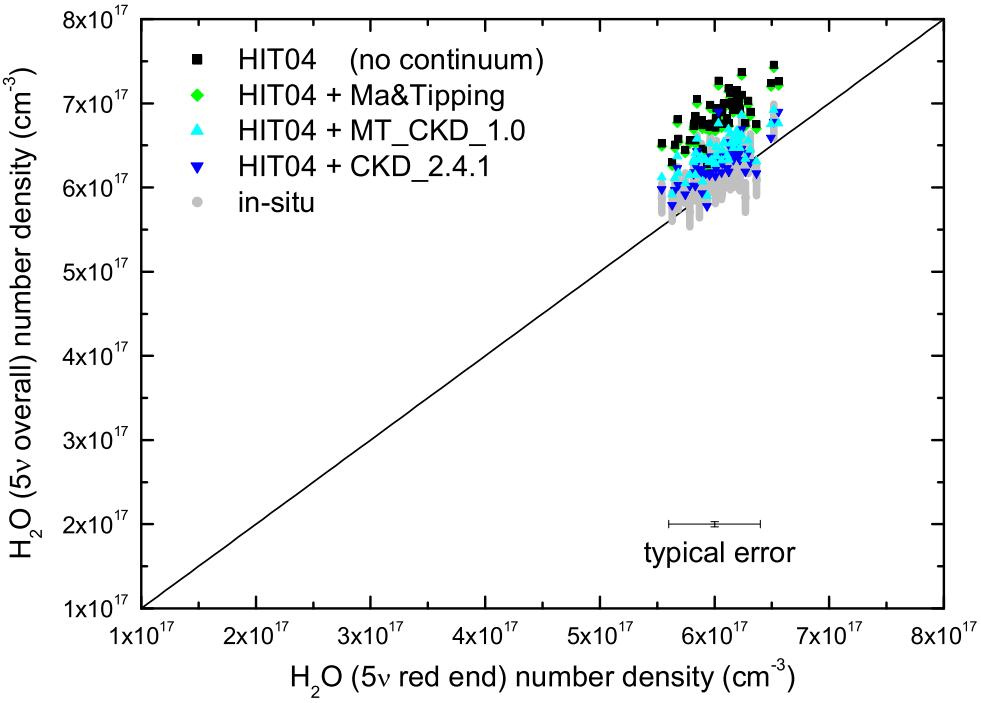

Figure 6.16: *Same as Figure 6.14 but for the 5ν water absorption band. Measurements in this spectral region were only performed during the tropical field campaign.*

The CKD_2.4.1 water continuum model seems to be the most adequate for the 5ν water band. Considering the error of the analysis, there is possibly agreement to the in-situ measurement and the spectroscopy applied to the interval of weak water absorption. The MT_CKD_1.0 water continuum model is suited slightly less than the CKD_2.4.1 model for describing continuum absorption. The largest discrepancy is found when the far wing line shape theory by Ma and Tipping is assumed to describe water continuum absorption. These results are close to the results with continuum absorption completely excluded from the analysis.

6.5.4 Intercomparison and Discussion

Based on the results presented in the previous section, the performance of the Ma and Tipping, MT_CKD_1.0 , and CKD_2.4.1 water continuum models in the three investigated water bands is summarized and a comparison to known experiments is given.

First, it can be concluded that atmospheric water vapor continuum absorption is detected. Considering only water monomer absorption in the spectral analysis leads to the conclusion that some absorption is definitely missing in the water reference. This shortcoming manifests in derived water number densities which are erroneously too high. Allowing for water continuum absorption the obtained water vapor number den-

sities are decreasing as the magnitude of the continuum part of absorption is increasing. This behavior is observed for the 4ν, $4\nu+\delta$ and 5ν water polyads as illustrated in the figures of the previous section. To complete the study, for each water continuum model the results obtained from all three water bands are compared. As measurements in all three absorption bands were only performed during the Alcântara field campaign, the discussion is restricted to this data. These measurements are best suited anyway due to the generally high water vapor concentration in the tropics, what makes for the most pronounced effects of continuum absorption. The comparison is illustrated in Figure 6.17 by the same type of correlation-plot well-established in the previous section. All shown measurements were performed by means of the more sophisticated multichannel technique. The wavelength intervals for the spectral analysis are given in the previous section and in Table 6.1.

Obviously, the water continuum absorption predicted by the Ma and Tipping far wing line shape theory cannot account for the observed magnitude of continuum absorption in all three water polyads. However, a detailed comparison of the results obtained in these water bands yields some differences. The water continuum absorption predicted for the 4ν polyad accounts for about 11% to the observed continuum absorption, whereas it is about 5% for the weaker 5ν polyad. Interestingly, a non significant continuum absorption accounting for only 0.5% is predicted for the $4\nu+\delta$ band. Actually it is assumed to be of similar magnitude as the absorption in the 5ν spectral region, since both water bands exhibit the same number of vibrational modes. This discrepancy may possibly be connected with the treatment of the water molecule's bending mode.

Both CKD water continuum models predict a substantial portion to the missing absorption. The magnitude is roughly twice as high in the 4ν polyad than it is in both other bands. Using the MT_CKD_1.0 model, the continuum absorption in the 4ν spectral region is predicted almost exactly (98%), and about half in the $4\nu+\delta$ and 5ν spectral regions (40% and 49%, respectively). Using the the older version CKD_2.4.1 instead of MT_CKD_1.0 yields continuum absorptions which are approximately a factor 1.3 larger in all three water bands. Thus, continuum absorption is overestimated in the 4ν polyad (133%) but still remains underestimated in the $4\nu+\delta$ and 5ν bands (51% and 65%, respectively).

Laboratory studies addressing water continuum absorption are largely performed in the thermal infrared [*Burch* 1981; *Tobin et al.* 1996; *Cormier et al.* 2002; *Cormier et al.* 2005]. Field measurements in the visible and near-infrared region are barely existing [*Sierk et al.* 2004]. It is questionable how the findings from the laboratory experiments can be applied to the short-wave spectral region, but exactly this procedure is performed

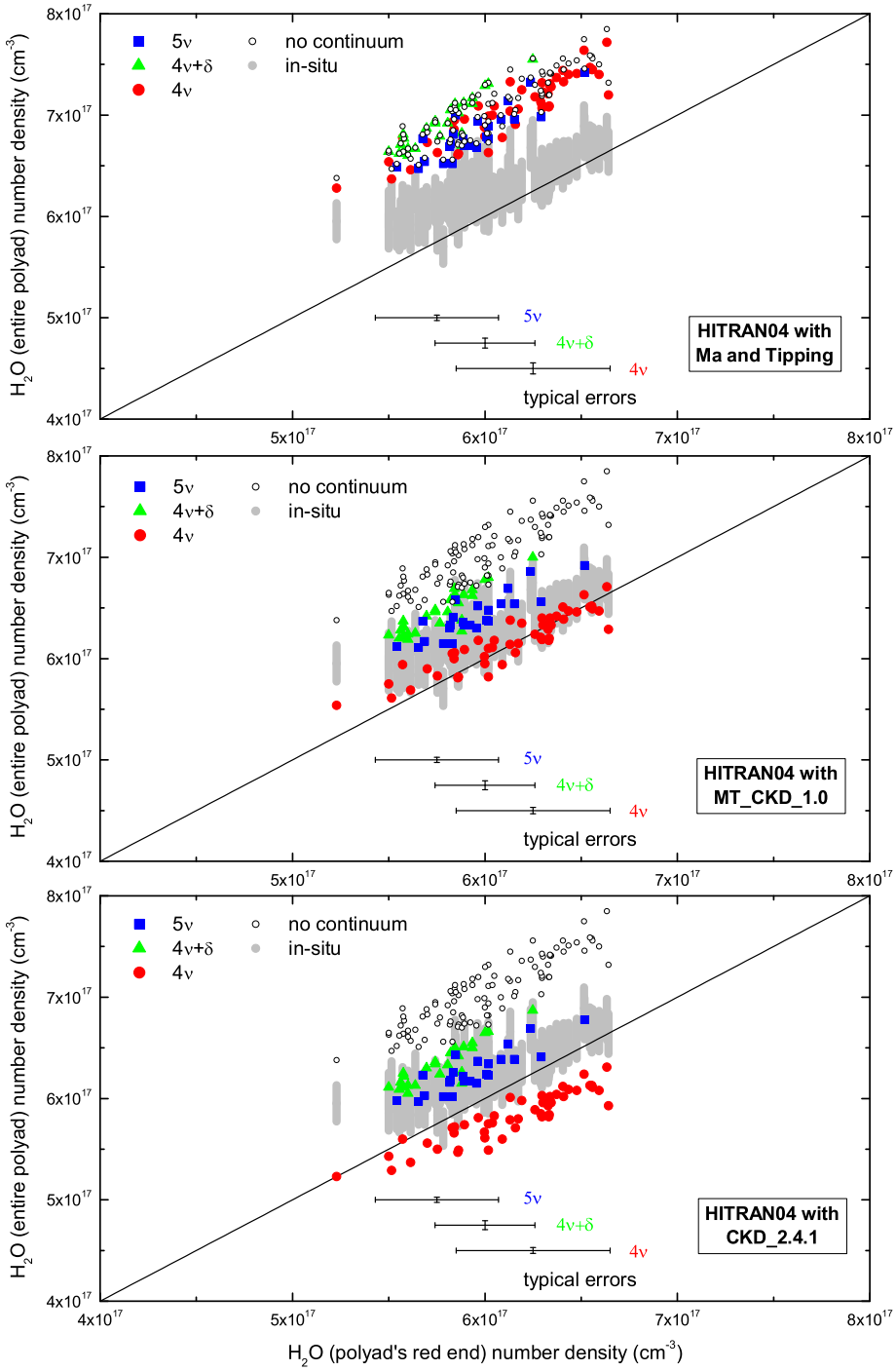

Figure 6.17: *Comparison of three water continuum models in the spectral region of the 4ν, 4ν+δ, and 5ν water band. Likewise to the figures in the previous section, the correlation is plotted when the analysis is applied to a wavelength interval covering either an entire water polyad or a small region located at its red end. The in-situ measurement is given by the shaded area. All data was acquired during the field campaign conducted in the tropics. Typical statistical errors are given separately for each water polyad at the bottom.*

for the semi-empirical CKD continuum models commonly used in radiative transfer codes. However, the semi-empirical CKD continuum models reasonably account for the observed magnitude of continuum absorption. The lately revised MT_CKD_1.0 version is somewhat in advance of the former CKD_2.4.1. However, remaining uncertainties in the spectroscopy prevents from drawing a firm conclusion. Recently, *Sierk et al.* [2004] carried out field measurements assessing water continuum absorption in the visible spectral region. In the 4ν water band they found almost exact agreement between their measurements and the CKD_2.4.1 model, while the MT_CKD_1.0 gives only 60% of the observed absorption. As their calculations are based on HITRAN2k, the difference to our values (133% and 98%, respectively) is possibly caused by the fact that we use HITRAN04. Referring to the case study in Section 6.3.2 the spectral line data is considerably modified by the database update as evident in Figure 6.7. Therefore, the Alcântara measurements are additionally evaluated by using HITRAN2k water references for the analysis applied to the entire 4ν spectral region. The HITRAN04 water cross section is used for the retrieval in the weakly absorbing 744.5 – 756 nm interval, since inconsistent results with the in-situ measurements are obtained when HITRAN2k is used. Indeed, the CKD_2.4.1 model predicts 88% and the MT_CKD_1.0 65% of the observed water continuum absorption in the reanalysis, which is close to the results of *Sierk et al.* [2004]. This demonstrates the sensitivity of the water continuum absorption on the used spectral line database.

The magnitude of water continuum absorption as predicted by the Ma and Tipping far wing line shape theory is not sufficient to account for the observed continuum absorption in the visible and near infrared spectral region. In contrast, the experimental study by *Cormier et al.* [2002] is in good agreement with the Ma and Tipping at wavelengths around 10 µm. However, the authors attribute remaining discrepancies to the presence of water dimers and subsequent experiments [*Cormier et al.* 2005] are in good agreement with the weakly bound binary complex model of *Vigasin* [2000]. Their findings are strongly suggestive of the important role played by atmospheric water dimers and water complexes. Recent laboratory measurements performed in the $\nu+\delta$ spectral region centered at 5 300 cm^{-1} also support the water dimer plus far wing description of the water vapor continuum [*Ptashnik et al.* 2004]. However, it is still a controversial issue to what extend bound or metastable water dimers are included in the Ma and Tipping theory [*Ptashnik* and *Tipping*, pers. comm.]. As the semi-empirical CKD continuum models have proven to be far more satisfactory to describe the observed magnitude of water continuum absorption, water dimers may be implicitly included in these models. A possible contribution of water dimers to the water continuum is discussed in Section 6.8. In the following section, a detailed study of water dimer absorption is presented first.

6.6 Water Dimer Absorption – A First Evidence ?

The calculation of the water dimer OH stretching mode transitions by *Low and Kjaergaard* [1999] predicts a fairly strong absorption band at a wavelength of 746 nm (Figure 5.2). This water dimer band, labelled $|0\rangle_f|4\rangle_b$, is situated at the red end of the 4ν water polyad where interfering water monomer absorption should be small. In this spectral range, atmospheric water dimer absorption may be directly accessible by the DOAS technique. However, the spectral retrieval of water dimer absorption is complicated due to uncertainties of the band position (±5 nm, *Low and Kjaergaard* [1999]) and band broadening (15 – 200 cm^{-1} FWHM, *Vaida et al.* [2001]). The calculated water dimer band strength is accurate to 10% [*Low and Kjaergaard* 1999].

Previous studies by *Daniel et al.* [1999] and *Hill and Jones* [2000] addressing atmospheric water dimer absorption in the visible and near-infrared spectral regions yielded negative results (Section 5.1). Based on the present Long Path DOAS measurements, a first evidence of atmospheric water dimer absorption by the $|0\rangle_f|4\rangle_b$ OH stretching mode transitions[9] was reported recently [*Pfeilsticker et al.* 2003]. Water dimer absorption is indicated by the quadratic dependence of its partial pressure upon that of the water monomer, obeying Equation 3.13. The results are in reasonable agreement with the known thermochemistry [*Curtiss et al.* 1979] and predicted spectroscopic signature [*Low and Kjaergaard* 1999] of the water dimer. Unfortunately, it has to be conceded that the observed absorption feature is much likely not caused by the water dimer, since the earlier findings could not be confirmed by subsequent measurements, neither by those carried out at similar ambient conditions in the mid-latitudes (Lilia, Brittany, 2003), nor by those performed at considerably higher water vapor concentrations in the tropics (Alcântara, Brazil, 2004/2005). The arguments leading to the statement of observed atmospheric water dimer absorption as well as possible shortcomings and the negative results of the subsequent measurements are discussed below.

6.6.1 Line of Argument

The detection of atmospheric water dimer absorption by the $|0\rangle_f|4\rangle_b$ OH stretching mode transitions as reported in *Pfeilsticker et al.* [2003] is based on the field measurements performed during the campaign in Dagebüll, 2002. Eight individual spectra recorded in multi channel mode are available. The corresponding water vapor partial pressures range between 6.7 mbar and 14.4 mbar (Table 5.1). The measurements were performed on four different days, whereas for each day two successive spectra were recorded. The evaluation of each pair of spectra yields consistent result, substantiating the reliability of the spectral retrieval.

[9] The inclusion of the HOH bending modes [*Schofield and Kjaergaard* 2003] was not yet available.

The 744.5 – 756 nm wavelength interval is chosen for the spectral analysis. There, water monomer absorption is not in saturation. The Bxl-Reims water monomer reference [*Coheur et al.* 2002] is used and is allowed for a shift and first order stretch in wavelength. A polynomial of third order is applied to account for broadband absorption and scattering. In a first run of the analysis, a prominent spectral feature remains in the residuals of both spectra recorded on the day of highest water vapor partial pressure. Then in a second run, the water dimer absorption cross section by *Low and Kjaergaard* [1999] (Lorentzian band profile), free in wavelength shift and first order stretch, is additionally fitted to the residual structure of the first run. From the analysis results, a band center position of 749.5 nm and a band full width at half maximum of 19.4 cm^{-1} is derived. By fixing the water dimer absorption cross section to these values, the remaining six spectra corresponding to lower water vapor pressures are analyzed. Figure 6.18 shows the analysis of the spectrum recorded on May 10th at a temperature of 292.4 K and a water vapor partial pressure of 14.4 mbar. The obtained water dimer peak absorption is $2.5 \pm 0.3 \times 10^{-9}$ cm^{-1}.

As the total statistical detector noise for the applied number of 27 detector readouts (each spectrum is a sum of 27 detector readouts) is clearly less than 10^{-3} (Table 5.2), the remaining residual structures are of systematic nature, mainly due to unremoved small water monomer absorption features. Similarly good spectral fits are obtained when the HITRAN2k [*Rothman et al.* 2003] water reference is used, but not when the ESA-WV data [*Schermaul et al.* 2001] was taken as a reference. In fact, using the latter yields much larger residual structures of unremoved water monomer absorption (see also Figure 6.6).

Quadratic Dependence on Water Monomer Absorption:

The quadratic dependence of the water dimer partial pressure on that of the water monomer is used as an indicator for water dimer absorption (Equation 3.13). Combining this with the Lambert-Beer law (Equation 4.7) yields

$$\varepsilon_{WD} = \sigma_{WD} \times p_{H_2O}^2 \times K_P(T) \tag{6.1}$$

where $\varepsilon_{WD} = \tau/L$ is the measured water dimer's extinction coefficient, σ_{WD} is the absorption cross section, $p_{H_2O}^2$ is the water monomer partial pressure squared and $K_P(T)$ is the water dimer equilibrium constant. The water dimer absorption cross section is obtained by the relation $\sigma_{WD} = S/(\pi\Gamma)$, where S is the band strength and Γ is the band's half width at half maximum (Equation 4.3). Fitting the analysis results into Equation 6.1 yields the predicted quadratic dependence (Figure 6.19). Admittedly, the number of measurements is small and the analysis errors are large. In order to draw a firm conclusion weather or not atmospheric water dimer absorption is detected, further evidence is required.

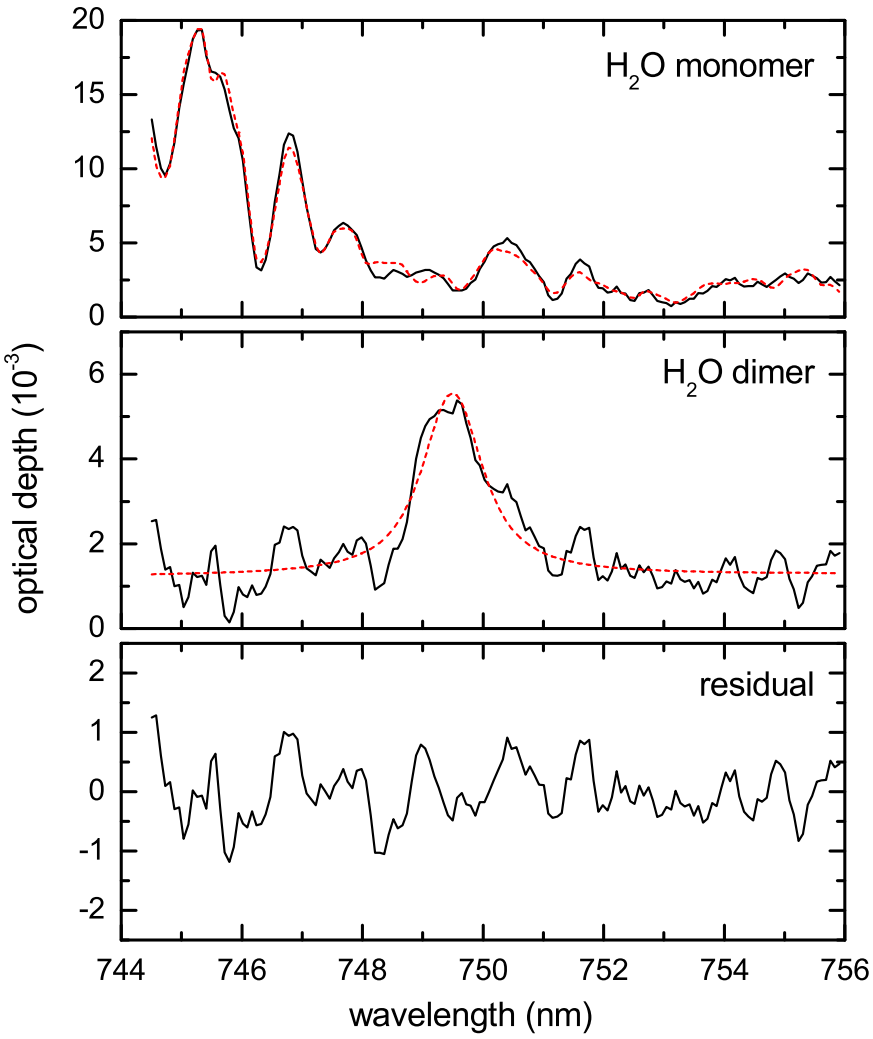

Figure 6.18: *Atmospheric absorption in the 744.5 – 756 nm wavelength interval:* **(a)** *water monomer absorption,* **(b)** *water dimer absorption by the* $|0\rangle_f|4\rangle_b$ *OH stretching mode transitions,* **(c)** *residual structure. The dashed traces show the inferred absorption and the solid lines the residual absorption plus the absorption inferred for the respective gas.*

Consistency with Spectroscopic Data:

The obtained band position of 749.5 nm is in agreement with the spectroscopic calculation of *Low and Kjaergaard* [1999], predicting the band center to be located at (746±5) nm. The observed band width of 19.4 cm^{-1} agrees with the fact, that vibrational overtones are expected to be broader than the fundamental transitions with typical values of 11 – 15 cm^{-1} [*Huang and Miller* 1989; *Huisken et al.* 1996; *Tso et al.* 1998]. However, there are concerns that the observed overtone band appears to be too narrow and a band broadening larger than 40 cm^{-1} should be more reliable [*Tso et al.* 1998; *Vaida et al.* 2001; *Suhm and Pfeilsticker* 2004].

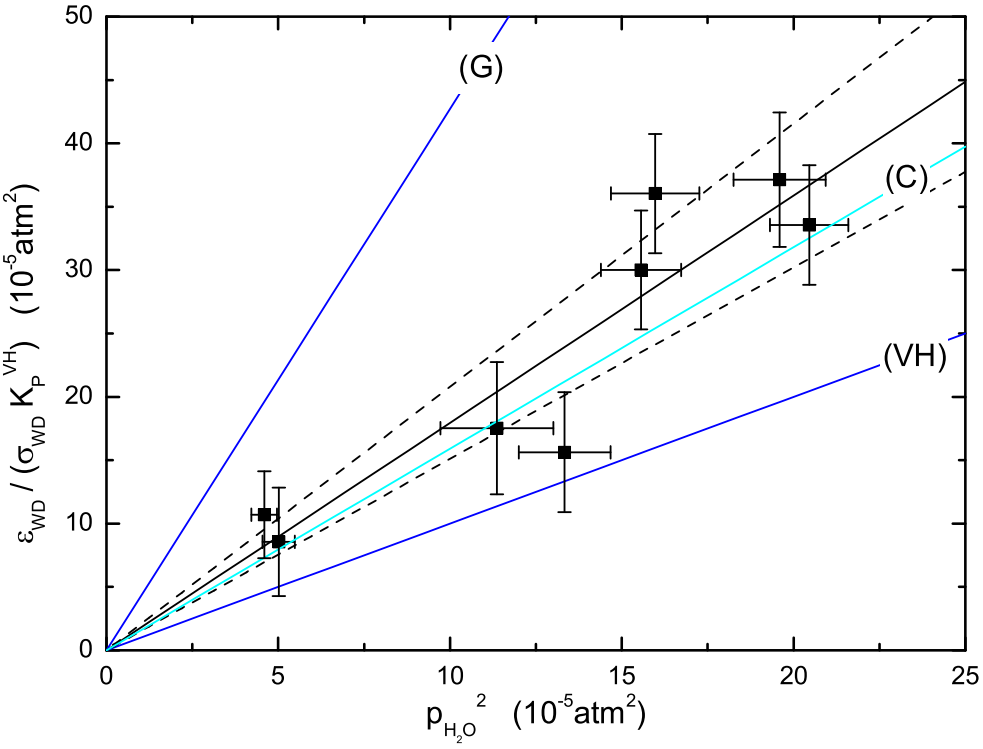

Figure 6.19: *Water dimer absorption as a function of the water monomer partial pressure squared, according to Equation 6.1. K_P^{VH} is the water dimer equilibrium constant of Vaida and Headrick [2000]. The solid black line shows the error-weighted linear fit and both dashed lines the 95% confidence interval. The lines labelled (C), (VH), and (G) indicate the predictions based on the band strength of Low and Kjaergaard [1999] and the thermochemical values of Curtiss et al. [1979], Vaida and Headrick [2000] and Goldman et al. [2001], respectively. The (C)- and (G)-lines are obtained by scaling the 1:1 (VH)-line by the ratio of the equilibrium constants K_P^C/K_P^{VH} and K_P^G/K_P^{VH}, respectively.*

Consistency with Thermochemical Data:

The use of known thermochemical values for the water dimer formation (Table 3.1), together with the measured band width and predicted band strength of *Low and Kjaergaard* [1999], allowed to constrain the water dimer equilibrium constant to a value of $(0.048 \pm 0.006)\,\mathrm{atm}^{-1}$. This is in good agreement with the laboratory experiment of *Curtiss et al.* [1979] (Figure 6.19). The agreement is remarkable as *Curtiss et al.* [1979] measured the equilibrium constant in the temperature range of 353 – 423 K and no temperature correction to the enthalpy ΔH and entropy ΔS is applied when their results are extrapolated to the temperature of our measurements. Interestingly, the measurements carried out by *Ptashnik et al.* [2004] confirm our value of the water dimer equilibrium constant.

6.6.2 Measurements in the Tropics

Measurements in the tropics were performed in Brazil in 2004/05 (Chapter 5). Typical water vapor concentrations are about twice the maximum values of the mid-latitude campaigns, i. e. 28 mbar versus 14 mbar. This makes a rough estimate of 3.5 times the water dimer concentration, considering its quadratic dependence on the water monomer and a slight decrease of the dimer equilibrium constant due to the higher temperature. Additionally, the absorption light path was by a factor of 1.5 longer at the campaign in the tropics. Altogether, the optical depth of a water dimer absorption band is expected to be about 5 times larger for the tropical campaign than it is for the mid-latitude campaigns. This predicts an optical depth of somewhat more than 0.02 for the water dimer absorption band observed at 749.5 nm (Figure 6.18). Absorption by this band should be easily accessible by the DOAS technique at tropical conditions.

The detection of water dimer absorption is normally masked by strong overlapping water monomer absorption. Even at the predicted wavelength of the $|0\rangle_{\mathrm{f}}|4\rangle_{\mathrm{b}}|0\rangle$ water dimer band, interfering absorption by the water monomer is present. Further, in regions of weak water vapor absorption, water spectral line parameters are poorly characterized. This results in unaccounted water monomer absorption in the analysis residuals. At the spectral resolution of 0.45 nm FWHM as provided by the Acton 500 spectrograph,[10] individual water absorption lines cluster in unresolved bands of typical 1 nm width (see, e. g., upper panel in Figure 6.18). As the broadening of a water dimer band is expected to be equal to or somewhat larger than such an unresolved cluster of water monomer lines, measurements should be performed at higher spectral resolution. Thus, a second spectrograph (SPEX 750) providing a resolution of 0.15 nm FWHM was also operated at the campaign in the tropics. This setup leads to a qualitatively more confident distinction between water monomer and possible water dimer absorption. It also allows a more detailed characterization of water spectral line databases.

The analysis results of the high resolution measurements are presented by means of a case study. The spectrum was recorded on January 4, 2005 during nighttime between 0:57 and 1:35 UTC. The multi channel technique was applied. A total of 166 readouts was summed up, each with an integration time of about ten seconds. The ambient temperature was 27.5 °C and the in-situ water vapor partial pressure was 27.4 mbar. The increase in temperature, water vapor pressure, and absorption path length with respect to the Dagebüll campaign allows to estimate the peak optical depth of the water dimer absorption at 749.5 nm to be 0.02 in the tropical case. Note that a threefold increase of the instrument's resolution does not considerably affect the band's peak optical depth, as the true band profile should be resolved by both instruments. The observed water dimer band width of 19.4 cm^{-1} corresponds to 1.1 nm.

[10] Other LP-DOAS instruments are commonly operated with this setup.

The spectral retrieval is performed in the 747.5 – 751 nm wavelength interval, as the CRDS-Grenoble spectral line list is only available there for the time being. A total of eight water monomer references are fitted separately to the measurement. All water references are calculated for the exact ambient temperature and pressure. A polynomial of third order is fitted in all retrievals and the water references are free in wavelength shift and first order stretch.

The analysis results are show in Figure 6.20. Although the residuals vary strongly, depending on the water monomer reference used, no water dimer absorption at 749.5 nm with a peak optical depth of 0.02 and a band FWHM of 1.1 nm is apparent. If water dimer absorption remains unnoticed within the 747.5 – 751 nm wavelength interval, the band would be much broader and hence less intense at the same time. However, the prediction by *Schofield and Kjaergaard* [2003] indicates that the $|0\rangle_{\mathrm{f}}|4\rangle_{\mathrm{b}}|0\rangle$ water dimer band is most likely located at 746 nm and therefore outside this interval.

As indicated by the residual structures, the CRDS-Grenoble spectral line compilation is obviously of better quality than all other databases. This indicates the capability of cavity ring down spectroscopy to provide more accurate water vapor line parameters than currently existing. With a typical sensitivity of $3 \times 10^{-10}\,\mathrm{cm}^{-1}$, line intensities 50 times smaller than the weakest ones included in HITRAN04 are accessible [*Kassi et al.* 2005]. Especially the otherwise poorly characterized spectral regions of weak water lines benefit from such accurate measurements. Concerning the other line databases, their overall agreement with the measurement is poor, but the HITRAN-based compilations may be somewhat preferred. As expected, the HITRAN04 and Bxl-Reims references yield almost identical result. Marginal differences can only be recognized at closer inspection. The same is true for the ESA-WV and Partridge-Schwenke line compilations. Most unsuited are the identical 2k + PSWL and PS ← 2k line lists, which are a combined compilation of the HITRAN2k and Partridge-Schwenke data (see Section 4.5.1 or *Ptashnik and Shine* [2003]). For these line lists, the PS contribution is evident from 749.5 nm upwards, but the situation below 748 nm is questionable.

6.6.3 Discussion

Due to the fact that the spectral feature at 749.5 nm is seen in the Dagebüll but not in the tropical measurements, it is very likely not caused by water dimer absorption. Possible shortcomings as well as a reanalysis of the Dagebüll measurements are discussed. The reanalysis concentrates on both spectra recorded at the highest water vapor pressure since the observed absorption feature is most prominent there. Meanwhile, a revised calculation of the water dimer overtone spectrum, including the HOH-bending modes, is available [*Schofield and Kjaergaard* 2003]. But neither the band position nor the band strength of the $|0\rangle_{\mathrm{f}}|4\rangle_{\mathrm{b}}|0\rangle$ band has changed significantly.

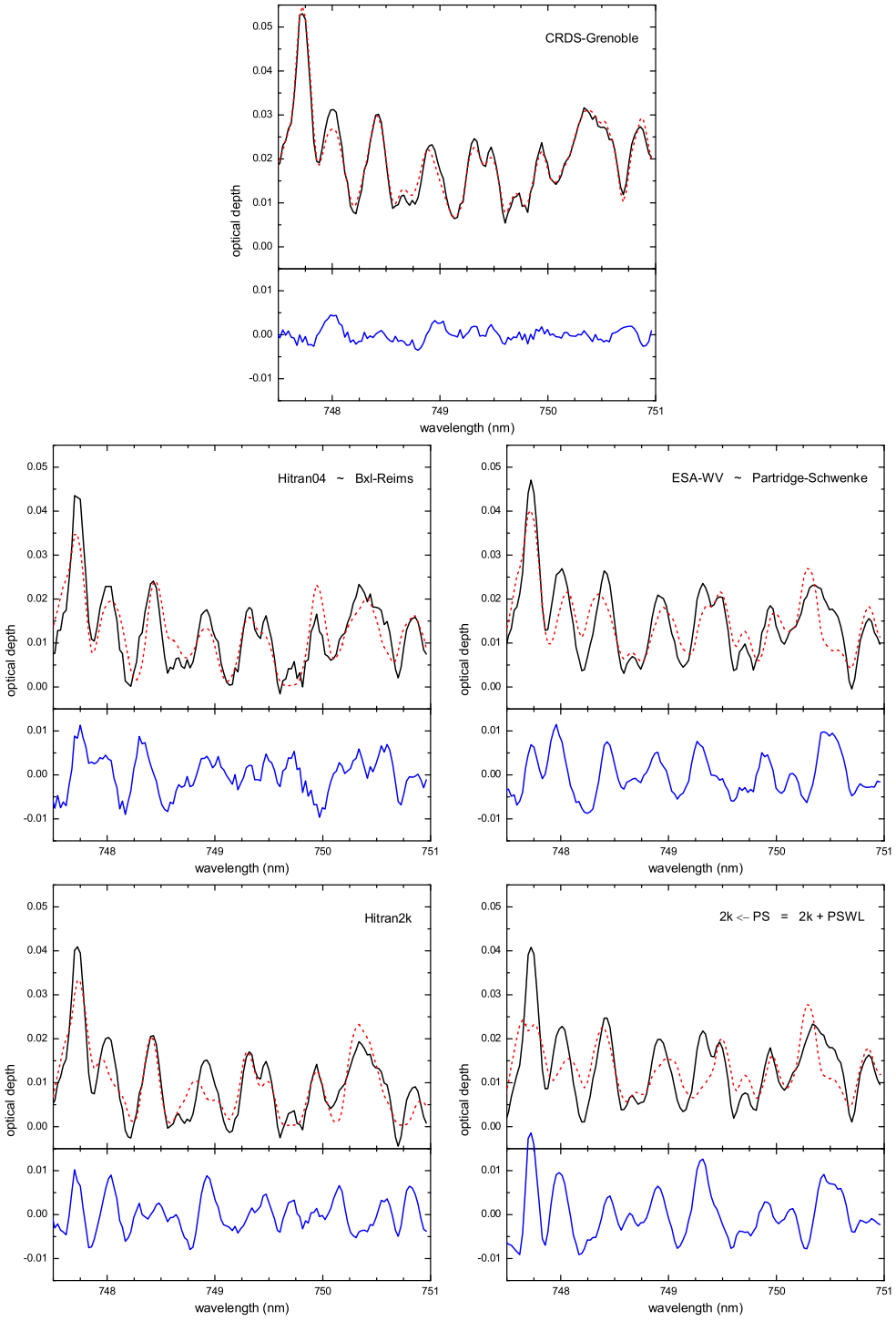

Figure 6.20: *Spectral analysis of one atmospheric spectrum, by successively fitting water monomer references based upon different spectral line databases. The retrieval is performed in the wavelength interval of potential water dimer absorption as observed by Pfeilsticker et al. [2003]. Black trace: Measurement; Dashed red trace: Water monomer reference; Blue trace: Residual. A polynomial of third order is fitted in each case and is already subtracted from the measurement.*

Concerning the LP-DOAS measurement technique, one crucial point well-known to be a source of error is ascribed to the Xenon lamp reference spectra. In fact, during the Dabebüll campaign these spectra are recorded by the use of an outdated lamp reference system. During the other field campaigns with the spectral feature at 749.5 nm being absent, Xenon lamp reference spectra are recorded by a more sophisticated system (see Section 4.2.6). Around wavelengths of intense Xenon emission lines, the spectral fit is hindered or almost impossible as the lamp's intensity is changing rapidly with time. Although no Xenon emission lines [NIST Atomic Spectra Database] are present in the 744.5 – 756 nm analysis interval, high pass filtered Xenon lamp spectra are also fitted to the measurements in order to account for possible narrowband structures induced by the Xenon lamp reference. It has to be emphasized that these concerns were already addressed in the earlier analysis. However, the reanalysis does not provide any indication, that the spectral signature at 749.5 nm is caused by the Xenon lamp.

For the Dagebüll spectra the retrieval never reached the theoretical detection limit given by statistical noise. The residuals are always dominated by unremoved water monomer absorption and the spectral analysis is very sensitive to the water reference data used. Initiated by our report of atmospheric water dimer absorption, *Kassi et al.* [2005] measured the water monomer spectrum in the narrow spectral region of 747.3 – 751.0 nm by using high resolution cavity ring down spectroscopy (Section 4.5.1). Our measurements carried out in the tropics demonstrate the good quality of this line compilation (Section 6.6.2). However, the CRDS-Grenoble measurements cover only a 3.7 nm wide spectral interval for the time being. For a proper analysis this interval is too small at the spectral resolution of the instrument operated during the Dagebüll campaign. For the purpose of using the CRDS-Grenoble line data in the reanalysis, a line compilation is generated from HITRAN04, by replacing all line data in that interval with the CRDS-Grenoble data. Figure 6.21 shows the spectral fits to the measurement performed on May 10, 2002 (the same spectrum as shown in Figure 6.18), when the line data of HITRAN04 and combined HITRAN04/CRDS-Grenoble is used. Apparently, the spectral retrieval is robust with respect to the water reference used. The HITRAN04/CRDS-Grenoble data however results in 15% less potential water dimer absorption, but the spectral feature at 749.5 nm remains existent. The characterization of water monomer absorption in the spectral region covered by the CRDS-Grenoble line data is improved. As the fit basically weights the spectral region where water absorption is strong, a more detailed investigation of the CRDS-Grenoble line data requires the analysis to be limited to the corresponding wavelength interval (Section 6.6.2).

In Section 6.3.1 the temperature dependence of the water monomer absorption cross section is discussed. The largest errors in the spectral retrieval due to an incorrect tem-

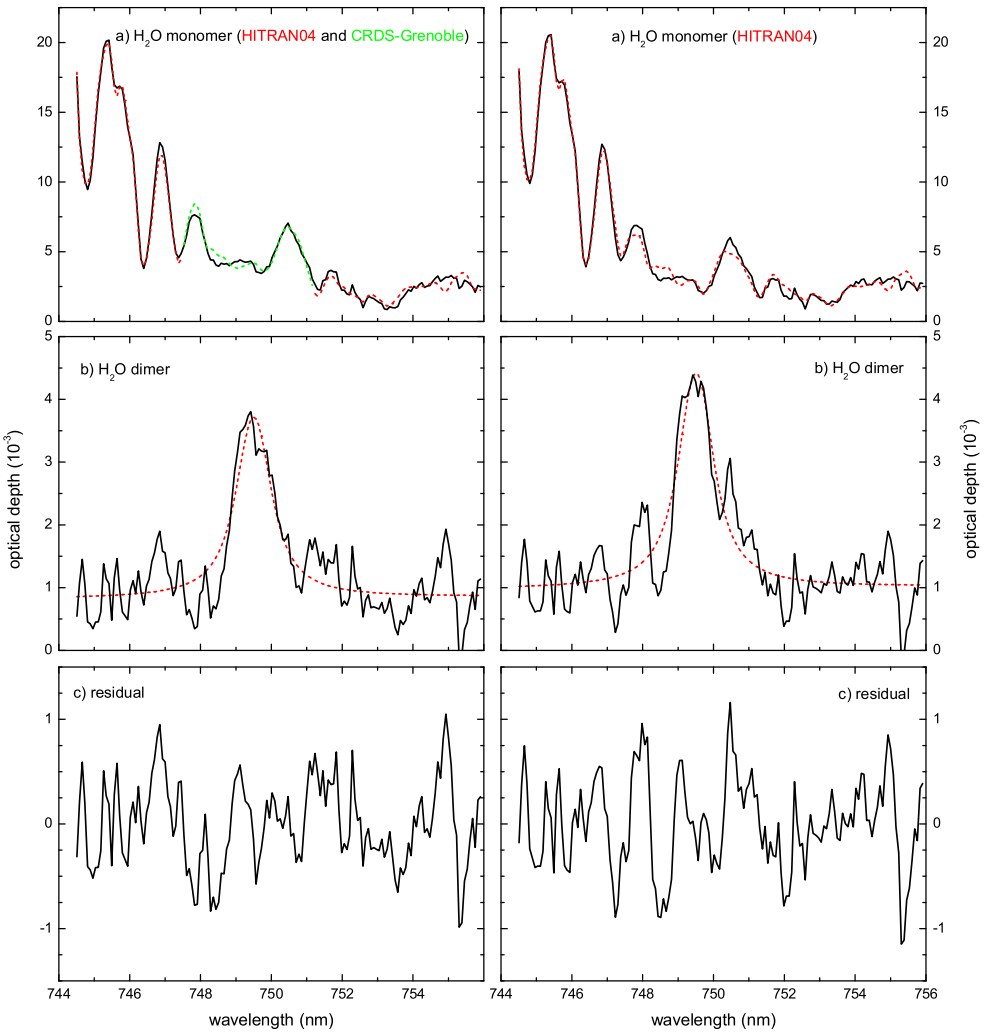

Figure 6.21: *Reanalysis of the atmospheric absorption spectrum shown in Figure 6.18:* **(a)** *water monomer absorption based on the HITRAN04 data (right hand side) or the combined HITRAN04 and CRDS-Grenoble data (left hand side),* **(b)** *water dimer absorption by the* $|0\rangle_f|4\rangle_b$ *OH stretching mode transitions,* **(c)** *residual structure. The dashed traces show the inferred absorption and the solid lines the residual absorption plus the absorption inferred for the respective gas.*

perature should occur at wavelengths near 750 nm (Figure 6.3). This is exactly where the observed water dimer absorption is located. However, it can be ruled out that the spectral feature at 749.5 nm is a temperature effect because of the following reasons: (1) For the spectral analysis, the water absorption cross section is calculated for the exact temperature of the measurement, i. e. 292.4 K for the spectrum recorded on May 10th; (2) This temperature is close to the temperature of 291.3 K at which the Bxl-Reims and hence HITRAN04 water line parameters were measured [*Coheur et al.* 2002; *Rothman*

et al. 2005]; (3) Further spectral features of similar magnitude should be present in the wavelength interval of 744.5 – 756 nm (Figure 6.3). (4) Using water absorption cross sections deviating up to 13 K in temperature do not considerably change the spectral retrieval.

As the water dimer absorption is not observed in the tropics and no deficiencies are identified in both the measurement technique and analysis procedure, it is assumed that the spectral feature at 749.5 nm is caused by an atmospheric absorber other than the water dimer. Checking molecular databases however do not yield any positive result. The observed band width seems to be too small for a molecular absorber anyway.

Nevertheless, it may be possible that the observed spectral structure is caused by short lived gases emitted from the ocean, since the light path traverses as close as two meters above the sea surface at times of high tide (Section 5.2.1). In fact, the time of the measurements performed on May 10, 2002, when the controversial absorption is most prominent, coincides exactly with the time of high tide (Table 5.1). The same is true for the measurements on May 14, 2002, where the unassigned absorption structure is also observed but less intense. The other Dagebüll measurements, in contrast, are performed during low tide, when sea water is almost absent along the absorption path. For those measurements the absorption at 749.5 nm is hardly detectable.

6.7 Water Dimer Absorption – Upper Limits

Based on the calculated water dimer absorption spectra by *Low and Kjaergaard* [1999] and *Schofield and Kjaergaard* [2003], a total of three absorption bands is predicted to be considerably offset in wavelength from strong water monomer absorption (Figure 5.2). These water dimer bands, labelled $|0\rangle_{\mathrm{f}}|4\rangle_{\mathrm{b}}|0\rangle$, $|0\rangle_{\mathrm{f}}|4\rangle_{\mathrm{b}}|1\rangle$ and $|0\rangle_{\mathrm{f}}|5\rangle_{\mathrm{b}}|0\rangle$ are located at the red end of the 4ν, $4\nu+\delta$ and 5ν water polyads at wavelengths of 746 nm, 667 nm and 613 nm, respectively. The spectroscopic data of these dimer bands is listed in Table 6.2. The calculated water dimer band strengths are accurate to 10% [*Low and Kjaergaard* 1999], but uncertainty exists for the band positions (±5 nm, *Low and Kjaergaard* [1999]) and the band broadening (15 – 200 cm^{-1} FWHM, *Vaida et al.* [2001]).

6.7.1 Analysis Results

In the following, the measurements performed with high spectral resolution during the tropical field campaign are considered. Only spectra recorded at nighttime and good atmospheric visibility, i. e. integration times less than one minute, are selected for the analysis. Spectra recorded during daytime are excluded from the analysis, as the correction for background stray light (see Section 4.3 for details) is poor: On the one hand, the long absorption path length results in a higher amount of scattered sunlight but a lower intensity of transmitted light than is usually present at small path

Table 6.2: *Spectroscopic data of three water dimer bands which are considerably offset to strong water monomer absorption [Schofield and Kjaergaard 2003].*

band	wavenumber (cm^{-1})	air wavelength (nm)	band strength (cm)	rel. strength
$\|0\rangle_f\|4\rangle_b\|0\rangle$	13 401	746.0	2.83×10^{-22}	1
$\|0\rangle_f\|4\rangle_b\|1\rangle$	14 987	667.1	1.15×10^{-23}	0.04
$\|0\rangle_f\|5\rangle_b\|0\rangle$	16 312	612.9	3.95×10^{-23}	0.14

lengths. On the other hand, when recording background spectra, it is not possible to mount a long pass filter to suppress the blue part of the second order spectrum. All nighttime spectra are recorded at almost the same ambient temperature of 27 – 28 °C and an average water vapor pressure of 27 mbar. As the deviation from average values is always small, a fixed water number density of 6.5×10^{17} cm^{-3} is assumed for all estimates of water dimer upper limits. After the analysis of the individual spectra, all residuals corresponding to the same spectral region are averaged.

The $|0\rangle_f|4\rangle_b|0\rangle$ Band

The $|0\rangle_f|4\rangle_b|0\rangle$ band is predicted to be the strongest of the three selected water dimer bands (Table 6.2) and therefore is predestined for studying possible water dimer absorption. The spectral retrieval is performed in the 740 – 754 nm wavelength interval. The HITRAN04 water monomer reference is fitted[11] and is allowed for a wavelength shift and a first order stretch. A polynomial of third order accounting for any continuum extinction is fitted. There is no improvement in the quality of the analysis when using the combined HITRAN04/CRDS-Grenoble line list, as the spectral fit outweighs the region of strong water absorption where only HITRAN04 data is available. Distinctive gradients in the residuals emerge at wavelengths covered by the CRDS-Grenoble line list, possibly caused by an incorrect baseline adjustment of the cavity ring down measurements.

Figure 6.22 shows the averaged residual of the analysis. From each individual measurement, the water monomer absorption and the fitted polynomial is removed and the residuals are averaged. The remaining differential spectral structures are of narrow width and therefore due to unremoved water monomer absorption. There is no obvious indication of water dimer absorption within the predicted spectral region of (746±5) nm. However, some weak broadband absorption is remaining in the residual

[11] The fitting procedure of optically thick spectra has to be applied due to line saturation.

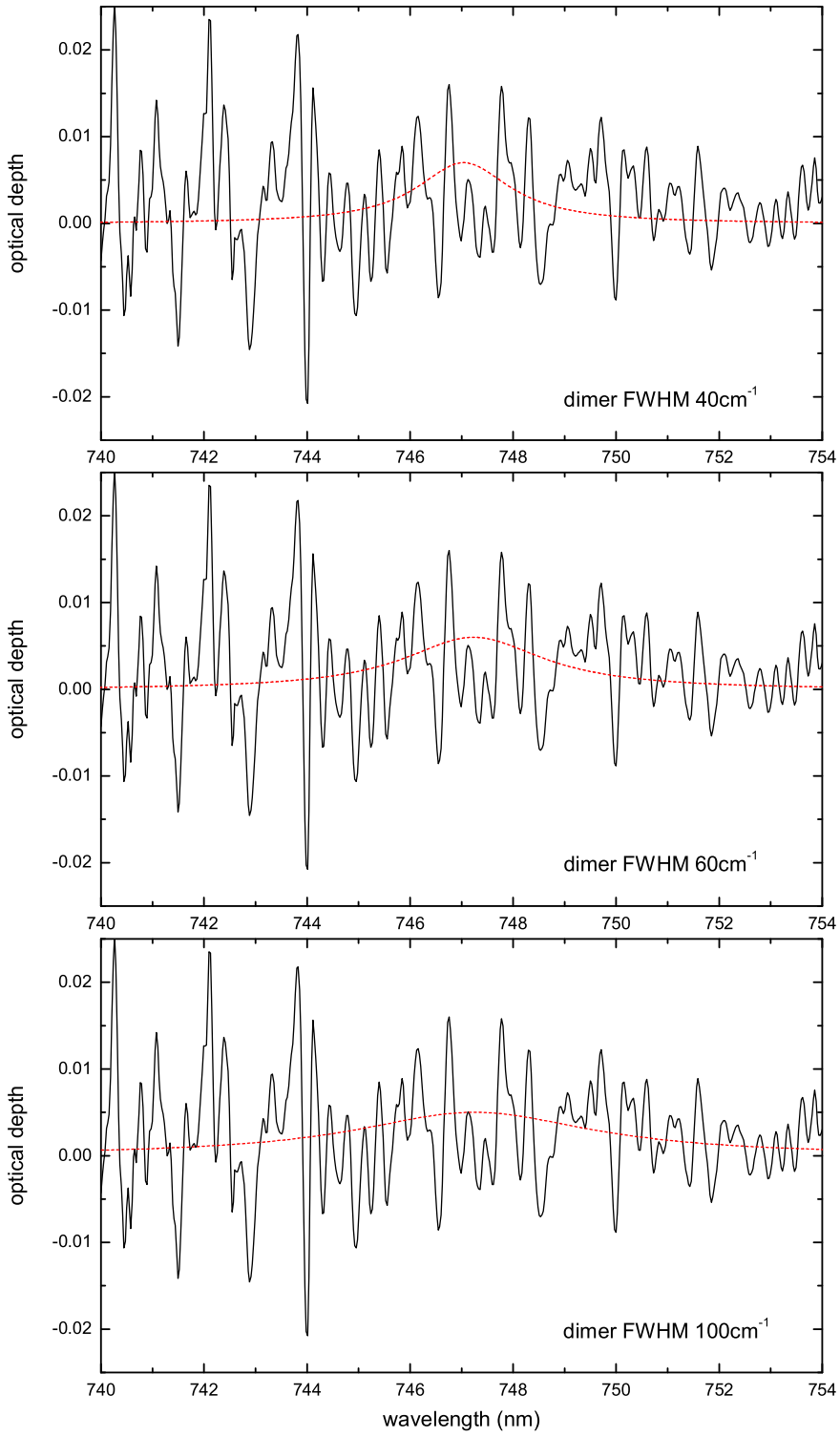

Figure 6.22: *Upper limits of water dimer absorption by the $|0\rangle_f|4\rangle_b|0\rangle$ band. The solid black line shows the averaged residual of the analysis, i. e. measurement minus HITRAN04 water reference minus a polynomial of third order. The dashed red lines indicate a best estimate of the water dimer absorption for three spectral band widths.*

around 747 nm, possibly caused by water dimers. The observed broadband absorption is consistent with a water dimer band full width at half maximum between 40 cm^{-1} and 100 cm^{-1}. A best estimate of water dimer absorption is superimposed the residual for three possible band broadenings. The inferred optical depths for the 40 cm^{-1}, 60 cm^{-1} and 100 cm^{-1} dimer spectra are 0.007, 0.006 and 0.005, respectively. Based on Equation 6.1, an upper limit of the water dimer equilibrium constant $K_P(T)$ is calculated from the $|0\rangle_f|4\rangle_b|0\rangle$ band strength, the band width, the corresponding inferred absorption, and the assumed water vapor number density of 6.5×10^{17} cm^{-3}. This results in $K_P(T) = 0.031\,atm^{-1}$ for a band width of 40 cm^{-1}, $K_P(T) = 0.040\,atm^{-1}$ for 60 cm^{-1}, and $K_P(T) = 0.055\,atm^{-1}$ for 100 cm^{-1}.

The $|0\rangle_f|5\rangle_b|0\rangle$ Band

The predicted band strength of the $|0\rangle_f|5\rangle_b|0\rangle$ band is only 14% the strength of its 4ν polyad counterpart (Table 6.2). Fortunately, the overlap with water monomer absorption is considerably less, since the $|0\rangle_f|5\rangle_b|0\rangle$ band is located well between the 5ν and $4\nu+\delta$ water polyads (Figure 5.2). Water dimer absorption may just be observable here, as for tropical conditions a peak optical depth around 0.001 is expected. This is slightly above the instrument's detection limit (Table 5.2). The spectral retrieval is performed in the 602 – 627 nm wavelength interval. The HITRAN04 water monomer reference is fitted and allowed for a wavelength shift and first order stretch. Further, the absorption cross sections of NO_2 [*Vandaele et al.* 2002], NO_3 [*Sander* 1986], and a polynomial of third order are fitted.

Figure 6.23 shows the averaged residual of the analysis. From each individual measurement, the absorption by water monomer, NO_2, NO_3, and the fitted polynomial is removed. Thereafter all residuals are averaged. Besides narrowband spectral structures of unremoved water monomer absorption a broadband feature around 614 nm is evident. This residual structure is consistent with water dimer absorption by the $|0\rangle_f|5\rangle_b|0\rangle$ band and a 40 – 60 cm^{-1} band full width at half maximum. However, there is no firm evidence that the broadband spectral feature is caused by water dimers, i. e. a quadratic dependence on the water monomer absorption cannot be obtained as the overall variation of water vapor concentrations is too small in the tropics. Two possible water dimer absorption spectra are superimposed the residual: (1) A band FWHM of 40 cm^{-1} and 1.2×10^{-3} peak optical depth; (2) A band FWHM of 60 cm^{-1} and 1.0×10^{-3} peak optical depth. According to Equation 6.1 the water dimer equilibrium constant is obtained from these numbers, the band strength (Table 6.2) and a water vapor number density of 6.5×10^{17} cm^{-3}. The results are $K_P(T) = 0.038\,atm^{-1}$ and $K_P(T) = 0.047\,atm^{-1}$ for a band broadening of 40 cm^{-1} and 60 cm^{-1}, respectively. The agreement with the results obtained from the absorption by the $|0\rangle_f|4\rangle_b|0\rangle$ water dimer band is fairly good when considering the rough estimates in both cases.

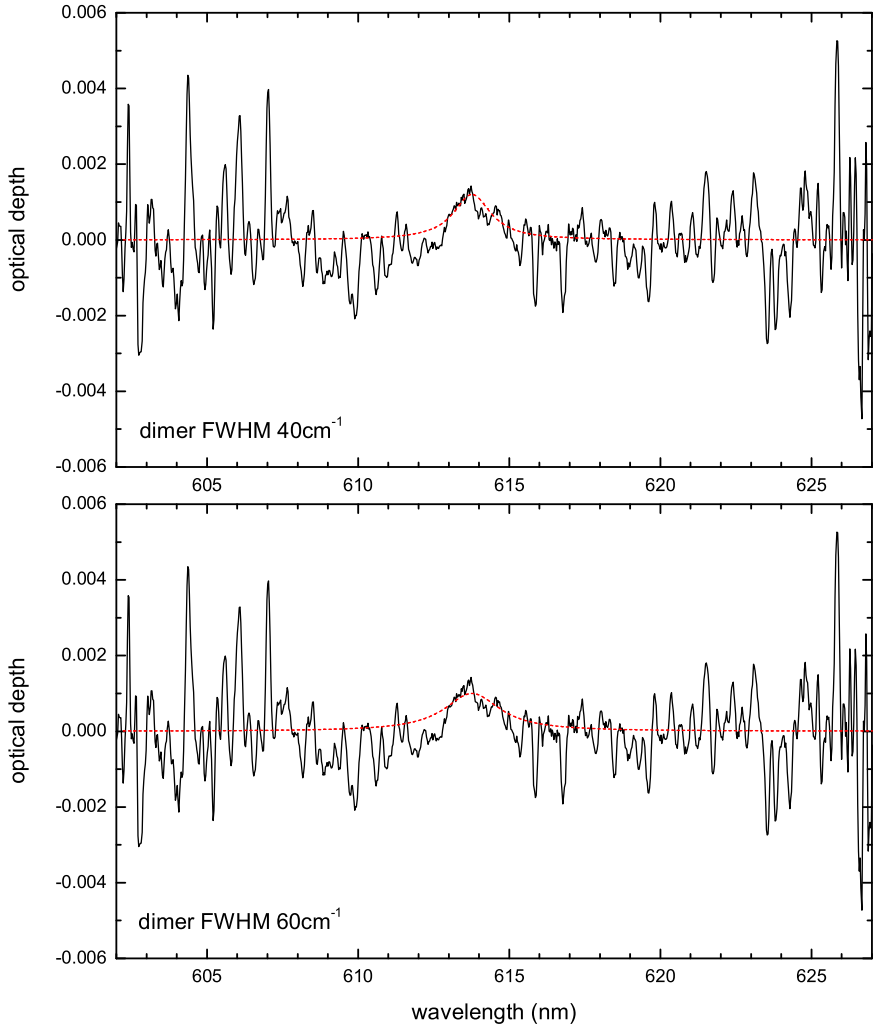

Figure 6.23: *Upper limits of water dimer absorption by the $|0\rangle_f|5\rangle_b|0\rangle$ band. The solid black line shows the averaged residual of the analysis, i. e. measurement minus HITRAN04 water reference, minus NO_2 absorption, minus NO_3 absorption, and minus a polynomial of third order. The dashed red lines indicate a best estimate of the water dimer absorption for two spectral band widths.*

NO_2 and NO_3 absorption may interfere in this spectral region. The absorption band of NO_3 is located at wavelengths above 620 nm and hence outside the region of interest. NO_2 absorbs strongest around 613 nm, but as its differential absorption cross section is small (4×10^{-20} cm^2) the detection limit of NO_2 is 0.5 ppbv (parts per billion volume). Accompanying measurements in the blue spectral region where NO_2 absorption is much stronger yield NO_2 concentrations usually below 0.5 ppbv, only occasionally peaking around 0.8 ppbv [*Schwärzle* 2005]. Therefore, it is assumed that NO_2 does not considerably interfere with a potential water dimer absorption in this region. In fact, there is hardly any absorption observed for both trace gases, NO_2 and NO_3.

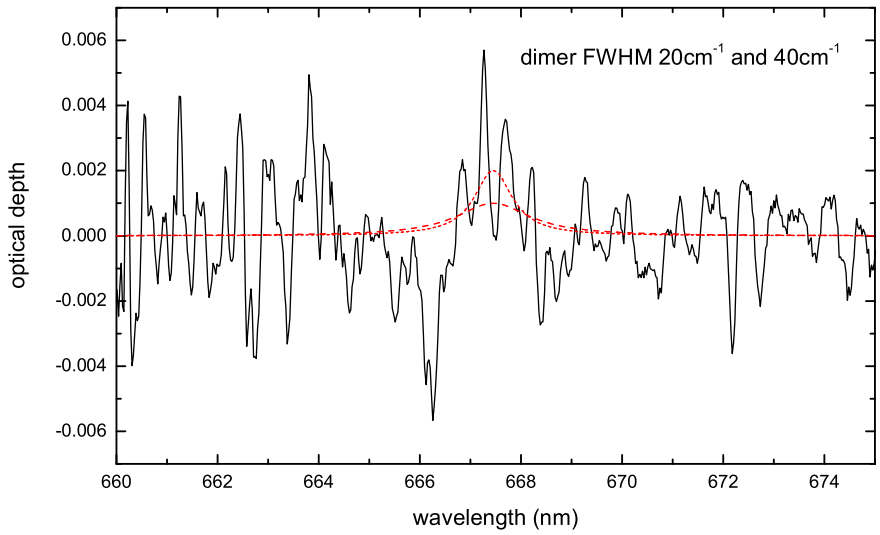

Figure 6.24: *Upper limits of water dimer absorption by the $|0\rangle_f|4\rangle_b|1\rangle$ band. The solid black line shows the averaged residual of the analysis, i. e. measurement minus HITRAN04 water reference, minus NO_3 absorption, and minus a polynomial of third order. The dashed red lines indicate a best estimate of the water dimer absorption for two spectral band widths.*

The $|0\rangle_f|4\rangle_b|1\rangle$ Band

Of all water dimer bands listed in Table 6.2, the $|0\rangle_f|4\rangle_b|1\rangle$ one is the weakest. Based on the upper limits inferred from the water dimer absorption of both other bands, it is not expected to detect any absorption here. However, the same analysis procedure is performed as before. The 660 – 675 nm wavelength interval is chosen for the spectral retrieval. The HITRAN04 water monomer reference is fitted and allowed for a wavelength shift and first order stretch. Further, the absorption cross section of NO_3 [*Sander* 1986] and a polynomial of third order are fitted to the measurement. Absorption by NO_2 is too weak to have to be considered here.

Figure 6.24 shows the averaged residual of the analysis. After removing the absorption by water monomer, NO_3, and the fitted polynomial from each individual measurement, all residuals are averaged. There is one spectral structure at 667.5 nm which is sufficiently broad to be related to water dimer absorption. This residual structure is consistent with a band's FWHM of about 20 cm^{-1}, but definitely less than 40 cm^{-1}. From both band widths and corresponding peak optical depths follows a water dimer equilibrium constant of about 0.11 atm^{-1}. However, if the observed absorption is caused by the $|0\rangle_f|4\rangle_b|1\rangle$ band, the optical depth of the much stronger $|0\rangle_f|4\rangle_b|0\rangle$ band should be 0.05 or 0.025 for a band width of 20 cm^{-1} or 40 cm^{-1}, respectively. Such a magnitude of absorption by the $|0\rangle_f|4\rangle_b|0\rangle$ band should easily be detectable, but it is not. Therefore, the absorption by the $|0\rangle_f|4\rangle_b|1\rangle$ band is probably below the detection limit. Considering the large residual structures, no reasonable upper limit can be obtained.

6.7.2 Discussion

Water dimer absorption by the $|0\rangle_f|4\rangle_b|0\rangle$ and $|0\rangle_f|5\rangle_b|0\rangle$ stretching mode transitions is possibly observed in the atmosphere at tropical ambient conditions. During that field campaign, the range of water vapor partial pressures was 24 – 29 mbar. The absorption by the $|0\rangle_f|5\rangle_b|0\rangle$ water dimer band is too weak to be detected at the low water vapor concentrations encountered at mid-latitudes, as this absorption is just above the detection limit for tropical conditions. The $|0\rangle_f|4\rangle_b|0\rangle$ water dimer band overlaps considerably with water monomer absorption. The quality of up to date water spectral line databases is insufficient to describe properly water monomer absorption in this spectral region. Therefore, absorption by the $|0\rangle_f|4\rangle_b|0\rangle$ water dimer band can only be roughly estimated from the high resolution measurements in the tropics. Concerning the low resolution measurement carried out in the tropics, the intensities of residual water monomer structures are smaller, but their typical width is considerably broader. This makes it impossible to estimate the underlying broadband water dimer absorption. In conclusion, there is no proof that the observed broadband absorption in Figures 6.22 and 6.23 is caused by water dimers. Absorption by the $|0\rangle_f|4\rangle_b|0\rangle$ and $|0\rangle_f|5\rangle_b|0\rangle$ water dimer bands is possibly not detected. The detection of water dimer absorption requires to check a quadratic dependence on the water monomer absorption. This is not possible due to large residual structures and an overall variation in water vapor concentrations by only 20% during the entire tropical campaign. However, the inferred absorptions can be considered as an upper limit, as any stronger absorption should have been detected.

The magnitude of the water dimer overtone band broadening is an open issue to date, but it is expected to increase with the number of overtones. Therefore, the band width of the fundamental transitions with typical values smaller than 15 cm^{-1} (FWHM) [*Huang and Miller* 1989; *Huisken et al.* 1996; *Tso et al.* 1998] is considered as a lower limit. *Vaida et al.* [2001] assume the overtone band broadening to be within the range of 15 – 200 cm^{-1}, with 40 cm^{-1} being the likeliest case. The theoretical study by *Tso et al.* [1998] predicts a water dimer band width of about 50 cm^{-1} (FWHM) for the v=3 spectral region. Lorentzian line shapes of tens of cm^{-1}, increasing in widths by factors of 2 to 3 between v=2 and v=5, are measured in spectra of polyatomic molecules of similar size to the water dimer [*Kjaergaard et al.* 1991; *Kjaergaard et al.* 1993]. Recent measurements of the water dimer first overtone absorption at 5 300 cm^{-1} by *Ptashnik et al.* [2004] yield band widths of 36 cm^{-1} and 56 cm^{-1} (FWHM), depending on the water continuum model used for their calculations of water reference spectra.

The present measurements of water dimer absorption suggest a band width of at least 40 cm^{-1} (FWHM) for the v=4 and v=5 overtone bands. A value near 60 cm^{-1} is very likely for the present observations and is also in agreement with the measurement of *Ptashnik et al.* [2004] (56 cm^{-1} FWHM for the v=2 spectral region). It is not possible

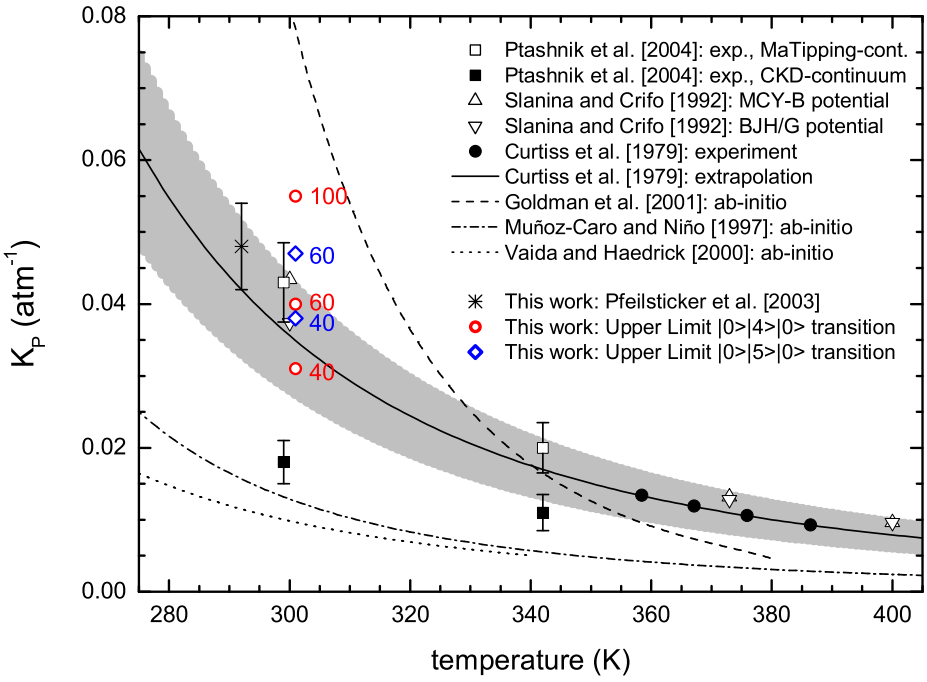

Figure 6.25: *Theoretical and experimental determinations of the temperature dependent water dimer equilibrium constant. The measurement of Curtiss et al. [1979] is extrapolated to lower temperatures, the uncertainty is given by the shaded area. Upper limits of the water dimer equilibrium constant derived from the absorption by the* $|0\rangle_f|4\rangle_b|0\rangle$ *and* $|0\rangle_f|5\rangle_b|0\rangle$ *dimer bands are plotted. The corresponding numbers indicate the assumed water dimer band's FWHM with units given in* cm^{-1}*. Additionally, the result based on the erroneously assigned water dimer absorption by Pfeilsticker et al. [2003] is shown.*

to infer an upper limit of the water dimer band broadening as any value larger than $60\,\mathrm{cm}^{-1}$ is also consistent with the measurements. A band broadening beyond $100\,\mathrm{cm}^{-1}$ is so large that even an estimate of water dimer absorption is not possible, unless there is much better improvement in water line databases.

Upper limits of the water dimer equilibrium constant are determined. The comparison of these results with other theoretical and experimental work is illustrated in Figure 6.25. As the results are obtained from averaged residuals of nighttime spectra in the tropics, a mean temperature of 301 K is assumed. The typical nighttime temperature does not deviate more than 1 K from this mean. Since the true water dimer band width is unknown, the upper limits are shown for all possible water dimer band widths for both the $|0\rangle_\mathrm{f}|4\rangle_\mathrm{b}|0\rangle$ and $|0\rangle_\mathrm{f}|5\rangle_\mathrm{b}|0\rangle$ water dimer band.

The derived water dimer equilibrium constants depend on the assumed water dimer band width and the corresponding water dimer absorption. The former is unknown and the latter is roughly estimated by visual judgement, i. e. a water dimer absorption

spectrum is visually fitted to the residuals (Figures 6.22 and 6.23). Since the true water dimer equilibrium constant has a fixed but unknown value, the water dimer absorption is expected to decrease proportionally as the band width increases. Surely, the visual judgement is influenced by this fact, but it is always performed consistently with the measurements. The main purpose of this procedure is not to determine exact values for the water dimer band width or absorption strength, but rather to narrow down the thermochemical properties, in particular the water dimer equilibrium constant. The overall agreement within all obtained equilibrium constants is very good, considering the sensitivity of an inferred water dimer absorption on the estimate of the visual fit.

The upper limits of the equilibrium constant agree well with the extrapolated data of *Curtiss et al.* [1979], the measurements by *Ptashnik et al.* [2004], and the calculations of *Slanina and Crifo* [1992]. Further, the comparatively small equilibrium constants as predicted by *Vaida and Headrick* [2000] and *Muñoz-Caro and Niño* [1997] also agree with the present measurements. The calculations of *Goldman et al.* [2001], in contrast, predict too high values to be in agreement with the upper limits. In conclusion, the present study suggests an upper limit of the water dimer equilibrium constant of $K_P(T) = 0.055\,\mathrm{atm}^{-1}$ at a temperature of 301 K. This estimate holds for a water dimer band width of less than $100\,\mathrm{cm}^{-1}$ (FWHM), a value which is assumed to be very plausible. Due to the magnitude of residual structures in the analysis, no reasonable estimate of an upper limit can be given if the water dimer band width is considerably larger than $100\,\mathrm{cm}^{-1}$ (FWHM). The consistency of the thermochemical data together with the spectroscopic prediction by *Schofield and Kjaergaard* [2003] may in fact indicate that the observed absorption at 747 nm and 614 nm is caused by water dimers.

Finally, the solar shortwave radiative forcing by atmospheric water dimers is discussed. Therefore, our estimates of water dimer absorption are compared and scaled to the results of *Ptashnik et al.* [2004], as they carried out extensive radiative transfer calculations. Considering their upper set of results only (open squares in Figure 6.25), the inferred water dimer absorption in the spectral region of $1\,500 - 17\,000\,\mathrm{cm}^{-1}$ is $1.5\,\mathrm{W/m}^2$ or about 2% of the total clear-sky absorption on a global average. The shortwave heating may reach $7.3\,\mathrm{W/m}^2$ for a tropical atmosphere with a water vapor column of $4.7\,\mathrm{g/cm}^2$ and overhead sun.

The water dimer shortwave absorption is proportional to the water dimer equilibrium constant and roughly proportional to the water dimer band width. A comparison to the measurements of *Ptashnik et al.* [2004] (FWHM = $56\,\mathrm{cm}^{-1}$ and $K_P(T) = 0.038\,\mathrm{atm}^{-1}$) allows to estimate the global mean shortwave heating potential by water dimers from our data: $0.8 - 1.2\,\mathrm{W/m}^2$ (FWHM = $40\,\mathrm{cm}^{-1}$); $1.4 - 1.5\,\mathrm{W/m}^2$ (FWHM = $60\,\mathrm{cm}^{-1}$); $3.5\,\mathrm{W/m}^2$ (FWHM = $100\,\mathrm{cm}^{-1}$). These numbers are an rough estimate of upper limits for the corresponding band widths. However, it is not possible to give an overall estimate since this requires to know an upper limit of the water dimer band width.

6.8 Summary of Water Continuum and Dimer Absorption

This section gives a summary and intercomparison of water vapor continuum and water dimer absorption as studied in detail in the previous sections. The obtained results are discussed on the basis of a case study reflecting the main issues of the water continuum dispute, i. e. the mechanisms contributing to water continuum absorption. Further, the problem of inaccurate and incomplete water spectral line databases is addressed.

In the case study water continuum absorption is assessed directly, i. e. a modeled water monomer reference spectrum is subtracted from the measurement and the residual is checked for water continuum and water dimer absorption. This approach is very similar to the procedure performed by *Ptashnik et al.* [2004].

A spectrum covering the region of the 4ν water polyad is chosen. It was recorded during the tropical field campaign on December 30, 2004 between 3:30 and 4:20 UTC. The multi channel technique was applied. A total of 90 readouts was summed up, each with an integration time of about 20 seconds. The ambient temperature and air pressure were 27.1 °C and 1007 mbar. All calculations of water monomer, water continuum, and water dimer references are performed for exactly these values. The in-situ measurement and the spectroscopy (744.5 – 756 nm interval) yield almost identical water number densities, $(6.34 \pm 0.19) \times 10^{17}$ cm^{-3} and $(6.33 \pm 0.38) \times 10^{17}$ cm^{-3}, respectively. The following reference spectra are calculated: (1) HITRAN04 water monomer, (2) CKD_2.4.1 water continuum, (3) MT_CKD_1.0 water continuum, (4) Ma and Tipping water continuum, (5) water dimer ($K_P = 0.04$ atm^{-1}, FWHM = 40 cm^{-1}, band strengths of *Schofield and Kjaergaard* [2003]). All references are convolved with the field instrument's line shape function (Acton 500 spectrograph).

The measured atmospheric optical depth is obtained from the measured spectrum $I(\lambda)$ by division with the light source spectrum $I_0(\lambda)$ and taking the negative logarithm. Then, the HITRAN04 water monomer reference is subtracted from the measurement. The remaining residual is plotted in Figure 6.26 by the black curve. Three main features are evident: (1) High frequency spectral structures, (2) a low frequency continuum absorption, and (3) a baseline absorption.

The baseline absorption results from the applied measurement technique and therefore cannot be corrected. For atmospheric long path measurements, the I_0-reference spectrum can only be obtained by reducing the absorption path length significantly using one of the systems described in Section 4.2.6. Both the atmospheric and I_0-spectrum are recorded with different optical geometry and highly different light throughput. A loss of intensity in the atmospheric spectrum is caused by scattering and divergence of the light beam being transmitted through the atmosphere. The scattering depends on wavelength ($\sim \lambda^{-4}$ for Rayleigh scattering and approximately $\sim \lambda^{-1.3}$ for Mie scatter-

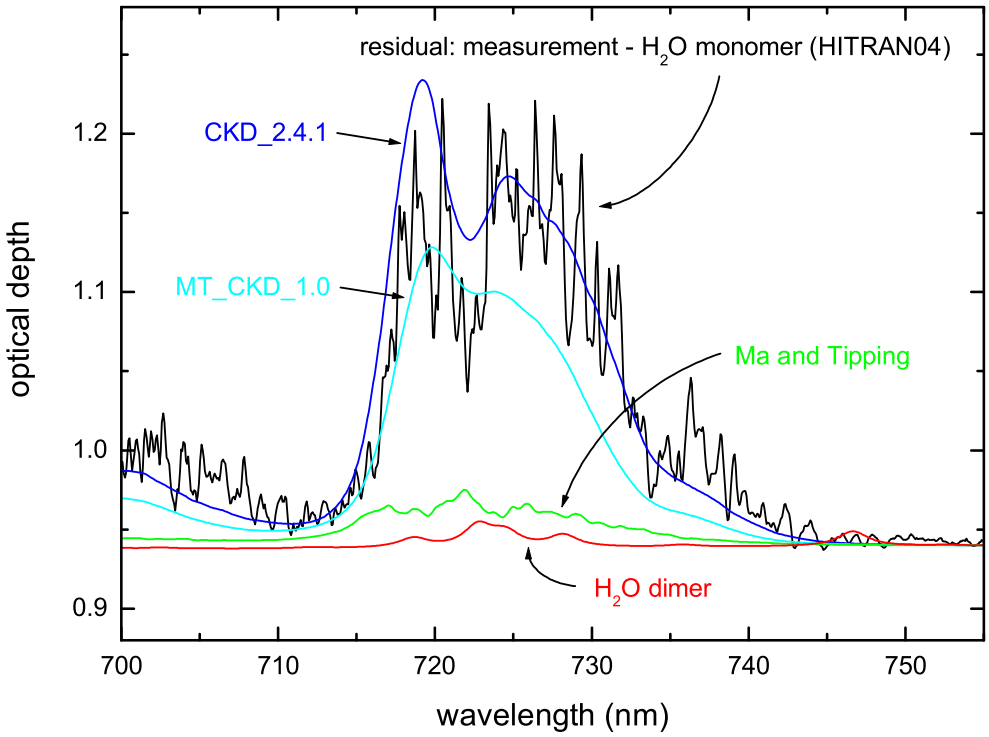

Figure 6.26: *Residual between measurement and HITRAN04 water monomer reference. Predicted water continuum and water dimer absorptions are superimposed, whereas a shift of constant optical depth is applied. Due to the measurement technique a correction by an unknown baseline would be required. For further details see accompanying text.*

ing), but as the spectral interval here is small, this causes only a slight curvature of the baseline absorption. Since the shape and magnitude of the baseline is unknown, a correction cannot be applied. In order to compare the residual with predicted water continuum and water dimer absorptions, these references have to be shifted in optical depth. Therefore, the baseline absorption is estimated for wavelength higher than 750 nm where absorption generally should be small. All references are shifted to match in this spectral region.

The high frequency residual structures are caused by water monomer absorption. There are two contributing effects: First, the accuracy of the spectral line database and second, the accuracy of the input water vapor number density. This number density is obtained from the in-situ measurement and the spectroscopy with almost equal magnitude and errors of 3% and 6%, respectively. Applying an usual DOAS analysis, i. e. fitting a reference to the measurement, any incorrectly assumed initial number density is accounted for by scaling the fitted reference. Of course, this correction is not applied by simply subtracting the water reference. An incorrect water vapor number

density as input data to the subtracted reference causes absolute and differential residual structures. Also for a DOAS analysis as shown in Figure 6.5 (see the panel with the HITRAN04 database used), differential residual structures of typically $\tau \approx 0.05$ remain versus $\tau \approx 0.1$ in the case study here. This implies that the inaccuracy of the HITRAN04 spectral line database accounts to a considerable extend for the high frequency residual structures seen in Figure 6.26. All other databases studied within this thesis perform similar to or even worse than HITRAN04 in the 4ν spectral region (Section 6.3.2). However, the good quality of line parameters obtained from high resolution cavity ring down spectroscopy [*Kassi et al.* 2005] has shown that there is much room for improving the spectral retrievals (Section 6.6.2). Because of inaccuracies in currently available spectral line databases, the theoretical LP-DOAS detection limit of $\tau = 10^{-3}$ can not be reached. Given this detection limit and a path length of 29 km, an absorption sensitivity of $\alpha = 3.5 \times 10^{-10}\,\mathrm{cm}^{-1}$ can be obtained. In order to benefit from the full capacity of the LP-DOAS technique, more accurate water vapor spectral line parameters are required. Measurements of these parameters should be performed with an absorption sensitivity in the order of $\alpha = 10^{-10}\,\mathrm{cm}^{-1}$.

The observed low frequency continuum absorption is compared with the predictions of the semi-empirical CKD water continuum models, the Ma and Tipping far wing line shape theory, and the water dimer approach. The true nature of water vapor continuum absorption has been a major concern for several decades. Interaction processes of two water molecules are of central importance for the water continuum absorption. There are three possibilities what may occur when two water molecules collide: A free collision, the formation of a metastable water dimer, or the formation of a truly bound water dimer (Section 3.1.3). However, the partitioning into these three types of pair states at atmospheric temperatures, as well as the link between this subdivision and the various water continuum and water dimer concepts is still a controversial issue.

For both semi-empirical CKD models, water continuum absorption is predicted with the right order of magnitude. The overall shape of both CDK continua is in reasonable agreement with the measurement. In the case study here, the CKD_2.4.1 water continuum is somewhat too large, whereas the MT_CKD_1.0 water continuum performs reasonably well. Extending the discussion to all measurements (Section 6.5) the CKD_2.4.1 continuum is always larger by about a factor of 1.3 than the MT_CKD_1.0 in all studied polyads. However, due to remaining uncertainties in the spectral analysis it is not possible to determine which version of the semi-empirical CKD models is superior. Differences occur comparing the water continuum absorption in the 4ν, $4\nu+\delta$, and 5ν bands. Whereas in the 4ν band both semi-empirical CKD models predict roughly the observed continuum absorption, it is only about half the required absorption in the other bands. This indicates deficiencies of adopting the CDK models in the short-wave

spectral region, while the model originally was derived from measurements in the microwave region. In conclusion, the semi-empirical CKD models predict the correct order of magnitude of water continuum absorption but do not provide any insight into the fundamental physics causing this continuum absorption. The CKD models basically treat water continuum absorption by applying a "pedestal" to each water monomer line, i. e. the line shape in the far wings is modified. However, this approach may include all effects leading to a change in a monomer's line shape and line intensity during a collision. In particular, the CKD models may implicitly include water dimer absorption.

The Ma and Tipping far wing line shape theory does not describe the measured water continuum absorption in the 4ν spectral region, neither in the case study here, nor in the further measurements (Section 6.5). The Ma and Tipping continuum is one order of magnitude too small. The shape of the Ma and Tipping continuum does not agree with the measurement as the predicted peak at 722 nm coincides with the observed absorption dip. The discrepancy between the Ma and Tipping continuum and the measurements performed in the 5ν band is one order of magnitude, whereas it is two orders of magnitude for the $4\nu+\delta$ band (Section 6.5).

The Ma and Tipping theory describes water continuum absorption by a deformation of a monomer's line shape as a consequence of a molecular collision, and further by collision-induced absorption (Section 3.2.2). However, the link to the subdivision into distinct type of bimolecular states as given by *Vigasin* [2003] remains unclear, as the far wing contribution is associated with free-free collisions, but collision-induced absorption includes bound-free, free-bound, and bound-bound effects [*Tipping*, pers. comm.]. Interestingly, when shifting the water dimer spectrum to lower wavelengths by about 2 nm, the Ma and Tipping continuum and the water dimer show similarities in their overall shapes. This may in fact indicate that water dimers are included in the Ma and Tipping theory to some extend. However, strong doubts remain that metastable or even bound water dimers are included therein by the collision-induced contribution [*Ptashnik*, pers. comm.]. The basic physical processes involved during a water-water collision are still matter of dispute.

Although the Ma and Tipping theory may leave room for a possible water dimer contribution to the total water continuum absorption, this is unlikely, as the predicted magnitude of water dimer absorption is even less than the Ma and Tipping continuum in the 4ν spectral region (see Figure 6.26; likewise results are found for the $4\nu+\delta$ and 5ν spectral regions). This finding is in good agreement with the failure of atmospheric water dimer detection (Sections 6.6 and 6.7). If the water dimer accounts for a considerable part to the observed water continuum absorption, the up-to-date water dimer spectroscopic and thermochemical properties combined (*Schofield and Kjaergaard* [2003]; Table 3.1; Figure 6.25) would be one order of magnitude in error. Concerning the ther-

mochemical properties, even the most optimistic estimate [*Goldman et al.* 2001] only results in a twofold increase of water dimer absorption with regard to the spectrum shown in Figure 6.26. One the other side, if the water dimer spectrum [*Schofield and Kjaergaard* 2003] is of considerable larger magnitude, the water dimer band located at 746 nm should be easily detectable. Further, the overall shape of the water dimer spectrum is not in agreement with the measurement.

It is known from laboratory measurements performed at very low temperatures that water dimers are existing (Section 3.2.3). Even at room temperature water dimers must form, as the intermolecular potential well depth (Table 3.1) is considerably lower than the kinetic energies of the colliding water molecules. For a binding potential discrete energy levels exist, causing discrete transitions to appear in the spectrum. However, the spectral band widths are determined by the water dimer lifetime. In order to observe discrete transitions in the visible and near-infrared spectral regions, overlapping strong water monomer lines have to be removed. For the time being, it is the inaccuracy and the incompleteness of existing water vapor spectral line databases and not the limit of the LP-DOAS technique which makes the detection of atmospheric water dimer absorption not possible.

7 Conclusion and Outlook

The presented thesis studies atmospheric water vapor continuum and water vapor dimer absorption in the visible and near infrared spectral region. The 4ν, $4\nu+\delta$ and 5ν water polyads are selected for the measurements, as three water dimer absorption bands are predicted to exist almost free of interference by strong water monomer absorption at the red ends of these water polyads [*Schofield and Kjaergaard* 2003]. The well established active Long Path DOAS technique is employed at three field measurement campaigns conducted in the mid-latitudes and the tropics: German North Sea Coast, 2002; French Atlantic Coast, 2003; Atlantic Coast of Northeastern Brazil, 2004/05. Near surface absorption paths length between 18 km and 29 km are realized and the ambient water vapor partial pressures range between 7 mbar and 29 mbar.

The performance of water vapor spectral line databases is investigated in the spectral region of the 4ν water polyad.

- The water vapor absorption cross section shows a strong temperature dependence, which may be a source of large errors and residual structures in DOAS evaluations.
- The quantification of water monomer absorption in the optically thick spectral region of the 4ν polyad is within 14% for all studied databases and is in overall good agreement with the in-situ measurement.
- The spectral line databases are studied in the optically thin spectral region of 742 – 756 nm, as water dimer absorption is predicted there. The HITRAN04 database [*Rothman et al.* 2005] performs well. Both the Partridge-Schwenke database [*Schwenke and Partridge* 2000] and the ESA-WV database [*Schermaul et al.* 2001] underestimate water monomer absorption by a factor of two.
- When the Partridge-Schwenke database is used, very large residual structures of unremoved water monomer absorption remain throughout the entire 4ν water polyad.
- The performance of the recently published line parameters of *Kassi et al.* [2005] is studied. The line data is only available in a 3.7 nm wide interval centered at 749.5 nm for the time being. Excellent agreement with our measurements is found. Residual water monomer structures are reduced by a factor of 3 compared to the HITRAN04 analysis.

Water vapor continuum absorption according to the Ma and Tipping far wing line shape theory and the semi-empirical CKD_2.4.1 and MT_CKD_1.0 models is studied. A possible contribution by the water dimer is considered.

- Atmospheric water vapor continuum absorption is detected in the visible and near infrared spectral region.

- Water continuum absorption is predicted with the right order of magnitude by both semi-empirical CKD models [*Clough et al.* 1989]. The overall shape of the CKD continua is in reasonable agreement with the measurement. With respect to water continuum absorption in the 4ν band, water continuum absorption is systematically underestimated by a factor of two in the $4\nu+\delta$ and 5ν bands by both models. Due to remaining uncertainties in the spectral analysis it is not possible to determine which version of the semi-empirical CKD models is superior.

- The Ma and Tipping far wing line shape theory [*Ma and Tipping* 1990] underestimates water continuum absorption by one order of magnitude in the 4ν and 5ν water bands, and by two orders of magnitude in the $4\nu+\delta$ water band.

- Water dimer absorption based on up-to-date spectroscopic and thermochemical data does not account for the observed magnitude of water continuum absorption.

Water dimer absorption is investigated in detail. The spectral analysis is based on the calculated overtone spectra of *Low and Kjaergaard* [1999] and *Schofield and Kjaergaard* [2003]. Three water dimer bands, $|0\rangle_{\mathrm{f}}|4\rangle_{\mathrm{b}}|0\rangle$ at 746 nm, $|0\rangle_{\mathrm{f}}|4\rangle_{\mathrm{b}}|1\rangle$ at 667 nm, and $|0\rangle_{\mathrm{f}}|5\rangle_{\mathrm{b}}|0\rangle$ at 613 nm are predicted to exist almost free of interference by strong water monomer absorption.

- The first evidence for atmospheric water dimer detection as reported recently by *Pfeilsticker et al.* [2003] has to be revoked, as the findings can not be confirmed by subsequent measurements, especially by those carried out in the tropics.

- Water dimer absorption is possibly observed in the tropics at 747 nm ($|0\rangle_{\mathrm{f}}|4\rangle_{\mathrm{b}}|0\rangle$ band) and at 614 nm ($|0\rangle_{\mathrm{f}}|5\rangle_{\mathrm{b}}|0\rangle$ band). A firm evidence of water dimer absorption requires to check a quadratic dependence on the water monomer absorption. This is not possible due to large residual structures of the spectral analysis and a weak variation (20%) of water vapor concentration. Water vapor concentrations at mid-latitudes are too low in order to detect these absorption signals. Water dimer absorption by the $|0\rangle_{\mathrm{f}}|4\rangle_{\mathrm{b}}|1\rangle$ band is below the detection limit.

- The measurements suggest a lower limit of the water dimer band FWHM of 40 cm^{-1}. Values up to 100 cm^{-1} are also consistent with the measurements.

- The upper limit of the water dimer equilibrium constant is $K_P(301\,\mathrm{K})$=0.055 atm^{-1} for any water dimer band broadening being smaller than 100 cm^{-1}. This result agrees well with the extrapolated data of *Curtiss et al.* [1979], the measurements of [*Ptashnik et al.* 2004], and the calculations of *Slanina and Crifo* [1992]. The upper limit also agrees with the small equilibrium constants of *Vaida and Headrick* [2000] and *Muñoz-Caro and Niño* [1997], but it disagrees with the theoretical study of *Goldman et al.* [2001] unless the water dimer band would be considerably broader than 100 cm^{-1}.

It was shown in the course of this thesis that significant atmospheric water vapor continuum absorption occurs in the visible and near-infrared spectral regions of the 4ν, $4\nu{+}\delta$ and 5ν water polyads. It is widely accepted by the atmospheric science community that water continuum absorption is caused by different mechanisms, the far wing contribution, collision-induced absorption, and the contribution by water dimers and further collision complexes. The water dimers can be classified into domains of truly bound dimers, metastable dimers, and free pair states. The correct partitioning into these domains at atmospheric temperatures and the link to water continuum theories and models are controversial issues to date. The Ma and Tipping far wing line shape theory falls short when describing the total observed water continuum absorption. It is still matter of dispute to what extend metastable and bound water dimers are included in this theory. In contrast, water continuum absorption is adequately described by the semi-empirical CKD water continuum models, but a fundamental physical understanding of water continuum absorption is still lacking. The CKD models may implicitly include water dimers.

A direct access to water dimer absorption was prevented by interfering residual structures due to unremovable water monomer absorption. It is the inaccuracy and the incompleteness of existing water vapor spectral line databases making it impossible to detect water dimer absorption in the visible and near-infrared spectral region. The theoretical LP-DOAS detection limit of $\alpha \approx 3 \times 10^{-10}\,\mathrm{cm}^{-1}$ was by far not achieved in the present measurements. In order to benefit from the full power of the LP-DOAS technique, high resolution measurements of the water monomer spectrum are required with a sensitivity in the order of $\alpha = 10^{-10}\,\mathrm{cm}^{-1}$. Such sensitive measurements are possible by cavity ring down spectroscopy as recently carried out by *Kassi et al.* [2005]. In particular, these measurements are most urgently needed in the wavelength regions where the water dimer $|0\rangle_\mathrm{f}|4\rangle_\mathrm{b}|0\rangle$ and $|0\rangle_\mathrm{f}|5\rangle_\mathrm{b}|0\rangle$ bands are predicted.

References

AFO (2005). Results of the German Atmospheric Research Programme - AFO 2000. Federal Ministry of Education and Research (BMBF). `http://www.afo-2000.de`.

Akhmatskaya, E. V., C. J. Apps, I. H. Hillier, A. J. Masters, N. E. Watt, and J. C. Whitehead (1997). Formation of H_2SO_4 from SO_3 and H_2O, catalysed in water clusters. *Chem. Commun.,* Vol. 7, 707.

Albrecht, B. A. (1989). Aerosols, cloud microphysics, and fractional cloudiness. *Science,* Vol. 245, 1227–1230.

Albritton, D. L., A. L. Schmeltekopf, and R. N. Zare (1976). An Introduction to the Least-Squares Fitting of Spectroscopic Data. In R. K. Narahari and M. W. Weldon (Eds.), *Molecular Spectroscopy: Modern Research*. Orlando, Florida, USA: Academic Press.

Allard, F., P. H. Hauschildt, D. R. Alexander, and S. Starrfield (1997). Model atmospheres of very low mass stars and brown dwarfs. *Ann. Rev. Astron. Astrophys.,* Vol. 35, 137–177.

Aloisio, S. and J. S. Francisco (1998). Existence of a hydroperoxy and water ($HO_2 \cdot H_2O$) radical complex. *J. Phys. Chem. A,* Vol. 102, 1899–1902.

Aloisio, S., J. S. Francisco, and R. R. Friedl (2000). Experimental evidence for the existence of the HO_2–H_2O complex. *J. Phys. Chem. A,* Vol. 104, 6597–6601.

Anderson, S. and K. Mauersberger (1992). Laser measurements of ozone absorption cross sections in the Chappuis band. *Geophys. Res. Lett.,* Vol. 19, 933–936.

Andreae, M. O., C. D. Jones, and P. M. Cox (2005). Strong present-day aerosol cooling implies a hot future. *Nature,* Vol. 435, 1187–1190.

Ardanuy, P. E., L. L. Stowe, and A. Gruber (1991). Shortwave, longwave, and net cloud-radiative forcing as determined from Nimbus-7 observations. *J. Geophys. Res.,* Vol. 96, 18537–18549.

Arking, A. (1996). Absorption of solar energy in the atmosphere: Discrepancy between model and observations. *Science,* Vol. 273, 779–782.

Arnold, F., T. Bührke, and S. Qiu (1990). Evidence for stratospheric ozone-depleting heterogeneous chemistry on volcanic aerosols from El Chichón. *Nature,* Vol. 348, 49–50.

Barker, H. W., J.-J. Morcrette, and G. D. Alexander (1998). Broadband solar fluxes and heating rates for atmospheres with 3 clouds. *Quart. J. Roy. Meteor. Soc.,* Vol. 124, 1245–1271.

Bennartz, R. and U. Lohmann (2001). Impact of improved near infrared water vapor line data on absorption of solar radiation in GCMs. *Geophys. Res. Lett.,* Vol. 28, 4591–4594.

Bernath, P. F. (2002). Water in sunspots and stars. *Highlights in Astronomy,* Vol. 12, 70–72.

Bess, T. D. and G. L. Smith (1993). Earth radiation budget: Results of outgoing longwave radiation from Nimbus-7, NOAA-9 and ERBS satellites. *J. Appl. Meteor.,* Vol. 32, 813–824.

Bevington, P. R. (1969). *Data Reduction and Error Analysis for the Physical Sciences*. New York: McGraw-Hill.

Bignell, K., F. Saiedy, and P. A. Sheppard (1963). On the atmospheric infrared continuum. *J. Opt. Soc. Am.,* Vol. 53, 466–479.

Bohren, C. F. and D. R. Huffman (1998). *Absorption and Scattering of Light by Small Particles*. New York: Wiley.

Braly, L. B., K. Liu, M. G. Brown, F. N. Keutsch, R. S. Fellers, and R. J. Saykally (2000). Terahertz laser spectroscopy of the water dimer intermolecular vibrations. II. $(H_2O)_2$. *J. Chem. Phys.,* Vol. 112, 10314–10326.

Bransden, B. H. and C. J. Joachain (1983). *Physics of Atoms and Molecules*. London: Longman.

Brauers, T., M. Hausmann, U. Brandenburger, and H.-P. Dorn (1995). Improvement of Differential Optical Absorption Spectroscopy using Multi-Channel-Scanning-Techniques. *Appl. Opt.,* Vol. 34, 4472–4479.

Burch, D. E. (1981). Continuum absorption by H_2O. Technical Report AFGL-TR-81-0300, US Air Force Geophysics Laboratory, Hanscom Air Force Base, MA, USA.

Burch, D. E., D. A. Gryvnak, and R. R. Patty (1967). Absorption of infrared radiation by CO_2 and H_2O. Experimental techniques. *J. Opt. Soc. Am.,* Vol. 57, 885–895.

Busarow, K. L., R. C. Cohen, G. A. Blake, K. B. Laughlin, Y. T. Lee, and R. J. Saykally (1989). Measurement of the perpendicular rotation-tunneling spectrum of the water dimer by tunable far infrared laser spectroscopy in a planar supersonic jet. *J. Chem. Phys.,* Vol. 90, 3937–3943.

Butler, J. H., M. L. Bender, S. A. Montzka, A. D. Clark, E. S. Saltzman, C. M. Sucher, J. P. Severinghaus, and J. W. Elkins (1999). A record of atmospheric halocarbons during the twentieth century from polar firn air. *Nature,* Vol. 399, 749–755.

Byrne, R. N., R. C. J. Somerville, and B. Subasilar (1996). Broken-cloud enhancement of solar radiation absorption. *J. Atmos. Sci.,* Vol. 53, 878–886.

Camy-Peyret, C. and A. A. Vigasin (Eds.) (2003). *Weakly Interacting Molecular Pairs: Unconventional Absorbers of Radiation in the Atmosphere*, Volume 27 of *NATO Science Series IV: Earth and Environmental Sciences*. Kluwer Academic Publishers.

Casanova, S. E. B., K. P. Shine, T. Gradiner, M. Coleman, and H. Pegrum (2005). Assessment of the consistency of near-infrared water vapor line intensities using high spectral resolution ground-based Fourier-transform measurements of solar radiation. *J. Geophys. Res.,*. accepted.

Castleman, A. W., J., R. E. Davies, H. R. Munkelwitz, I. N. Tang, and W. P. Wood (1975). Kinetics of association reactions pertaining to H_2SO_4 aerosol formation. *Int. J. Chem. Kinet. Symp.,* Vol. 1, 629–640.

Cess, R. D., G. L. Potter, J. P. Blanchet, G. J. Boer, A. D. D. Genio, M. Deque, V. Dymnikov, V. Galin, W. L. Gates, S. J. Ghan, J. T. Kiehl, A. A. Lacis, H. L. Treut, Z. X. Li, X.-Z. Liang, B. J. McAvaney, V. P. Meleshko, J. F. B. Mitchell, J.-J. Morcrette, D. A. Randall, L. Rikus, E. Roeckner, J. F. Roer, U. Schlese, D. A. Sheinin, A. Slingo, A. P. Sokolov, K. E. Taylor, W. M. Washington, R. T. Wetherald, I. Yagai, and M.-H.

Zhang (1990). Intercomparison and interpretation of climate feedback processes in 19 atmospheric general circulation models. *J. Geophys. Res.,* Vol. 95, 16601–16615.

Cess, R. D., M. H. Zhang, P. Minnis, L. Corsetti, E. G. Dutton, B. W. Forgan, D. P. Garber, W. L. Gates, J. J. Hack, E. F. Harrison, X. Jing, J. T. Kiehl, C. N. Long, J.-J. Morcrette, G. J. Potter, V. Ramanathan, B. Subasilar, C. H. Withlock, D. Young, and Y. Zhou (1995). Absorption of solar radiation by clouds: Observations versus models. *Science,* Vol. 267, 496–499.

Chagas, J. C. S., D. A. Newnham, K. M. Smith, and K. P. Shine (2001). Effects of improvements in near-infrared water vapor line intensities on short-wave atmospheric absorption. *Geophys. Res. Lett.,* Vol. 28, 2401–2404.

Charlson, R. J., J. E. Lovelock, M. O. Andreae, and S. G. Warren (1987). Oceanic phytoplankton, atmospheric sulphur, cloud albedo and climate. *Nature,* Vol. 326, 655–661.

Chýlek, P. and D. J. W. Geldart (1997). Water vapor dimers and atmospheric absorption of electromagnetic radiation. *Geophys. Res. Lett.,* Vol. 24, 2015–2018.

Clough, S. A., F. X. Kneizys, and R. W. Davies (1989). Line shape and water vapor continuum. *Atmos. Res.,* Vol. 23, 229–241.

Coheur, P.-F., S. Fally, M. Carleer, C. Clerbaux, R. Colin, A. Jenouvrier, M.-F. Mérienne, C. Hermans, and A. C. Vandaele (2002). New water vapor line parameters in the 26 000–13 000 cm^{-1} region. *J. Quant. Spec. and Rad. Transf.,* Vol. 74, 493–510.

Coker, D. F., R. E. Miller, and R. O. Watts (1985). The infrared predissociation spectra of water clusters. *J. Chem. Phys.,* Vol. 82, 3554–3562.

Coker, D. F., J. R. Reimers, and R. O. Watts (1985). The infrared absorption spectrum of water. *Austr. J. Phys.,* Vol. 35, 623–638.

Cormier, J. G., R. Ciurylo, and J. R. Drummond (2002). Cavity ringdown spectroscopy measurements of the infrarad water vapor continuum. *J. Chem. Phys.,* Vol. 103, 1030–1034.

Cormier, J. G., J. T. Hodges, and J. R. Drummond (2005). Infrared water vapor continuum absorption at atmospheric temperature. *J. Chem. Phys.,* Vol. 122, 114309–114309–10.

Crifo, J. F. (1990). Water clusters in the coma of Comet Halley and their effect on the gas density, temperature, and velocity. *Icarus,* Vol. 84, 414–446.

Crifo, J. F. and Z. Slanina (1991). The formation and role of water dimers in a cometary atmosphere, with application to Comet P/Halley. *Astrophys. Journal,* Vol. 383, 351–355.

Curtiss, L. A., D. J. Frurip, and M. Blander (1979). Studies of molecular association in H_2O and D_2O vapors by measurement of thermal conductivity. *J. Chem. Phys.,* Vol. 71, 2703–2711.

Czerny, M. and A. F. Turner (1930). Über den Astigmatismus bei Spiegelspektrometern. *Zeitschrift für Physik,* Vol. 61, 792.

Daniel, J. S., S. Solomon, H. G. Kjaergaard, and D. P. Schofield (2004). Atmospheric water vapor complexes and the continuum. *Geophys. Res. Lett.,* Vol. 31, L06118.

Daniel, J. S., S. Solomon, R. W. Sanders, R. W. Portmann, and D. C. Miller (1999). Implication for water monomer and dimer solar absorption from observations at Boulder, Colorado. *J. Geophys. Res.,* Vol. 104, 16785–16791.

D'Ans-Lax (1967). Taschenbuch für Chemiker und Physiker. Springer. Berlin, Heidelberg, New York.

Davies, R. W. (1978). The effect of finite geometry on the three-dimensional transfer of solar irradiance in clouds. *J. Atmos. Sci.,* Vol. 35, 1712–1725.

Davies, R. W., R. H. Tipping, and S. A. Clough (1982). Dipole autocorrelation function for molecular pressure broadening: A quantum theory which satisfies the fluctuation-dissipation theorem. *Phys. Rev. A,* Vol. 26, 3378–3394.

de Bievre, P., M. Gallet, N. E. Holden, and I. L. Barnes (1984). Isotopic Abundances and Atomic Weights of the Elements. *J. Phys. Chem. Ref. Data,* Vol. 13, 809–891.

Dines, W. H. (1917). The heat balance of the atmosphere. *Quart. J. Roy. Meteor. Soc.,* Vol. 43, 151–158.

Dudhia, A. (2004). Reference forward model version 4.24: Software user's manual. Technical Report PO-MA-OXF-GS-0003, Eur. Space Technol. Cent. (ESTEC), Eur. Space Agency (ESA), Paris, France.

Dyke, T. R., K. M. Mack, and J. S. Muenter (1957). The structure of water dimer from molecular beam electric resonance spectroscopy. *J. Chem. Phys.,* Vol. 66, 498–510.

Elsasser, W. M. (1938a). Far infrared absorption of atmospheric water vapor. *Astrophys. J.,* Vol. 87, 497–507.

Elsasser, W. M. (1938b). Note on Atmospheric Absorption Caused by the Rotational Water Band. *Phys. Review,* Vol. 53, 768–768.

Epifanov, S. Y. and A. A. Vigasin (1997). Subdivision of phase space for anisotropically interacting water molecules. *Mol. Phys.,* Vol. 90, 101–106.

Etheridge, D. M., L. Steele, R. J. Francey, and R. L. Langenfelds (1998). Atmospheric methane between 1000 A.D. and present: Evidence of anthropogenic emissions and climatic variability. *J. Geophys. Res.,* Vol. 103, 15979–15993.

Etheridge, D. M., L. Steele, R. L. Langenfelds, R. J. Francey, J.-M. Barnola, and V. I. Morgan (1996). Natural and anthropogenic changes in atmospheric CO_2 over the last 1000 years from air in Antarctic ice and firn. *J. Geophys. Res.,* Vol. 101, 4115–4128.

Fally, S., P.-F. Coheur, M. Carleer, C. Clerbaux, R. Colin, A. Jenouvrier, M.-F. Mérienne, C. Hermans, and A. C. Vandaele (2003). Water vapor line broadening and shifting by air in the 26000–13000 cm^{-1} region. *J. Quant. Spec. and Rad. Transf.,* Vol. 82, 119–131.

Fellers, R. S., C. Leforestier, L. B. Braly, M. G. Brown, and R. J. Saykally (1999). Spectroscopic determination of the water pair potential. *Science,* Vol. 284, 945–948.

Finlayson-Pitts, B. J. and J. N. Pitts, Jr. (2000). *Chemistry of the Upper and Lower Atmosphere*. San Diego: Academic Press.

Frankenberg, C. (2006). *Retrieval of methane and carbon monoxide using near infrared spectra recorded by SCIAMACHY onboard ENVISAT: Algorithm development and data analysis*. Ph. D. thesis, Institut für Umweltphysik, Universität Heidelberg, `http://www.ub.uni-heidelberg.de/archiv/6016`.

Frommhold, L. (1993). *Collision-induced Absorption in Gases*. Cambridge: Cambridge University Press.

Goldman, N., R. S. Fellers, M. G. Brown, L. B. Braly, C. J. Keoshian, C. Leforestier, and R. J. Saykally (2002). Spectroscopic determination of the water dimer intermolecular potential-energy surface. *J. Chem. Phys.,* Vol. 116, 10148–10163.

Goldman, N., R. S. Fellers, C. Leforestier, and R. J. Saykally (2001). Water dimers in the atmosphere: Equilibrium constant for water dimerization from the VRT(ASP-W) potential surface. *J. Phys. Chem. A,* Vol. 105, 515–519.

Goldman, N., C. Leforestier, and R. J. Saykally (2004). Water dimers in the atmosphere II: Results from the VRT(ASP-W)III potential surface. *J. Phys. Chem. A,* Vol. 108, 787–794.

Goldman, N. and R. J. Saykally (2004). Elucidating the role of many-body forces in liquid water. I. Simulations of water clusters on the VRT(ASP-W) potential surfaces. *J. Chem. Phys.,* Vol. 120, 4777–4789.

Goody, R. M. and Y. L. Yung (1989). *Atmospheric Radiation: Theoretical Basis*. New York: Oxford University Press.

Greenblatt, G. D., J. J. Orlando, J. B. Burkholder, and A. R. Ravishankara (1990). Absorption measurements of oxygen between 330 and 1140 nm. *J. Geophys. Res.,* Vol. 95, 18577–18582.

Hall, A. and S. Manabe (1999). The role of water vapor feedback in unperturbed climate variability and global warming. *J. Clim.,* Vol. 12, 2327–2346.

Halthore, R. N., S. Nemesure, S. E. Schwartz, D. G. Imre, A. Berk, E. G. Dutton, and M. H. Bergin (1998). Models overestimate diffuse clear-sky surface irradiance: A case for excess atmospheric absorption. *Geophys. Res. Lett.,* Vol. 25, 3591–3594.

Harrison, E. F., P. Minnis, B. R. Barkstrom, V. Ramanathan, R. D. Cess, and G. G. Gibson (1990). Seasonal variation of cloud radiative forcing derived from the Earth Radiation Budget Experiment. *J. Geophys. Res.,* Vol. 95, 18687–18703.

Hausmann, M., U. Brandenburger, T. Brauers, and H.-P. Dorn (1999). Simple Monte Carlo methods to estimate the spectra evaluation error in differential-optical-absorption spectroscopy. *Appl. Opt.,* Vol. 38, 462–475.

Haywood, J. M. and K. P. Shine (1995). The effect of anthropogenic sulfate and soot aerosol on the clear sky planetary radiation budget. *Geophys. Res. Lett.,* Vol. 22, 603–606.

Held, I. M. and B. J. Soden (2000). Water vapor feedback and global warming. *Ann. Rev. Energy Env.,* Vol. 25, 441–475.

Hermes, T. (1999). *Lichtquellen und Optik für die Differentielle Optische Absorptionsspektroskopie*. Diploma thesis, Institut für Umweltphysik, Universität Heidelberg.

Hettner, G. (1918). Über das ultrarote Absorptionsspektrum des Wasserdampfes. *Ann. Phys.,* Vol. 55, 476–496.

Hill, C. and R. Jones (2000). Absorption of solar radiation by water vapor in clear and cloudy skies: Implications for anomalous absorption. *J. Geophys. Res.,* Vol. 105, 9421–9428.

Hill, T. (1956). *Statistical Mechanics*. New York: McGraw-Hill.

Hönninger, G. (2002). *Halogen Oxide Studies in the Boundary Layer by Multi Axis Differential Optical Absorption Spectroscopy and Active Longpath-DOAS*. Ph. D. thesis, Institut für Umweltphysik, Universität Heidelberg, `http://www.ub.uni-heidelberg.de/archiv/1940`.

Hönninger, G., C. von Friedeburg, and U. Platt (2004). Multi axis differential optical absorption spectroscopy (MAX-DOAS). *Atm. Chem. and Phys.,* Vol. 4, 231–254,.

Huang, Z. S. and R. E. Miller (1989). High-resolution near-infrared spectroscopy of water dimer. *J. Chem. Phys.,* Vol. 91, 6613–6631.

Huisken, F., M. Kaloudis, and A. Kulcke (1996). Infrared spectroscopy of small size-selected water clusters. *J. Chem. Phys.,* Vol. 104, 17–25.

Humlíĉek, J. (1982). Optimized computation of the Voigt and complex probability functions. *J. Quant. Spec. and Rad. Transf.,* Vol. 82, 472.

Huneycutt, A. J. and R. J. Saykally (2003). Building Solutions – One Molecule at a Time. *Science,* Vol. 299, 1329.

Hunt, G. E., R. Kandel, and A. T. Mecherikunnel (1986). A history of presatellite investigations of the earth's radiation budget. *Rev. Geophys.,* Vol. 24, 351–356.

Imre, D. G., E. H. Abramson, and P. H. Daum (1996). Quantifying cloud-induced shortwave absorption: An examination of uncertainties and of recent auguments for large excess absorption. *J. Appl. Meteor.,* Vol. 35, 1991–2010.

IPCC (2001). *Climate Change 2001: The Scientific Basis. Contribution of Working Group I to the Third Assessment Report of the Intergovernmental Panel on Climate Change*, [Houghton, J. T. and Y. Ding and D. J. Griggs and M. Noguer and P. J. van der Linden and X. Dai and K. Maskell and . A. Johnson (Eds.)]. Cambridge University Press, Cambridge, UK and New York, NY, USA.

Jayne, J. T., U. Pöschl, Y.-M. Chen, D. Dai, L. T. Molina, D. R. Worsnop, C. E. Kolb, and M. J. Molina (1997). Pressure and temperature dependence of the gas-phase reaction of SO_3 with H_2O and the heterogeneous reaction of SO_3 with H_2O/H_2SO_4 surfaces. *J. Phys. Chem. A,* Vol. 101, 10000–10011.

Junge, C. E. (1961). Vertical profiles of condensation nuclei in the stratosphere. *J. Atmos. Sci.,* Vol. 18, 501–509.

Kassi, S., P. Macko, O. Naumenko, and A. Campargue (2005). The absorption spectrum of water near 750 nm by CW-CRDS: contribution to the search of water dimer absorption. *Phys. Chem. Chem. Phys.,* Vol. 7, 2460–2467.

Keeling, C. D., R. B. Bacastow, A. E. Bain-Bridge, C. A. Ekdahl, P. R. Guenther, L. S. Waterman, and J. F. S. Chin (1976). Atmospheric carbon dioxide variations at Mauna Loa Observatory, Hawaii. *Tellus,* Vol. 28, 538.

Keeling, C. D. and T. P. Whorf (2005). Atmospheric CO_2 records from sites in the SIO air sampling network. In trends: A compendium of data on global change. Carbon Dioxide Information Analysis Center, Oak Ridge National Laboratory, U.S. Department of Energy, Oak Ridge, Tenn., U.S.A. (`http://cdiac.ornl.gov/trends/co2/sio-mlo.htm`).

Kell, G. S., G. E. McLaurin, and E. Whalley (1968). PVT properties of water. II. Virial coefficients in the range 150°–450°C without independent measurement of vapor volumes. *J. Chem. Phys.,* Vol. 48, 3805–3813.

Kell, G. S., G. E. McLaurin, and E. Whalley (1989). *Proc. R. Soc. London Ser. A,* Vol. 425, 49–71.

Kern, C., S. Trick, B. Rippel, and U. Platt (2006). Applicability of light-emitting diodes as light sources for active differential optical absorption spectroscopy measurements. *Appl. Opt.,* Vol. 45, 2077–2088.

Keutsch, F. N. and R. J. Saykally (2001). Water clusters: Untangling the mysteries of the liquid, one molecule at a time. *PNAS,* Vol. 98, 10533–10540.

Kiehl, J. T. and K. E. Trenberth (1997). Earth's annual global mean energy budget. *Bull. Am. Met. Soc.,* Vol. 78, 197–208.

Kjaergaard, H. G., B. R. Henry, and A. W. Tarr (1991). Intensities in local mode overtone spectra of dimethyl ether and acetone. *J. Chem. Phys.,* Vol. 94, 5844–5854.

Kjaergaard, H. G., T. W. Robinson, D. L. Howard, J. S. Daniel, J. E. Headrick, and V. Vaida (2003). Complexes of importance to the absorption of solar radiation. *J. Phys. Chem. A,* Vol. 107, 10680–10686.

Kjaergaard, H. G., D. M. Turnbull, and B. R. Henry (1993). Intensities of CH- and CD-stretching overtones in 1,3-butadiene and 1,3-butadiene-d_6. *J. Chem. Phys.,* Vol. 99, 9438–9452.

Knoll, P., R. Singerand, and W. Kiefer (1990). Improving spectroscopic techniques by a scanning multi channel technique. *Appl. Spectr.,* Vol. 44, 776–782.

Kolb, C. E., J. T. Jayne, D. R. Worsnop, M. J. Molina, R. F. Meads, and A. A. Viggiano (1994). Gas phase reaction of sulfur trioxide with water vapor. *J. Am. Chem. Soc.,* Vol. 116, 10314–10315.

Kraus, S. (2003). DOASIS software. Institut für Umweltphysik, Universität Heidelberg. `http://www.iup.uni-heidelberg.de/institut/forschung/groups/atmosphere/software`.

Kuntz, M. (1997). A new implementation of the Humlíĉek algorithm for the calculation of the Voigt profile function. *J. Quant. Spec. and Rad. Transf.,* Vol. 57, 819–824.

Levenberg, K. (1944). A method for the solution of certain non-linear problems in least squares. *Quart. Appl. Math.,* Vol. 2, 164–168.

Li, Z. (1998). Infuence of absorbing aerosols on the inference of solar surface radiation budget and cloud absorption. *J. Clim.,* Vol. 11, 5–17.

Li, Z., H. W. Barker, and L. Moreau (1995). The variable effect of clouds on atmospheric absorption of solar radiation. *Nature,* Vol. 376, 486–490.

Li, Z. and L. Moreau (1996). Alteration of atmospheric solar absorption by clouds: Simulation and observation. *J. Appl. Meteor.,* Vol. 35, 653–670.

Lide, D. R. (1995). *Handbook of Chemistry and Physics* (76 ed.). Boca Raton: CRC Press.

Liou, K.-N. (1992). *Radiation and Cloud Processes in the Atmosphere: Theory, Observations and Modeling*. New York: Oxford Univ. Press.

Loerting, T. and K. R. Liedl (2000). Toward elimination of discrepancies between theory and experiment: The rate constant of the atmospheric conversion of SO_3 to H_2SO_4. *Proc. Natl. Acad. Sci. USA,* Vol. 97, 8874–8878.

Lovejoy, E. R., D. R. Hanson, and L. G. Huey (1996). Kinetics and products of the gas-phase reaction of SO_3 with water. *J. Phys. Chem.,* Vol. 100, 19911–19916.

Low, G. R. and H. G. Kjaergaard (1999). Calculation of OH-stretching band intensities of the water dimer and trimer. *J. Chem. Phys.,* Vol. 110, 9104–9115.

Lubin, D., J.-P. Chen, P. Pilewskie, V. Ramanathan, and F. P. J. Valero (1996). Microphysical examination of excess cloud absorption in the tropical atmosphere. *J. Geophys. Res.,* Vol. 101, 16961–16972.

Ma, Q. and R. H. Tipping (1990). Water vapor continuum in the millimeter spectral region. *J. Chem. Phys.,* Vol. 93, 6127–6139.

Ma, Q. and R. H. Tipping (1991). A far wing line shape theory and its application to the water continuum absorption in the infrared region. I. *J. Chem. Phys.,* Vol. 95, 6290–6301.

Ma, Q. and R. H. Tipping (1992a). A far wing line shape theory and its application to the water foreign-broadened water continuum absorption. III. *J. Chem. Phys.,* Vol. 97, 818–828.

Ma, Q. and R. H. Tipping (1992b). A far wing line shape theory and its application to the water vibrational bands (II). *J. Chem. Phys.,* Vol. 96, 8655–8663.

Ma, Q. and R. H. Tipping (1999a). The averaged density matrix in the coordinate representation: Application to the calculation of the far-wing line shapes for H_2O. *J. Chem. Phys.,* Vol. 111, 5909–5921.

Ma, Q. and R. H. Tipping (1999b). The density matrix of H_2O - N_2 in the coordinate representation: A Monte Carlo calculation of the far-wing line shape. *J. Chem. Phys.,* Vol. 112, 574–584.

Ma, Q. and R. H. Tipping (2002). The frequency detuning correction and the asymmetry of line shapes: The far wings of H_2O-H_2O. *J. Chem. Phys.,* Vol. 116, 4102–4115.

Machida, T., T. Nakazawa, Y. Fujii, S. Aoki, and O. Watanabe (1995). Increase in the atmospheric nitrous oxide concentration during the last 250 years. *Geophys. Res. Lett.,* Vol. 22, 2921–2924.

Marquardt, D. W. (1963). An algorithm for least squares estimation of non-linear parameters. *Soc. Indust. Appl. Math,* Vol. 11, 431–441.

Marshak, A., A. Davis, W. Wiscombe, and R. Cahalan (1995). Radiative Smoothing in Fractal Clouds. *J. Geophys. Res.,* Vol. 100, 26247–26261.

Marshak, A., A. Davis, W. Wiscombe, and R. Cahalan (1997). Inhomogeneity effects of cloud shortwave absorption measurements: Two-aircraft simulations. *J. Geophys. Res.,* Vol. 102, 16619–16637.

Marshak, A., A. Davis, W. Wiscombe, and R. Cahalan (1998). Radiative effects of sub-mean free path liquid water variability in stratiform clouds. *J. Geophys. Res.,* Vol. 103, 19557–19567.

Muñoz-Caro, C. and A. Niño (1997). Effect of anharmonicities on the thermodynamic properties of the water dimer. *J. Phys. Chem. A,* Vol. 101, 4128–4135.

McClatchey, R. A., W. S. Benedict, S. A. Clough, D. E. Burch, R. F. Calfee, K. Fox, L. S. Rothman, and J. S. Garing (1973). AFCRL atmospheric absorption line parameters compilation. Technical Report AFCRL-TR-73-0096, Air Force Cambridge Research Laboratories, Hanscom Air Force Base, MA, USA.

McGlashan, M. L. and C. J. Wormald (2000). The isothermal Joule-Thomson coefficient of steam measured from T=313.00 K to T=413.19 K. *J. Geophys. Res.,* Vol. 32, 1489–1503.

Mentel, T. F., D. Bleilebens, and A. Wahner (1996). A study of nighttime nitrogen oxide oxidation in a large reaction chamber – the fate of NO_2, N_2O_5, HNO_3, and O_3 at different humidities. *Atm. Env.,* Vol. 30, 4007–4020.

Mhin, B. J., S. J. Le, and K. S. Kim (1993). Water-cluster distribution with respect to pressure and temperature in the gas phase. *Phys. Rev. A,* Vol. 48, 3764–3770.

Mie, G. (1908). Beiträge zur Optik trüber Medien, speziell kolloidaler Metallösungen. *Annalen der Physik,* Vol. 25, 377–445.

Mitsel, A. A., I. V. Ptashnik, K. M. Firsov, and A. B. Fomin (1995). Efficient technique for line-by-line calculating the transmittance of the absorbing atmosphere. *Atmos. Oceanic Opt.,* Vol. 8, 847–850.

Mlawer, E., D. Tobin, and S. Clough (2004). A revised perspective on the water vapor continuum: the MT_CKD model. In preparation (`http://rtweb.aer.com/continuum_frame.html`).

Mlawer, E. J., S. A. Clough, P. D. Brown, and D. C. Tobin (1999). Recent developments in the water vapor continuum. In *Ninth ARM Science Team Meeting Proceedings*, March 22-26, San Antonio, TX, pp. 1–6.

Morokuma, K. and C. Muguruma (1994). Ab initio molecular orbital study of the mechanism of the gas phase reaction SO_3 + H_2O: Importance of the second water molecule. *J. Am. Chem. Soc.,* Vol. 116, 10316–10317.

Mozurkewich, M. and J. G. Calvert (1988). Reaction probability of N_2O_5 on aqueous aerosols. *J. Geophys. Res.,* Vol. 93, 15889–15896.

Myhre, G., F. Stordal, K. Restad, and I. S. A. Isaksen (1998). Estimation of the direct radiative forcing due to sulphate and soot aerosols. *Tellus,* Vol. 50B, 463–477.

National Academy of Sciences (1994). *Solar influences on global change*. Washington D.C.: National Academy Press.

Neftel, A., E. Moor, H. Oeschger, and B. Stauffer (1985). Evidence from polar ice cores for the increase in atmospheric CO_2 in the past two centuries. *Nature,* Vol. 315, 45–47.

Noxon, J. F., R. B. Norton, and W. R. Henderson (1978). Observation of atmospheric NO_3. *Geophys. Res. Lett.,* Vol. 5, 675–678.

Noxon, J. F., R. B. Norton, and E. Marovich (1980). NO_3 in the troposphere. *Geophys. Res. Lett.,* Vol. 7, 125–128.

Page, R. H., J. G. Frey, Y.-R. Shen, and Y. T. Lee (1984). Infrared predissociation spectra of water dimer in a supersonic molecular beam. *Chem. Phys. Lett.,* Vol. 106, 373–376.

Partridge, H. and D. W. Schwenke (1997). The determination of an accurate isotope dependent potential energy surface for water from extensive ab initio calculations and experimental data. *J. Chem. Phys.,* Vol. 106, 4618–4639.

Paul, J. B., C. P. Collier, J. J. Scherer, A. O'Keefe, and R. J. Saykally (1997). Direct measurement of water cluster concentrations by infrared cavity ringdown laser absorption spectroscopy. *J. Phys. Chem. A,* Vol. 101, 5211–5214.

Paul, J. B., R. A. Provencal, C. Chapo, K. Roth, R. Casaes, and R. J. Saykally (1999). Infrared cavity ringdown spectroscopy of the water cluster bending vibrations. *J. Phys. Chem. A,* Vol. 103, 2972–2974.

Peixoto, J. P. and A. H. Oort (1992). *Physics of Climate*. New York: Springer.

Penndorf, R. (1957). Tables of the refractive index for standard air and the rayleigh scattering coefficient for the spectral region between 0.2 and 200 μ and their application to atmospheric optics. *J. Opt. Soc. Am.,* Vol. 47, 176–182.

Penner, J. E., C. C. Chuang, and K. Grant (1998). Climate forcing by carbonaceous and sulphate aerosols. *Clim. Dyn.,* Vol. 14, 839–851.

Penner, S. S. and P. Varanasi (1967). Spectral absorption coefficients in the pure rotation spectrum of water vapor. *J. Quant. Spec. and Rad. Transf.,* Vol. 7, 687–690.

Peters, C. (2005). *Studies of Reactive Halogen Species (RHS) in the Marine and mid-Latitudinal Boundary Layer by Active Longpath Differential Optical Absorption Spectroscopy*. Ph. D. thesis, Institut für Umweltphysik, Universität Heidelberg, `http://www.ub.uni-heidelberg.de/archiv/5650`.

Pfeilsticker, K., F. Erle, O. Funk, L. Marquard, T. Wagner, and U. Platt (1998). Optical path modifications due to tropospheric clouds: Implications for zenith sky measurements of stratospheric gases. *J. Geophys. Res.,* Vol. 103, 25323–25336.

Pfeilsticker, K., F. Erle, and U. Platt (1997). Absorption of solar radiation by atmospheric O_4. *J. Atmos. Sci.,* Vol. 54, 933–939.

Pfeilsticker, K., A. Lotter, C. Peters, and H. Bösch (2003). Atmospheric detection of water dimers via near-infrared absorption. *Science,* Vol. 300, 2078–2080.

Pilewskie, P. and F. Valero (1995). Direct observations of excess solar absorption by clouds. *Science,* Vol. 257, 1626–1629.

Platt, U. (1994). Differential optical absorption spectroscopy (DOAS). In W. M. Sigrist (Ed.), *Air Monitoring by Spectroscopic Techniques*, pp. 27–84. New York: John Wiley & Sons.

Platt, U., D. Perner, and H. Pätz (1979). Simultaneous measurement of atmospheric CH_2O, O_3, and NO_2 by differential optical absorption. *J. Geophys. Res.,* Vol. 84, 6329–6335.

Platt, U., D. Perner, A. M. Winer, G. W. Harris, and J. N. Pitts, Jr. (1980). Detection of NO_3 in the polluted troposphere by differential optical absorption. *Geophys. Res. Lett.,* Vol. 7, 89–92.

Platt, U., A. M. Winer, H. W. Biermann, R. Atkinson, and J. N. Pitts, Jr. (1984). Measurement of nitrate radical concentrations in continental air. *Environ. Sci. Technol.,* Vol. 18, 365–369.

Polyansky, O. L. (1985). One-dimensional approximation of the effective rotational Hamiltonian of the ground state of the water molecule. *J. Molec. Spectrosc.,* Vol. 112, 79–87.

Ptashnik, I. V. (2005). Natural water dimers absorption: known and "unknown" experiments. In preparation.

Ptashnik, I. V. and K. P. Shine (2003). Calculation of solar radiative fluxes in the atmosphere: the effect of updates in spectroscopic data. *Atmos. Oceanic Opt.,* Vol. 16, 251–255.

Ptashnik, I. V., K. M. Smith, K. P. Shine, and D. A. Newnham (2004). Laboratory measurements of water vapour continuum absorption in spectral region 5000–5600 cm-1: Evidence for water dimers. *Quart. J. Roy. Meteor. Soc.,* Vol. 130, 2391–2408.

Ramanathan, V. (1975). Greenhouse effect due to chlorofluorocarbons - Climatic implications. *Science,* Vol. 190, 50–52.

Ramanathan, V., R. D. Cess, E. F. Harrison, P. Minnis, B. R. Barkstrom, E. Ahmad, and D. Hartmann (1989). Cloud radiative forcing and climate: Results from the Earth Radiation Budget Experiment. *Science,* Vol. 243, 57–63.

Ramanathan, V., B. Subasilar, G. J. Zhang, W. Conant, R. D. Cess, J. T. Kiehl, H. Grassl, and L. Shi (1995). Warm pool heat budget and shortwave cloud forcing: A missing physics. *Science,* Vol. 267, 499–503.

Ramanathan, V. and A. Vogelmann (1997). Greenhouse effect, atmospheric solar absorption and the Earth's radiation budget: From the Arrhenius-Langley era to the 1990s. *Ambio,* Vol. 26, 38–46.

Reimers, J. R. and R. O. Watts (1984). The structure and vibrational spectra of small clusters of water molecules. *Chem. Phys.,* Vol. 85, 83–112.

Reimers, J. R., R. O. Watts, and M. L. Klein (1982). Intermolecular potential functions and the properties of water. *Chem. Phys.,* Vol. 64, 95–114.

Reiner, T. and F. Arnold (1993). Laboratory flow reactor measurements of the reaction SO_3 + H_2O + M yields H_2SO_4 + M: Implications for gaseous H_2SO_4 and aerosol formation in the plumes of jet aircraft. *Geophys. Res. Lett.,* Vol. 20, 2659–2662.

Rosenkranz, P. W. (1985). Pressure broadening of rotational bands. I. A statistical theory. *J. Chem. Phys.,* Vol. 83, 6139–6144.

Rossow, W. B., A. W. Walker, and L. C. Garder (1993). Comparison of ISCCP and other cloud amounts. *J. Climate,* Vol. 6, 2394–2418.

Rossow, W. B. and Y.-C. Zhang (1995). Calculation of surface and top of atmosphere radiative fluxes from physical quantities based on ISCCP data set 2. Validation and first results. *J. Geophys. Res.,* Vol. 100, 1167–1197.

Rothman, L. S., A. Barbe, D. C. Benner, L. R. Brown, C. Camy-Peyret, M. R. Carleer, K. Chance, C. Clerbaux, V. Dana, V. M. Devi, A. Fayt, J.-M. F. P., R. R. Gamache, A. Goldman, D. Jacquemart, K. W. Jucks, W. J. Lafferty, J.-Y. Mandin, S. T. Massie, V. Nemtchinov, D. A. Newnham, A. Perrin, C. P. Rinsland, J. Schroeder, K. M. Smith, M. A. H. Smith, K. Tang, R. A. Toth, J. V. Auwera, P. Varanasi, and K. Yoshino (2003). The HITRAN molecular spectroscopic database: edition of 2000 including updates through 2001. *J. Quant. Spec. and Rad. Transf.,* Vol. 82, 5–44.

Rothman, L. S., D. Jacquemart, A. Barbe, D. C. Benner, M. Birk, L. R. Brown, M. R. Carleer, C. C. Jr., K. Chance, L. H. Coudert, V. Dana, V. M. Devi, J.-M. F. P., R. R. Gamache, A. Goldman, J.-M. Hartmann, K. W. Jucks, A. G. Maki, J.-Y. Mandin, S. T. Massie, J. Orphal, A. Perrin, C. P. Rinsland, M. A. H. Smith, J. Tennyson, R. N. Tolchenov, R. A. Toth, J. V. Auwera, P. Varanasi, and G. Wagner (2005). The HITRAN 2004 molecular spectroscopic database. *J. Quant. Spec. and Rad. Transf.,* Vol. 96, 139–204.

Rothman, L. S., C. P. Rinsland, A. Goldman, S. T. Massie, D. P. Edwards, J.-M. Flaud, A. Perrin, C. Camy-Peyret, V. Dana, J.-Y. Mandin, J. Schroeder, A. McCann, R. R. Gamache, R. B. Wattson, K. Yoshino, K. V. Chance, K. Jucks, L. R. Brown, V. Nemtchinov, and P. Varanasi (1998). The HITRAN Molecular Spectroscopic Database and HAWKS (HITRAN Atmospheric Workstation): 1996 Edition. *J. Quant. Spec. and Rad. Transf.,* Vol. 60, 665–710.

Sander, S. P. (1986). Temperature dependence of the NO_3 absorption spectrum. *J. Phys. Chem.,* Vol. 90, 4135–4142.

Schenter, G. K., S. M. Kathmann, and B. C. Garrett (2002). Equilibrium constant for water dimerization: Analysis of the partition function for a weakly bound system. *J. Phys. Chem. A,* Vol. 106, 1557–1566.

Scherer, M., M. Havenith, R. Mauersberger, and T. L. Wilson (1998). A search for $(H_2O)_2$ in the Galaxy and toward comet Hale-Bopp. *Astron. Astrophys.,* Vol. 335, 1070–1076.

Schermaul, R., R. C. M. Learner, D. A. Newnham, J. Ballard, N. F. Zobov, D. Belmiloud, and J. Tennyson (2001). The water vapor spectrum in the region 8 600–15 000 cm^{-1}: Experimental and theoretical studies for a new spectral line database. II. Linelist Construction. *J. Molec. Spectrosc.,* Vol. 208, 43–50.

Schermaul, R., R. C. M. Learner, D. A. Newnham, R. G. Williams, J. Ballard, N. F. Zobov, D. Belmiloud, and J. Tennyson (2001). The water vapor spectrum in the region 8 600–15 000 cm^{-1}: Experimental and theoretical studies for a new spectral line database. I. Laboratory Measurements. *J. Molec. Spectrosc.,* Vol. 208, 32–42.

Schneider, E. K., B. P. Kirtman, and R. S. Lindzen (1999). Tropospheric water vapor and climate sensitivity. *J. Atmos. Sci.,* Vol. 36, 1649–1658.

Schofield, D. P. and H. G. Kjaergaard (2003). Calculated OH-stretching and HOH-bending vibrational transitions in the water dimer. *Phys. Chem. Chem. Phys.,* Vol. 5, 3100–3105.

Schwärzle, J. (2005). *Spektroskopische Messung von Halogenoxiden in der marinen atmosphärischen Grenzschicht in Alcântara/Brasilien.* Diploma thesis, Institut für Umweltphysik, Universität Heidelberg.

Schwenke, D. W. and H. Partridge (2000). Convergence testing of the analytic representation of an ab initio dipole moment function for water: Improved fitting yields improved intensities. *J. Chem. Phys.,* Vol. 113, 6592–6597.

Sierk, B., S. Solomon, J. S. Daniel, R. W. Portmann, S. I. Gutman, A. O. Langford, C. S. Eubank, E. G. Dutton, and K. H. Holub (2004). Field measurements of water vapor continuum absorption in the visible and near-infrared. *J. Geophys. Res.,* Vol. 109, D08307.

Sierk, B., S. Solomon, J. S. Daniel, R. W. Portmann, S. I. Gutman, A. O. Langford, C. S. Eubank, K. H. Holub, and S. V. Florek (2003). Field test of spectral line intensity parameters for tropospheric water vapor. *J. Geophys. Res.,* Vol. 108, 4351.

Slanina, Z. (1988). A theoretiacl evaluation of water oligomer populations in the Earth's atmosphere. *J. Atmos. Chem.,* Vol. 6, 185–190.

Slanina, Z. and J.-F. Crifo (1992). A refined evaluation of the gas-phase water-dimerization equilibrium constant within non-rigid BJH- and MCY-type potentials. *Int. J. Thermophys.,* Vol. 13, 465–476.

Smith, B. J., D. J. Swanton, J. A. Pople, H. F. S. III, and L. Radom (1990). Transition structures for the interchange of hydrogen atoms within the water dimer. *J. Chem. Phys.,* Vol. 92, 1240–1247.

Snell, R. L., J. E. Howe, N. R. Erickson, M. L. N. Ashby, E. A. Bergin, S. C. Kleiner, G. J. Melnick, B. M. Patten, R. Plume, J. R. Stauffer, V. Tolls, Z. Wang, Y. F. Zhang, P. F. Goldsmith, M. Harwit, D. A. Neufeld, D. G. Koch, R. Schieder, G. Winnewisser, and G. Chin (1999). Water in Molecular Clouds. *Bull. Am. Met. Soc.,* Vol. 31, 1465.

Soden, B., S. Tjemkes, J. Schmetz, R. Saunders, J. Bates, B. Ellingson, R. Engelen, L. Garand, D. Jackson, G. Jedlovec, T. Kleespies, D. Randel, P. Rayer, E. Salathe, D. Schwarzkopf, N. Scott, B. Sohn, S. de Souza-Machado, L. Strow, D. Tobin, D. Turner, P. van Delst, and T. Wehr (2000). An intercomparison of radiation codes for retrieving upper-tropospheric humidity in the 6.3-mm Band: A report from the first GVaP Workshop. *Bull. Am. Met. Soc.,* Vol. 81, 797–808.

Solomon, S., R. W. Portman, R. W. Sanders, and J. S. Daniel (1998). Absorption of solar radiation by water vapor, oxygen and related collision pairs in the Earth's atmosphere. *J. Geophys. Res.,* Vol. 103, 3847–3858.

Staehelin, J., J. Thudium, R. Buehler, A. Volz-Thomas, and W. Graber (1994). Trends in surface ozone concentrations at Arosa (Switzerland). *Atm. Env.,* Vol. 28, 75–87.

Stephens, G. L. (1996). How much solar radiation do clouds absorb? *Science,* Vol. 271, 1131–1133.

Stephens, G. L. and S. C. Tsay (1990). On the cloud absorption anomaly. *Quart. J. Roy. Meteor. Soc.,* Vol. 116, 671–704.

Stockwell, W. R. and J. G. Calvert (1983). The mechanism of the HO–SO_2 reaction. *Atm. Env.,* Vol. 17, 2231–2235.

Stogryn, D. E. and J. O. Hirschfelder (1959). Contribution of bound, metastable and free molecules to the second virial coefficient and some properties of double molecules. *J. Chem. Phys.,* Vol. 31, 1531–1545.

Stutz, J. (1991). *Charakterisierung von Photodiodenzeilen zur Messung stratosphärischer Spurenstoffe*. Diploma thesis, Institut für Umweltphysik, Universität Heidelberg.

Stutz, J. (1996). *Messung der Konzentration troposhärischer Spurenstoffe mittels Differentieller Optischer Absorptions Spektroskopie: Eine neue Generation von Geräten und Algorithmen*. Ph. D. thesis, Institut für Umweltphysik, Universität Heidelberg.

Stutz, J. and U. Platt (1992). Problems in Using Diode Arrays for Open Path DOAS Measurements of Atmospheric Species. *Proc. EOS/SPIE Symp. Berlin, Optical Methods in the Atmospheric Chemistry,* Vol. 1715, 329–340.

Stutz, J. and U. Platt (1996). Numerical Analysis and Estimation of the Statistical Error of Differential Optical Absorption Spectroscopy Measurements with Least-Squares methods. *Appl. Opt.,* Vol. 35, 6041–6053.

Stutz, J. and U. Platt (1997). Improving longpath differential optical absorption spectroscopy with a quartz-fiber mode mixer. *Appl. Opt.,* Vol. 36, 1105–1115.

Suck, S. H., A. E. Wetmore, T. S. Chen, and J. L. Kassner (1982). Role of various water clusters in IR absorption in the 8-14-micron window region. *Appl. Opt.,* Vol. 21, 1610–1614.

Suhm, M. A. and K. Pfeilsticker (2004). How Broad Are Water Dimer Bands? *Science,* Vol. 304, 823–824.

Tennyson, J. and O. L. Polyansky (1998). Water on the Sun: the Sun yields more secrets to spectroscopy. *Contemporary Physics,* Vol. 39, 283–294.

Thorne, A. P. (1988). *Spectrophysics* (2 ed.). London, New York: Chapman and Hall.

Tipping, R. H. and Q. Ma (1995). Theory of the water vapor continuum and validations. *Atm. Res.,* Vol. 36, 69–94.

Tobin, D. C., L. L. Strow, W. J. Lafferty, and W. B. Olson (1996). Experimental investigation of the self- and N_2-broadened continuum within the ν_2 band of water vapor. *Appl. Opt.,* Vol. 35, 4724–4734.

Tso, H. C. W., D. J. W. Geldart, and P. Chýlek (1998). Anharmonicity and cross section for absorption of radiation by water dimer. *J. Chem. Phys.,* Vol. 108, 5319–5329.

Tsuji, T. (1995). Molecules in the Atmospheres of Brown Dwarfs. In *ASP Conf. Ser. 81: Laboratory and Astronomical High Resolution Spectra*, pp. 566.

Twomey, S. (1977). The influence of pollution on the short wave albedo of clouds. *J. Atmos. Sci.,* Vol. 34, 1149–1152.

Vaida, V., J. S. Daniel, H. G. Kjaergaard, L. M. Goss, and A. F. Tuck (2001). Atmospheric absorption of near infrared and visible solar radiation by the hydrogen bonded water dimer. *Quart. J. Roy. Meteor. Soc.,* Vol. 127, 1627–1644.

Vaida, V. and J. E. Headrick (2000). Physicochemical properties of hydrated complexes in the Earth's atmosphere. *J. Phys. Chem. A,* Vol. 104, 5401–5412.

van Roozendael, M. and C. Fayt (2001). WinDoas 2.1. Belgium Institute for Space Aeronomie (BIRA-IASB). `http://www.aeronomie.be/`.

Van Thiel, M., E. D. Becker, and G. C. Pimentel (1957). Infrared studies of hydrogen bonding of water by the matrix isolation technique. *J. Chem. Phys.,* Vol. 27, 486–490.

Vandaele, A. C., C. Hermans, S. Fally, M. Carleer, R. Colin, M.-F. Mérienne, A. Jenouvrier, and B. Coquart (2002). High-resolution Fourier Transform Measurement of the NO_2 visible and near-infrared Absorption Cross-section: Temperature and Pressure Effects. *J. Geophys. Res.,* Vol. 107, 4348. `http://www.oma.be/BIRA-IASB/Scientific/Topics/Lower/LaboBase/Laboratory.html`.

Varanasi, P. and S. Chudamani (1987). Self- and N_2-broadened spectra of water vapor between 7.5 and 14.5 microns. *J. Quant. Spec. and Rad. Transf.,* Vol. 38, 407–412.

Vernon, M. F., D. J. Krajnovich, H. S. Kwok, J. M. Lisy, Y. R. Shen, and Y. T. Lee (1982). Infrared vibrational predissociation spectroscopy of water clusters by the crossed laser-molecular beam technique. *J. Chem. Phys.,* Vol. 77, 47–57.

Vigasin, A. A. (1998). *Molecular Complexes in Earth's, Planetary, Cometary and Interstellar Atmospheres*, Chapter Statistical physics and thermodynamics of bimolecular complexes, pp. 1–33. Singapore: World Scientific.

Vigasin, A. A. (2000). Water vapor continuous absorption in various mixtures: possible role of weakly bound complexes. *J. Quant. Spec. and Rad. Transf.,* Vol. 64, 25–40.

Vigasin, A. A. (2003). Bimolecular absorption in atmospheric gases. In C. Camy-Peyret and A. A. Vigasin (Eds.), *Weakly Interacting Molecular Pairs: Unconventional Absorbers of Radiation in the Atmosphere*, Volume 27 of *NATO Science Series IV: Earth and Environmental Sciences*, pp. 23–47. Kluwer Academic Publishers.

Wahner, A., T. F. Mentel, and M. Sohn (1998). Gas-phase reaction of N_2O_5 with water vapor: Importance of heterogeneous hydrolysis of N_2O_5 and surface desorption of HNO_3 in a large teflon chamber. *Geophys. Res. Lett.,* Vol. 25, 2169–2172.

Wallace, L., P. Bernath, W. Livingston, K. Hinkle, J. Busler, B. Guo, and K. Zhang (1995). Water on the Sun. *Science,* Vol. 268, 1155–1558.

Wang, X., Y. G. Jin, M. Suto, L. C. Lee, and H. E. O'Neal (1988). Rate constant of the gas phase reaction of SO_3 with H_2O. *J. Chem. Phys.,* Vol. 89, 4853–4860.

Wiscombe, W. J. (1980). Improved Mie scattering algorithms. *Appl. Opt.,* Vol. 19, 1505–1509.

Wiscombe, W. J., R. M. Welch, and W. W. Hall (1984). The effect of very large drops on cloud absorption. Part I: Parcel models. *J. Atmos. Sci.,* Vol. 41, 1336–1355.

WMO (2002). *Scientific Assessment of Ozone depletion: 2002.* World Meteorological Organization Global Ozone Research and Monitoring Project, Report No. 47.

Worden, H., R. Beer, and C. P. Rinsland (1997). Airborne infrared spectroscopy of 1994 western wildfires. *J. Geophys. Res.,* Vol. 102, 1287–1300.

Yao, M.-S. and A. D. D. Genio (1999). Effect of cloud parameterization on the simulation of climate changes in the GISS GCM. *J. Clim.,* Vol. 12, 761–779.

Zwart, E., J. J. ter Meulen, W. L. Meerts, and L. H. Coudert (1991). The submillimeter rotation tunneling spectrum of the water dimer. *J. Molec. Spectrosc.,* Vol. 147, 27–39.

Dankeschön & Thank you & Obrigado

Last but not least, I would like to thank all those people who have contributed to the successful completion of this work.

An erster Stelle danke ich Prof. Dr. Klaus Pfeilsticker für die interessante Themenstellung und die Übernahme der Begutachtung dieser Arbeit. Durch seine Vorschläge und Anregungen hat er diese Arbeit stets gefördert und mir immer wieder die Impulse gegeben, die schließlich zu ihrem Gelingen beitrugen.

Mein besonderer Dank gilt Herrn Prof. Dr. Ulrich Platt für die freundliche Aufnahme am Institut für Umweltphysik.

Ich danke Herrn Prof. Dr. Frank Arnold für die freundliche Übernahme der Begutachtung dieser Arbeit.

Vielen Dank an alle, die mich bei den Messkampagnen begleitet haben, mit ihrer tatkräftigen Unterstützung stets zur Hilfe standen und für eine kurzweilige Zeit während der langen Kampagnen sorgten. Besonders hervorheben möchte ich Christina Peters, die alle drei Kampagnen mitbestritten hat und immer mit Rat und Tat zur Seite stand. Sie hat die kompletten Vorbereitungen für die Kampagnen in Dagebüll und in der Bretagne übernommen und dabei ihr großes Organisationstalent bewiesen. Ein großes Dankeschön geht auch an Julia Schwärzle für ihre Mithilfe während der Kampagne in Brasilien. Desweiteren danke ich den Kampagnenbegleitern, Gerd, Anastasia, Roman, Stefan, Nicole, Frank und Oli für eine schöne und abwechslungsreiche Zeit.

Bei der DLR-MORABA bedanke ich mich besonders bei Peter Turner und Hansulrich Steimle für die Hilfe bei der Planung und Organisation der Kampagne in Alcântara.

Quería agradecer a todas as pessoas do "Centro de Lançamento de Alcântara" que contribuíram para o sucesso do projeto. Especialmente quería agradecer ao diretor pela permissão, assim como ao Coronel Moura, à Otilia, e ao Ribamar. Sem a ajuda deles a execução do projeto não seria possível.

Performing cavity ring down measurements of water vapor absorption by Alain Campargue and coworkers is highly acknowledged. I would like to thank Igor Ptashnik for his support in technical questions about the line-by-line radiative transfer codes. Further, my thanks go to Qiancheng Ma and Richard H. Tipping for providing up-to-date water vapor continuum data.

Vielen Dank an Hartmut, André, Marcel und Frank für anregende fachliche Diskussionen und für die Hilfestellung bei der WinDOAS-Auswertung .

Ein großes Dankeschön geht an Katja, Roland, Christoph, Frank, Marcel und Udo für das unermüdliche Korrekturlesen dieser Arbeit.

Der gesamten Arbeitsgruppe danke ich für die stets gute Atmosphäre am Institut. Hervorheben möchte ich meine Zimmerkollegen Marcel, Christoph und Martin, sowie alle die immer wieder für eine Auflockerung des Büroalltages sorgten: Tina, Thomas, Frank, André, Hartmut, Klaus, Julia, Katja, Strick, Gerd, Jutta, Thierry, Roland, Susanne, Linda, Oli, Lena, Uli, ...

Schließlich bedanke ich mich ganz besonders bei meinen Eltern für die fortwährende Unterstützung während meines Studiums und meiner Doktorarbeit.